ABSTRACT

ELECTRIC-FIELD-DRIVEN PROCESSES IN MULTIPHASE FLUID SYSTEMS

by
Qian Lei

Advantages of using electric fields in miniaturized apparatuses for a wide range of applications are revealed by numerous experimental and theoretical studies over the last several decades as it offers a simple and efficient method for manipulation of multiphase fluid systems. This approach is considered to be especially beneficial for control of boiling processes and colloidal suspensions considered in the presented work.

Boiling. Today's trends for enhancing boiling heat transfer in terrestrial and space applications focus on removal of bubbles to prevent formation of a vapor layer over the surface at a high overheat. In contrast, this dissertation presents a new boiling regime that employs a vapor-air bubble residing on a small heater for minutes and driving cold water over the surface to provide high heat flux. Single-bubble boiling of water was investigated under normal gravity and low gravity in parabolic flights. Experiments demonstrated a negligible effect of gravity level on the rate of heat transfer from the heater. Due to self-adjustment of the bubble size, the heat flux provided by boiling rose linearly up with increasing heater temperature and was not affected by a gradually rising water temperature. The fast response and stable operation of single-bubble boiling over a broad range of temperatures pave the way for development of new devices to control heat transfer by forming surface domains with distinct thermal properties and wettability.

Suspensions. The response of polarized particles suspended in a host fluid to an external electric field is widely employed in various applications through the ability to vary reversibly the suspension structure and viscosity (often referred to as electrorheological

effect). It has been known for centuries that the application of a strong electric field to a suspension of polarized particles will cause the particles to form head-to-tail chains along the field direction gradually coalescing into thick columns. A new phenomenon in suspensions of polarized particles was discovered by Kumar, et al. 2005; Agarwal, et al. 2009. They found that under certain conditions chains formed by particles in an alternating current (AC) electric field rearrange in the plane perpendicular to the field direction into a cellular pattern of particle-free domains surrounded by particle-rich walls. The main goal of our study was to find key variables affecting the formation of these structures in a suspension of polarized particles subjected to external alternating (AC) and direct (DC) current fields. Experiments were conducted on suspensions of positively and negatively polarized particles. As expected, the application of a strong AC field caused the particles in all tested suspensions to form chains along the field direction. However, rearrangement of chains into a cellular structure was achieved only in suspensions of negatively polarized particles. By accounting solely for dipole-dipole interaction between polarized particles exposed to an electric field, current theories fail to describe the formation of a cellular structure since they predict that the field effects should depend on the square of the particle polarizability and therefore be the same for negatively and positively polarized particles. Based on our findings, it is suggested that the formation of a cellular structure by negatively polarized particles is driven by weak multi-particle repulsion. Presented results demonstrate that the coupling of AC and DC fields provides a powerful technique for control, manipulation and assembly of polarized particle in various applications.

ELECTRIC-FIELD-DRIVEN PROCESSES IN MULTIPHASE FLUID SYSTEMS

by
Qian Lei

A Dissertation
Submitted to the Faculty of
New Jersey Institute of Technology
in Partial Fulfillment of the Requirements for the Degree of
Doctor of Philosophy in Chemical Engineering

Otto H. York Department of Chemical and Materials Engineering

December 2021

APPROVAL PAGE

ELECTRIC-FIELD-DRIVEN PROCESSES IN MULTIPHASE FLUID SYSTEMS

Qian Lei

Dr. Boris Khusid, Dissertation Advisor — Date
Professor of Chemical and Materials Engineering, NJIT

Dr. Kamalesh K. Sirkar, Committee Member — Date
Distinguished Professor of Chemical and Materials Engineering, NJIT

Dr. Piero M. Armenante, Committee Member — Date
Distinguished Professor of Chemical and Materials Engineering, NJIT

Dr. Sagnik Basuray, Committee Member — Date
Associate Professor of Chemical and Materials Engineering, NJIT

Dr. Wen Zhang, Committee Member — Date
Associate Professor of Civil and Environmental Engineering, NJIT

Dr. Lou Kondic, Committee Member — Date
Distinguished Professor of Mathematical Sciences, NJIT

BIOGRAPHICAL SKETCH

Author: Qian Lei

Degree: Doctor of Philosophy

Date: December 2021

Undergraduate and Graduate Education:

- Doctor of Philosophy in Chemical Engineering,
  New Jersey Institute of Technology, Newark, New Jersey, 2021

- Master of Science in Pharmaceutical Engineering,
  New Jersey Institute of Technology, Newark, New Jersey, 2014

- Bachelor of Science in Pharmaceutical Science,
  Hebei Medical University, Shijiazhuang, P. R. China, 2012

Major: Chemical Engineering

Publications and Presentations:

E. Elele, Y. Shen, J. Tang, Q. Lei, B. Khusid, G. Tkacik, C. Carbrello. Mechanical Properties of Polymeric Microfiltration Membranes, *Journal of Membrane Science*, 591, 117351 (2019).

E. Elele, Y. Shen, J. Tang, Q. Lei, B. Khusid. Single-Bubble Water Boiling on Small Heater under Earth's and Low Gravity, *nature partner journals Microgravity* 4, 21 (2018).

B. Khusid, Y. Shen, E. Elele, Q. Lei (NJIT), K.L. Guerra, F. Leitz (USBR). Method and Device for Testing the Effectiveness of Magnetic Treatment of Feed Water for Reducing Mineral Scaling in Reverse Osmosis Processes, *U.S. non-provisional patent No. US 10,648,957 B2*, May 12, 2020; provisional patent No 62/437,939, Dec 22, 2016.

Q. Lei, B. Khusid, L. Kondic, A. D. Hollingsworth, P. M. Chaikin, W. V. Meyer, A. J. Reich. Colloidal Crystallization under Microgravity, American Society for Gravitational and Space Research (ASGSR) Annual Meeting, Nov 3-6, 2021, Baltimore, MD.

Q. Lei, B. Khusid, L. Kondic, A. D. Hollingsworth, P. M. Chaikin, W. V. Meyer, A. J. Reich. Temperature Gradient Effects in Colloids of Ellipsoidal Particles under Microgravity, American Society of Mechanical Engineers (ASME) - The International Mechanical Engineering Congress and Exposition (IMECE) 2021 Virtual Conference, November 1–4, 2021.

Q. Lei, B. Khusid. Disorder-Order Transition in Colloids of Ellipsoidal Particles in Microgravity, American Society of Mechanical Engineers (ASME) - The International Mechanical Engineering Congress and Exposition (IMECE) 2021 Virtual Conference, November 1–4, 2021.

Q. Lei, B. Khusid, L. Kondic, A. D. Hollingsworth, P. M. Chaikin, W. V. Meyer, A. J. Reich. Building Colloidal Crystals under Microgravity, 10th Annual International Space Station Research and Development Virtual Conference, August 16, 2021

Q. Lei, B. Khusid, L. Kondic, A. D. Hollingsworth, P. M. Chaikin, W. V. Meyer, A. J. Reich. Phase Transitions in Colloids under Microgravity, American Physical Society March (APS MAR) Virtual Meeting, March 15, 2021

Q. Lei, B. Khusid, L. Kondic, A. D. Hollingsworth, P. M. Chaikin, W. V. Meyer, A. J. Reich. Crystallization of Hard-Sphere Colloids, American Physical Society -Mid-Atlantic Section (APS – MAS) Virtual Meeting, December 6, 2020

Q. Lei, E. Elele, B. Khusid. Electric Field Driven Aggregation of Negatively and Positively Polarized Particles in Dilute Suspensions, American Physical Society (APS) March Virtual Meeting 2020, March 3, 2020.

B. Khusid, E. Elele, Q. Lei. Electric Field-Driven Structuring in Polarized Colloids, American Society for Gravitational and Space Research (ASGSR) Annual Meeting, Nov 20-23, 2019, Denver, CO.

Q. Lei, E. Elele, B. Khusid. Electric-Field-Driven Structuring in Dilute Suspensions of Positively and Negatively Polarized Particles, the 16th Frontiers in Applied and Computational Mathematics jointly with 11th Northeastern Complex Fluids & Soft Matter, May 23-24, 2019, Newark, NJ

E. Elele, Q. Lei, B. Khusid. Electric Field Driven Phase Transition in a Confined Suspension of Negatively Polarized Particles, American Physical Society Division of Fluid Dynamics (APS – DFD) Annual Meeting 2018, NJIT, Newark, NJ.

B. Khusid, E. Elele, Q. Lei. Single-Bubble Boiling on Small Heater under Earth's and Low Gravity, 33th Annual Meeting of the American Society for Gravitational and Space Research (ASGSR), October 25-28, 2017, Seattle, Washington.

Q. Lei. Microgravity Experiments on Electric Field-Driven Phase Transitions in Colloids in the International Space Station, 2017 Dana Knox Student Research Showcase, April 19, 2017, NJIT.

Q. Lei. Commercialization of Testing Method & Device Developed by NJIT & U.S. Bureau of Reclamation for Assessment of the Effectiveness of Commercially Available Electro-Magnetic Water Softeners, Annual NJIT Innovation Day, April 10, 2017, NJIT.

Q. Lei, B. Khusid, M. Kahn. Commercialization of Method and Device Developed by NJIT & U.S. Bureau of Reclamation for Testing & Assessment of the Effectiveness of Commercially Available Electro-Magnetic Water Softeners, National Science Foundation (NSF) I-Corp Phase I Site at NJIT Meeting, March 22, 2017, NJIT.

B. Khusid, E. Elele, Q. Lei. Electric Field Driven Mesoscale Phase Transition in Polarized Colloids, American Physical Society Division of Fluid Dynamics (APS – DFD) Annual Meeting, November 20-22, 2016, Portland, OR.

B. Khusid, E. Elele, Q. Lei. Electric Field-Driven Structuring in Suspensions, American Institute of Chemical Engineers Annual Meeting, November 13-18, 2016, San Francisco, CA.

Y. Shen, J. Tang, Q. Lei, E. O. Elele, K. Guerra, F. Leitz, B. Khusid, K. K. Sirkar, A. R. Greenberg. Effects of Magnetic Treatment of Feed Solution on Scale Formation in Reverse Osmosis, 24th Annual North American Membrane Society (NAMS) Meeting, June 2, 2014, Houston, TX.

J. Tang, E. Elele, Q. Lei, B. Khusid. Magnetic Field Effect on Ionic Solutions, Membrane Science Engineering and Technology (MAST) Industrial Advisory Board Meeting (IAB), April 7, 2014, NJIT.

谨以此论文献给我的父亲雷兴长，我的母亲吴永萍。
感谢你们一直以来的支持，鼓励和包容。

This dissertation is dedicated to my beloved father Xinchang Lei, mother Yongpin Wu.
For your support, encouragement and unconditional love.

ACKNOWLEDGMENT

Firstly, I have a strong desire for expressing my genuine thankfulness to my dissertation advisor, Dr. Boris Khusid, for his consistent guidance, immense knowledge to support my research throughout the whole program and his tolerance, enthusiasm, and inspiration to light my way in academics. He is not only the advisor in my PhD program who encourages the successful completion of the degree requirements and timely graduation, but also the mentor in my growth and development by constructing a meaningful education to guide me towards becoming a grown researcher. I am sincerely grateful for having him to serve as my dissertation advisor.

A high appreciation to Dr. Ezinwa Elele for the direct involvement in my research as a friend and a colleague and providing brilliant suggestions, professional skills and profound experience to illuminate my road in the PhD program. I would also like to extend my thanks to Dr. Kamalesh K. Sirkar, Dr. Piero M. Armenante, Dr. Sagnik Basuray, Dr. Wen Zhang and Dr. Lou Kondic for accepting to serve as my committee. All your helpful suggestion and instructive comments have enhanced my dissertation very much.

I am grateful for financial support in part by projects form NSF CBET/Center for the Advancement of Science in Space (the ISS National Lab) grants 1832260, NASA/New Jersey Institute of Technology Space Act Agreement, and the NSF I/UCRC Membrane Science Engineering and Technology (MAST) Center.

Lastly, I would like to express my deepest gratitude to my family. To my father, Xinchang Lei and my mother, Yongpin Wu, for their endless love and support when I chose to continue my education abroad, and to my girlfriend, Yu Ouyang, for her encouragement and company in my rough time.

TABLE OF CONTENTS

TABLE OF CONTENTS
(Continued)

Chapter **Page**

TABLE OF CONTENTS
(Continued)

Chapter **Page**

LIST OF TABLES

LIST OF TABLES
(Continued)

Table **Page**

LIST OF FIGURES

LIST OF FIGURES
(Continued)

Figure **Page**

LIST OF FIGURES
(Continued)

Figure **Page**

LIST OF FIGURES
(Continued)

Figure **Page**

LIST OF FIGURES
(Continued)

Figure **Page**

LIST OF FIGURES
(Continued)

Figure **Page**

LIST OF FIGURES
(Continued)

Figure **Page**

LIST OF FIGURES
(Continued)

Figure **Page**

LIST OF FIGURES
(Continued)

Figure **Page**

LIST OF FIGURES
(Continued)

Figure **Page**

LIST OF FIGURES
(Continued)

Figure **Page**

LIST OF FIGURES
(Continued)

Figure **Page**

LIST OF FIGURES
(Continued)

Figure **Page**

LIST OF FIGURES
(Continued)

Figure **Page**

LIST OF FIGURES
(Continued)

Figure **Page**

LIST OF FIGURES
(Continued)

Figure **Page**

LIST OF FIGURES
(Continued)

Figure **Page**

3.89 Schematics of 2D −> 3D transformation with typical durations of events to form a cellular pattern of particle-free domains across the interelectrode gap in a suspension by applying a weak DC field and then a strong high frequency field …… 148

3.90 Morphology of cellular patterns. a) the number of particle-rich wall/islands as a function of the area fraction covered by particles; b) the number of particle-free domains as a function of the area fraction covered by solvent for 2D->3D transformation of the cellular pattern. Experiments conducted on suspensions of polyethylene particles (40-48 μm) and (53-75 μm) in Mazola oil and Cargill Envirotemp FR3 oil for different interelectrode gaps 0.5-2.0 mm. DC field 0.03 kV/mm applied in first 30 min and then the AC field 1.5 kV/mm, 100 Hz was added for 30 min ..…..…..…

LIST OF FIGURES
(Continued)

Figure **Page**

LIST OF FIGURES
(Continued)

Figure **Page**

LIST OF FIGURES
(Continued)

Figure **Page**

LIST OF FIGURES
(Continued)

Figure **Page**

LIST OF FIGURES
(Continued)

Figure **Page**

CHAPTER 1

RESEARCH OBJECTIVE

1.1 Background

Numerous experimental and theoretical studies over the last several decades demonstrated advantages of using electric fields in miniaturized apparatuses for a wide range of applications as it offers a simple and efficient method for controlling the motion and manipulation of multiphase fluid systems. This approach is considered to be especially beneficial for control of boiling processes and suspensions under microgravity.

For example, advantages of using an externally imposed electric field to affect characteristics of saturated pool boiling and bubble dynamics under microgravity are discussed in [1,2]. The use of electric fields to control the arrangement of polarized colloidal particles employs the electrorheological effect discovered by Winslow [3] about seventy years ago. It is referred to as electrorheological as the particle rearrangement in response to an electric field changes the apparent viscosity of a suspension by an order of up to 100,000. Manipulation of colloidal particles by applying an electric field is currently used in numerous applications ranging from optics and photonics to bioscience and biotechnologies and more recently in three-dimensional (3D) printing. Contrary to terrestrial applications, the particle transport under microgravity will not be affected by gravity effects, such as particle sedimentation, convection and jamming.

1.2 Dissertation Outline

The ultimate goal of the presented research is to scrutinize the effect of an electric field on boiling and suspensions. Single-bubble water boiling on a millimeter-sized heater under Earth's and low gravity is considered in Chapter 2. A potential application is related to control of heat transfer in hot spots where the heat flux is much higher than the average which occur in miniaturized electronic and photonic systems. Assembly and transport of polarized colloidal particles guided by an applied electric field is considered in Chapter 3. Experiments are carried out on negatively neutrally-buoyant suspensions to avoid the undesirable effects of gravity. The main focus is on understanding mechanisms underlying the formation of cellular patterns discovered in [4]. Similar experiments on a comparison of neutrally buoyant suspensions of small-size (1microns) positively polarized particles and negatively polarized particles are also conducted to provide a fundamental insight for non-neutrally buoyant suspensions expected to be conducted in the International Space Station in future. A potential application is related to manufacturing in space by utilizing unique advantages of microgravity.

CHAPTER 2

SINGLE-BUBBLE WATER BOILING ON SMALL HEATER UNDER EARTH'S AND LOW GRAVITY

2.1 Abstract

Today's trends for enhancing boiling heat transfer in terrestrial and space applications focus on removal of bubbles to prevent formation of a vapor layer over the surface at high overheat. In contrast, this dissertation presents a new boiling regime that employs a vapor-air bubble residing on a small heater for minutes and driving cold water over the surface to provide high heat flux. Single-bubble boiling of water was investigated under normal gravity and low gravity in parabolic flights. Experiments demonstrated a negligible effect of gravity level on the rate of heat transfer from the heater. Due to self-adjustment of the bubble size, the heat flux provided by boiling rose linearly up with increasing heater temperature and was not affected by a gradually rising water temperature. The fast response and stable operation of single-bubble boiling over a broad range of temperatures pave the way for development of new devices to control heat transfer by forming surface domains with distinct thermal properties and wettability. The bubble lifetime can be adjusted by changing the water temperature. The ability of heating water on millimeter scales far above 100°C without an autoclave or a powerful laser provides a new approach for processing of biomaterials and chemical reactions.

2.2 Introduction

Miniaturization of electronic and photonic systems is challenged by a dramatic increase in the power dissipation per unit volume with the occurrence of hot spots where the heat flux is much higher than the average. Force-flow cooling by gas or liquid appears insufficient to remove local high heat fluxes [5, 6]. Boiling that involves evaporation of liquid in a hot spot and condensation of vapor in a cold region can remove a significantly larger amount of heat through the latent heat of vaporization [7]. It is therefore considered as the most promising cooling technology for future microgravity applications [8, 9]. Boiling begins at a certain value of the heater temperature, termed the onset of nucleate boiling, with the appearance of bubbles in surface imperfections. The classical scenario of the pool boiling on Earth under normal gravity, g_E, in which a heater is submerged in a stagnant liquid is that a bubble, once formed, will grow driven by liquid evaporation and detach from the surface [7]. As the bubble departs, a hot liquid is pushed away from the surface and replaced with a cooler liquid from the bulk. An increase in the heater temperature, T_h, activates more nucleation sites and accelerates the vapor production, bubble growth and departure. The nonlinear nature of these phenomena causes the heat flux q_h to rise rapidly with the heater superheat [10, 11] as $q_h \sim (T_h - T_{sat})^m$, where T_{sat} is the liquid saturation temperature at a given pressure and m ranges from 3 to 5. Eventually the heat flux reaches a maximum (termed the critical heat flux) when bubbles growing in adjacent cites merge together and cover the heater surface with vapor. Heat transfer is then drastically reduced as the heated surface is totally blanketed with an insulating vapor film [7].

Extensive studies of nucleate boiling on small heaters were conducted over the past two decades under normal gravity, low gravity and hypergravity [12-22]. It was

demonstrated that the relative contribution of the buoyancy and surface tension to the energy transfer away from the heater can be characterized by the ratio of the characteristic heater size L_h to the capillary length $L_c = \sqrt{\gamma_l/g(\rho_l - \rho_v)}$ specified by the liquid surface tension γ_l, liquid ρ_l and vapor ρ_v densities, and gravity acceleration g. The classical scenario of boiling occurs at a sufficiently large L_h/L_c (large heaters or high gravity) when the buoyancy facilitates removal of bubbles from the surface. A threshold depends on the heater geometry and liquid properties. Boiling at small L_h/L_c (small heaters or low gravity) is dominated by capillary forces and thermocapillary convection around bubbles [19-22]. Nucleated bubbles in this case are observed to slide over the heater, detach (even in microgravity due to the vapor recoil) and hover close to the heater, coalescing with satellite bubbles [12-22]. Once bubbles form a vapor layer covering the heated surface, heat transfer is dramatically reduced.

The appearance of a vapor film on the surface at high superheat is the bottleneck to the performance of boiling heat transfer on relatively large and small heaters. Accordingly, current methods for heat transfer enhancement focus on removal of bubbles to prevent the creation of a vapor film [8-12, 14-16, 22]. In contrast, we present a new boiling regime of water in which a vapor-air bubble / to a small heater for minutes at temperature up to about 280^0C provides a heat flux up to ~1.2 MW/m^2, even though this value lies within the range of maximum heat fluxes on horizontal surfaces under normal gravity [7].

2.3 Experimental Setup and Method

Generally, flight and ground experiments were conducted in a rectangular UV-Vis quartz cuvette, Cole-Parmer, Chicago, IL (Figure 2.1) equipped with a thin-film (1.3mm thick) temperature resistance sensor (Innovative Sensor Technology, Las Vegas, NV). A PDMS slab (~6.3mm thick) mounted at the cuvette bottom was fabricated from Sylgard 184, Dow Corning, Midland, MI. Heating DC voltage was provided with DIGI-35A and DIGI-185 (Electro Industries, Chicago, IL) and Hewlett Packard 6207B /Agilent 6207B. The voltage drop in electric circuits (Figure 2.1) was recorded at 500 Hz with the data acquisition system U6-Pro Data Logger, LabJack, Lakewood, CO. The bubble motion was recorded at 13.95 fps with a DCC1545M-USB 2.0 CMOS camera, Thorlabs, Newton, NJ. The temperature below the water surface was recorded in ground experiments with a data logger TW-23039-64, Type K, Cole-Parmer, IL. HV pulses were generated with an amplifier Model 10/40 (slew rate 0.75kV/μs) Trek, Lockport, NY and an Agilent Waveform Generator Model 33220a. The conditions of 31 experiments (three in flights and 28 on Earth); the number of experiments replicated for the same heating regime, mean and standard deviations for the heat flux, heater temperature and bubble departure time; and the description and results of common statistical tests used for analysis of measurements to demonstrate the reproducibility of data are listed in Results Section. All measurements were included in the analysis.

Specifically, the flight setup (Figure 2.2(a)) consists of Module 1 and Module 2. Both modules are assembled on 1/8 in. aluminum 6061 T6 plate, 24 in. x 24 in., plates (8 in Figure 2.2(b)) whose sharp edges box are padded with soft materials. In flight, these plates were bolted to the aircraft floor grid with AN-6 3/8 in. diameter steel bolts. Modules

1 and 2 were designed to withstand "g-forces" up to $9g_E$ along horizontal axis, up to $2g_E$ along positive vertical axis and up to $6g_E$ along negative vertical axis (crash conditions). Stress–strain analysis of the setup components was conducted using guidelines [19].

Module 1 (Figure 2.2(b)) comprises (1) a high voltage (HV) amplifier (Model 10/40, slew rate 0.75kV/μs, Trek, Lockport, NY) and (2) a function generator (Agilent Waveform Generator, Model 33220a). The HV amplifier and the function generator are secured with 2 in. x 2 in. x ¼ in. 90 degree aluminum 6061-T6 angle bars in the front, back and sides. These angle bars are fastened to the aluminum plate (8 in Figure 2.2(b)) with 10-32 x 1/2 in. alloy steel screws. Module 2 (Figure 2.2(b)) comprises (3) an enclosure box; (4) a laptop (Latitude E6500, Dell, Austin, TX) mounted on the top of the box; two low voltage direct current (DC) power sources (5, DIGI-35A, 0-30V at 0-3A; 6, DIGI-185, 0-18V at 0-5A; both from Electro Industries, Chicago, IL) and (7) a power strip with a 14AWG extension cord and a 15A circuit breaker. The top and sides of the enclosure box, 22 in. x 10.25 in. x 9.5 in., are constructed by bolting polycarbonate sheets to 1 in. x 1 in. x 1/8 in. 90 degree aluminum 6061-T6 angle bars with ¼-20 x 1 in. grade 8 alloy steel bolts. The enclosure top is extended to hold the power strip (7 in Figure 2.2(b)) that distributes power to the HV amplifier, function generator, DC power sources, laptop, and lighting source. The camera is plugged into the laptop. The box angle bars, DC power sources, and components mounted inside the box (Figure 2.2(c) and 2.3(a)) are fastened to 1/8 in. aluminum 6061 T6 plate (8 in Figure 2.2(b)) with 10-32 x 1/2 in. alloy steel screws. The box sharp edges are padded with soft materials (Figure 2.2(a)). Figures 2.2(c) and 2.3(a,b) show the layout of components within the enclosure box: (a) a light source (83-873 LED Backlight Illumination, Edmund Optics, Barrington, NJ); (b) two rectangular cuvettes (12.5mm x

12.5mm x 45mm, inner cross-section 10mm x 10mm; UV-Vis, Quartz Cuvettes, Cole-Parmer, Chicago, IL) mounted on (c) an X-Y positioning stage (39-930, 70mm Travel, X-Y Axis Positioning Stage, Edmund Optics, Barrington, NJ); (d) a data acquisition system (U6-Pro Data Logger, LabJack, Lakewood, CO); (e) a camera with lenses (DCC1545M-USB 2.0 CMOS Camera (1280 x 1024 pixels, monochrome, frame rates up to 250 fps, equipped with zoom lens MVL 7000, Thorlabs, Newton, NJ); signal in experiments was mainly recorded at 13.95 fps by the laptop (4 in Figure 2.2) and (f) a camera/lens mount (03-665, V-Block Base with Clamps, Edmund Optics, Barrington, NJ).

Every cuvette in Module 2 is equipped with a thin-film temperature resistance sensor (P0K1.232.4W.B.010, Innovative Sensor Technology, Las Vegas, NV) acting as a resistance heater. The sensor is embedded into a polydimethylsiloxane (PDMS) slab (~6.3mm thick) mounted at the cuvette bottom such that the open sensor cover is lying in the horizontal plane of the slab surface (Figure 2.1). The slab was fabricated from Sylgard 184 using Silicone Elastomer Kit (Dow Corning, Midland, MI) and cured at room temperature. The sensor is connected in series with a DC power source to provide voltage for heating and a resistor (RadioShack, the nominal value of 8 Ohm/20W connected to DIGI-35A and 8 Ohm/10W connected to DIGI-185, the measured resistance of both, 8.3 Ohm, used in calculations). The voltage drop across this resistor is recorded at 500 Hz by the data acquisition system and used to compute the electrical current through the sensor, the power supplied to the sensor, and the sensor resistance. The sensor resistance is used to calculate its temperature from the linear calibration curve, resistance vs. temperature, provided by the manufacturer and validated by our measurements. The following modifications can be made in Earth's experiments: equip a cuvette with a temperature data

logger (TW-23039-64, Type K, Cole-Parmer, IL) connected to the laptop to record the temperature slightly below the liquid surface, use another heating circuit to measure the sensor temperature (once heating is turned off) by applying 3V DC, and take a Hewlett Packard 6207B /Agilent 6207B DC power source, 0-160V at 0-0.2A to provide a larger DC voltage for heating liquid.

The cuvette is loaded with a test liquid and then closed with a plastic lid (Figure 2.3(b)). A long energized electrode coated with Teflon is mounted in the cuvette lid (Figure 2.3(b)) such that its tip is located in the vicinity of the heater. This electrode is connected to the HV amplifier to generate a strong alternating current (AC) electric field in the liquid. The voltage reversals in an AC field reduces the accumulation of electric charge in the liquid. Compared to conventional electric techniques using a DC field generated by inserting bare electrodes in the liquid, the chances of short circuit, sparking, electrochemical deterioration of a liquid and electro-corrosion of the system components would be greatly reduced. The electrical impedance between this electrode and the sensor measured in distilled water by applying 200V AC decreases with the applied frequency from about several 10^4 MOhm at 1 Hz to about several 10^2MOhm at 100 Hz and to several 10 MOhm at 1 kHz with the resistance capacitance phase shift of about 5^0 within this frequency range. A train of successive rectangular high-voltage (HV) pulses of alternating polarity, 3-4 kV at frequency up to 100 Hz, was applied to this electrode to affect boiling. Due to the high value of the electrical impedance, the power supplied to the water by these HV pulses was less than 0.2 W.

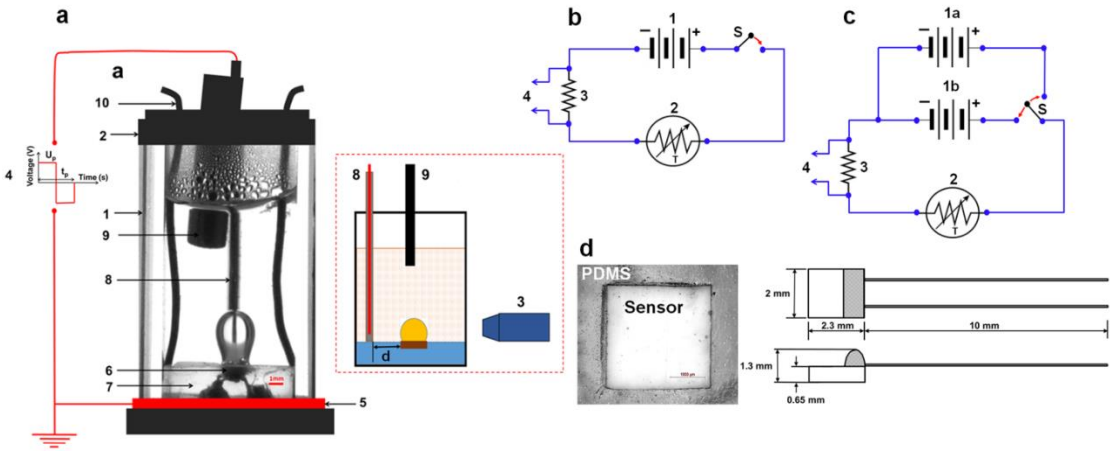

Figure 2.1 Cell: **(a)** Front and side views: 1**.** cuvette with liquid; 2. cover; 3. camera, signal recorded by a laptop over the entire experiment; 4. connection to amplifier for generating high voltage pulses of alternating polarity; 5. grounded electrode; 6. temperature resistance sensor (heater); 7, PDMS slab; 8. energized electrode coated with Teflon at 2 mm from the heater, 9. temperature probe in ground experiments; 10. connection to heating circuit. Electrical circuits: **(b)** flight: 1, heating DC power source; **(c)** Earth: 1a, heating DC power source; 1b, 3V DC power source; S, switch; **(**both **b, c)** 2. heater; 3. resistor; 4. connection to acquisition system; **(d)** photo of platinum sensor P0K1.232.4W.B.010 in PDMS slab whose silver wires (diameter 0.25mm, length 10.0mm) were soldered to power lead copper wires (Gauge 36 copper wire, length ~4mm); sensor sketch reproduced with permission from Innovative Sensor Technology, Las Vegas, NV.

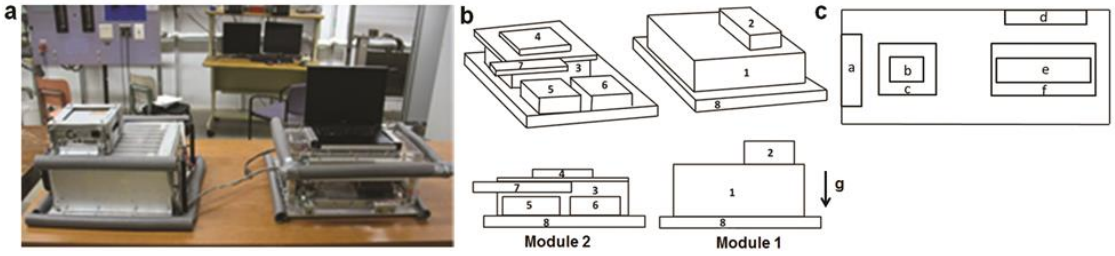

Figure 2.2 Flight setup: (a) Module 1 (left) and Module 2 with a laptop on the top (right), (b) Layout of components of Modules 1 and 2, (c) Layout of components within the enclosure in Module 2.

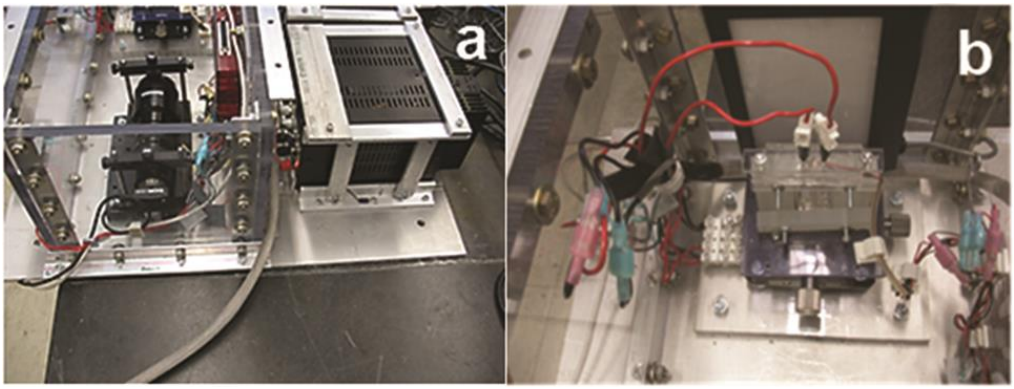

Figure 2.3 Module 2 components: (a) The camera mounted in the enclosure box (*left*) and the DC power source adjacent to the box (*right*), (b) Two rectangular cuvettes mounted on the X-Y positioning stage with the light source behind. The cuvette lid is equipped with a long electrode coated with Teflon that is connected to the HV amplifier.

2.4 Material Properties

Table 2.1 PDMS and Metals at Room Temperature

Material	Specific gravity, kg/m^3	Specific heat, kJ/kg·K	Thermal conductivity, W/m·K	Thermal diffusivity, m^2/s
PDMS*[1]	970	1.46	0.15	$1.06 \cdot 10^{-7}$
Silver*[2]	10490	0.23	406	$1.68 \cdot 10^{-4}$
Copper*[3]	8940	0.39	385	$1.10 \cdot 10^{-4}$
Platinum*[4]	21400	0.13	71.6	$2.57 \cdot 10^{-5}$

Source: *[1]Mark, J. E. (ed). Polymer Data Handbook, 2nd Ed (Oxford, England: Oxford Univ. Press, 2009)
*[2]https://www.engineeringtoolbox.com/metal-alloys-densities-d_50.html
*[3]https://www.engineeringtoolbox.com/specific-heat-metals-d_152.html
*[4]https://www.engineeringtoolbox.com/thermal-conductivity-metals-d_858.html

Table 2.2 Water [25-28] at 1 atm, $T_{sat}=100^0C$

Density, liquid	Density, vapor	Specific heat, liquid	Latent heat of vaporization	Surface tension	Temperature derivative of surface tension
958 kg/m^3	0.6 kg/m^3	4.2 kJ/kg·K	2,257 kJ/kg	58.9 mN/m	-0.19 mN/m·K

Viscosity, liquid	Thermal conductivity, liquid	Thermal diffusivity, liquid	Prandl, liquid	Viscosity, vapor	Liquid volumetric expansion
0.28 mPa·s	0.68 W/m·K	$1.7 \cdot 10^{-7}$ m^2/s	1.72	$1.2 \cdot 10^{-2}$ mPa·s	$7.5 \cdot 10^{-4}$ 1/K

The Antoine equation for saturated water vapor pressure [24-26]

$$\log_{10} P_{eq,w} = A - B/(C + T) \tag{2.1}$$

with A=8.14019, B=1810.94, C=244.485, where the vapor pressure is in Torr and the temperature is in °C.

Table 2.3 Air [24-26] at 100^0C

Density	Viscosity
0.95 kg/m^3	$2.2 \cdot 10^{-2}$ mPa·s

Diffusion coefficients of molecules in water vapor were estimated using the empirical correlation proposed by Fuller, Schettler, and Giddings: [27,28]

$$d_{AB} = \frac{10^{-3} T^{1.75} (1/M_A + 1/M_B)^{1/2}}{P\left[(\sum v)_A^{\frac{1}{3}} + (\sum v)_B^{\frac{1}{3}}\right]^2} \tag{2.2}$$

where d_{AB} is the diffusivity in cm^2/s, P is the total pressure in atm, M is the molecular weight, T is the temperature in K, and $\sum v$ is the diffusion volume of a component. [27,28]

Table 2.4 Diffusion Coefficients in Water Vapor at 1 atm and 100^0C

Molecule	Molecular Weight	v	d_{AB}, cm^2/s
O_2	32	16.6	0.39
N_2	28	17.9	0.39
H_2O	18	12.7	0.48

2.5 Results

The data in a variety of experimental conditions is collected to conduct statistical analysis. The conditions of experiments carried out in parabolic flights and on Earth are listed in Tables 2.5-2.9. Every flight brought a collection of data on the heat flux and heater temperature for the same heating regime through measurements for consecutive parabolic arcs. Values of the mean, standard deviation (STD) and relative standard deviation (%RSD) for these datasets are listed in Table 2.5. The Ljung-Box (LB) Q-test and the Anderson-Darling (AD) test in MATLAB 2017a (also see NIST/SEMATECH e-Handbook of Statistical Methods, http://www.itl.nist.gov/div898/handbook) were taken to explore whether deviations from the mean over the entire dataset for a particular heating regime were random quantities. The LB test was used to examine the presence of m (=20) autocorrelations of the residuals to assess the hypothesis that they are independently distributed, so that any observed correlations in the residuals come from randomness of the sampling process. This hypothesis is rejected if a $p-$value computed for the level of significance α that corresponds is relatively small. The AD test was used to assess whether residuals are from a population with a normal distribution. This hypothesis is rejected if a computed $p-$ value is relatively small. The $p-$values listed in Table 2.5 for LB and AD tests indicate that two hypotheses that the residuals were random quantities and that they were normally distributed cannot be rejected at a significance level of α=5%.

A similar approach was taken to analyze measurements in experiments on Earth with heating cycles when the heating DC voltage was periodically turned on for 20s and then off for 60s (Table 2.6). Every experiment included 30 cycles and was conducted twice. As a result, 60 values of heat flux were collected for the same heating regime through

measurements for consecutive cycles in two experiments. The LB and AD statistical tests in MATLAB 2017a were used to explore whether deviations from the mean over the entire dataset for a particular heating regime were random quantities and whether they were normally distributed. The p −values listed in Table 2.6 for LB and AD tests indicate that two hypotheses that the residuals were random quantities and that they were normally distributed cannot be rejected at a significance level of α=5%. However, the dataset for 15V passed the LB test but failed the AD test at this α-level, indicating that the deviations from the mean were random quantities, but not normally distributed. A pass in the AD test for the 15V data set was observed at 1% significance level. Values of the mean, standard deviation and relative standard deviation for measurements in experiments on Earth with continuous heating are listed in Table 2.7.

For all experiments in Tables 2.5-2.7, the heat flux $\mathrm{q_h}$ rises linearly with increasing the heater temperature $\mathrm{T_h}$ as

$$\mathrm{q_h(kW/m^2)} = (4.63 \pm 0.15)(\mathrm{T_h} - 19.28℃) \tag{2.3}$$

with the coefficient of determination $\mathrm{r^2} = 0.970$.

Deviations between values given by this equation and measurements are normally distributed random quantities at the 95% confidence level with the p −values 0.917 and 0.179 for the AD and LB tests, respectively.

Table 2.5. Flight Experiments

Day	DC voltage	Pulses	Number of parabolas	Heat flux, Mean ± STD, MW/m^2 Heater temperature, Mean ± STD, ^{0}C	LB test; p- value	AD test; p- value
1	20V	3kV/20 kHz	28	0.533±0.012 (%RSD 2.28)	0.618	0.662
				119.7±10.1 (%RSD 8.4)	0.643	0.562
2	22.4V	4kV/20 kHz	27	0.630±0.016 (%RSD 2.48)	0.697	0.274
				146.1±11.3 (%RSD 7.8)	0.701	0.331
3	22.4V	4kV/10 kHz	30	0.621±0.022 (%RSD 3.55)	0.167	0.730
				152.6±16.5 (%RSD 10.8)	0.172	0.134

Table 2.6 Experiments On Earth With 30 Heating Cycles; DC Voltage On for 20s and Off for 60s; Two Experiments Conducted Under the Same Conditions

No	DC voltage	Pulses	Heat flux, Mean ± STD, MW/m^2 Heater temperature, Mean ± STD, ^{0}C	LB test; p- value	AD test; p- value
1	15V	No	0.309±0.001 (%RSD 0.38)	0.935	0.023
			106.6±1.4 (%RSD 1.4)	0.871	0.072
2	20V	No	0.512±0.012 (%RSD 2.34)	0.243	0.508
			139.7±2.5 (%RSD 1.8)	0.318	0.254
3	22.4V	No	0.619±0.010 (%RSD 1.76)	0.937	0.073
			154.4±2.3 (%RSD 1.5)	0.827	0.202
4	25V	No	0.724±0.013 (%RSD 1.80)	0.738	0.101
			183.8±3.0 (%RSD 1.6)	0.721	0.250
5	30V	No	0.974±0.017 (%RSD 1.78)	0.102	0.223
			228.6±2.6 (%RSD 1.1)	0.066	0.345
6	35V	No	1.185±0.018 (%RSD 1.52)	0.228	0.071
			281.3±3.2 (%RSD 1.1)	0.274	0.125
7	20V	4kV/20Hz	0.526±0.012 (%RSD 2.28)	0.933	0.161
			128.3±2.8 (%RSD 2.2)	0.357	0.119
8	22.4V	4kV/20Hz	0.632±0.018 (%RSD 2.85)	0.384	0.067
			153.3±2.8 (%RSD 1.8)	0.586	0.292

Table 2.7 Experiments On Earth With Continuous Heating; Three Experiments (With Pulses) and Four experiments (Without Pulses) Conducted Under the Same Conditions

No	DC voltage	Pulses	Heat flux, Mean ± STD, MW/m^2	Heater temperature, Mean ± STD, ^{o}C
1	5V	No	0.048±0.002 (%RSD 4.15)	47.1±6.3 (%RSD 13.3)
2	10V	No	0.158±0.007 (%RSD 4.15)	61.2±9.3 (%RSD 15.2)
3	15V	No	0.325±0.013 (%RSD 4.01)	102.6±7.2 (%RSD 7.0)
4	20V	No	0.539±0.025 (%RSD 4.71)	136.0±8.2 (%RSD 6.0)
5	22.4V	No	0.654±0.030 (%RSD 4.53)	152.7±7.5 (%RSD 4.9)
6	25V	No	0.800±0.052 (%RSD 6.50)	185.9±7.3 (%RSD 5.0)
7	27.5	No	0.880±0.016 (%RSD 1.77)	225.8±9.6 (%RSD 4.3)
8	30V	No	1.000±0.024 (%RSD 2.44)	255.7±12.9 (%RSD 5.0)
9	35V	No	1.197±0.023 (%RSD 1.92)	268.9±13.5 (%RSD 5.0)
10	5V	4kV/20Hz	0.071±0.003 (%RSD 4.53)	34.6±3.3 (%RSD 9.4)
11	10V	4kV/20Hz	0.184±0.005 (%RSD 2.74)	48.3±3.3 (%RSD 9.4)
12	15V	4kV/20Hz	0.331±0.010 (%RSD 2.92)	85.0±5.0 (%RSD 5.8)
13	20V	4kV/20Hz	0.543±0.012 (%RSD 2.21)	126.5±1.2 (%RSD 1.0)
14	22.4V	4kV/20Hz	0.681±0.010 (%RSD 1.46)	141.3±4.7 (%RSD 3.4)
15	25V	4kV/20Hz	0.793±0.007 (%RSD 0.86)	176.5±5.0 (%RSD 2.8)
16	30V	4kV/20Hz	1.040±0.020 (%RSD 1.92)	231.4±12.6 (%RSD 5.4)
17	20V	4kV/1Hz	0.491±0.007 (%RSD 1.43)	132.2±0.8 (%RSD 0.6)
18	20V	4kV/10Hz	0.501±0.011 (%RSD 2.19)	131.1±1.1 (%RSD 0.9)
19	20V	4kV/50Hz	0.517±0.008 (%RSD 1.55)	127.6±1.1 (%RSD 0.8)
20	20V	4kV/100Hz	0.495±0.012 (%RSD 2.42)	130.3±1.6 (%RSD 1.2)

Measurements of the departure time of the first bubble formed on the heater after applying DC voltage and the liquid temperature T_s at this instant for experiments on Earth are listed in Tables 2.8 and 2.9. For both heating modes, the departure of this bubble occurred in the range of liquid bulk temperatures T_s ~ 50-80℃ and showed the same dependence on the heat flux $T_s(℃) = (27.2 \pm 0.93)q_h(\mathrm{MW/m^2}) + 44.96 \pm 1.13℃$ with $r^2 = 0.966$.

Deviations between values given by this equation and measurements are normally distributed random quantities at the 95% confidence level with the p −values 0.588 and 0.564 for the AD and LB tests, respectively.

Table 2.8 Experiments On Earth; 30 Heating Cycles 20s On/60s Off; Two Experiments Conducted Under the Same Conditions

No	DC voltage	Pulses	Departure time of the first bubble, Mean ± STD, min	Liquid temperature T_s Mean ± STD, ^oC
1	20V	No	37.0±0.9 (%RSD 2.5)	58.5±3.5 (%RSD 6.0)
2	22.4V	No	33.7±1.9 (%RSD 5.6)	62.0±2.8 (%RSD 4.5)
3	25V	No	33.0±0.9 (%RSD 2.7)	64.0±1.4 (%RSD 2.2)
4	30V	No	25.7±1.9 (%RSD 7.4)	72.5±2.1 (%RSD 2.9)
5	35V	No	21.7±1.9 (%RSD 8.7)	79.5±2.1 (%RSD 2.6)
6	20V	4kV/20Hz	35.7±2.8 (%RSD 7.8)	59.5±2.1 (%RSD 3.5)
7	22.4V	4kV/20Hz	35.0±1.9 (%RSD 5.4)	62.5±0.7 (%RSD 1.1)
8	25V	4kV/20Hz	34.3±0.9 (%RSD 2.6)	66.5±2.1 (%RSD 3.2)
9	30V	4kV/20Hz	27.0±1.9 (%RSD 7.0)	74.0±2.8 (%RSD 3.8)
10	35V	4kV/20Hz	20.3±2.0 (%RSD 9.8)	80.0±1.4 (%RSD 1.8)

Table 2.9 Experiments On Earth With Continuous Heating; Three Experiments (With Pulses) and Four Experiments (Without Pulses) Conducted Under the Same Conditions

No	DC voltage	Pulses	Departure time of the first bubble, Mean ± STD, min	Liquid temperature T_s Mean ± STD, ^oC
1	15V	No	9.1±0.5 (%RSD 5.5)	54.7±3.2 (%RSD 5.9)
2	20V	No	6.9±1.0 (%RSD 14.5)	61.7±1.5 (%RSD 2.4)
3	22.4V	No	5.7±1.2 (%RSD 21.0)	63.0±2.0 (%RSD 3.2)
4	25V	No	3.8±0.6 (%RSD 15.8)	64.3±2.5 (%RSD 3.9)
5	30V	No	2.6±0.5 (%RSD 19.2)	69.0±5.3 (%RSD 7.7)
6	35V	No	1.6±0.5 (%RSD 31.2)	77.0±2.0 (%RSD 5.0)
7	15V	4kV/20Hz	8.0±0.8 (%RSD 10.0)	54.3±3.5 (%RSD 6.4)
8	20V	4kV/20Hz	5.6±1.6 (%RSD 28.6)	59.3±3.1 (%RSD 5.2)
9	22.4V	4kV/20Hz	5.0±0.3 (%RSD 6.0)	62.3±1.5 (%RSD 2.4)
10	25V	4kV/20Hz	3.6±0.4 (%RSD 15.8)	65.7±2.1 (%RSD 3.2)
11	30V	4kV/20Hz	3.1±0.4 (%RSD 12.9)	71.0±3.6 (%RSD 5.1)
12	35V	4kV/20Hz	1.7±0.3 (%RSD 17.6)	79.0±1.0 (%RSD 1.3)

The conditions of experiments carried out in parabolic flights and on Earth are listed in (Table 2.5-2.9). Low gravity measurements were conducted in three days of parabolic flights in NASA Boeing 727. A flight provided two sets of consecutive parabolic arcs, each with 15-s freefall at acceleration $\sim 10^{-2} g_E$ preceded and followed by periods of acceleration $\sim 1.3 g_E$ for 50-60s where g_E is the normal gravity acceleration; the second set also included two parabolas simulating the gravity of the Moon ($1.62 m/s^2$) and Mars ($3.71 m/s^2$). Following guidelines [23], a flight setup was designed to withstand "crash g-

forces" up to $9g_E$ along horizontal axis, up to $2g_E$ along positive vertical axis and up to $6g_E$ along negative vertical axis (Section 2.3). The setup was equipped with two cuvettes shown in Figure 2.1 for simultaneous testing of different liquids. Experiments were carried out on 3M Novec HFE-7100 (3M, St. Paul, MN) and distilled water from a local pharmacy with conductivity $\sigma_l \sim 2 \cdot 10^{-4}\,S/m$ and dielectric constant $\varepsilon_l \sim 78$ measured before experiments. Here we present data only for water. Due to the limited space of the paper, experiments on HFE-7100 for which a conventional boiling regime was observed will be reported elsewhere. For water at room temperature, L_c equals 2.7mm on Earth and 27mm for freefall. A cuvette (Figure 2.1) was loaded with 1 mL of water and then closed with a plastic lid. As a liquid in a cooling system utilized over a long period of time usually accumulates dissolved air, experiments were carried out with the cuvette lid that was not airtight to maintain atmospheric pressure inside the cuvette. A platinum temperature resistance sensor, serving as a heater, was embedded into a polydimethylsiloxane (PDMS) slab such that the heating surface was in contact with water (Figure 2.1(d)). The ratios of the heating surface width and length (Figure 2.1(d)) to the capillary length were respectively 0.74, 0.85 for experiments on Earth and 0.074, 0.085 in flight. The interior contact angles of water on the heater surface and PDMS measured at room temperature were respectively 74±3^o (hydrophilic) and 107±2^o (hydrophobic). The heater was connected in series with a resister R_0 and a direct current (DC) power source that provided voltage U_{DC} to the heater (Figure 2.1). The voltage drop across this resistor U_R was measured to compute the voltage drop on the heater $\Delta U_h = U_{DC} - U_R$, the electrical current $I_h = U_R/R_0$, the power $I_h \Delta U_h$ that varied from about 0.5W to 5.5W and the heater resistance $R_h = \Delta U_h / I_h$ that was used for calculating its temperature T_h from the linear

calibration curve R_h vs. T_h. The values of heat flux $q_h = I_h \Delta U_h / S_h$ reported in Figure 2.1-2.2 and Figure 2.7-2.8 correspond to the total power provided to the heater. Expressions [29] were used to estimate the heat loss from the heater through the power lead wires and directly into the PDMS slab. Calculations presented in Section 2.5 indicate that the heat loss increased with raising the heater temperature from about 9% at $T_h \approx 50℃$ to 13% at $T_h \approx 270℃$. Additional two parameters were measured on Earth due to flight limitations: (i) the temperature T_s slightly below the water surface by probe 9 in Figure 2.1(a) to estimate the bulk liquid temperature and (ii) the heater temperature T_h when the heating power source was turned off by applying 3V DC to the heater (Figure 2.1(c)). For the latter, the generated power ~ 0.075W might raise the heater temperature by $\sim 2℃$.

Heat loss from the heater is evaluated. When a heating voltage is applied to the heater (Figure 2.1), transient heat conduction from the heater into the PDMS slab lasts $\sim b^2/\alpha_s \sim 340s$, where b is the slab thickness and α_s is the PDMS thermal diffusivity (Table 2.1). During this time, the rate of heat transfer into the slab can be estimated by taking the expression [29] for the heat flux at the surface of a semi-infinite solid whose surface temperature changes instantaneously from the room temperature $T_r \approx 25℃$ *to* T_h

$$\dot{Q}_{trans}(t) \approx k_s S_h (T_h - T_r)/\sqrt{\pi \alpha_s t} \tag{2.4}$$

with $k_s S_h/\sqrt{\pi \alpha_s t} < 6.9 \cdot 10^{-4}\, W/℃$ for $t > 3s$, where S_h is the heater surface area and k_s is the PDMS thermal conductivity (Table 2.1). After that, the rate of heat transfer into the slab can be estimated by using the expression[25] for the heat flux from a circular disk on the surface of a semi-infinite solid with area equal to the heater surface area

$$\dot{Q}_{steady} \approx 4k_s(T_h - T_r)\sqrt{S_h/\pi} \quad (2.5)$$

with $4k_s\sqrt{S_h/\pi} = 7.3 \cdot 10^{-4}\ W/°C$.

Transient heat conduction from the heater through the silver and the copper wires (Figure 2.1) lasts less than 1s due to a high thermal diffusivity of metals (Table 2.1). After that, the rate of heat transfer can be estimated by calculating the total thermal resistance R_{total} of the silver and copper wires connected with the soldering joints (Figure 2.1). The wire thermal resistance is equal to its length divided by the cross-sectional area and the thermal conductivity (Table 2.1).The thermal resistance of the soldering joint can be estimated by using the expression[20] for the conduction shape factor of a sphere of diameter $c \sim 1.1$ mm with temperature T_j buried in a semi-infinite solid with temperature T_r

$$\dot{Q}_{sphere} = 2k_s\pi c(T_j - T_r)/(1 - \frac{c}{4z}) \quad (2.6)$$

where $z \sim 3$mm is the distance from the sphere center to the solid surface. Taking the silver wire to be connected in series with the copper wire and the soldered joint that are connected in parallel, we obtain

$$\dot{Q}_{power\ lead} \approx (T_h - T_r)/R_{total} \quad (2.7)$$

with $1/R_{total} \approx 2.2 \cdot 10^{-3}\ W/°C$.

The presented estimates indicate that heat loss from the heater occurred mainly through the power lead wires. The total heat loss given by Equation (2.5) and Equation (2.7) increased with raising the heater temperature T_h from about 9% at $T_h \approx 50℃$ to 13% at $T_h \approx 270℃$.

Since electric fields are widely used to enhance boiling heat transfer [18, 26-29] the cuvette was equipped with electrodes to investigate the field effects on single-bubble boiling. Conventional electric techniques are limited to low conducting liquids because of using bare electrodes inserted into the liquid. To avoid this limitation, a train of successive rectangular high-voltage (HV) pulses of alternating polarity, U_p = 3-4 kV at frequency $1/t_p$ up to 100 Hz, was applied to water via the insulated energized electrode inserted into the water and the grounded electrode placed under the cuvette (Figure 2.1(a)). The power supplied by HV pulses was less than 0.2 W (Section 2.5). As the electric stress exerted on a liquid is proportional to the square of the field strength, the application of these pulses kept the electric stress at a constant level. The motion of charge carriers in a liquid subjected to an electric field depends on the ratio [34] between the charge relaxation time $t_{rel} = \varepsilon_0 \varepsilon_l / \sigma_l$ and the period of HV pulses t_p, where ε_0 is the vacuum permittivity. As $t_{rel} \sim 5\mu s \ll t_p$ in our experiments, ions in water followed the field, thereby reducing the accumulation of charge due to voltage reversals. The proposed design offers the ability of applying an electric force to liquids with much higher electrical conductivity as the chance of short circuit, sparking, and electro-corrosion are drastically reduced.

All flight heating tests were performed in the presence of HV pulses (Table 2.5). Heating DC voltage 20V or 22.4V and HV pulses were simultaneously turned on when the aircraft began to freefall. Once the aircraft began to accelerate, they were turned off to

avoid the contribution of buoyancy and electric field driven convection. They were also turned off as the aircraft maneuvered for about 10 min to begin flying the second set of parabolas.

A large bubble rapidly formed on the heater during the first freefall. Its footprint was gradually increasing in size, until anchoring on the heater edges after a couple of minutes. It was staying on the heater over the first set of parabolas and detached during the acceleration period of one of parabolas during the second set (Figure 2.4(a)). Specifically, a bubble formed in the first freefall was remaining on the heater for total of 20 parabolas (32 min) in the first flight, 27 (41 min) in the second flight and 19 parabolas (36 min) in the third flight. As the firstly formed bubble detached, another one formed and stayed on the heater until the end of the flight. During a freefall, a bubble staying on the heater emitted sporadically tiny bubbles that were carried away with the flow. As the aircraft was accelerating, these tiny bubbles rose to the water surface and popped up due to buoyancy. The heater temperature and heat flux during a freefall period stabilized within 2s after applying DC voltage. Variations of heat flux values from parabola to parabola measured at the same heating regime were lying within 2-4% (Table 2.5).

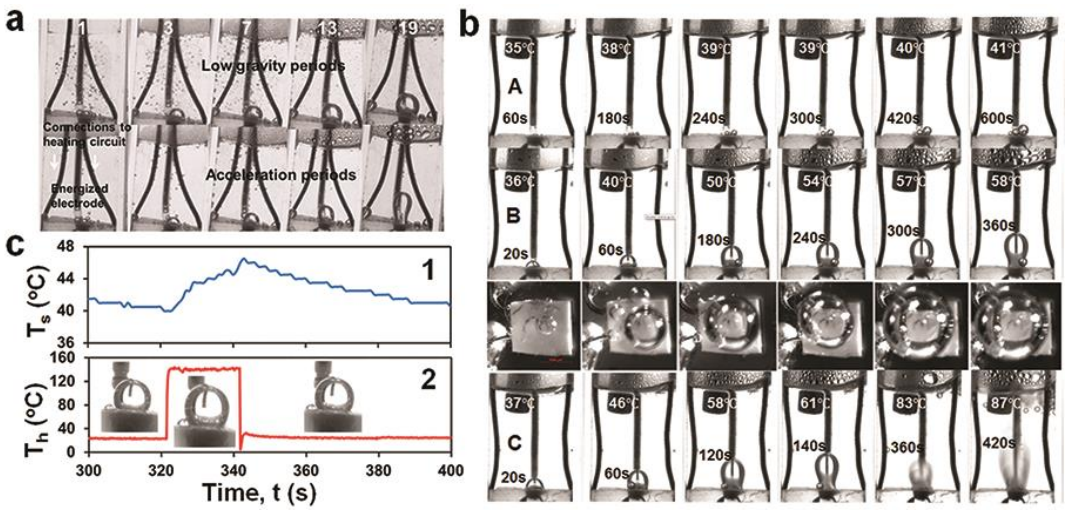

Figure 2.4. Thermal regimes: (**a**) Flight, parabolas (number shown); 22.4V DC & 4kV/20Hz pulses applied in freefall (top row) and switched off during acceleration (bottom row); (**b**) Earth, continuous heating, no HV pulses; T_s and heating time shown; applied V DC: 10 (A); 20 (B); 30 (C) see heat flux for A, B, C in Fig. 4(a). (**c**) Earth, heating cycles 20V DC & 4kV/20Hz pulses 20s on/60s off, temperatures: 1, T_s; 2, T_h.

Experiments on Earth were carried out under conditions of continuous heating and heating cycles with DC voltage 20s on/60s off (Table 2.6; Table 2.7). Variations of heat flux values measured at the same heating regime were lying within 1-6% (Table 2.6; Table 2.7). A consistent performance of single-bubble boiling was observed for both heating modes. To avoid rapid deterioration of the PDMS slab around the heater, experiments were conducted for heater temperatures below 270^0C. Photos in Figure 2.4(b) illustrate bubbles formed under continuous heating. Tiny bubbles appeared on the heater at 10V DC for which T_h was below 100^0C (Figure 2.4(b)A) were mainly due to the release of air dissolved in water as its solubility decreased with temperature. A single bubble formed on the heater when T_h was above 100^0C. Side and top images in Figure 2.4(b)B show the evolution of the first bubble appeared at 20V DC. The first bubble formed at 30V DC is shown on images in Figure 2.4(b)C from 20 to 140s. As can be seen in Figure 2.4(b)B&C, the bubble foot gradually expanded until reaching the heater edge. While the heater temperature T_h

and heat flux q_h stabilized within several seconds after applying DC voltage, the bulk temperature of water for both heating modes gradually rose due to the low rate of heat transfer out of the cuvette. This feature was used to investigate the effect of water temperature on single-bubble boiling. The timescale of changes in water temperature T_s for continuous heating was about 5 min for voltage greater than 10V DC (Section 2.5). The amplitude of water temperature variation in a heating cycle was in the range 2-6^{0}C, gradually increasing with applied DC voltage. The timescale of changes in water temperature from cycle to cycle were much smaller than that for continuous heating since the electric power averaged over a cycle was four times smaller. Plots and photos in Figure 2.4(c) illustrate variations of T_h, T_s and the bubble size in a typical heating cycle. When the heater temperature dropped down once the heating was off, the bubble shrank due to condensation of water vapor (Figure 2.4(a) in flight and Figure 2.4(c) on Earth). While the heater temperature and heat flux did not change in the process of boiling, the height h, volume V, and cap surface area S of the pinned bubble were gradually increasing due to the rising water temperature (Figure 2.5(a-d)). Figure 2.5(e,f) illustrate a change in the bubble volume ΔV caused by vapor condensation after the heating was turned off and the air volume fraction in the bubble (calculated as $1 - \Delta V/V$) with the number N of heating cycles.

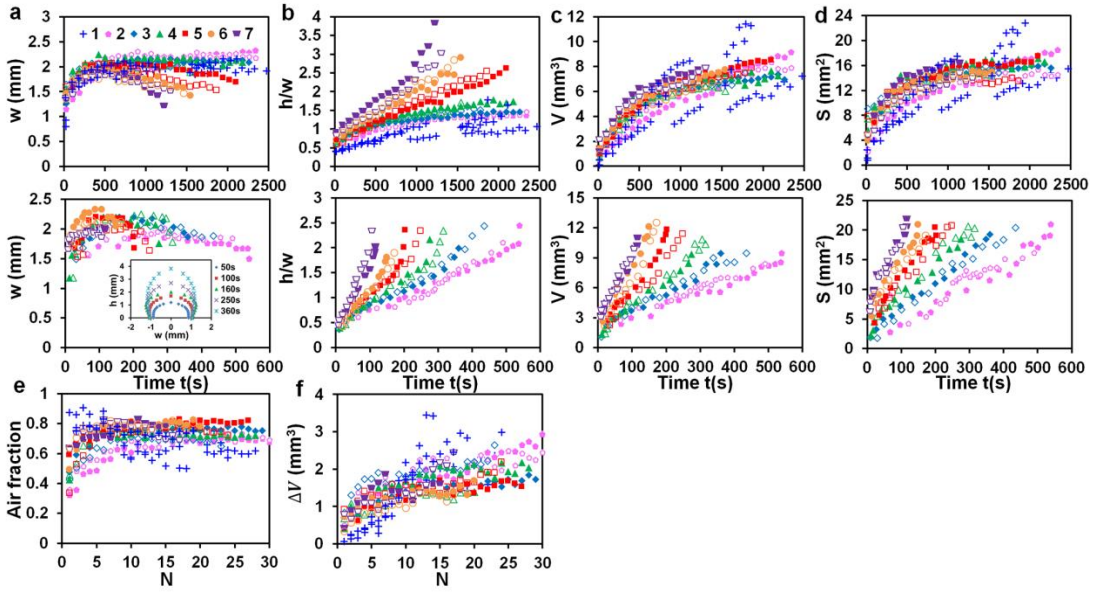

Figure 2.5 Thermal regimes. (**a-d)** Bubble width w, height h, ratio h/w, volume V, and cap surface area S in heating period; curves terminate after departure of the first bubble: Flight 1, 20V DC & 3kV/20Hz; 22.4V DC & 4kV/20Hz; 22.4V DC & 4kV/10Hz, pulses applied in freefall and switched off during acceleration; Earth 2-7, heating cycles 20s on/60s off (top row) and continuous heating (bottom row) with 4kV/20Hz pulses (empty symbols) and without HV pulses (filled symbols); applied V DC: 15 (2); 20 (3); 22.4 (4); 25 (5); 30 (6); 35 (7); inset 20 V DC. **(e, f)** Changes of the bubble volume ΔV due to water vapor condensation as heating was turned off and the air fraction in the bubble $(1 - \Delta V/V)$ vs. the number N of heating cycles for regimes listed in (**a-d)**. V, S, and ΔV were computed by integration of the shape profile along the bubble image (Section 2.5). Results of statistical analysis of measurements are listed in Table 2.1-2.3.

Thermal regime of water was calculated. The cuvette in Earth's experiments was equipped with a temperature data logger to record the temperature T_s slightly below the water surface. Relative changes of T_s with time t after several tens of seconds of continuous heating are well approximated by a linear expression with a single time scale: $\ln[(T_m - T_s)/(T_m - T_r)] = -t/\tau_h$, where T_m is the final steady-state temperature, $T_r \approx 25$℃ is the room temperature, and τ_h is the characteristic time scale. The values of T_m and τ_h were obtained by maximizing the square of the Pearson correlation coefficient r^2 between $ln[(T_m - T_s)/(T_m - T_r)]$ and time t. Figure 2.6 illustrates the dependence of T_m

and τ_h on the applied heating DC voltage. The corresponding values of r^2 lie in the range 0.962 ± 0.014.

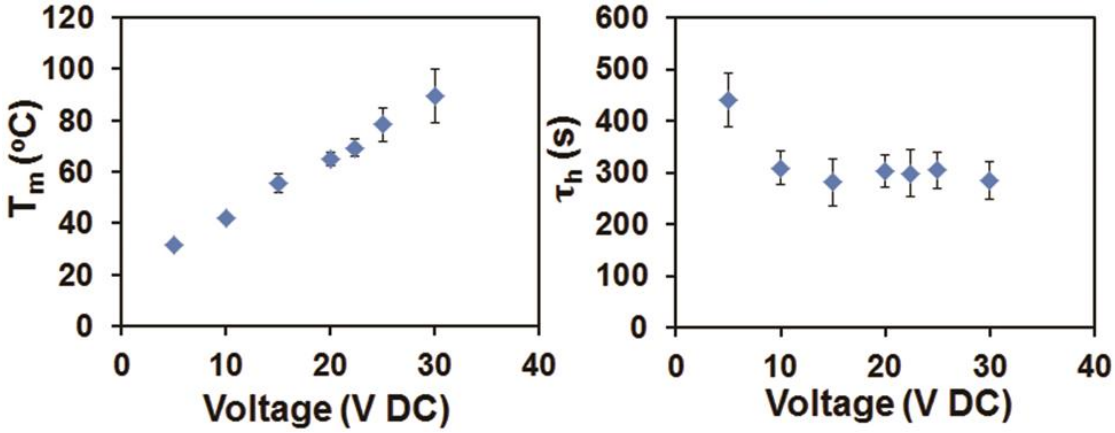

Figure 2.6. The dependence of T_m and τ_h on applied heating DC voltage.

The bubble volume and cap surface area are calculated. Video images of the bubble evolution indicated that the bubble contour could be approximated as axisymmetric and thereby expressed as $r(z)$, where r is the distance from a point on the bubble contour to the central axis perpendicular to the heater plane and z is the distance from this point to the heater plane. Accordingly, the bubble volume V and the bubble cap surface area S are $V = \pi \int_0^h r^2 dz$ and $S = 2\pi \int_0^h r\sqrt{1 + (dr/dz)^2} dz$, where h is the bubble height.

To find $r(z)$, we formed a uniform grid of $n + 1$ points along the central axis of a bubble in a video image ($z_i = (i-1)\,h/n$ for $i = 1, \ldots, n+1$) and measured distances from points on the bubble contour with each of these z-coordinates to the central bubble axis using NIS Advanced Imaging software (Nikon Instruments, Melville, NY). The integrals were then calculated following the trapezoidal rule:

$$V = \frac{\pi h}{2n}\sum_{i=1}^{n}(r_{i+1}^2 + r_i^2) \tag{2.8}$$

$$S = \frac{\pi h}{n}\sum_{i=1}^{n}\left(r_{i+1}\sqrt{1 + (dr/dz)_{i+1}^2} + r_i\sqrt{1 + (dr/dz)_i^2}\right) \tag{2.9}$$

where derivatives dr/dz at the internal and boundary points of the grid were computed as $\left(\frac{dr}{dz}\right)_i = \frac{r_{i+1}-r_{i-1}}{2h}$ *at* $1 < i < n$, $\left(\frac{dr}{dz}\right)_1 = \frac{r_2-r_1}{h}$ *and* $\left(\frac{dr}{dz}\right)_{n+1} = \frac{r_{n+1}-r_n}{h}$.

It was found that taking 11 points along the bubble contour provided sufficient accuracy in estimating V and S. In particular, the errors in calculation of the volume and surface area of a spherical cap of diameter D and height h, $V_{cap} = \frac{\pi h}{6}(3D^2/4 + h^2)$ and $S_{cap} = \pi(D^2/4 + h^2)$, based on measurements of coordinates of 11 points are respectively less than 1% and 3%.

Points A, B, C in Figure 2.7(a) mark regimes shown in Figure 2.4(b). The maximum efficiency of HV pulses was achieved at 20 Hz (Figure 2.7(a) inset) at which the heat flux increased by about 10% at the same heater temperature. In flight and in both heating modes on Earth, the heat flux q_h of a pinned bubble was found to rise linearly to 1.2 MW/m^2 with increasing heater temperature T_h to about 280^{0}C as (Figure 2.7(a), Table 2.5-2.7)

$$q_h(kW/m^2) = (4.63 \pm 0.15)(T_h - 19.28℃) \tag{2.10}$$

with the coefficient of determination $r^2 = 0.970$. Deviations between values given by this equation and measurements are normally distributed random quantities at the 95%

confidence level (Table 2.5-2.7). The remarkable independence of q_h and T_h from a gradually rising water temperature (Figure 2.7(b)) was caused by self-adjustment of the bubble size. As Figure 2.7(c, d) show, data points in Figure 2.5 on the bubble height to width ratio h/w and the fraction of water vapor in the bubble $\Delta V/V$ being plotted against T_s fell within a relatively narrow band for all heating regimes up to $T_s \sim 80°C$. While the bubble size increased with T_s, the fraction of water vapor in the bubble tended to decrease. Figure 2.7(e) illustrates the dependence of the bubble volume and cap surface area normalized by bubble height to width ratio 2h/w ratio; the bubble base diameter was about 2 mm in flight and on Earth. Data points for flight experiments fell close to the curve for a spherical cap and data for all experiments on Earth grouped together below this curve. A bubble residing on the heater eventually divided into two parts by forming a large bubble that departed from the heater and a small bubble pinned to the heater. The remaining bubble grew to about the same size and then divided by forming another departing bubble. This process repeated itself several dozens of times, each time faster and faster, and finally produced a vapor plume whose size was increasing with water temperature (Figure 2.4(b)C, images at 360s and 420s). The lifetime of the first bubble formed on the heater after applying DC voltage was much longer for heating cycles than for continuous heating due to a slowly rising water temperature (Figure 2.7(f)). For both heating modes, the departure of this bubble occurred in the range of liquid bulk temperatures $T_s \sim 50 - 80°C$ and showed the same dependence on the heat flux (Figure 2.7(f) inset, Table 2.6; Table 2.7):

$$T_s(°C) = (27.2 \pm 0.93) q_h(MW/m^2) + 44.96 \pm 1.13°C \quad (2.11)$$

with the coefficient of determination $r^2 = 0.966$. Deviations between values given by this equation and measurements are normally distributed random quantities at the 95% confidence level (Table 2.8; Table 2.9).

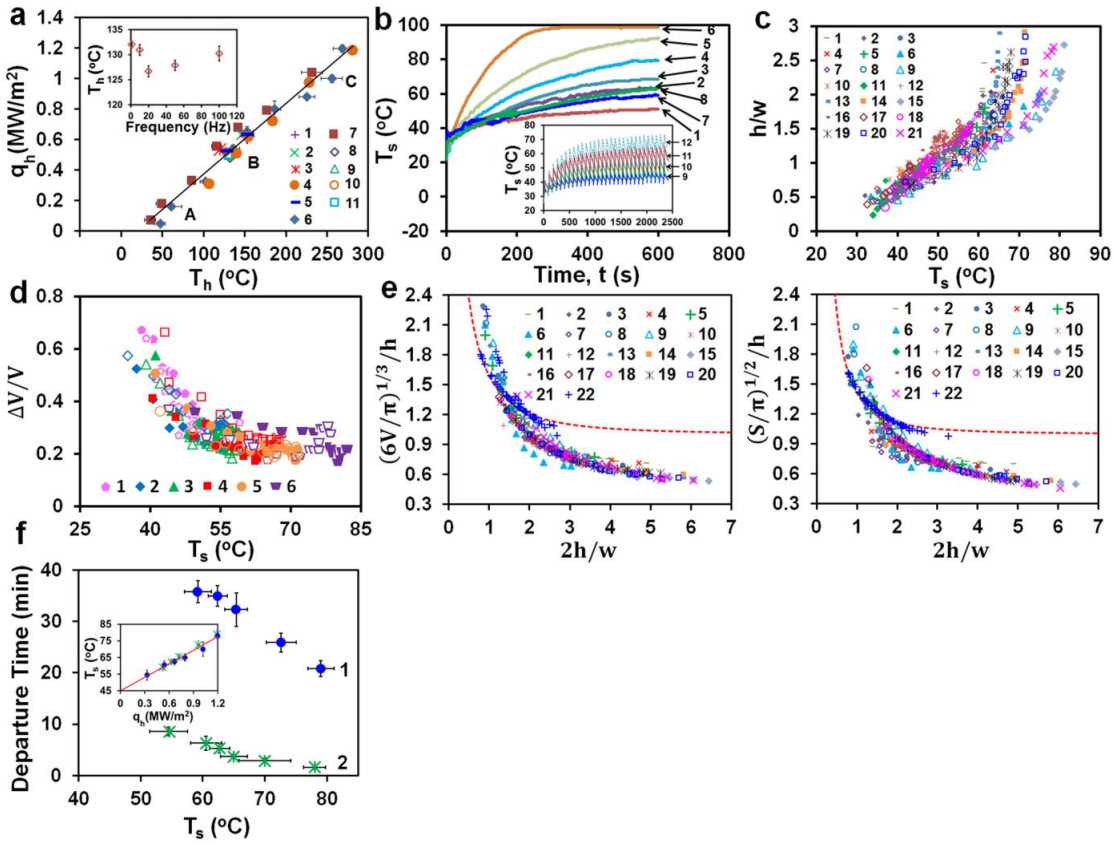

Figure 2.7 Effects of increasing heating DC voltage: (**a**) Stabilized heat flux q_h vs. heater temperature T_h. Flight: 1, 20V DC & 3kV/20Hz; 2, 22.4V DC & 4kV/20Hz; 3, 22.4V DC & 4kV/10Hz; Earth, heating cycles 20s on/60s off: 4, no HV pulses (points for 15, 20, 22.4, 25, 30, 35 V DC); 5, with 4kV/20Hz pulses (points for 20, 22.4 V DC); Earth, continuous heating: 6, no HV pulses (points for 5, 10, 15, 20, 22.4, 25, 27.5, 30, 35 V DC); 7, with 4kV/20Hz pulses (points for 5, 10, 15, 20, 22.4, 25, 30 V DC); 8-11, 20 V DC with 4kV pulses at 1 (8); 10 (9); 50 (10); 100 (11) Hz. Points A, B, C mark regimes in Fig. 2(b). Inset: Earth, continuous heating 20 V DC: T_h vs. frequency of 4kV pulses. (**b**) Earth, T_s, continuous heating: without HV pulses for 15 (1), 20 (2), 22.4 (3), 25 (4), 30 (5), 35 (6) V DC and with 4kV/20Hz pulses for 20 (7), 22.4 (8) V DC. Inset: heating cycles 20s on/60s off without HV pulses for: 15 (9), 20 (10), 25 (11), 30 (12) V DC. (**c**) Earth, bubble height to width ratio h/w vs. T_s for continuous heating: no HV pulses for 15 (1), 20 (2); 22.4 (3), 25 (4); 30 (5); 35 (6) V DC and with 4kV/20Hz pulses for 20 (7), 22.4 (8), 35 (9) V DC; heating cycles 20s on/60s off: no HV pulses for 15 (10), 20 (11), 22.4 (12), 25 (13), 30 (14), 35 (15) V DC and with 4kV/20Hz pulses for 15 (16), 20 (17), 22.4 (18), 25 (19), 30 (20), 35 (21) V DC. (**d**) Earth, relative changes of bubble volume $\Delta V/V$ as heating turned off vs. T_s for heating cycles 20s on/60s off with 4kV/20Hz pulses (empty symbols) and without HV pulses (filled symbols): 15 (1), 20 (2), 22.4 (3), 25 (4), 30 (5), 35 (6) V DC. (**e**) The bubble volume V and cap surface area S normalized by the bubble height h vs. bubble height to width ratio 2h/w for experiments on Earth, 1-21 as listed in (**c**), and in flight 22, 20V DC & 3kV/20Hz; 23, 22.4V DC & 4kV/20Hz; 24, 22.4V DC & 4kV/10Hz. The dashed line represents the spherical cap. (**f**) Earth, times of bubble departure vs. liquid temperature T_s for 1, heating cycles 20s on/60s off and 2, continuous heating. Points for 15V DC (only for regime 2 as a bubble remained on the heater after 40 min of cycles), 20, 22.4, 25, 30, 35V DC (data with and without 4kV/20Hz pulses within error bars) arranged from left to right. Inset: T_s vs. heat flux. Results of statistical analysis of measurements are listed in Table 2.8-2.9. Error bars in (a) and (f) represent standard deviations.

Flow velocities around a pinned bubble shown in Figure 2.8 were computed by tracking individual tiny bubbles formed in flight (seen in Figure 2.4(a)) and beads seeded in the water in Earth experiments. Two toroidal eddies circulating around the bubble in the opposite directions were formed in flight (Figure 2.8(a)). They pushed the hot water away from the bubble interface into the bulk and the cooler water from the bulk toward the bubble base with velocity ~1-3 mm/s. Similar eddies and a narrow vertical plume, rising from the bubble top with the velocity nearly twice greater than in the vortex flows, appeared under heating on Earth (Figure 2.8(b-e)). However, the plume contribution to the heat flux was remarkably insignificant (Figure 2.7(a)). The vortex flows intensity slightly increased with increasing the applied DC voltage and decreased as the heating was turned off. Application of HV pulses made the vortex flows more stable. In flight and on Earth, the top of a pinned bubble was observed to oscillate (SI3, video2) at frequencies $\nu_b \sim 2-4\text{Hz}$ with amplitude A_b that increased with water temperature from 10-30μm at $T_s \sim 25℃$ to 100μm at $T_s \sim 80℃$ and was not affected by HV pulses. Velocities of bubble oscillations $\sim \nu_b A_b = (20-120)\ \mu\text{m/s}$ were much smaller than vortex flow velocities (Figure 2.8).

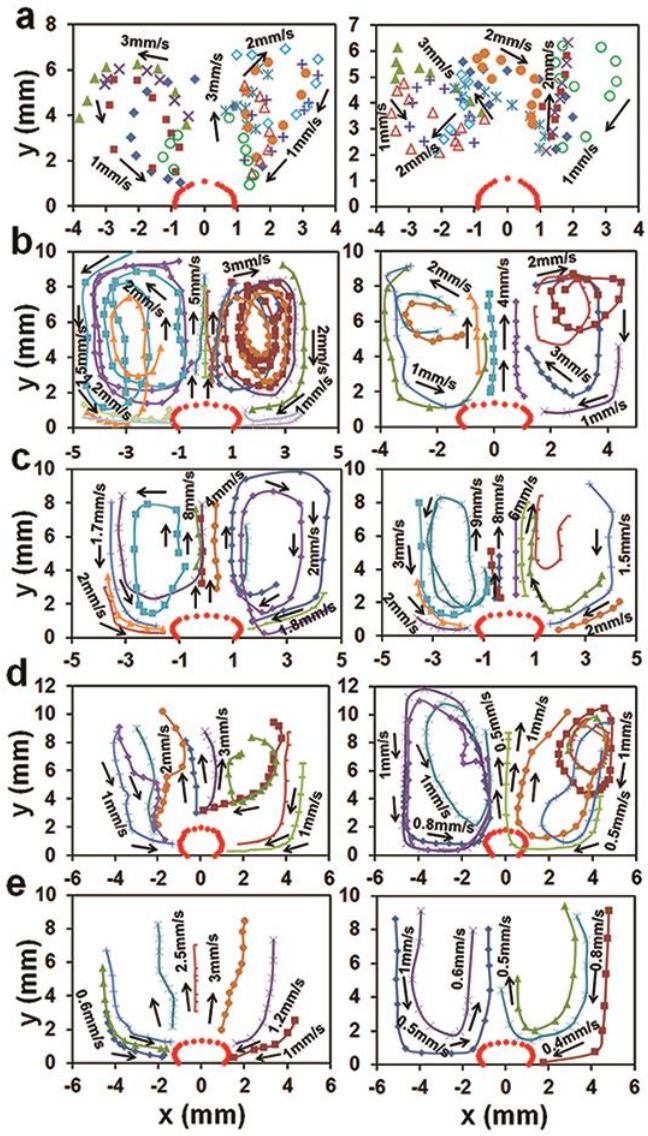

Figure 2.8 Flow patterns in the cuvette vertical plane: (**a**) Flight, *left:* freefall, 22.4V DC with 4kV/20Hz pulses; right: acceleration, no heating and pulses. (**b**, **c**) Earth, continuous heating: (**b**) 22.4 DC, (**c**) 30 V DC; with 4kV/20Hz pulses (*left*), without pulses (*right*). (**d**, **e**) Earth, heating cycles 20V DC 20s on/60s off: (**d**) with 4kV/20Hz pulses; (**e**) without HV pulses; heating ON (left), OFF (right). Symbols indicate trajectories of 10 individual microbubbles for (**a)** and individual 75-90 μm blue polyethylene microspheres (1.00g/cm^3, Cospheric, Santa Barbara, CA) on Earth: (**b**) 12 particles for left and 11 for right; **(c)** 12 for left and right; (**d**) 10 for left and right; (**e**) 8 for left and 5 for right.

The basic feature of a single-bubble boiling recorded in our experiments is the appearance of a large bubble that is staying for minutes on a relatively small heater on

Earth (L_h/L_c ~0.8) and in flight (L_h/L_c ~ 0.08) up to 270^0C at the water bulk temperature up to 80^0C (Figure 2.7). This bubble behavior was not observed in previous studies of water boiling on relatively large and small heaters under normal and low gravity. Specifically, bubbles of a similar size were reported at high heat fluxes and low subcooling in boiling water on large horizontal flat heaters on Earth ($L_h/L_c \geq 1$) [25-39]. They formed via vigorous lateral coalescence among small bubbles and departed from the heater in less than ~0.1-0.3s. In parabolic flights, bubble liftoff diameters from about 2 mm to 20 mm were observed in boiling water on flat heaters for $L_h/L_c \sim 1.8$ (Ref. 36) and ~ 3.7 (Ref. 37). However, these bubbles formed, grew and departed in about 10-12 s. Depending on the level of subcooling, several different modes of boiling water on thin horizontal wires were observed in experiments on Earth [42-50] for $L_h/L_c \sim 0.0046 - 0.370$, and in drop towers and parabolic flights [52-54] for $L_h/L_c \sim 0.0009 - 0.0030$, where L_h is the wire radius: large bubble boiling, coexisting boiling, and explosive small bubble boiling. In particular, raising the heater temperature for saturated boiling under normal [42] and low gravity [51] gradually increased the heat flux and the size of a vapor bubble covering the wire until it became totally blanked. As a result, the local maxima and minima in the curve heat flux vs. heater temperature for saturated boiling on Earth were found to vanish at [44] $L_h/L_c \leq 0.0096$. However, the formation of a large single bubble engulfing the wire was not observed in the Space Shuttle experiments [54] on subcooled boiling at $L_h/L_c \sim 0.0003$. But instead, a set of discrete bubbles formed on a wire, grew up to 4-6 mm and departed within about 10 min. An abrupt transition from the formation of individual bubbles which sprang from the heating surface in all radial directions to the formation of a thick, stable vapor film over the entire cylindrical heater was recorded for saturated boiling in parabolic

flight [54] at $L_h/L_c \sim 0.17$. The lateral motion of bubbles over the heating surface leading to their coalescence were observed in subcooled boiling on single and twisted submillimeter wires on Earth [45-51] and in parabolic flights [52,53]. Bubbles with diameters ranging from about 0.01 to 1.6 mm and departing from the heater in ~ 0.1 - 0.3s on Earth and ~1- 18s in flight were recorded in these experiments. Depending on the heat flux and subcooling level, bubbles staying on a heater were observed to eject liquid, vapor-liquid or fog-like jets flowing with velocities ~0.5-15 cm/s into the bulk liquid [45-53]. In ground experiments, the jets formed in the direction opposite to the gravity vector whereas in low gravity they formed in both directions from the wire [53]. These jets were concluded to be one of the important factors for overall heat transfer in subcooled boiling and the thermoscapillary force due to an interfacial temperature gradient (the Marangoni effect) was suggested as the dominant mechanism of jet formation [39-48]. In contrast, a liquid plume rising from the bubble top was observed only in our ground experiments (Figure 2.8) and its contribution to the heat flux appeared to be insignificant (Figure 2.7(a)).

2.6 Discussion

Presented results demonstrate that energy was transferred away from the heater by evaporating water at the bubble base, condensing vapor on the bubble cap, and then by circulating flow to the bulk water. To evaluate basic parameters needed for understanding physical mechanisms underlying the energy transfer, we use data in Figures 2.5 and 2.7 at $T_h = 155^0C$, $q_h = 0.6\,MW/m^2$ taken as characteristic and properties of water and air [25-28] (Section 2.4) at the saturation temperature of water $T_{sat} = 100^0C$ at 1atm, also as characteristic.

2.6.1 Flows of Vapor and Air inside the Bubble

The mass flow rate of liquid evaporating inside the bubble can be estimated as $\dot{m}_v = q_h S_h / h_{fg} \sim 1.2\,mg/s$ since the contribution of energy to heat the liquid flowing into the bubble and cool the condensate formed on the bubble cap is relatively small $c_{pl}(T_{sat} - T_r)/h_{fg} \sim 0.14$, where c_{pl} and h_{fg} are the water specific heat capacity and latent-heat of vaporization and the room temperature $T_r \approx 25℃$. A liquid flows into the bubble over the heated surface at the bubble footprint in the layer whose thickness δ_l (Figure 2.9(a)) can be evaluated from the mass balance $\delta_l \sim \dot{m}_v/\pi D\rho_l v_l \sim 0.2mm$ by taking $D \sim 2mm$ for the bubble base diameter and $v_l \sim 1mm/s$ for the liquid velocity according to data in Figure 2.5. The time it takes to heat this liquid is $t_l \sim \delta_l^2/\alpha_l \sim 0.2s$, α_l is the water thermal diffusivity. When the temperature of this liquid rises above T_{sat}, tiny vapor bubbles would form and grow with a velocity of the order of several of m/s since the Jacob number $Ja_h = \rho_l c_{pl}(T_h - T_{sat})/\rho_v h_{fg} \sim 164$ corresponds to the inertia dominated regime [56-59]. Once reaching the liquid surface, they burst and release vapor into the bubble interior. The length of the thin liquid-vapor region at the bubble footprint (1 in Figure 2.9(a)) through which heat is transferred away from the heater can be estimated as $l_l \sim v_l t_l \sim 0.24mm$. To evaluate variation of the local temperature across the heater, we took the solution of a steady-state conduction problem for the temperature of a rectangular heater from which heat is conducted outside through its edges [60]. In this case, the maximum and minimum local temperatures are respectively achieved at the heater center and the edges. Calculations presented in subsection 2.6.1.1 indicate that a difference between these values and the average heater temperature T_h increased from about 0.35^0C to 4.5^0C with raising T_h from 100^0C to 270^0C in our experiments (Figure 2.7(a)).

2.6.1.1 Calculations of temperature difference across the heater. The steady state conduction problem for the temperature of a rectangular heater ($2L \times 2l$) of thickness H is used for estimating variations of the local temperature across the heater. The heat generation is considered to be uniform. The heat is transferred away from the heater only through its edges that are maintained at the temperature T_0. The solution if this two-dimensional problem is given by the following equation [60]

$$T - T_0 = \frac{\dot{Q}L}{4Hk_h l}\left\{\frac{1}{2}\left[1 - \left(\frac{x}{L}\right)^2\right] - \frac{16}{\pi^3}\sum_{n=0}^{\infty}\frac{(-1)^n}{(2n+1)^3}\left[\frac{\cosh\frac{(2n+1)\pi y}{2L}}{\cosh\frac{(2n+1)\pi l}{2L}}\right]\cos\frac{(2n+1)\pi x}{2L}\right\} \qquad (2.12)$$

where is k_h is the heater thermal conductivity, $\dot{Q}$ is the total generated heat and $-L \leq x \leq L$, $-l \leq y \leq l$. The maximum temperature T_{max} is achieved at the heater center at $x = y = 0$ and the minimum temperature at its edges

$$T_{max} - T_0 = \frac{\dot{Q}L}{4Hk_h l}\xi_m\left(\frac{l}{L}\right) \qquad (2.13)$$

with $\xi_m\left(\frac{l}{L}\right) = \frac{1}{2} - \frac{16}{\pi^3}\sum_{n=0}^{\infty}\frac{(-1)^n}{(2n+1)^3\cosh\frac{(2n+1)\pi l}{2L}}$.

The average temperature T_{aver} of the heater is

$$T_{aver} - T_0 = \frac{\dot{Q}L}{4Hk_h l}\xi_a\left(\frac{l}{L}\right) \tag{2.14}$$

with $\xi_a\left(\frac{l}{L}\right) = \frac{1}{3} - \frac{64}{\pi^5}\sum_{n=0}^{\infty}\frac{\tanh\frac{(2n+1)\pi l}{2L}}{(2n+1)^5} = \frac{1}{3} + \frac{64}{\pi^5}\left[\sum_{n=0}^{\infty}\frac{1-\tanh\frac{(2n+1)\pi l}{2L}}{(2n+1)^5} - \varsigma(5)\left(1-\frac{1}{2^5}\right)\right]$, where the Riemann zeta function $\varsigma(5) = \sum_{n=1}^{\infty}\frac{1}{n^5} = 1.0369277551$. Taking $2L = 2mm$ and $2l = 2.3mm$, we obtain $\xi_m = 0.2914$ and $\xi_a = 0.1393$ that yields

$$T_{max} - T_0 = 0.0728\frac{\dot{Q}L}{Hk_h l} \quad \text{and} \quad T_{aver} - T_0 = 0.0348\frac{\dot{Q}L}{Hk_h l} \tag{2.15}$$

In in our experiments, the average heater temperature increased from 100^0C to 270^0C with raising the total heat from about 0.5W to 5.5W (Figure 2.6(a) in the paper). Taking $H = 0.65mm$ (Figure 2.1(d) in the paper) and the platinum thermal conductivity (Table 2.1) for k_h in Equation (2.15), we find that $T_{max} - T_{aver}$ and $T_{aver} - T_0$ increased from about 0.35^0C to 4.5^0C with raising $\dot{Q}$ from 0.5W to 5.5W.

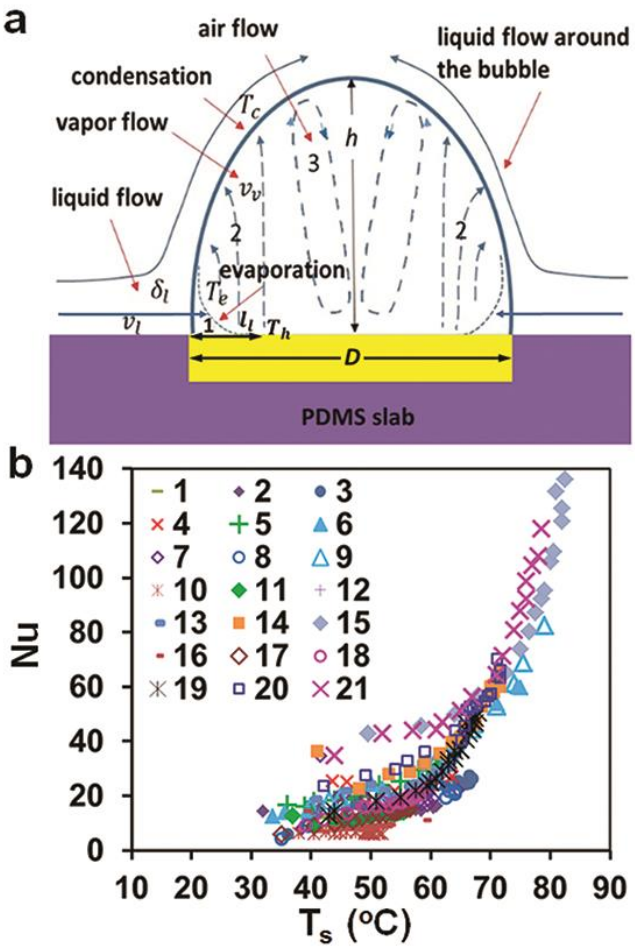

Figure 2.9 (a) Schematic of single-bubble boiling: 1, layer of thickness δ_l and length l_l at the bubble footprint where cold liquid flowing into the bubble with velocity v_l vaporizes; 2, vapor streaming toward the bubble cap with velocity v_v; 3, non-condensable air constituents accumulating away from the bubble cap; T_e and T_c, evaporation and condensation temperatures; h and D, bubble height and base diameter. (b) Earth, the Nusselt number Nu for heat transfer between bubble cap and surrounding liquid vs. T_s for continuous heating and heating cycles, 1-21 as listed in Figure 2.7(c).

Estimates for the mass flux and velocity of the vapor formed in a thin layer at the bubble footprint (1 in Figure 2.9(a)) yield $j_v \sim \dot{m}_v/S_l \sim 0.6\,\mathrm{mg/mm^2 \cdot s}$ and $v_v \sim j_v/\rho_v \sim 1\,\mathrm{m/s}$, where $S_l \sim \pi D\sqrt{\delta_l^2 + l_l^2} \sim 2\mathrm{mm}^2$ is the area where liquid vaporizes. An estimate for the velocity of condensate formed on the bubble cap of area $S \sim 10\mathrm{mm}^2$ (data in Figure 2.5(d)) $v_{lc} \sim \dot{m}_v/\rho_l S \sim 0.1\mathrm{mm/s}$ shows that vapor condensation does not drive

the liquid circulation around the bubble as v_{lc} is substantially smaller than flow velocities in Figure 2.8.

Non-condensable air constituents (oxygen and nitrogen) brought by the liquid into the bubble are carried with the streaming vapor toward the bubble cap and remain there while the vapor condenses. The diffusive flux of the air away from the bubble surface can balance the vapor flow only within a thin layer of thickness $\sim d_a/v_v \sim 40\mu m$, d_a is the diffusion coefficient of air constituents in water vapor (Section 2.4). As the volume of this layer $\sim d_a S/v_v$ is much smaller than the air volume in the bubble (data in Figure 2.5(e,c)), air carried with the streaming vapor would accumulates away from the bubble cap (region 3 in Figure 2.9(a)). Driven by the vapor flowing along the bubble cap (region 2 in Figure 2.9(a)), the velocity with which the air circulates inside the bubble is $v_a \sim v_v \sim 1\ m/s$. Flow of vapor and air is laminar as the Reynolds numbers are $Re_v \sim \varrho_v v_v h/\eta_v \sim 120$ and $Re_a \sim \varrho_a v_a h/\eta_a \sim 120$, where $h \sim 3.6$ mm is the bubble height (data in Figure 2.5(b)) and ϱ_v, η_v and ϱ_a, η_a are the vapor and air density and dynamic viscosity. An estimate for the vapor volume $l_l S \sim 2.4 mm^3$ is consistent with data on a change in the bubble volume ΔV in Figure 2.5(f) caused by vapor condensation. The time to replenish the vapor condensed as the heating is turned off $\sim \rho_v l_l S/\dot{m}_v \sim 1.2s$ is also consistent with observed changes of the bubble size in heating cycles in flight and on Earth (data in Figure 2.4(a,c)).

Once the three-phase contact line along the liquid layer inside a bubble resides on the well-wetted heater surface, the vapor region would be located above the heater surface as the interior contact angle is smaller than 90^0 (Figure 2.9(a)). If the bubble grows by moving the liquid layer beyond the heater edge, vapor would come in contact with the PDMS surface since the interior contact angle of water on the hydrophobic PDMS surface

is larger than 90^0. This situation can occur only when the PDMS temperature is greater than the dew point of water vapor. Otherwise, the bubble would shrink due to vapor condensation. This negative feedback facilitates anchoring of a bubble to the heater if the temperature of the surrounding surface is below the dew point.

2.6.2 Flow of Liquid around the Bubble

It is laminar as the Reynolds number is $Re_l \sim \varrho_l v_l h/\eta_l \sim 12$, where the liquid velocity $v_l \sim 1 mm/s$ (data in Figure 2.8) and η_l is the liquid dynamic viscosity. This flow might be generated by the surface tension force along the bubble cap [7,12,18-21,61] due to the temperature variation ΔT_b or by the shear stress exerted on the liquid-bubble interface by the flow of vapor and air inside the bubble. It is conceivable that both factors operate during the heating period, whereas the flow of vapor and air ceases when the heating is switched off (data in Figure 2.8(d,e)). The stress balance at the bubble surface for the former $\eta_l v_l/h \sim (d\gamma_l/dT)\Delta T_b/h$ yields $\Delta T_b \sim 1.5 \cdot 10^{-3} °C \ll T_h - T_r$. For the latter $\eta_l v_l/h \sim \eta_v v_{v,\tau}/h$ and/or $\eta_l v_l/h \sim \eta_a v_{a,\tau}/h$, it yields $1 - 2\, cm/s$ for the velocity of vapor $v_{v,\tau}$ and air $v_{a,\tau}$ tangent to the liquid-bubble interface that is much smaller that the velocity of vapor and air inside the bubble ~ 1m/s. These estimates indicate that the liquid flow around the bubble is highly sensitive to subtle processes at the bubble cap and requires a more careful study.

2.6.3 Heat Transfer at the Bubble Cap

To estimate temperatures of the liquid-vapor region T_e and at the bubble cap T_c (Figure 2.9(a)), we used the Hertz-Knudsen equation for the vapor mass flux j_v with the accommodation coefficient $\xi \sim 0.01 - 0.1$ for stagnant water surfaces [58]. Calculations

presented in subsection 2.6.3.1 yield $T_e \approx 114℃$, $T_c \approx 96℃$ for $\xi \sim 0.01$ and $T_e \approx 101℃$, $T_c \approx 99.7℃$ for $\xi \sim 0.1$. As the bubble cap temperature for both values of ξ is close to T_{sat} and T_s represents the bulk liquid temperature, the Nusselt number for heat transfer from the bubble cap to the surrounding liquid on Earth can be evaluated as

$$Nu = q_h S_h h / k_l S(T_{sat} - T_s), \tag{2.16}$$

where k_l is the liquid thermal conductivity and variations of the heat flux at the bubble cap $q_h S_h / S$ and the bubble height h with T_s were computed using data on q_h, S and h at a fixed applied voltage in Figure 2.5. Remarkably, values of Nu plotted in Figure 2.9(b) for both heating regimes lie within a relatively narrow band, increasing with T_s from about 20 at room temperature to 140 at $T_s \sim 80℃$. We compared these values with the data predicted by correlations for convective heat transfer from a vapor bubble of diameter condensing in a flow of subcooled water [63,64] and the buoyancy convection heat transfer from the cap of a solid hemisphere [65]. The former yielded $Nu \sim 2.5$ and the latter $Nu \sim 11$ for our experimental conditions (see subsection 2.6.3.2). These estimates clearly demonstrate that another mechanism contributes to energy transfer from the bubble cap to the surrounding liquid.

2.6.3.1 Temperatures in the liquid-vapor region and at the bubble cap. To estimate temperatures of the liquid-vapor region $\mathbf{T_e}$ and the bubble cap $\mathbf{T_c}$ (Figure 2.9(a) in the paper), we used the Hertz-Knudsen equation for the dependence of the vapor mass flux $\mathbf{j_v}$ on the vapor pressure $\mathbf{P_v}$ and temperature T

$$j_v = \frac{2\xi}{2-\xi}\sqrt{\frac{M_w}{2\pi R_{gas} T}}\left(P_{eq,w}(T) - P_v\right) \tag{2.17}$$

with the water molecular weight M_w, the gas constant R_{gas}, the saturated vapor pressure $P_{eq,w}(T)$ computed using the Antoine equation Equation (2.1) and the accommodation coefficient $\xi \sim 0.01 - 0.1$ for stagnant water surfaces [62]. P_v inside the bubble can be approximated as 1atm as $dT/dP_{eq,w} \sim 2.8 \cdot 10^{-4} K/Pa$ and thereby temperature variations caused by the vapor flow pressure $\rho_v v_v^2 \sim 0.6 Pa$ and surface tension pressure $4\gamma_l/D \sim 110 Pa$ are insignificant. The flux of vapor condensing at the bubble cap can be estimated as $j_c \sim -S_l j_v/S$ with $S = 10 m^2$.

For our experimental conditions, Equation (2.17) yields $T_e \approx 114℃$, $T_c \approx 96℃$ for $\xi \sim 0.01$ and $T_e \approx 101℃$, $T_c \approx 99.7℃$ for $\xi \sim 0.1$.

2.6.3.2 Convective Nusselt numbers. It is instructive to compare the Nusselt numbers in Figure 2.9(b) in the paper with the data predicted by correlations for convective heat transfer from a vapor bubble flowing in subcooled water [63] and the buoyancy convection heat transfer from the cap of a solid hemisphere [65]. The Nusselt number for the convective heat transfer from a vapor bubble of diameter $\boldsymbol{D(t)}$ condensing in a flow of subcooled water is given by the following expression [63]

$$Nu(t) = 0.6 Re^{1/2} Pr_l^{1/3}\left(1 - 1.20 Ja^{9/10} Fo_0^{2/3}\right) \tag{2.18}$$

where $\mathrm{Re} = \varrho_l v_B D/\eta_l$ is the Reynolds for the bubble velocity v_B relative to the liquid, Pr_l is the liquid Prandtl number, $\mathrm{Ja} = \rho_l c_{pl}\Delta T_{sub}/\rho_v h_{fg}$ is the Jacob number for the water subcooled temperature ΔT_{sub}, and $\mathrm{Fo}_0 = \alpha_l t/D_0^2$ with the initial bubble diameter D_0 accounts for thickening of the thermal boundary layer around a bubble with time t.

Experiments [63] were conducted over the range of Re and Ja close to our experiments. As the first term in Equation (2.18) represents the Nusselt number similar to that for a plate [64], Equation (2.18) for our experimental conditions with $D_0 = h$, $v_B = v_l = 1\mathrm{mm/s}$ (Figure 2.8 in the dissertation) and $\Delta T_{sub} = 75℃$ yields Nu decreasing from the initial 2.5 to zero at $\sim 2.6\mathrm{s}$.

An attempt to use data on the buoyancy convection heat transfer from the cap of a solid hemisphere [65] of radius r_H by taking $r_H = h$ and the Rayleigh number $\mathrm{Ra}_H = g\beta_l\Delta T r_H^3/\nu_l\alpha_l \sim 5\cdot 10^5$, where β_l is the liquid volumetric expansion, predicted $v_H \sim \alpha_l \mathrm{Ra}_H^{1/2}/r_H \sim 3.3\,\mathrm{cm/s}$ for the liquid velocity that overestimates velocity measurements in our Earth's experiments (Figure 2.8 in the dissertation) and yields

$$\mathrm{Nu}_H = 0.415\mathrm{Ra}_H^{1/4} \sim 11 \tag{2.19}$$

We attribute large values of Nu in Figure 2.9(b) to periodic injection of a vapor-air mixture from the bubble caused by periodic overheating of the liquid layer near the bubble cap. Taking $j_c h_{fg}$ with $j_c \sim -S_l j_v/S$ for the heat flux of vapor condensing on the bubble cap, the time period and length it takes to heat the cool liquid flowing with the velocity v_l along the bubble cap from T_r to T_c can be estimated using the energy balance equation as $t_c \sim \pi \mathrm{Ja}_c^2 \alpha_l/4v_{vc}^2 \sim 0.15\mathrm{s}$ and $v_l t_c \sim 0.15\mathrm{mm}$, where $\mathrm{Ja}_c = \rho_l c_{pl}(T_c - T_r)/\rho_v h_{fg} \sim 210$

and $v_{vc} \sim j_c/\rho_v \sim 0.2\,m/s$. When the local liquid temperature rises above T_c, the rate of vapor condensation decreases and the local gas pressure under the bubble cap builds up, eventually jetting vapor mixed with air into the surrounding liquid. Once the layer of overheated liquid is blown away from the bubble cap and replaced by a colder liquid, the liquid temperature at this spot drops down below T_c causing the rate of vapor condensation to increase and thereby to stop gas injection. Then, the local liquid temperature begins to rise and the process repeats itself again and again. The estimate for the frequency of local overheating $\sim 1/t_c \sim 7Hz$, correlates well with the frequency range of bubble cap oscillations observed in flight and ground experiments. In low gravity, periodic injection of a vapor-air mixture created circulating tiny bubbles (Figure 2.4(a) and SI2, video1) whose stability in the bulk liquid was caused by the residual air. On Earth, it generated plumes rising through the bulk liquid and releasing the trapped air by bubbling at the water surface (SI3, video2). In both cases, the rate of heat transfer from the bubble was drastically enhanced by increasing the area of the vapor-liquid interface. The proposed mechanism is consistent with the observation that Nu given by Equation (2.16) (Figure 2.9(b)) depends only on the water temperature. The flow circulation time within the cuvette $t_f \sim 20s$ (Figure 2.7) is sufficient for the liquid flowing away from the bubble to transfer the acquired heat to the bulk by thermal conduction across closed streamlines as the characteristic length $\sqrt{2\alpha_l\, t_f} \sim 3mm$ is comparable to half the cuvette width. Note that the frequency range of local liquid overheating is lower by more than an order of magnitude compared to intense capillary waves causing the violent emission of micrometer-sized bubbles from a condensing vapor bubble in the so-called microbubble emission boiling (MEB) regime [59,66-68].

2.6.4 Bubble growth and Detachment

Bubble evolution is mainly governed by normal stresses at the bubble interface since the contribution of tangential stresses estimated above is relatively small. The normal stresses include the surface tension pressure, liquid hydrostatic pressure, and dynamic pressures of liquid and condensing vapor. The role of the dynamic pressure of liquid flow driven by the bubble growing at the timescale of the order of minutes (Figure 2.5(a-d)) is insignificant as the ratio between its value and the surface tension pressure $4\gamma_l/D$ is $\sim 2 \cdot 10^{-6}$. The contribution of the vapor dynamic pressure can be neglected[65-68] only if the ratio $\rho_v \dot{V}_v^2/\pi^2 D^3 \gamma_l$ is smaller than $2.5 \cdot 10^{-6}$, where $\dot{V}_v = qS_h/\rho_v h_{fg}$ is the vapor flow rate inside the bubble. An extremely low flow rate is required because the vapor velocity increases rapidly when the bubble neck shrinks radially. In our experiments at $T_h > 100℃$ where q_h was varying from 0.3 to $1.2 MW/m^2$ (Figure 2.7(a)), this ratio ranging from $1.3 \cdot 10^{-4}$ to $2.1 \cdot 10^{-3}$ exceeded significantly this limitation. Nevertheless, the quasi-static equation for a pinned bubble [69-72] that considers only the surface tension and hydrostatic pressures provides some understanding of the bubble behavior. In particular, the dimensionless solution of this equation predicts that the bubble shape is fully characterized by its relative height $2h/D$ and the Bond number $Bo = (D/2L_c)^2$. In boiling, the bubble height is determined by the thermal balance across the bubble cap that is expressed in terms of Nu specified by T_s (Figure 2.9(b)). This feature explains why dimensionless characteristics of bubbles in ground experiments plotted against T_s for various values of q but all with $Bo \sim 0.16$ for $100℃$ would group together (Figure 2.7(c,d)). It also explains a more elongated shape of bubbles observed in ground experiments compared to a spherical shape of bubbles formed in flight at $Bo \sim 1.6 \cdot 10^{-3}$ (Figure 2.7(e)).

Within the framework of the quasi-static equation, the greatest value of the relative bubble height $2h_{max}/D$ at a particular value of Bo for which the neck becomes zero is assumed to represent a bubble that divides into two parts in the neck region, one forming a departing bubble and the other a new pinned bubble [70-72]. Expressions [71,72] for the bubble at zero neck predict height $h_{max} = 5.4\text{mm}$ with the width 3.1mm and volume $V_d = 26.4\text{mm}$ for $\text{Bo}\sim0.16$ and $\text{D}\sim2\text{mm}$ occurred in our ground experiments. While we observed a similar mode of bubble departure, a bubble at this instant was more elongated and its volume was two-three times smaller, depending on the heating regime (Figure 2.5(c)). These estimates and experimental data on the bubble departure time (Figure 2.7(f), Equation (2.11)) indicate that the bubble pinch-off was strongly influenced by the vapor flow rate at the bubble base that is determined by the heat flux.

2.7 Conclusion

Single-bubble boiling of water on a millimeter-sized well-wetted heater was recorded under normal gravity and low gravity in parabolic flights. The gravity contribution to the heat transfer was insignificant. The lifetime of a bubble on the heater varied from 1 to about 40 min, depending on the heating mode and water temperature. Due to self-adjustment of the bubble size, the heat flux provided by boiling rose linearly up to about 1.2MW/m^2 with increasing heater temperature and was not affected by a gradually rising water temperature. The application of high-voltage pulses increased the heat flux by about 10% at the same heater temperature. Estimates of basic flow and heat transfer parameters provided insight into physical mechanisms underlying single-bubble boiling. As the rate of heat transfer from the bubble cap exceeded predictions of convective models by more than an order of magnitude, it was attributed to periodic injection of a vapor-air mixture from the bubble to

the surrounding liquid. While the quasi-static model for the bubble growth explained similarity in dependence of the bubble shape on water temperature for different heating regimes, the observed bubble pinch-off was strongly influenced by the vapor flow rate at the bubble base.

The fast response and stable operation of single-bubble boiling over a broad range of temperatures pave the way for development of new devices to control heat transfer by forming surface domains with distinct thermal properties and wettability. The bubble lifetime can be adjusted by changing the water temperature. The ability of heating water on millimeter scales far above 100°C without an autoclave or a powerful laser provides a new approach for processing of biomaterials and chemical reactions. The replacement of PDMS with high-temperature insulation would make it possible to increase the heater temperature to 320-350^{0}C needed to initiate the spinodal decomposition of water.

CHAPTER 3

ELECTRIC-FIELD-DRIVEN PHENOMENA IN COLLOIDS OF POLARIZED PARTICLES

3.1 Abstract

To explore the effect of particle polarizability on the formation of a cellular pattern, our experiments are conducted on dilute suspensions of near-neutrally buoyant positively and negatively polarized micrometer-sized particles. As soon as a strong field is applied, particles formed chains along the field direction in both suspensions. However, the rearrangement of chains into a cellular pattern occur only in suspensions of negatively polarized particles. Considering the binary particle-particle interaction, current theories for polarized particles predict that the field effect depends on the square of the particle polarizability and therefore should be the same for negative and positive polarized particles. Our experiments demonstrate that this prediction is limited to the first stage of process when particles formed chains along the field direction. Based on experimental presented in this dissertation, it is suggested that the formation of a cellular pattern by negatively polarized particles is driven by the weak multi-particle repulsion. Future microgravity experiments on non-neutrally buoyant suspensions of polarized particles in the International Space Station are expected to reveal the effects of gravity on the formation of cellular patterns.

3.2 Introduction

3.2.1 Polarization of Particles in an Electric Field

Following the application of an electric field, positive and negative electric charges in a polarizable material move slightly in opposite directions from their equilibrium positions

thereby causing the material to gain an electric dipole moment in the field direction. A magnitude of the electric dipole moment for a system of two point charges, positive $+q$ and negative $-q$ (Figure 3.1), is [73]:

$$\mathbf{p} = q\mathbf{d} \tag{3.1}$$

where **p** is a dipole moment, **d** is the displacement vector pointing from the negative charge to the positive charge and $\boldsymbol{E_{ext}}$ is the applied external electric field. Although the adjacent positive charge head and negative charge tail of an internal dipole cancels each other in the bulk, cancellation does not occur at the bounding surfaces. Instead, the dipole heads create a positive surface charge on one of the surfaces and the dipole tails create a negative surface charge on the opposite surface. These two opposite surface charges generate an internal electric field in the direction opposite to the direction of the dipoles and therefor to an externally applied electric field.

A dipole moment acquired by a spherical dielectric particle of radius a and dielectric permittivity ε in a uniform electric field $\boldsymbol{E_{ext}}$ in SI units is [73] (Figure 3.2)

$$\mathbf{p} = 3\varepsilon_o \beta v_p \mathbf{E_{ext}} \tag{3.2}$$

where $\beta = (\varepsilon - 1)/(\varepsilon + 2)$ is the particle polarizability in vacuum, ε in the particle dielectric constant, ε_o is the vacuum permittivity equal to $8.85 \cdot 10^{-12}$ Farad per meter (F/m), and v_p is the particle volume.

When an AC (alternating current) electric field $\mathbf{E_{ext}} = \mathbf{E_o} cos(\omega t)$, with $\mathbf{E_o} = \mathrm{E}_{0,x}\boldsymbol{e}_x + \mathrm{E}_{0,y}\boldsymbol{e}_y + \mathrm{E}_{0,z}\boldsymbol{e}_z$ being the field amplitude, is applied to a conducting sperical particle suspended in a conducting fluid, the induced dipole moment can be written as [74]

$$\mathbf{p} = 3\varepsilon_0 \varepsilon v_p [Re[\beta(\omega)]\mathbf{E_o} cos(\omega t) - Im[\beta(\omega)]\mathbf{E_o} sin(\omega t)] \tag{3.3}$$

with the particle polarizabilty

$$\beta(\omega) = \frac{\varepsilon_p^*(\omega) - \varepsilon_f^*(\omega)}{\varepsilon_p^*(\omega) + 2\varepsilon_f^*(\omega)} = Re[\beta(\omega)] + iIm[\beta(\omega)] \tag{3.4}$$

where $\varepsilon_p^* = \varepsilon_p'(\omega) - i\varepsilon_p''(\omega)$ is the complex dielectric constant of the particle and $\varepsilon_f^* = \varepsilon_f'(\omega) - i\varepsilon_f''(\omega)$ is the complex dielectric constant of the fluid, both at the field frequency ω. The imaginary part of the complex dielectric constant is related to the electric conductivity $\sigma_p(\omega)$ of the particle and of the fluid $\sigma_f(\omega)$ as $\varepsilon_p''(\omega) = \sigma_p(\omega)/\varepsilon_0\omega$ and $\varepsilon_f''(\omega) = \sigma_f(\omega)/\varepsilon_0\omega$ that describes the electric energy loss due to the generated electric current. The relative loss of the electric energy is referred to as the dissipation factor or as the loss tangent $tan\theta_p = \varepsilon_p''(\omega)/\varepsilon_p'(\omega)$ and $tan\theta_f = \varepsilon_f''(\omega)/\varepsilon_f'(\omega)$. The sign of **p** in Equeation (3.3) depends on a difference between the complex dielectric constants of the particles and the fluid.

3.2.2 Electrophoresis and Dielectrophoresis

When a polarized particle is subjected to a spatially non-uniform electric field $\mathbf{E}_{\boldsymbol{ext}}$, a force exerted on this particle includes two terms as there two main phenomena to occur: electrophoresis (EL) and dielectrophoresis (DEP) [74]

$$\mathbf{F} = \mathbf{F}_{\boldsymbol{el}} + \mathbf{F}_{dep} = Q_p\mathbf{E}_{\boldsymbol{ext}} + (\mathbf{p}\cdot\nabla)\mathbf{E}_{\boldsymbol{ext}} \tag{3.5}$$

where $Q_p\mathbf{E}_{\boldsymbol{ext}} = Q_p\left(\mathrm{E}_{ext,x}\boldsymbol{e}_x + \mathrm{E}_{ext,y}\boldsymbol{e}_y + \mathrm{E}_{ext,z}\boldsymbol{e}_z\right)$ and $(\mathbf{p}\cdot\nabla)\mathbf{E}_{\boldsymbol{ext}} = p_{\boldsymbol{x}}\frac{\partial \mathrm{E}_{ext,x}}{\partial x}\boldsymbol{e}_x + p_{\boldsymbol{y}}\frac{\partial \mathrm{E}_{ext,y}}{\partial y}\boldsymbol{e}_y + p_{\boldsymbol{z}}\frac{\partial \mathrm{E}_{ext,z}}{\partial z}\boldsymbol{e}_z$, Q_p and $\mathbf{p}$ are the particle charge and dipole moment.

The first term in Equation (3.5) represents the electrophoretic force $\mathbf{F_{el}}$ that drives a charged particle suspended in a fluid toward the electrode of an opposite charge

$$\mathbf{F_{el}} = Q_p\mathbf{E_{ext}} \tag{3.6}$$

The ability of a charged particle to move through a host fluid in a DC (direct current) electric field is characterized by its electrophoretic mobility that is proportional to the particle charge Q_p and inversely proportional to the size of particle a and the fluid viscosity η_f [75]

$$\mu_p = \frac{Q_p}{6\pi\eta_f a} \tag{3.7}$$

The mobility is measured as the ratio of the particle velocity V_d to the field strength E_{ext}

$$\mu_p = V_d/E_{ext} \tag{3.8}$$

The electrophoretic mobility of a particle μ_p is characterized by zeta-potential ζ. Zeta potential represents the potential difference between the fluid and the stationary layer of fluid ions attached to the particle [75]. The thickness of this layer is characterized by the Debye length k^{-1}. If the Debye length is very thin compared to the particle radius, $ka \gg 1$, the particle mobility is given by the Smoluchowski equation [75] $\mu_p = \varepsilon_0\varepsilon_f\varsigma/\eta_f$ and the particle charge in Equation (3.7) is $Q_p = 6\pi\varepsilon_0\varepsilon_f\varsigma a$. If the double layer is very thick compared to the particle radius, $ka \ll 1$, the particle mobility is given by the Hückel equation [75] $\mu_p = 2\varepsilon_0\varepsilon_f\varsigma/3\eta_f$ and the particle charge in equation (3.7) is $Q_p = 4\pi\varepsilon_0\varepsilon_f\varsigma a$. The Smoluchowski model is valid for most aqueous solutions (large ε_f and high ionic strength), where the Debye length is usually only a few nanometers. The Hückel model is useful for non-polar fluids (low ε_f and low ionic strength), where Debye length is much larger.

The second term in equation (3.5) represents the dielectrophoretic force. It does not require a particle to be charged. It caused by the particle polarization in the presence of an electric field and equals to the product of the particle dipole moment and the gradient of the field strength. Since the particle dipole moment is proportional to the field strength, the dielectrophoretic force appears to be proportional to the gradient of the square of the field strength and strongly depends on the frequency of the electric field and a difference in polarizability of the particle and the fluid and the particles shape and size.

Electrophoretic effects vanish in an AC field at a sufficiently high field frequency due to the zero time average of the total particle displacement caused by the electrophoretic force. Specifically, for the field $\mathbf{E_{ext}} = \mathbf{E_o} cos(\omega t)$, where $\mathbf{E_o} = \mathrm{E}_{0,x}\boldsymbol{e}_x + \mathrm{E}_{0,y}\boldsymbol{e}_y + \mathrm{E}_{0,z}\boldsymbol{e}_z$ is the field amplitude, the total particle displacement over the period $2\pi/\omega$ of the field oscillation is $\mu_p \int_t^{t+2\pi/\omega} \mathbf{E_o} cos(\omega t) dt = 0$.

In contrast, dielectrophoresis operates in high-frequency fields [74] because the dielectrophoretic force averaged over field oscillations gives a nonzero value: $\frac{\omega}{2\pi}\int_t^{t+2\pi/\omega}[\mathbf{E_o} cos(\omega t)]^{\mathbf{2}} dt = \frac{1}{2}\left(E_{0,x}^2 + E_{0,y}^2 + E_{0,z}^2\right)$ as $\frac{\omega}{2\pi}\int_t^{t+2\pi/\omega}[cos(\omega t)]^{\mathbf{2}} dt = \frac{1}{2}$. Using Equations (3.3) and (3.5) for a spherical particle and taking into account that $\frac{\omega}{2\pi}\int_t^{t+2\pi/\omega} sin(\omega t)cos(\omega t) dt = 0$, we obtain the following expression for the dielectric force [74]

$$\mathbf{F_{dep}} = \frac{3}{2}\varepsilon_0 \varepsilon_f' v_p Re[\beta(\omega)] \nabla \langle \mathbf{E}_{\mathrm{ext}}^2 \rangle \tag{3.9}$$

where $\langle \cdot \rangle$ denotes time averaging over the field oscillation $\nabla \langle \mathbf{E}_{\mathrm{ext}}^2 \rangle = \frac{1}{2}\left(\frac{\partial E_0^2}{\partial x}\boldsymbol{e_x} + \frac{\partial E_0^2}{\partial y}\boldsymbol{e_y} + \frac{\partial E_0^2}{\partial z}\boldsymbol{e_z}\right)$ is the gradient of the AC field averaged over the period of AC field oscillation. For a low conducting fluid, the dissipation factor $tan\theta_f$ is small and the imaginary part of ε_f^* can be neglected.

The value of $\beta(\omega)$ of the particle can be calculated from measurements of the concentration dependence of the complex dielectric constant $\varepsilon_s^*(\omega)$ of a suspension in low

AC electric fields. This calculation employs the following Maxwell-Wagner expression for a suspension of randomly distributed particles [76, 77]

$$\frac{\varepsilon_s^* - \varepsilon_f^*}{\varepsilon_s^* + 2\varepsilon_f^*} = c\beta(\omega) \tag{3.10}$$

where c is the particle volume fraction.

Depending on the sign of Re(β) in Equation (3.9), a particle moves toward the regions of a high field strength (positive dielectrophoresis) or a low field strength (negative dielectrophoresis) (Figure 3.3). The particle polarizability strongly depends on the frequency of an electric field. Therefore, it is possible for a particle to experience either positive DEP or negative DEP depending on the field frequency. The reason is that the orientation of the dipole depends largely on the accumulation of charge on either side of the particle-fluid interface. If a sufficiently high-frequency AC electric field is applied then charges in the particle and the fluid do not have time to move and $\beta(\omega) = \frac{\varepsilon_p'(\omega) - \varepsilon_f'(\omega)}{\varepsilon_p'(\omega) + 2\varepsilon_f'(\omega)}$, where $\varepsilon_p'(\omega)$ and $\varepsilon_f'(\omega)$ are the real parts of the high frequency dielectric constants [74]. At low field frequency, $\beta(\omega)$ is determined by the electric conductivity of the particle and the fluid [74] $\beta(\omega) = \frac{\sigma_p(\omega) - \sigma_f(\omega)}{\sigma_p(\omega) + 2\sigma_p(\omega)}$

3.2.3 Structure Formation in Colloidal Suspensions in Strong Electric Fields

A colloidal suspension is prepared by dispersing solid particles in a host fluid. The ability of an electric field to assemble and manipulate particles in a colloidal suspension is currently employed in a wide range of applications as it offers a simple and efficient

method to control the particle motion and arrangement [78-84]. Examples include fabrication of nanoscale and microscale materials for microelectronic and photonic devices and various sensors. One of significant applications is related to electrorheological (ER) fluids which are suspensions of highly polarizable non-conducting particles (up to 50 micrometers diameter) in an electrically insulating fluid [85, 86]. The ability of ER fluids to change the apparent viscosity reversibly by an order of up to 100,000 in response to an applied electric field is used in fast acting hydraulic valves, clutches and electromechanical actuators [85, 86].

When a colloidal suspension is exposed to an electric field, particles acquire dipole moments and begin to interact with one another via dipole forces. If the mutual attraction or repulsion of dipoles (Figure 3.4) is sufficiently strong, it causes a colloid to undergo reversible phase transitions from a random arrangement of particles into a variety of ordered aggregation patterns, such as chains and columns along the field direction that can aggregate to form sheets and colloidal crystals (Figure 3.5). In particular, a drastic change of the apparent viscosity of ER fluids is caused by formation of particle chains and columns in an electric field.

The relative strength of dipolar forces between colloidal particles is characterized by a dimensionless parameter that expresses the ratio of the electric energy to the thermal energy [74,78]:

$$\lambda = \frac{v_p \varepsilon_0 \varepsilon_f E_{ext}^2 \beta^2}{4 k_B T} \tag{3.11}$$

where v_p is the particle volume, k_B is the Boltzmann constant and T is the temperature. As can be seen in Equation (3.11), the dipolar interaction between particles induced by an electric field is proportional to β^2whose magnitude depends on the field frequency and the mismatch of dielectric constants and conductivities between particles and a host fluid. As it specified by β^2, colloids of positively ($\beta > 0$) and negatively ($\beta < 0$) polarized particles are expected to form similar structures in a uniform electric field. Electric field-induced structure formation occurs for a sufficiently large λ when the dipolar forces dominate. Theory [87,88] predicts the field-induced phase separation of a colloid in two phases for a relatively strong electric field, one with lower particle content and the other with higher particle content. The phase diagram of a colloid subjected to a uniform field, being expressed in terms of the particle volume fraction, c, versus the relative field strength, λ, is shown in Figure 3.6. The single-phase region on this diagram represents the random spatial arrangement of particles in a relatively low field (small λ). The two-phase region corresponds to the appearance of regions with higher and lower content of particles in a sufficiently strong field (large λ). However, this theory does not predict the shape and arrangement of these regions formed as the field induced separation proceeds.

Tunable control of competition between the interparticle colloidal forces (van der Waals forces, electrical double layer forces, steric forces, hydrophobic forces, etc.) and induced dipolar forces displays a rich variety of structures formed by particles in strong electric fields [89-95]. Structures form in two distinct steps. Firstly, because of the anisotropy of dipolar forces between individual particles, particles tend to form head-to-tail chains parallel to the direction of an applied electric field (Figure 3.4), which happens over a time scale t_a. Particle chains observed in numerous experiments typically span the

entire gap between electrodes. The time it takes particles to form chains can be estimated by balancing dipolar forces and viscous forces due to the motion of these particles a fluid of viscosity η_f that yields $t_a = 2\eta_f \xi(c)/5\varepsilon_0\varepsilon_f\beta^2 E_{ext}^2$ with the concentration dependent factor $\xi(c) \approx \left[(\pi/6c)^{5/3} - 1\right]$ [24]. This estimate agrees well with experimental data on chain formation in ER fluids in sufficiently strong electric fields [97]. It is found that formation of particle chains in relatively low frequency electric fields can also be assisted by electrophoretic forces [96]. During the second step, chains, multi-chain columns and some remaining free particles slowly drift together or away from one another to coalesce and form thick columns along the field direction that are encircled by the fluid. The second step is much longer than t_a [98, 99].

The first theory for the chain coalescence and formation of colloidal crystals was developed in [100]. They analyzed dipolar interaction between two chains formed by non-conducting spherical particles dispersed in a non-conducting fluid in a sufficiently strong electric field. Each particle is assumed to acquire a dipole moment **p** in the field direction given by Equation (3.2) with $\beta = (\varepsilon_p - \varepsilon_f)/(\varepsilon_p + 2\varepsilon_f)$. The chains are considered to span the gap between two parallel electrodes. It was found [29] that the electric field generated by a chain oscillates along the field direction with period of the particle diameter $2a$ and decays exponentially with distance away from the chain with the decay length a / π. The interaction between two chains appears to be repulsive when they are in register and attractive when they are out of register (Figure 3.7a, b). Interactions between chains cause them to coalesce and eventually form a body-centered tetragonal (bct) colloidal crystal that has an energy lower than other structures (Figure 3.7(c)). These predictions were confirmed

by experiments on ER fluids [85] and model colloids [98, 99, 102-104] and MD simulations for systems of dipolar particles [105-111].

Although numerous experiments have been performed to study aggregation driven by dipole-dipole interaction between polarized particles, a rich variety of patterns that have been observed could also have been influenced by gravity effects such as particle sedimentation, convection and jamming, which often compete with dipolar forces during the slowly evolving structure formation. Low gravity experiments conducted in parabolic flight [112] revealed that the presence of even weak gravity forces in a suspension of non-buoyancy-matched particles significantly changes the particle patterns formed by exposure of a polarized suspension to an electric field. These observations demonstrate that study of field driven colloidal processes under terrestrial conditions requires precise matching of densities between the particles and the suspending fluid to avoid undesirable gravity effects.

In experiments [113] the extraneous effects were minimized, if not eliminated altogether, for studying the influence of dipolar interactions on structure formation. It was achieved: (a) by using a suspension of neutrally buoyant polyalphaolefin spheres (45 and 90 μm) in Mazola corn oil with $[\beta(\omega)] \approx -0.15$, (b) by employing (AC) fields of high strength, (c) by working with relatively large frequencies where electrophoresis and electro-convection were suppressed, and (d) by using a low-conducting fluid. In contrast to previous experiments that focus on the particle arrangement along the field direction, the main emphasis was on the particle arrangement in the plane perpendicular to the field direction. Surprisingly, a new phase transition was observed in these experiments, which has never been reported in the past. Following the application of an AC field, the particles (seen as white spots in photos in Figure 3.8) aggregated head-to-tail into chains that bridged

the gap between the electrodes, remaining uniformly distributed in the plane perpendicular to the field direction. The chains then began to coalescence laterally to form thicker multi-chain columns, also maintaining their uniform spatial distribution. A novel, unexpected transition was that the columns began slowly moving radially outward, creating particle-free domains spanning the gap between the electrodes. However, the process of column coalescence continued as the columns moved radially. The particle-free domains (seen as black voids in photos in Figure 3.8) grew until they interfered with one another, at which point a steady cellular pattern, in which large-scale particle-free domains (voids) were encircled by particle-rich thin walls (seen as white in photos in Figure 3.8), was established. The formation of similar cellular patterns was then observed [114] on suspensions of 0.8 μm silica spheres dispersed in a refractive index matched solvent of water/dimethyl sulfoxide (15/85 by volume) (Figure 3.9). Using data on dielectric constants of silica (~ 3.7 [116]) and water/dimethyl sulfoxide solutions (~ 49 [117]), the relative particle polarizability in suspensions used in [114] can be estimated as $Re[\beta(1\ MHz)] \approx -0.44$.

Surprisingly, the equilibrium characteristic size of particle-free domains observed in [113,114] scales linearly with the electrode gap thickness and appears to be insensitive to the particle size and the field strength and frequency. These features suggest that this phase transition is of a mesoscale type, i.e., at a scale larger than the particle size but comparable to the gap between electrodes. Such ultralow-density cellular structures have potential applications as macroporous materials since they are 10–100 times emptier than conventional porous materials. We need to emphasize that columns confined between electrodes in experiments [113,114] behave effectively as infinite chains and columns considered in the model of [100] as their end charges are cancelled by image charges

induced in the conducting electrodes (Figure 3.7 (a), (b)). There is therefore no repulsion between chains and columns associated with the bound charges at their ends that initiates their rearrangement in the plane perpendicular to the field direction as observed in ferrofluids, magnetic emulsions and magneto-rheological fluids confined between non-magnetic plates [115].

The reported ability to tune the characteristic size of cellular domains (Figures. 3.8 and 3.9) by using the particle concentration and the size of a gap between electrodes as control parameters, suggests a new means for manipulating the particle patterns and offers the potential to develop novel routes for controlling colloids and creating materials with tailored structures. However, no physical explanation has been provided so far for the observed spontaneous rearrangement of the columns into a large-scale cellular pattern. Specifically, numerous MD simulations of the field-induced behavior of dipolar particles confined between electrodes predict the formation of particle chains and columnar clusters made of several chains along the field direction that tend to crystallize in a body-centered tetragonal arrangement of the particles [105-111]. However, the appearance of cellular patterns similar to those shown in Figures 3.8 and 3.9 was not found in these studies, which thus remains as an open issue and still awaits an explanation.

Experiments on neutrally buoyant suspensions of polarized particles that we will be carried out in the dissertation should be helpful in providing the necessary framework for understanding mechanisms underlying formation of cellular patterns and developing models for their description. Microgravity experiments on non-neutrally buoyant suspensions of polarized particles in the International Space Station are expected to reveal the effects of gravity on the formation of cellular patterns.

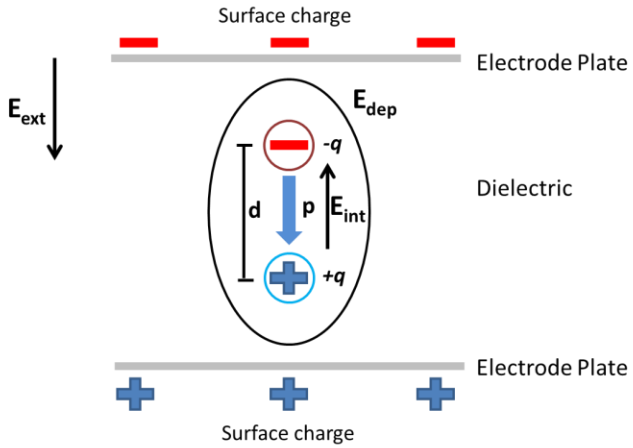

Figure 3.1 A polarized dielectric material for two point-charges model.

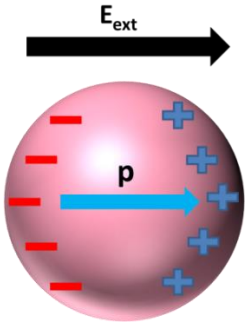

Figure 3.2 Dielectric sphere in an external field $\boldsymbol{E_{ext}}$ showing the polarization charge that forms the dipole.

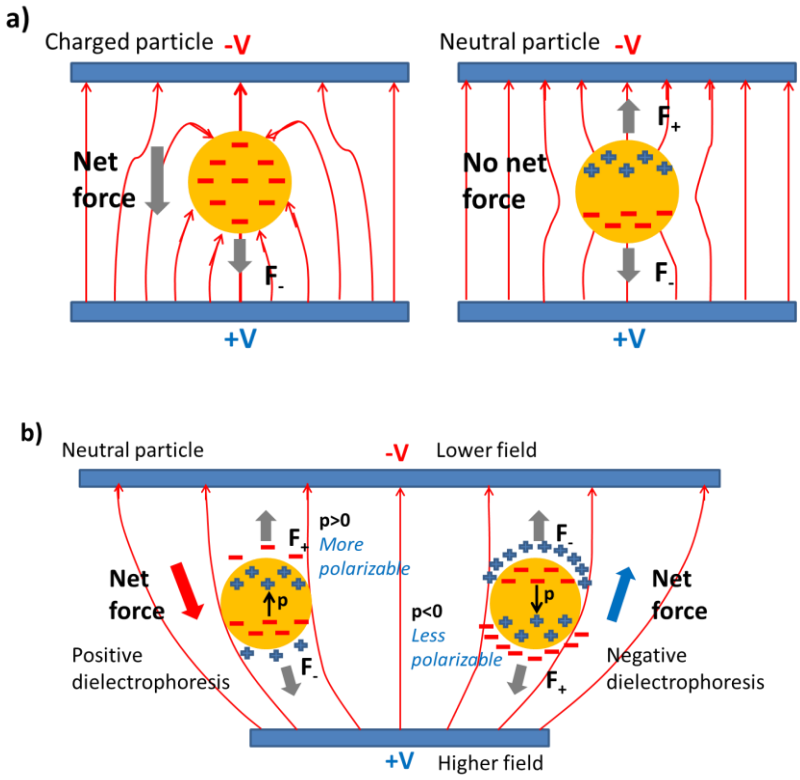

Figure 3.3 Electrophoresis and dielectrophoresis. a) Electrophoresis in DC field; b) Dielectrophoresis in AC field.

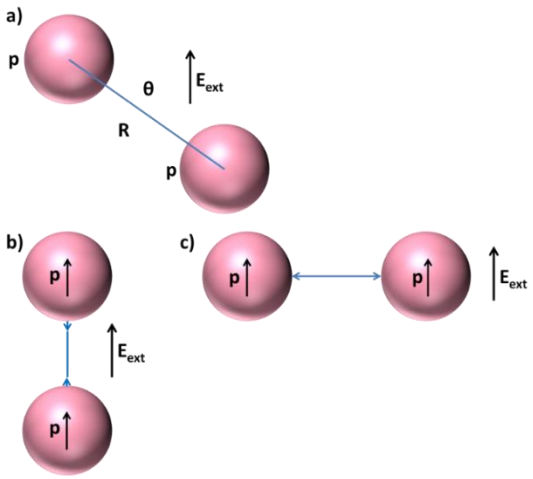

Figure 3.4 (a) Dipolar interaction of two particles. (b) Two polarized particles attract one another when the angle θ between the electric field vector $\boldsymbol{E_{ext}}$ and the line connecting the centers of these particles $\boldsymbol{R}$ is smaller that a critical angle $\theta_c \approx 55^{\circ}$. (c) Two polarized particles repel each other if θ is greater than θ_c.

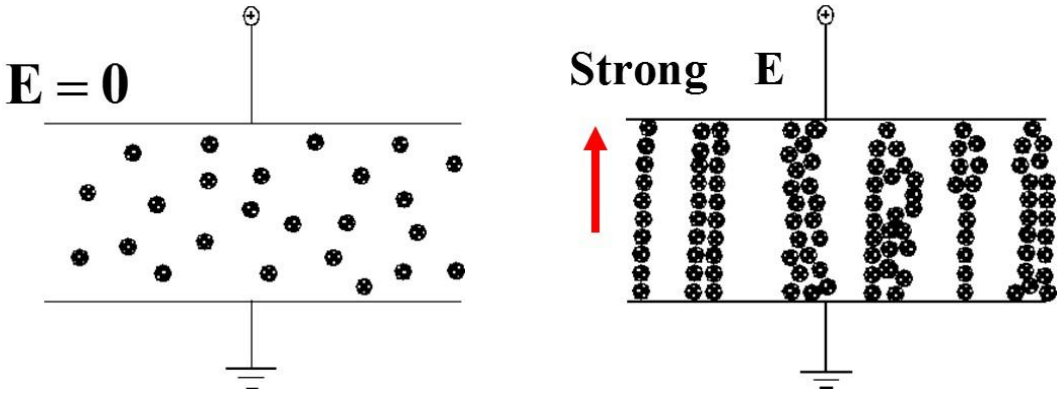

Figure 3.5 The application of a strong electric field to a colloidal suspension causes randomly arranged particles (*left*) form chains and columns along the field direction (*right*).

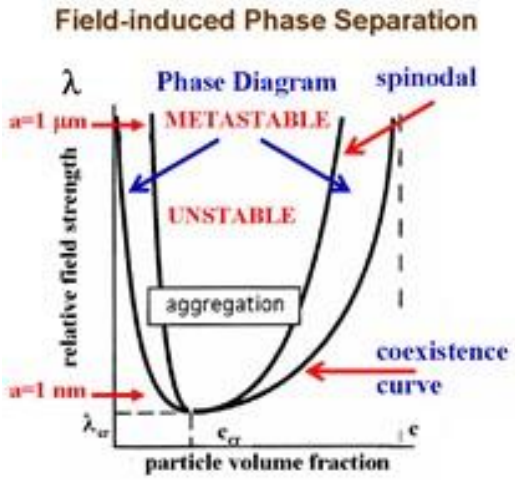

Figure 3.6 The phase diagram of a colloid subject to a uniform field: particle concentration, c, versus the relative field strength, λ.
Source: [87,88].

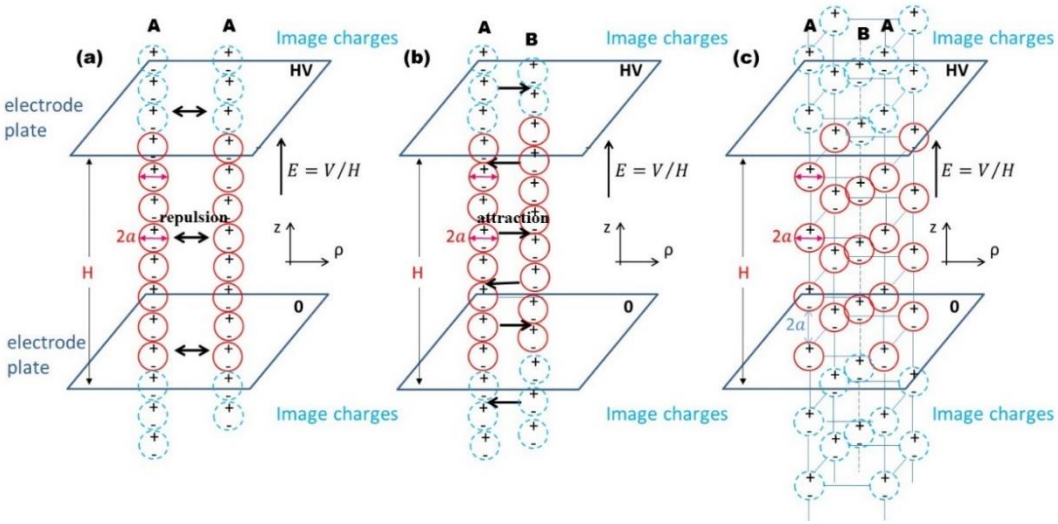

Figure 3.7 Interaction of two chains: (a) repulsion and (b) attaction; (c) Three-dimensional body-centered tetragonal (bct) structure formed by chains. Image dipoles are shown by dashed lines; particle diameter *2a*.
Source: [100].

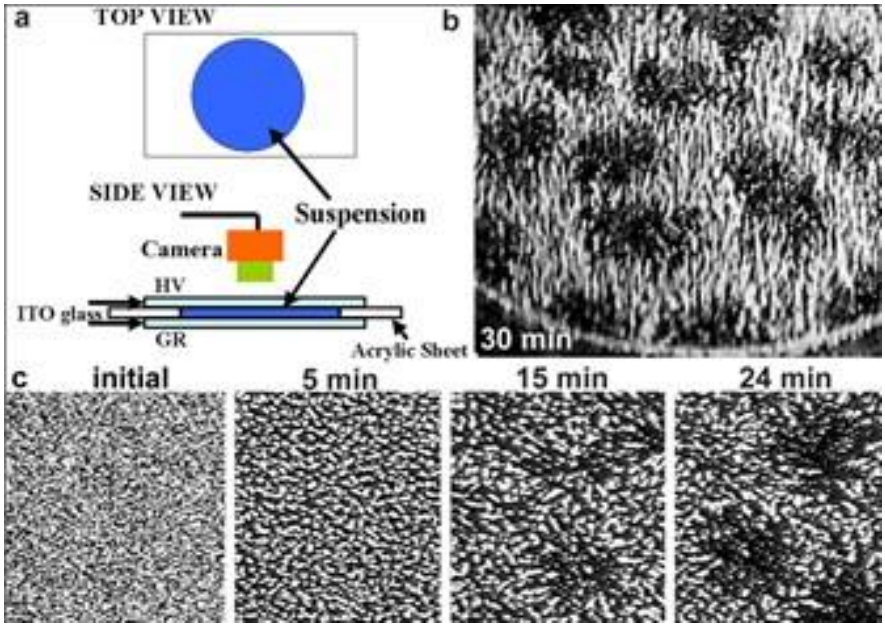

Figure 3.8 Formation of a cellular pattern in the plane perpendicular to the field direction. The particles are seen as white spots and the particle-free domains as black; 87 μm particles, cavity diameter 1.5 in (38.1 mm), electrode gap 1.8 mm, (a) experimental setup; (b) 2 v/v% particle volume fraction, view from an angle 30° to the electrodes, electric field 1.7 kV/mm, 0.1kHz; (c) 3 v/v% particle volume fraction, field-induced column rearrangement.
Source: [113].

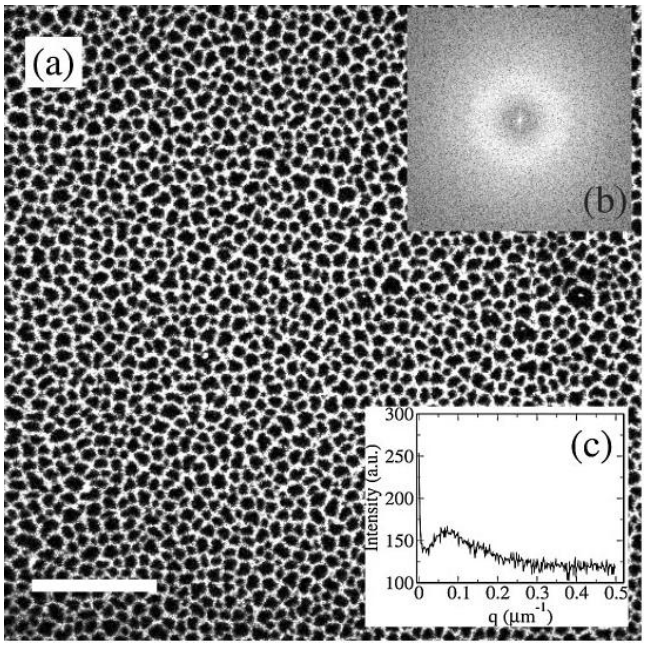

Figure 3.9 (a) A cellular pattern in the plane perpendicular to the field direction. The particles are seen as white spots and the particle-free domains as black; 0.8 μm particles, cavity width 125 μm, electrode gap 60 μm, 0.6% particle volume fraction, scale bar 625 μm, electric field 1 kV/mm; (b) A 2D Fourier transform of (a); (c) The peak in the average radial intensity profile in (b) corresponds to the center-center distance between particle-free domains.
Source: [114].

3.3 Materials and Experimental Methods

3.3.1 Experimental Setup

Experimental procedures used in this work were similar to [113]. Figure 3.12 shows a schematic design and operation concept of experiments to study structures formed in a suspension exposed to an electric field. Experiments are conducted at room temperature.

3.3.1.1 Sample cell. A 4" x 4" acrylic glass spacer with a slot bored in the middle served as a sample cell. One slot end was covered with a transparent 3" x 3" glass electrode of thickness 0.5 mm coated with ITO (Indium Tin Oxide) conducting layer with surface resistivity 15 Ohm/Sq (Nanocs, Burlington, MA). This glass electrode was glued to the

spacer with an epoxy resin (Devcon Adhesive Cartridge 14260 High Strength Epoxy, McMaster Carr, Robbinsville, NJ) and left to cure overnight at room temperature. Once a suspension sample was injected into the slot using a syringe (M717 1CC Luer Slip Syringe, McMaster-Carr, Robbinsville, NJ), the cell was covered with another transparent ITO glass electrode. Experiments were conducted in circular and square cells of different sizes to vary the cell surface area (diameters of circular cells 1”; 1.5”x1.5”, 1”x1” and 0.5”x0.5”) and the gap between electrodes (0.1, 0.5, 1, 1.5 and 2.0 mm). The parallelism of electrodes was controlled by measuring thickness of spacer in both sides using Nikon SMZ-25 zoom stereo microscope (ProScan II, Prior Scientific, Rockland, MA) installed with NIS-Element Advanced Imaging software Version 4.6 (Nikon Instruments, Melville, NY, USA) accuracy in μm.

3.3.1.2 Electric field configurations. An electric field in a sample cell with two glass electrodes was generated by applying voltage to the ITO layer of one electrode and grounding the ITO layer of the other electrode. The voltage was generated by a high voltage amplifier (Model 10/40; Trek, Lockport, NY). The voltage magnitude and variation with time was controlled by a two-channel programmable waveform generator (Tektronix AFG 320, Beaverton, OR) connected to the high voltage amplifier. One generator channel was used to produce an AC signal and the other a DC offset.

To study the influence of direct contact between a suspension and conducting surfaces on the suspension behavior, experiments were conducted with three arrangements of ITO glass electrodes: both electrodes with conducting ITO layers inside or outside the cell and one electrode with the conducting ITO layer inside the cell and the other with the conducting ITO layer outside (Figure 3.10). Effects of direct contact between a suspension

and conducting surfaces were also tested by performing two experiments in which ITO layers of both electrodes were located inside the cell and partly covered with a 70 μm thick insulating fluoropolymer release liner (3M, St. Paul, MN). In one experiment, the ITO layers were covered with this film except for two circular holes of 0.75" diameter made with a hand punch. In the other, the ITO layers were covered only over two circular sections of 0.75" diameter. A suspension in both experiments was observed using transmitted light (Figure 3.10).

To explore the effect of the bulk conductivity of ITO glass electrodes on the suspension behavior, a bottom glass electrode in a cell was replaced with a 1.5 mm thick insulating quartz plate covered with a conducting tape (3M Aluminum Foil Tape 1115B, St. Paul, MN). As this tape was not transparent, the suspension was observed using reflected light (Figure 3.11) provided by a Dolan-Jenner Mi-150 series fiber optic illuminator (Boxborough, MA).

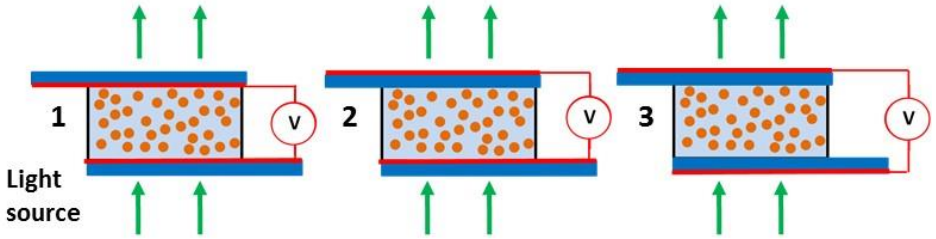

Figure 3.10 Arrangement of transparent ITO-coated glass electrodes in a sample cell: 1, both conducting ITO layers inside; 2, ITO conducting layers of one electrode inside and of the other outside; 3, ITO conducting layers of both electrodes outside.

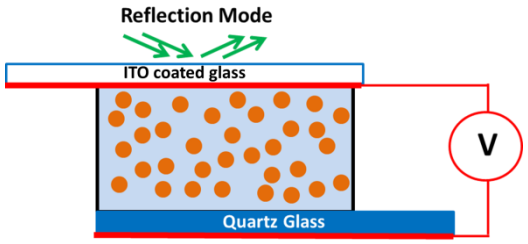

Figure 3.11 A schematic of a cell with an insulating quartz plate covered with a conducting tape on the top and an ITO-coated glass electrode on the top.

3.3.1.3 Imaging system. The arrangement of particles in the plane parallel to electrodes was observed in an upright Nikon SMZ-25 zoom stereo microscope equipped with a Nikon P2 MFU (motorized focus unit), a motorized stage (ProScan II, Prior Scientific, Rockland, MA) and NIS-Element Advanced Imaging software (Nikon Instruments, Melville, NY, USA). This system offers a zoom ratio of up to 25:1, can capture a stack of images in vertical direction and provides a large horizontal field-of-view by scanning in two directions. Videos and still images were acquired with a high resolution ORCA Flash 4.0 V2 Digital CMOS camera, Hamamatsu, Japan (2048 × 2048 6.5μm × 6.5μm pixels, exposure time 1ms to 10s and 30 frames per second (fps) at full resolution). Figure 3.12 illustrates a schematic design and operation concept of experiments. A photo of an experimental setup is presented in Figure 3.13.

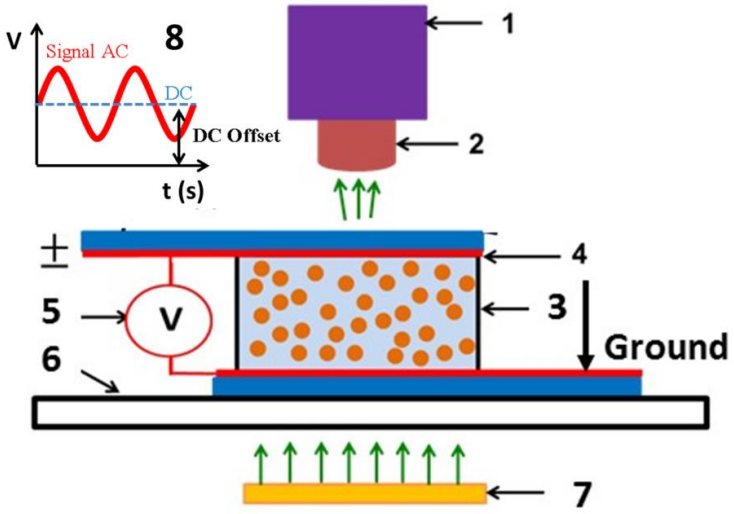

Figure 3.12 Experimental setup: 1, camera; 2, microscope eyepiece; 3, cell with both glass electrodes having conducting ITO layers; 4, inside; 5, high voltage amplifier; 6, microscope motorized stage; 7, microscope illumination system; 8, applied AC voltage with DC offset.

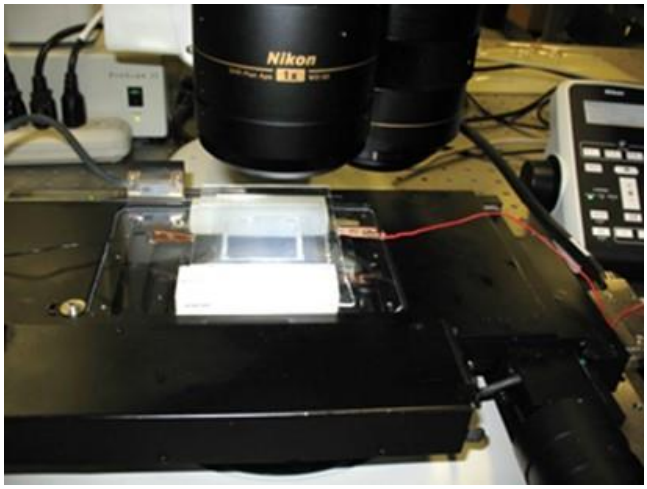

Figure 3.13 A sample cell L x W=1.5"x1.5" with electrode gap H=2 mm, is placed on the microscope motorized stage above the microscope illumination system.

3.3.1.4 Strength of electric field in a suspension. The strength of an electric field in a suspension is $E = U_s/H$, where H is the gap between electrodes filled with a suspension and U_s is the voltage drop across the gap. When conducting layers of both electrodes are in direct contact with a suspension, U_s is equal to an applied voltage U_0. When conducting

surface layers of one or both electrodes are not in a direct contact with a suspension, U_s/U_0 is equal to the ratio of the electrical impedance of the suspension $Z_s^*(\omega)$ to the total electrical impedance of the sample cell $Z^*(\omega)$. The latter combines $Z_s^*(\omega)$ and the electrical impedance of the glass plates $Z_g^*(\omega)$ connected in series (Figure 3.14), where ω is the frequency of an applied AC voltage

$$\frac{U_s}{U_0} = \frac{1}{1 * \frac{(L-H)\varepsilon_s^*(\omega)}{H\varepsilon_g^*(\omega)}} \tag{3.12}$$

where $\varepsilon_s^*(\omega) = \varepsilon_s'(\omega) - i\varepsilon_s''(\omega)$ and $\varepsilon_g^*(\omega) = \varepsilon_g'(\omega) - i\varepsilon_g''(\omega)$ are the complex permittivity of the suspension and the ITO glass plate at the frequency ω and L is the separation between the conducting layers (Figure 3.14); $L = H + 2L_g$ when conducting ITO layers of both electrodes are located outside of the cell and $L = H + L_g$ when the conducting ITO layer of only one electrode is located outside, L_g is the thickness of the glass plate.

The real part of the complex permittivity $\varepsilon'(\omega)$ of a material characterizes accumulation of electric energy at the frequency ω of an applied field whereas the imaginary part ε'' represents the AC conductivity equal to $\sigma(\omega) = \omega\varepsilon_0\varepsilon''$, where $\varepsilon_0 = 8.85 \cdot 10^{-12}\, F/m$ is the vacuum permittivity. At relatively high frequencies, the real part of complex permittivity ε' approaches a constant value while the imaginary part ε'' goes to zero. At low frequencies, ε' remains finite whereas the imaginary part increases as $\varepsilon''(\omega) \approx \sigma_0/\omega\varepsilon_0$, where σ_0 is the DC conductivity. Accordingly, Equation (3.12) yields

$\frac{U_S}{U_0} \approx \frac{1}{1*\frac{(L-H)\varepsilon_S'(\omega)}{H\varepsilon_g'(\omega)}}$ for high frequencies and $\frac{U_S}{U_0} \approx \frac{1}{1*\frac{(L-H)\sigma_{0S}}{H\sigma_{0g}}}$ for low frequencies.

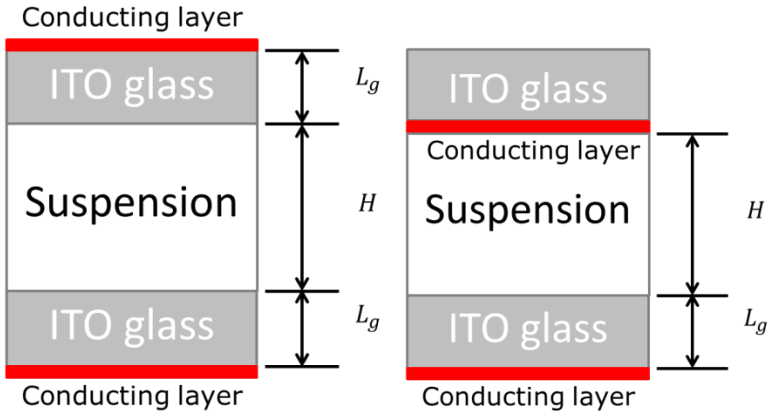

Figure 3.14 Voltage drop in a suspension for different arrangement of conducting ITO layers of glass electrodes in a sample cell.

3.3.2 Materials

3.3.2.1 Solvents and particles. Mazola Corn Oil (ACH Food Companies, Inc., Oakbrook Terrace, IL), Envirotemp FR3 and E200 dielectric fluids (Cargill Industrial Specialties, Minneapolis, MN), and silicone oil (Millipore Sigma, St. Louis, MO) with non-ionic surfactant Brij 30 (Millipore Sigma, St. Louis, MO) were used as solvents. Spherical polyethylene particles (53-75 µm and 40-48 µm) were obtained from Millipore Sigma and spherical polyalphaolefin particles (S-391-N1, 4-5 µm) from Shamrock Technologies Inc., Newark, NJ. Polyalphaolefin particles, VYBAR 253 Polymer (>1 mm) were obtained from Baker Hughes, a GE company, Houston, TX and milled under liquid nitrogen using a 6850 Freezer/Mill (SPEX CertiPrep Freezer/Mills, Metuchen, NJ). The milled particles were then sieved using a shaker to obtain the size distribution (75-90 µm). Suspensions with particle volume concentrations ranged from 1 v/v% to 15v/v% were prepared by weighing the appropriate amount of particles using an OHAUS Scout Pro balance (OHAUS,

Parsippany, NJ) and mixing with a solvent. When the surfactant Brij 30 was added to a suspension, a solvent was vigorously mixed with a desired amount of Brij 30 and then particles were added and mixed. Particles were easily dispersed by shaking or using a magnetic stirrer.

A suspension of negatively polarized particles was prepared by dispersing nearly neutrally buoyant poly-alpha-olefin (PAO) spheres S-391-N1, 4-5μm (Shamrock Technologies Inc., Newark, NJ) in Mazola corn oil (ACH Food Companies, Inc., Oakbrook Terrace, IL) with density 0.92 g/cm^3 and viscosity 59.8 cP. The particle settling velocity is 0.012 μm/s measured that corresponds to a difference 0.068 g/cm^3 between the densities of the particles and the fluid. To confirm the distribution of particle size by observing the external morphology using SEM, the SEM images of poly-alpha-olefin particles are shown in Figure 3.15. A particle size distribution determined from SEM image showed the large variation in the particle size. The particles are in the range of 1-10 μm with average diameter size of 4.43μm (Figure 3.16).

A suspension of positively polarized particles was prepared by dispersing polystyrene/polyaniline core–shell spheres (PS/PANI) 1-2 μm [138] in silicone oil (Millipore Sigma, St. Louis, MO) with density 0.96 g/cm^3 and viscosity 48.2 cP. The PS/PANI particles were provided by Dr. Hyoung Jin Choi, Professor of Polymer Science & Engineering at Inha University, Korea. The particle settling velocity is 0.002 μm/s measured that corresponds to a difference 0.078 g/cm^3 between the densities of the particles and the fluid.

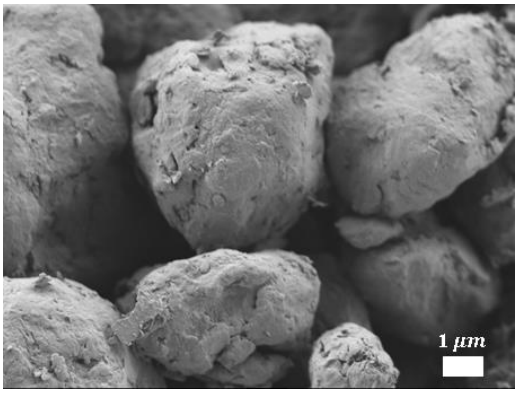

Figure 3.15 SEM images of poly-alpha-olefin particles (4-5 μm)

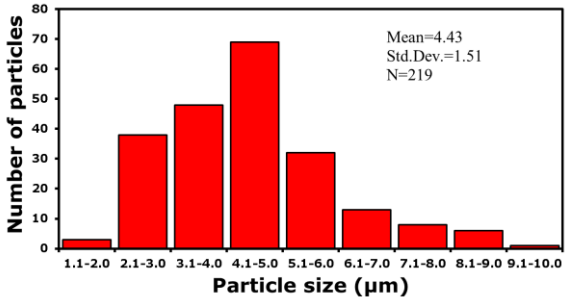

Figure 3.16 A histogram of the distribution of particle size obtained by measurements of poly-alpha-olefin particles from the SEM images.

3.3.2.2 Particle and solvent density, viscosity and dielectric constant. To measure the density of solvent oil and particle, the mass and volume of the sample were determined at room temperature using an OHAUS Scout Pro balance (OHAUS, Parsippany, NJ) and a 100ml Azlon® Squat form cylinders (Azlon, Rochester, NY). Densities were calculated by $\rho = m/V$. For determining the viscosity η of Mazola corn oil, FR3 oil and silicone oil, according to the ASTM D 445, a 200 Cannon-Fenske Routine Viscometer (CANNON, State College, PA) with 0.1cSt/s calibration constant of viscometer *C* was chose to measure kinematic viscosity v. The time t is measured for a fixed volume of liquid to flow under gravity through the capillary of a calibrated viscometer at room temperature. The kinematic

viscosity (determined value) is the product of the measured flow time and the calibration constant of the viscometer

$$v = C \cdot t \tag{3.13}$$

The dynamic viscosity, η in unit cP, can be obtained by multiplying the kinematic viscosity, ν in unit cSt, by the density, ρ, of the liquid

$$\eta = v \cdot \rho \tag{3.14}$$

The electrical properties are measured on a Broadband Dielectric Spectrometer BDS-80 (Novocontrol, Germany). The density, viscosity and electrical properties of solvents and particles at room temperature are listed in Table 3.1 and 3.2.

Table 3.1 Solvent Properties at Room Temperature

Solvent Type	Density (g/cm^3)	Viscosity (cP)	Dielectric Constant at 100Hz	Conductivity at 100Hz (S/m)
FR3 oil	0.92±0.02	29.4±0.1	3.1	5.27E-10
Mazola oil	0.92±0.02	59.8±0.4	2.81	3.19E-10
Silicone oil	0.96±0.01	48.2±0.2	2.42	4.80E-10

Table 3.2 Particle Properties at Room Temperature

Particles	Density(g/cm^3)	Particle Size(μm)
Polyethylene	0.94±0.03	40-48
Polyethylene	0.94±0.01	53-75
Polyalphaolefin	0.95±0.01	4-5
Polyalphaolefin	0.92±0.02	75-90
Polystyrene/polyaniline core–shell spheres	1.05±0.03	1-2

3.3.2.3 Particle settling velocity. Particles used in this study were near neutrally buoyant in a solvent to suppress the particle sedimentation over experimental time scales. The settling velocity of particles was measured in a 5 v/v % suspension placed into a 7mL Hellma Absorption Cuvette, Semi Micro (Millipore Sigma, St Louis MO). 3mL of a suspension was poured into a cuvette and let standing until particles settled at the bottom. The particle settling velocity was calculated from recording the position of the particle front. The properties of particles are listed in Table 3.3. A difference between densities of particles and oil, $\Delta\rho$, was them estimated from the equation for the particle settling velocity $\Delta\rho = \rho_p - \rho_f = \frac{9}{2}\frac{\eta v}{g a^2}$,where η is the fluid viscosity, a is the particle radius, v is the particle settling velocity, g is the gravitational acceleration, ρ_p is the particle density, ρ_f is the fluid density. This expression comes from the balance of the buoyancy force $F_g = \frac{4}{3}(\rho_p - \rho_f) g \pi a^3$ and as the Stokes's drag force $F_d = 6\pi\eta a v$.

Table 3.3 Difference Between Particle and Oil Densities at Room Temperature

Particles & Solvent	Settling Velocity (μm/s)	Sedimentation Time over 1 mm Gap (hr)	$\Delta\rho$ (g/cm^3)
Polyethylene particles (40-48μm) in Mazola oil	0.056±0.0053	5	0.0034±0.00031
Polyethylene particles (53-75μm) in Mazola oil	0.056±0.0022	5	0.0017±0.000099
Polyalphaolefin particles (4-5 μm) in Mazola oil	0.012±0.00094	23	0.068±0.0051
Polyalphaolefin particles (75-90 μm) in Mazola oil	< 0.0058	> 48	$< 9.45E-05$
Polystyrene/polyaniline core–shell spheres (1-2 μm) in silicone oil	< 0.002	> 48	< 0.078

3.3.2.4 Particle electrophoretic mobility. Measurements of the dependence of the particle electrophoretic velocity on the field strength were conducted in a Hellma Absorption Cuvette, Semi Micro (Millipore Sigma, St Louis, MO). The setup shown in Figure 3.17) was assembled by arranging two transparent ITO coated glass electrodes, 1" x 3", parallel to each other and gluing them to both sides of two 2-mm acrylic spacers by epoxy resin to form a window through which the particle motion was recorded. The cuvette was filled with a dilute suspension, typically about 0.2 v/v %. Two methods were used to measure the particle electrophoretic mobility. In one of them, an AC voltage $U(t) = U_0\cos(\omega t)$ with $U_0 \sim 0.2\text{k}V - 1kV$ generated by the high-voltage generator was applied to the electrodes. In the other, a DC voltage $U \sim 0.02\text{k}V - 1kV$ generated by a Harrison 6207B DC Power Supply (Hewlett Packard, Paramus, NJ) was applied to the electrodes. The particle motion in both cases was recorded with a camera using a horizontally oriented Nikon SMZ-25 microscope (Garden City, NY). When an AC voltage was used, the amplitude of the particle oscillations A_p was measured from the video and the mobility was calculated as

$$\mu_p = v_p/E \tag{3.15}$$

where $v_p = \omega A_p$ is the particle velocity, $E = U_0/H$ is the electric field strength and H is the separation between electrodes. When a DC voltage was used, the distance of the particle displacement L_p over a certain time t was measured from the video. The particle mobility was then calculated as

$$\mu_p = v_p/E \tag{3.16}$$

where $v_p = L_p/t$ is the particle velocity, $E = U_0/H$ is the electric field strength and H is the separation between electrodes.

It is known that the application of an electric field to a low conducting liquid can generate electro-convection due to the non-homogeneity of the liquid polarization, heating, charge injection from electrodes, etc. [118]. The important feature of all these phenomena is that the liquid velocity becomes proportional to E^m with the power $m > 1$. To suppress the contribution of liquid electro-convection, measurements of the particle velocity v_p were conducted at frequency $v = 0.1\text{Hz}$ for fields up to 0.5kV/mm to find the field strengths for which μ_p remains insensitive to an applied field. The experimental results showed that the particle electrophoretic mobility in silicone oil and Mazola oil without and with addition of Brij 30 surfactant is independent of the field strength at $E_{DC} < 0.1\text{kV/mm}$, indicating that the contribution of the fluid motion is insignificant (Figures 3.18(a) and 3.18(b)). It increases with the field strength for higher fields due to the fluid motion.

Experiments on the effect of a DC field on pattern formation were therefore conducted at $E_{DC} < 0.1 kV/mm$ to avoid the contribution of electro-convection on the particle motion. Measurements of the particle electrophoretic mobility were then used to estimate the particle charge as $Q_p = 6\pi\eta_f a\mu_p$ where η_f is liquid viscosity and a is the particle radius (Table 3.4).

To validate measurements of the particle electrophoretic mobility in our device, it was also measured on Malvern Zetasizer Nano ZSP (Malvern, United Kingdom). This instrument employs a highly sensitive technique of dynamic light scattering to measure the particle velocity in a very low electric field to avoid the contribution of the particle electric interactions. It therefore does not allow measuring the field dependence of the particle electrophoretic mobility. Measurements of the particle size distribution and the particle electrophoretic mobility in a 2 v/v% suspension of polyalphaolefin particles (4-5μm) in Mazola oil are respectively presented in Figure 3.19 and Table 3.5. A plot in Figure 3.19 indicates that the average particle size is about 2 μm that is smaller than the average particle size measured on SEM images (Figure 3.16). This difference can be attributed to degradation of particles in Mazola oil or to the dynamic light scattering technique used in Malvern Zetasizer. However, values of the electrophoretic mobility of polyalphaolefin particles measured in our device (Table 3.4) and on Malvern Zetasizer (Table 3.5) are consistent.

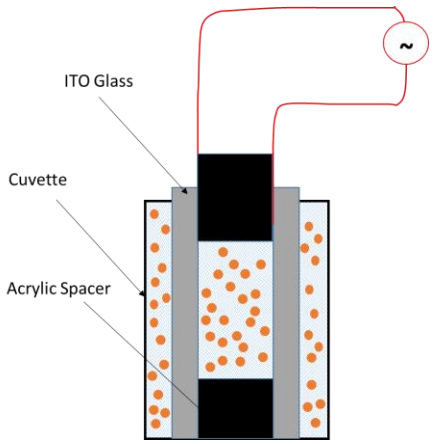

Figure 3.17 A device for measuring the particle electrophoretic mobility

Table 3.4 Particle Mobility and Particle Charge in Different Liquids

Particle	Solvent	$-\mu_p$(m^2/V·s)	STD	-Q_p(C)	STD
Polyethylene, 53-75 µm	FR3 oil/0%B30	9.19E-11	2.78E-11	3.40E-15	1.17E-15
Polyethylene, 53-75 µm	Mazola oil/0%B30	1.02E-10	1.42E-11	3.76E-15	1.214E-15
Polyalphaolefin, 75-90 µm	Mazola oil/0%B30	8.23E-11	3.35E-11	4.06E-15	1.172E-15
Polyalphaolefin, 4-5 µm	Mazola oil/0%B30	1.71E-10	4.83E-11	4.22E-16	1.36E-16
Polyethylene, 40-48 µm	Mazola oil/0%B30	1.42E-10	1.46E-11	9.91E-15	1.06E-15
Polyethylene, 40-48 µm	Mazola oil/1%B30	4.86E-11	1.48E-12	3.52E-15	1.07E-16
Polyethylene, 40-48 µm	Silicone oil/0%B30	2.52E-10	1.41E-11	1.51E-14	8.19E-16
Polyethylene, 40-48 µm	Silicone oil/1%B30	4.72E-10	6.52E-11	2.73E-14	3.77E-15
Polystyrene/polyaniline core–shell spheres, 1-2 µm	Silicone oil	5.05E-10	7.77E-11	2.29E-16	3.43E-17

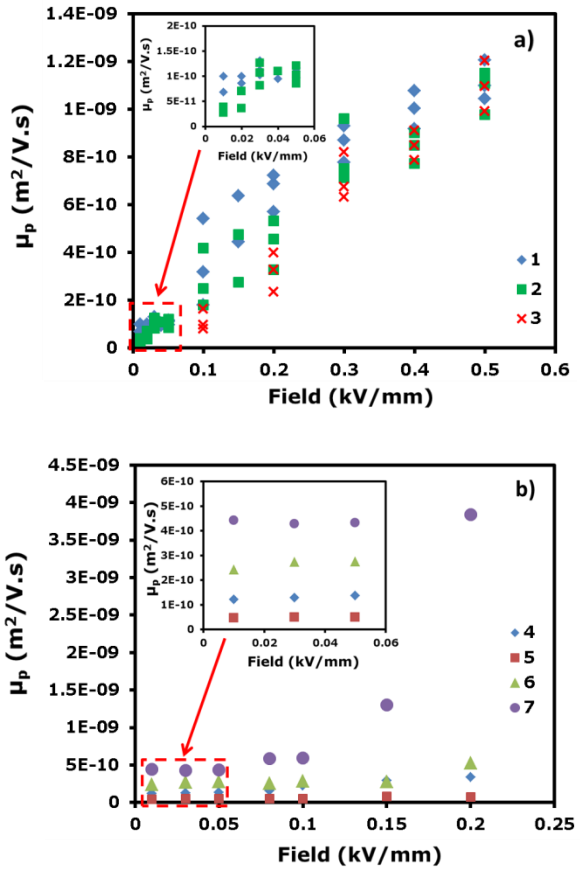

Figure 3.18 Particle electrophoretic mobility in AC and DC fields: **a)** 1, Polyethylene particles (53-75 μm) in a DC field in FR3 Oil; 2, Polyalphaolefin particles (75-90 μm) in a DC field in FR3 Oil; 3, Polyethylene particles (53-75μm) in an AC field $w = 0.1Hz$ in FR3 Oil; (Inset: $E_{DC} < 0.1\ kV/mm$). **b)** 4, Polyethylene particles (53-75 μm) in a DC field in Mazola Oil without Brij 30; 5, Polyethylene particles (53-75 μm) in a DC field in Mazola Oil with 1 v/v% Brij 30; 6, Polyethylene particles (53-75 μm) in a DC field in Silicone Oil without Brij 30; 7, Polyethylene particles (53-75 μm) in a DC field in Silicone Oil with 1 v/v% Brij 30; (Inset: $E_{DC} < 0.1\ kV/mm$).

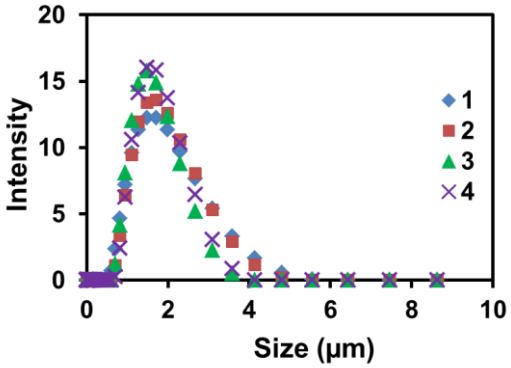

Figure 3.19 Size distribution of polyalphaolefin particles in Mazola oil measured on Malvern Zetasizer.

Table 3.5 Electrophoretic Mobility of Polyalphaolefin Particles (4-5 μm) in Mazola Oil Measured on Malvern Zetasizer

	Zeta Potential (mV)	Mobility (μm·cm/V.s)	Mobility (m^2/V.s)
1	-367	-0.02026	-2.03E-10
2	-159	-0.008762	-8.76E-11
3	-368	-0.0203	-2.03E-10
4	-344	-0.01903	-1.90E-10

Figure 3.20 presents measurements of the electrophoretic mobility of PAO particles (4-5 μm) in Mazola oil (60 cP) and PS/PANI particles (~1 μm) in silicone oil (50 cP) in AC and DC fields. The contribution of electroconvection is negligible for $E_{DC} \leq 0.1\mathrm{kV/mm}$. Measuremensts on Malvern Zetasizer in a very low electric field yield consistent data: $\mu_p = -(1.10 \pm 0.54) \cdot 10^{-10} m^2/V \cdot s \cdot$ for PAO particles and $\mu_p = -(5.05 \pm 0.78) \cdot 10^{-10} m^2/V \cdot s$ for PS/PANI particles.

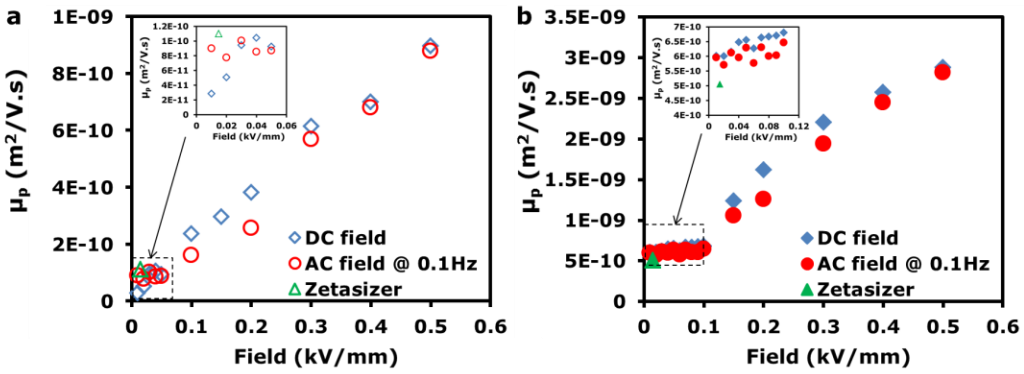

Figure 3.20 Measurements of the electrophoretic mobility ($-\mu_p$) of PAO particles (4-5µm) in Mazola oil **(a)** and PS/PANI particles (~1µm) in silicone oil **(b)** in AC and DC fields (Inset: $E \leq 0.1 kV/mm$).

3.3.2.5 Particle polarizability. A high-resolution Broadband Dielectric Spectrometer (BDS-80, Novocontrol,, Germany) (Figure 3.21) measures the frequency dependence of the complex permittivity $\varepsilon^*(\omega) = \varepsilon'(\omega) - i\varepsilon''(\omega)$ of liquids, powders and thin films as a function of temperature. It covers wide ranges of frequency (10^{-6}-10^{9}Hz) and temperature (-200°C - +400°C) needed to investigate molecular motion at different scales.

A sample is subjected to a sinusoidal voltage input $U(t) = U_0 \cos(\omega t)$ with $U_0 \sim 20mV - 3.2V$ and the current amplitude and the phase shift between the current and the applied voltage are measured $I(t) = I_0 \cos(\omega t - \varphi) = Real\left(I^* e^{i\omega t}\right)$ where $Real$ denotes the real part of a complex number, $I^* = I' - iI''$, $I_0 = \sqrt{I'^2 + I"^2}$ and $\tan\varphi = I''/I'$. These measurements are used to compute the complex impedance and then the complex permittivity of the sample $Z^*(\omega) = Z' + iZ" = \frac{U_0}{I' - iI''} = \frac{U_0}{I_0} e^{i\varphi}$ and $\varepsilon^*(\omega) = \varepsilon' - i\varepsilon'' = \frac{-i}{\omega Z^*(\omega)} \cdot \frac{\varepsilon_l}{C_{cell}}$, where ε_l is dielectric permittivity of a standard liquid (pure hexane, Millipore Sigma, 99%+) and the C_{cell} is the capacity of the sample cell loaded with the standard liquid.

For solid materials, a sample is placed between additional external parallel plate electrodes BDS 1301 in order to form a sandwich capacitor as shown in Figure 3.22. For measurements of properties of ITO glass, quartz glass, 3M Fluoropolymer release liner in our experiments, a sample is placed between two parallel electrodes to form a sandwich capacitor. Cylindrical gold plated electrodes BDS 1301 are available with the 10/20/30/40 mm diameter. After preparation, the sandwich capacitor is mounted between the electrodes of the BDS1200 sample cell. The electrode spacing is adjusted to the sample thickness. For liquids or powders, additional spacers or the liquid cell BDS 1308 can be used (Figure 3.23). For measurements of suspensions, a sample that does not fit the gap between electrodes can flow around the upper electrode. Two seal rings attached to the Teflon isolation prevent the evaporation of a liquid sample out of the cell. BDS1308 is mounted in the same way as the standard sandwich capacitor between the electrodes of the BDS1200*. Before testing a sample, the calibration factor should be calculated from measurements of the dielectric constant of a standard liquid. Pure hexane (Millipore Sigma, 99%+) with the dielectric constant, 1.89 at 20ºC was used to calibrate BDS 80.

The frequency dependence of the particle polarizability $\beta(\omega)$ was calculated from Equation (3.10) based on data for the concentration dependence of the suspension complex permittivity. The average of three measurements of the complex permittivity on BDS 80 with the BDS 1308 liquid sample cell were taken for a suspension with a fixed particle concentration. The polarizability of various types of particles suspended in Mazola corn oil and FR3 industrial oil are lying within the range $Real[\beta(\omega)] \sim -0.15 - -0.23$; Table 3.6 and Figures 3.24 -3.27. The value of $Real[\beta(\omega)]$ first increases and then decreases with increasing the amount of Brij 30 surfactant in Mazola oil; Table 3.7 and Figures 3.28-3.33.

The value of $Real[\beta(\omega)]$ of particles suspended in silicone oil decreases with addition of 1v/v% Brij 30 surfactant from -0.30 to -0.38; Table 3.8 and Figures 3.34-3.38.

Figure 3.21 Novocontrol BDS 80 high-resolution broadband dielectric spectrometer (BDS-80).

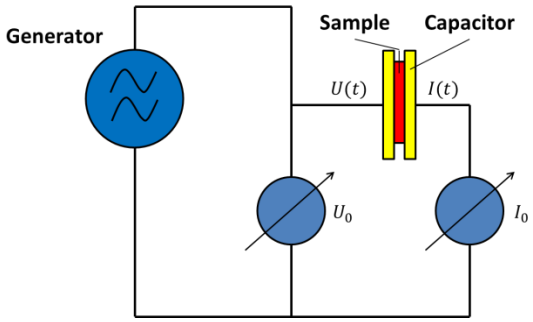

Figure 3.22 Principles of sample measurement in a broadband dielectric spectrometer (BDS-80)*.
**Source: http://www.novocontrol.de/php/turn_key_bds.php.*

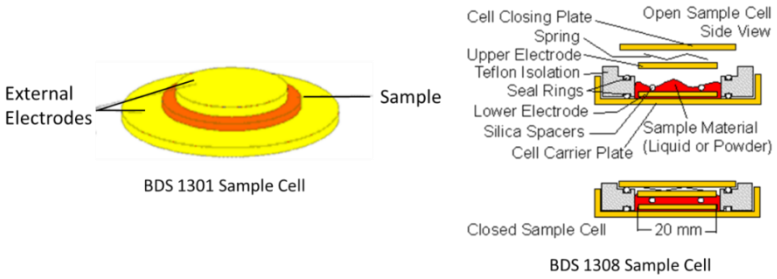

Figure 3.23 Sample cell for BDS 80*.
**Source: https://www.novocontrol.de/php/sa_cell_overview.php*

Table 3.6 Polarizability of Particles Suspended in FR3 Oil and Mazola Oil

Solvent Type in Suspension	Particle Type in Suspension	Real(β)
FR3 oil	Polyethylene (40-48 μm)	-0.23
FR3 oil	Poly-alpha-olefin (4-5 μm)	-0.21
Mazola oil	Polyethylene (53-75 μm)	-0.15
Mazola oil	Poly-alpha-olefin (75-90 μm)	-0.15
Mazola oil	Poly-alpha-olefin (4-5 μm)	-0.16

Table 3.7 Polarizability of Particles Suspended in Mazola Oil and Brij 30

Solvent Type in Suspension	Particle Type in Suspension	Real(β)
Mazola oil with 0v/v% Brij 30	Polyethylene (53-75 μm)	-0.15
Mazola oil with 0.5v/v% Brij 30	Polyethylene (53-75 μm)	-0.09
Mazola oil with 1v/v% Brij 30	Polyethylene (53-75 μm)	-0.07
Mazola oil with 1.5v/v% Brij 30	Polyethylene (53-75 μm)	-0.11
Mazola oil with 2v/v% Brij 30	Polyethylene (53-75 μm)	-0.12
Mazola oil with 3v/v% Brij 30	Polyethylene (53-75 μm)	-0.3

Table 3.8 Polarizability of Particles Suspended in Silicone Oil and Brij 30

Solvent Type in Suspension	Particle Type in Suspension	Real(β)
Silicone oil with 0v/v% Brij 30	Polyethylene (40-48 μm)	-0.28
Silicone oil with 0v/v% Brij 30	Polyethylene (53-75 μm)	-0.31
Silicone oil with 1v/v% Brij 30	Polyethylene (40-48 μm)	-0.39
Silicone oil with 1v/v% Brij 30	Polyethylene (53-75 μm)	-0.39
Silicone oil with 0v/v% Brij 30	Polystyrene/polyaniline core–shell spheres (1-2 μm)	0.7

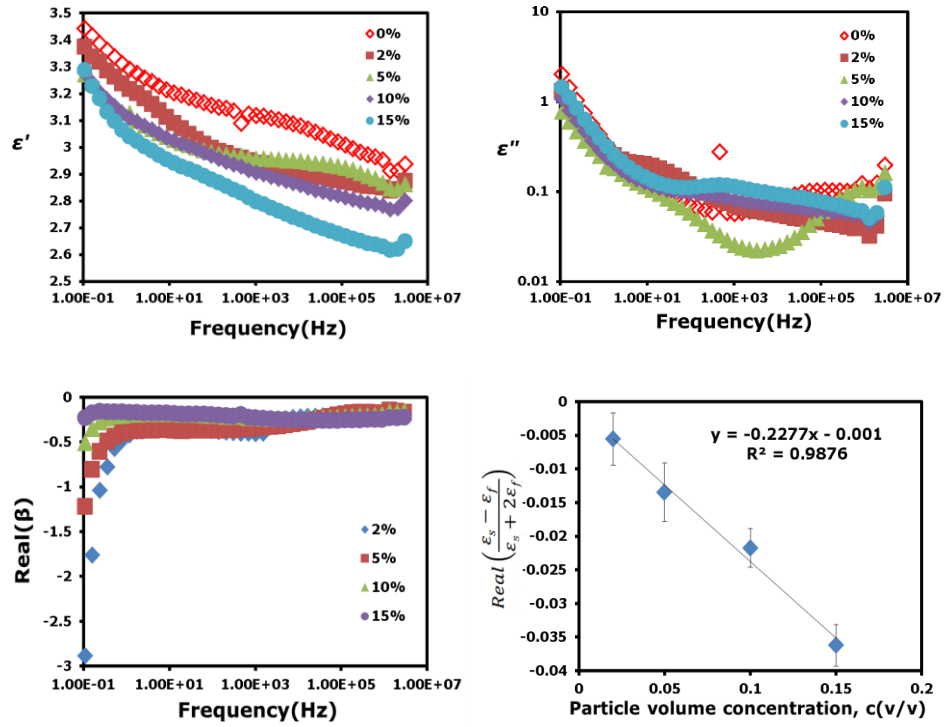

Figure 3.24 Measurements of dielectric properties of suspensions of polyethylene particles (40-48 μm) in FR3 oil.

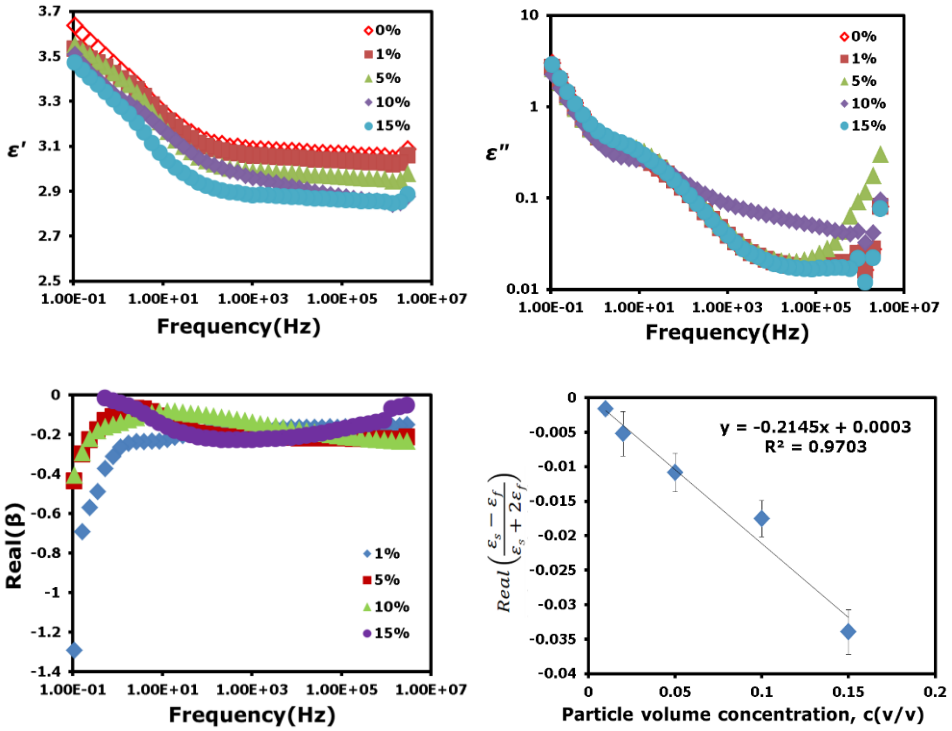

Figure 3.25 Measurements of dielectric properties of suspensions of poly-alpha-olefin particles (4-5 μm) in FR3 oil.

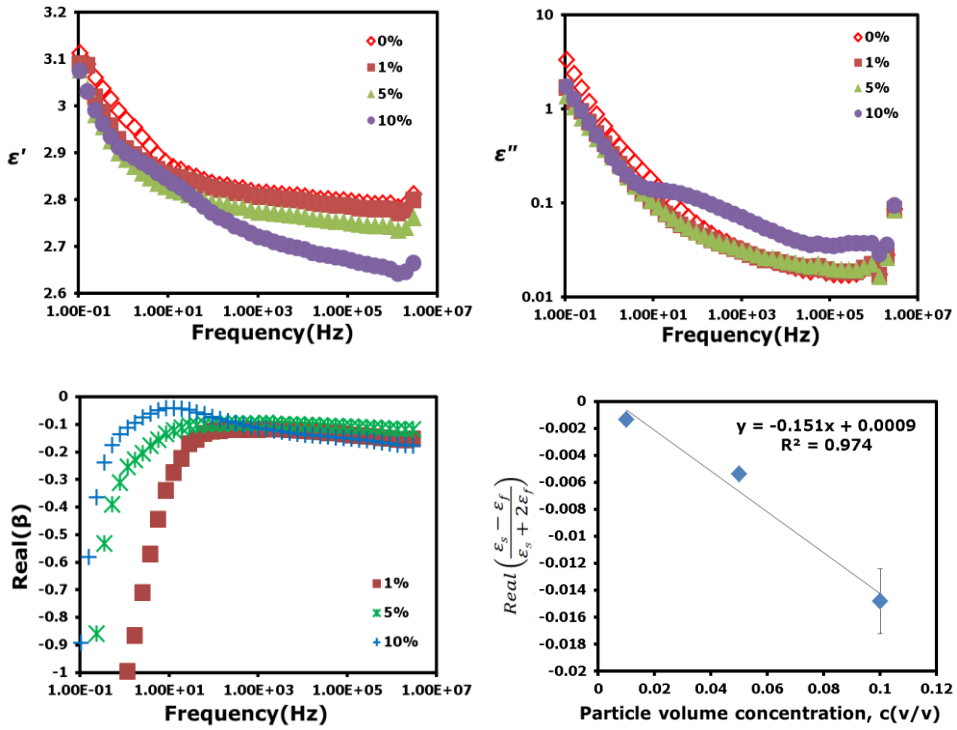

Figure 3.26 Measurements of dielectric properties of suspensions of polyethylene particles (53-75 μm) in Mazola oil.

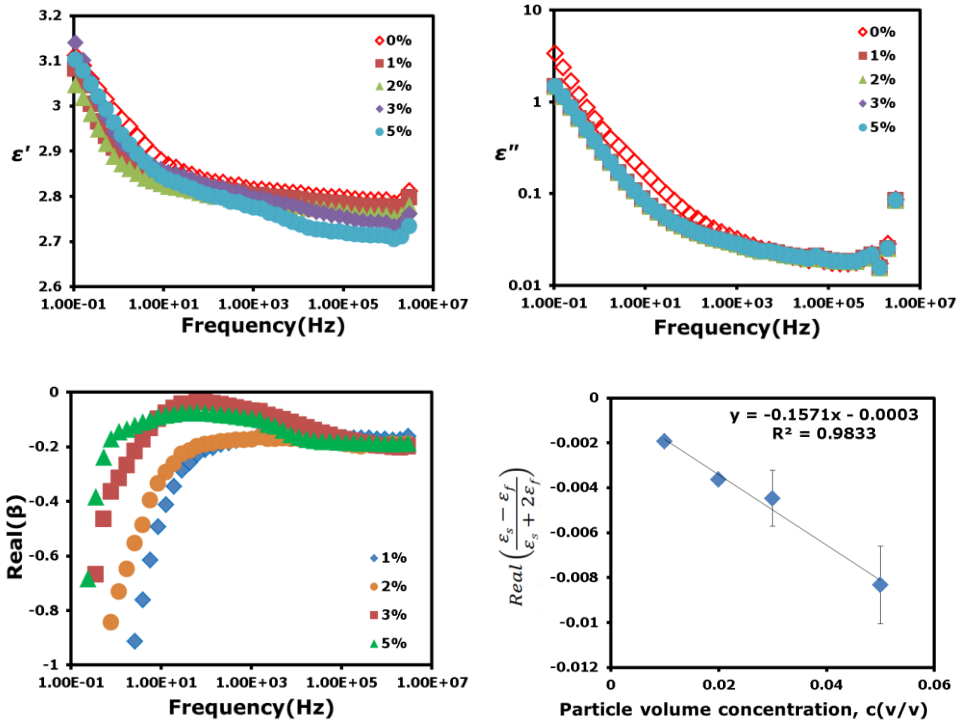

Figure 3.27 Measurements of dielectric properties of suspensions of poly-alpha-olefin particles (4-5 μm) in Mazola oil.

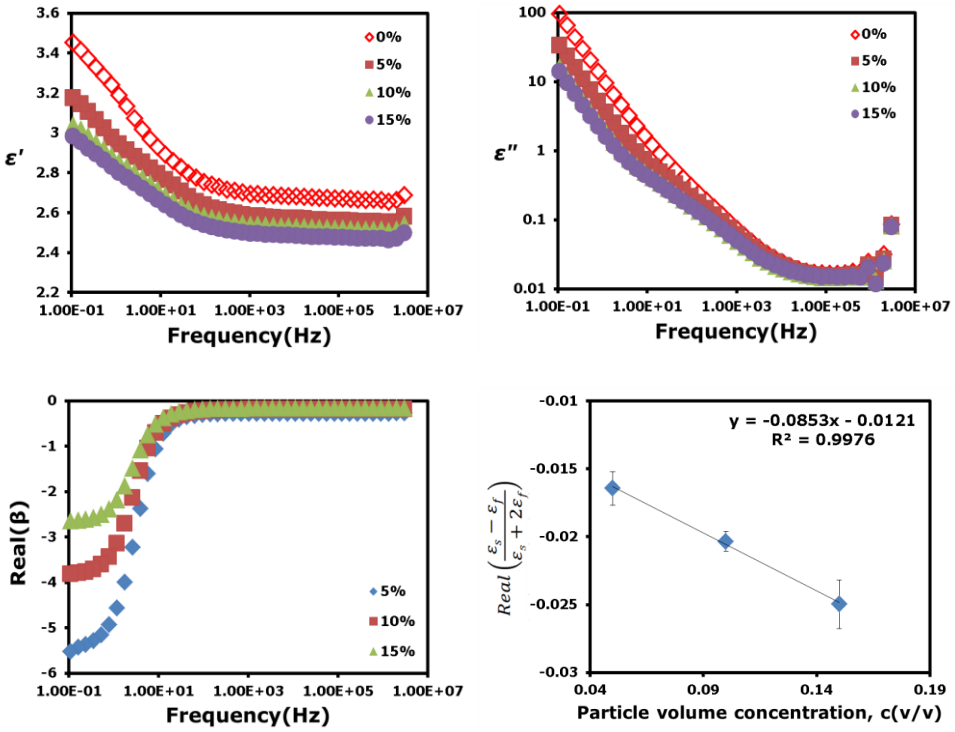

Figure 3.28 Measurements of dielectric properties of polyethylene particles (53-75 μm) in Mazola oil with 0.5v/v% Brij 30.

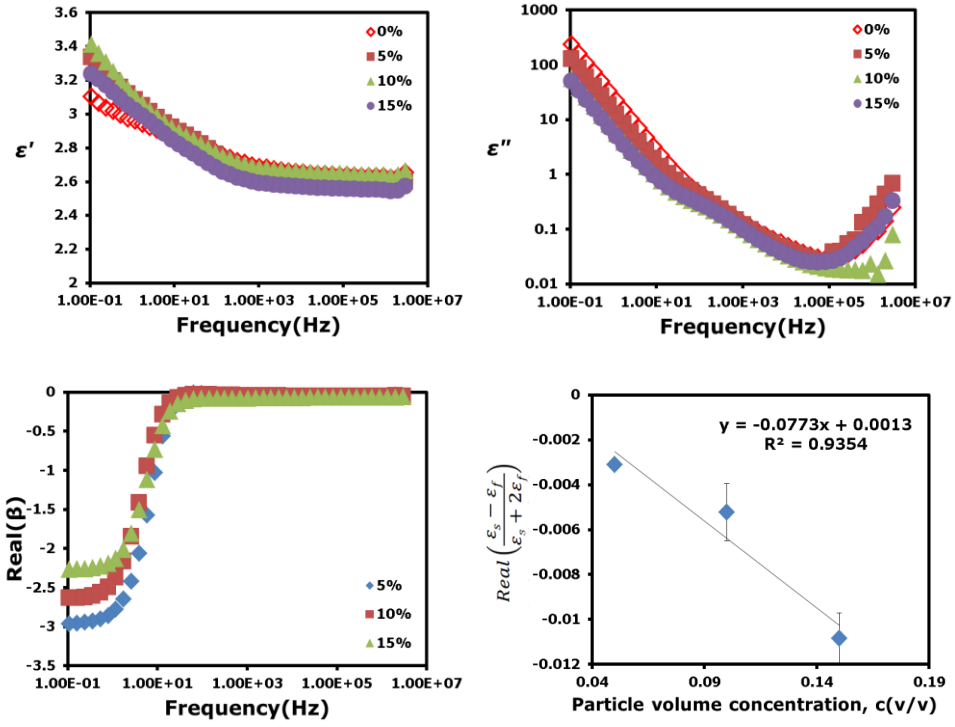

Figure 3.29 Dielectric properties measurements of polyethylene particles (53-75 μm) in Mazola oil with 1v/v% Brij 30.

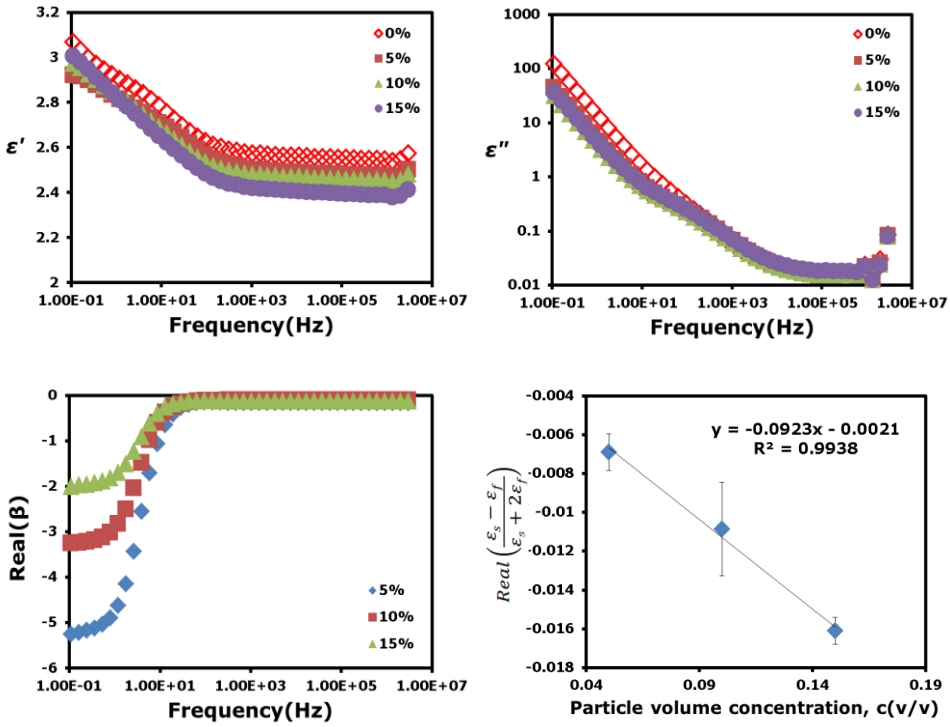

Figure 3.30: Measurements of dielectric properties of suspensions of polyethylene particles (53-75 μm) in Mazola oil with 1.5 v/v% Brij 30.

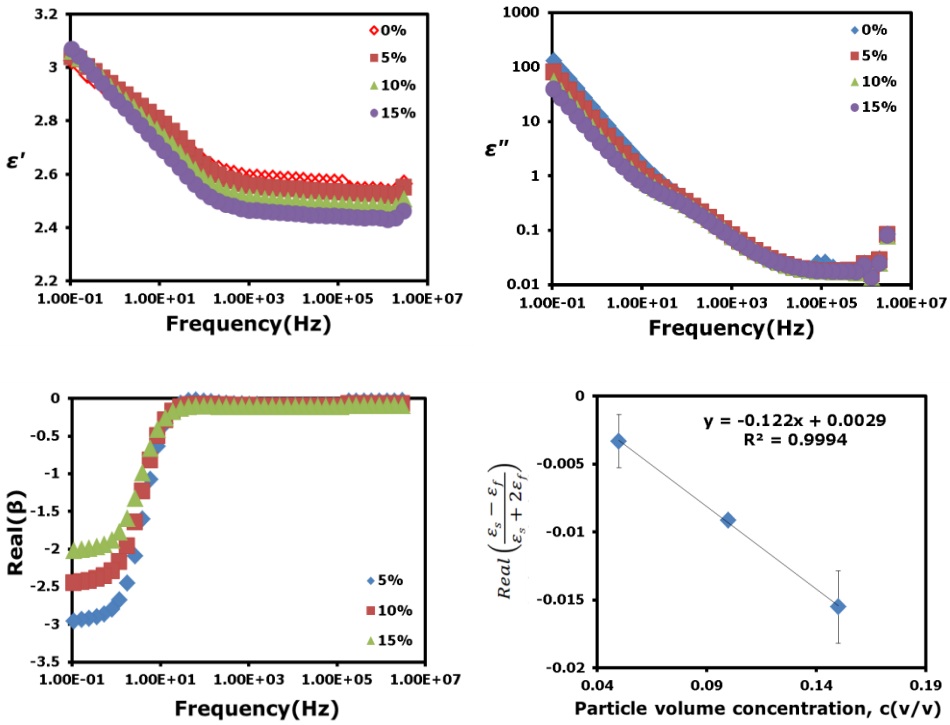

Figure 3.31 Measurements of dielectric properties of suspensions of polyethylene particles (53-75 μm) in Mazola oil with 2 v/v% Brij 30.

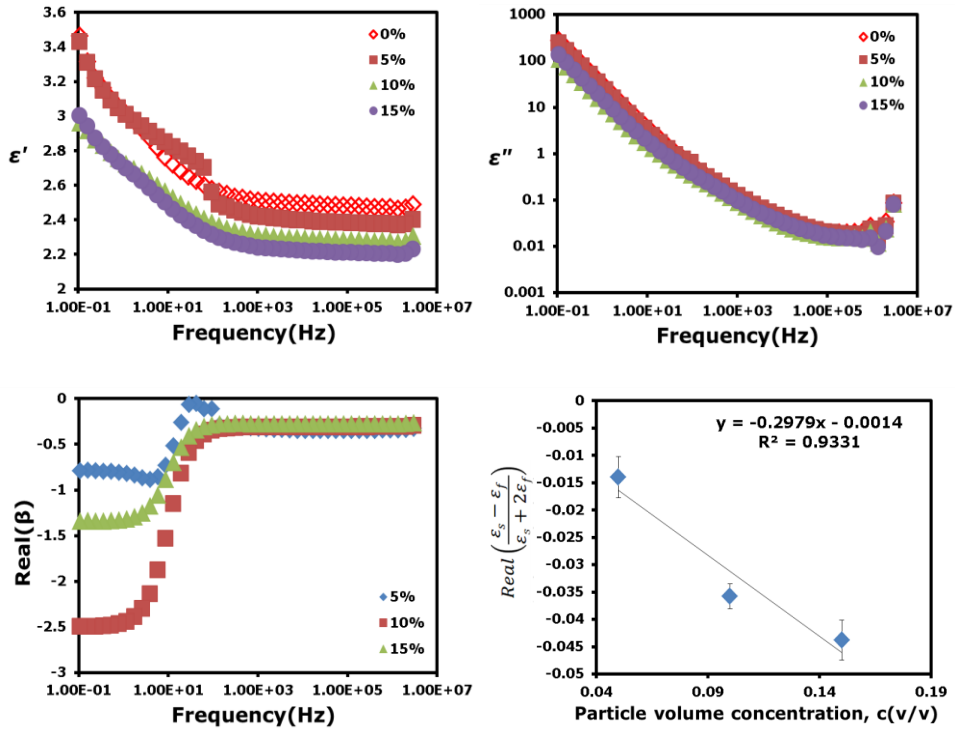

Figure 3.32 Measurements of dielectric properties of suspensions of polyethylene particles (53-75 μm) in Mazola oil with 3 v/v% Brij 30.

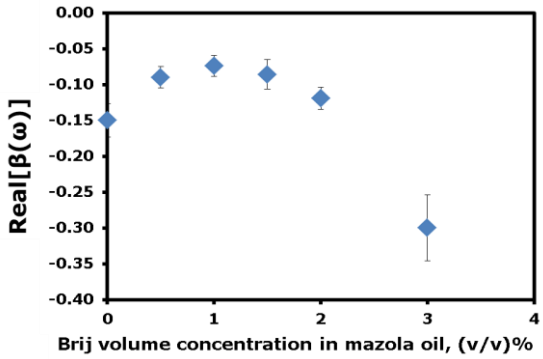

Figure 3.33 Real [β] of suspensions of polyethylene particles (53-75 μm) in Mazola oil with Brij 30 as a function of the Brij 30 volume fraction in Mazola oil.

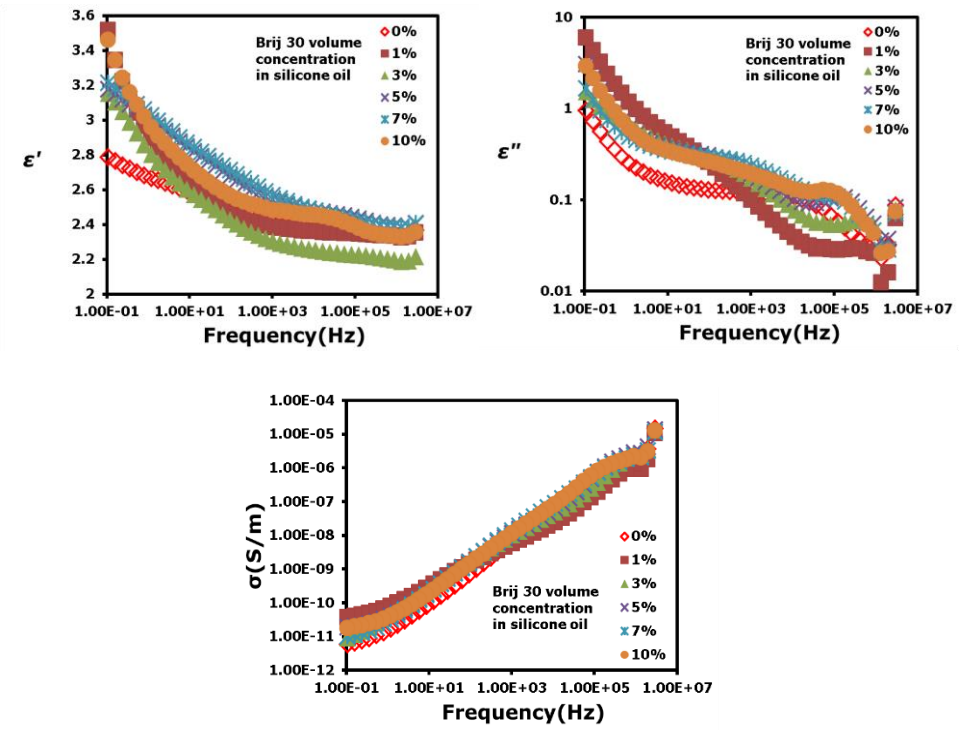

Figure 3.34 Measurements of dielectric properties of Silicone oil with different volume fractions of Brij 30.

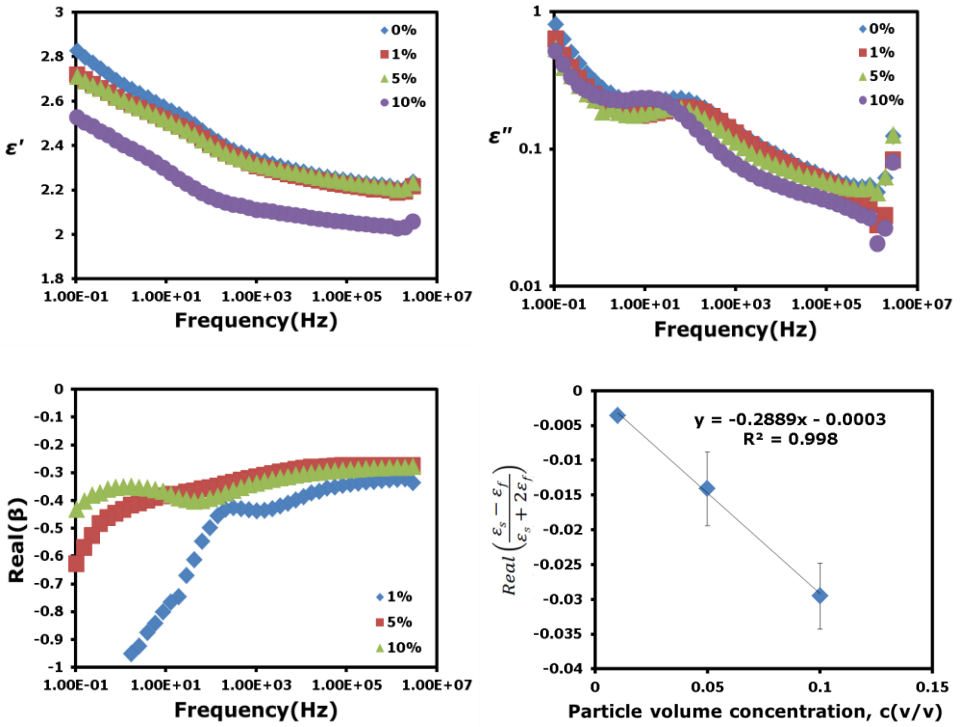

Figure 3.35 Measurements of dielectric properties of suspensions of polyethylene particles (40–48 µm) in silicone oil without Brij 30.

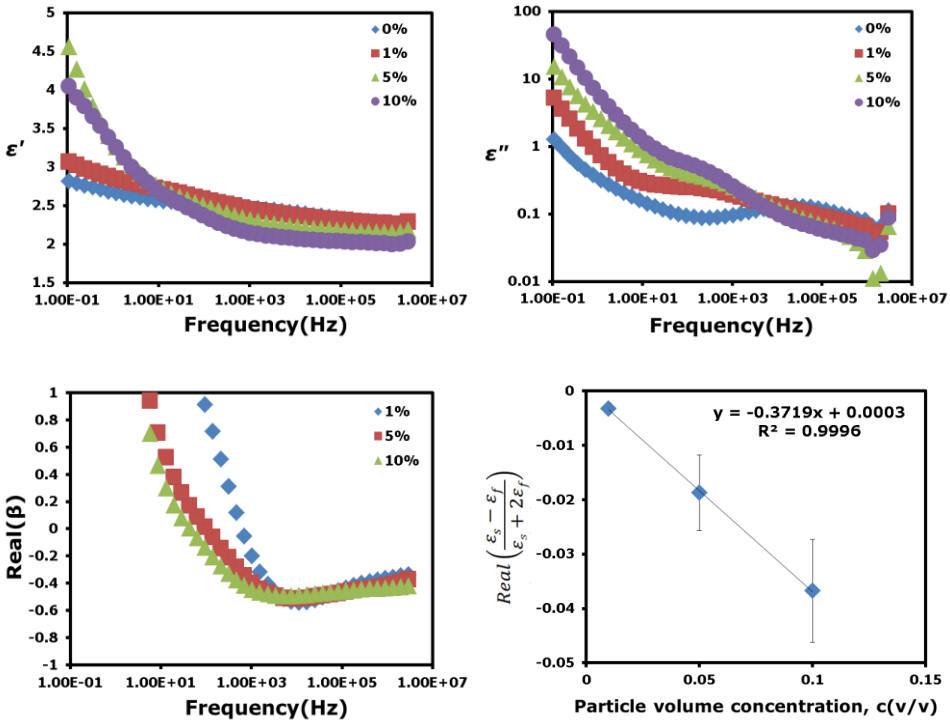

Figure 3.36 Measurements of dielectric properties of suspensions of polyethylene particles (40–48 µm) in silicone oil with 1 v/v% Brij 30.

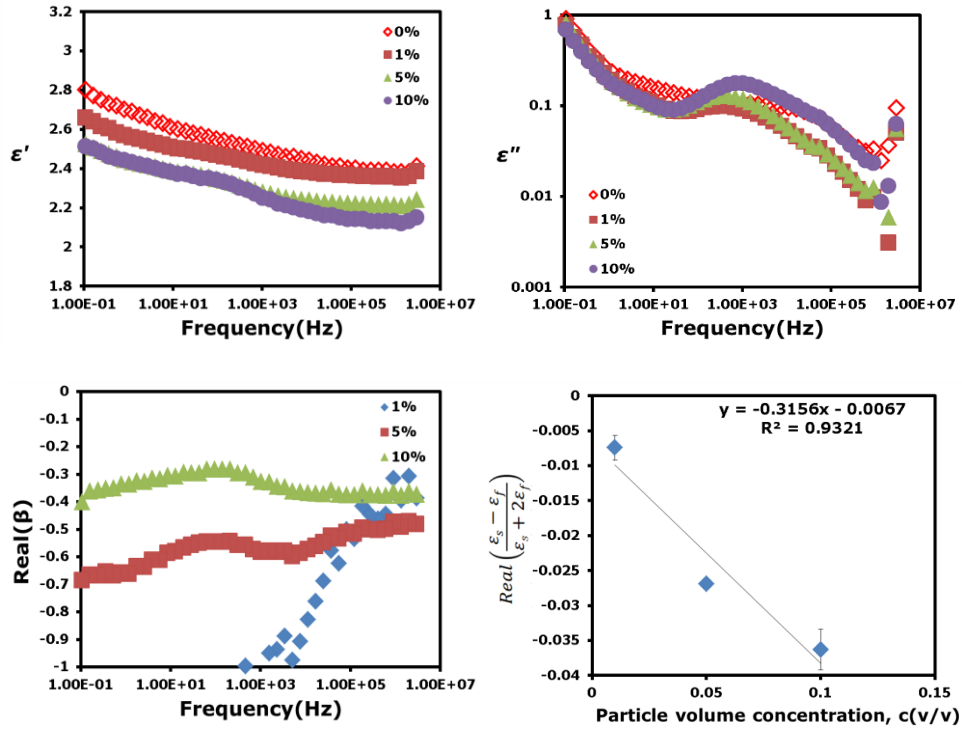

Figure 3.37 Measurements of dielectric properties of suspensions of polyethylene particles (53–75 µm) in silicone oil without Brij 30.

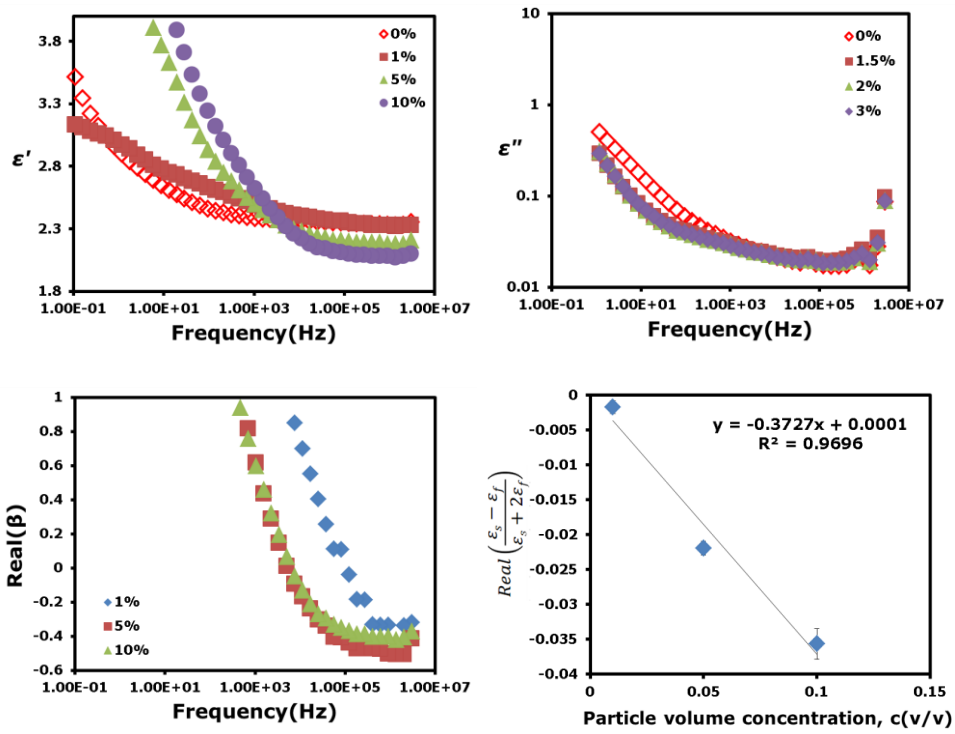

Figure 3.38 Measurements of dielectric properties of a suspension of polyethylene (53–75 µm) particles in silicone oil with 1 v/v% Brij 30.

For comparison, measurements of dielectric properties as a function of frequency are presented in Figure 3.39(a) for suspensions of PAO particles in Mazola corn oil and PS/PANI particles in silicone oil. For the PAO particles dispersed in Mazola corn oil, $Re(\beta)$ decreases from -0.05 to -0.2 over the frequency range from 0.1 kHz to 10kHz while $Im(\beta) \approx 1 \times 10^{-3}$ over this frequency range. For the PS/PANI particle dispersed in silicone oil, $Re(\beta)$ decreases from 0.7 to 0.4 over the frequency range from 0.1kHz to 10kHz, while $Im(\beta)$ decreases from 0.24 at 1 kHz to 0.12 at 100kHz as shown in Figure 3.39(b) and 3.39(c).

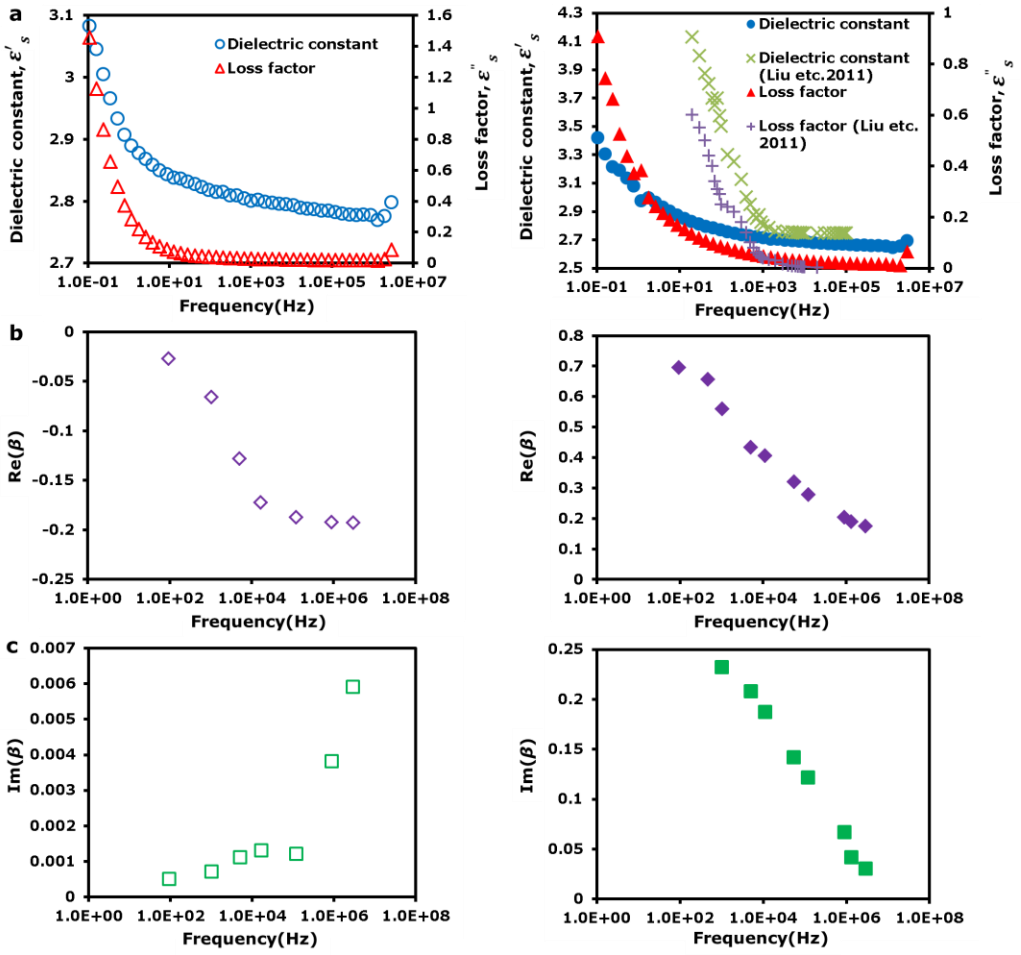

Figure 3.39 Dielectric properties of suspensions: left: PAO particles in Mazola oil, and right: PS/PANI particles in silicone oil. (a) the frequency dependence of the real and imaginary parts of the complex dielectric permittivity for suspensions: left: 1 v/v% PAO particles in Mazola corn oil and right: 0.5 v/v% PS/PANI particles in silicone oil; 10v/v% PS/PANI particles in silicone oil data from Liu el at. (2011) [138]. (b) the frequency dependence of the real part: left: PAO particles and right: PS/PANI particles; polarizability calculated from the Maxwell-Wagner expression. (c) the frequency dependence of the imaginary part: left: PAO particles and right: PS/PANI particles; polarizability calculated from the Maxwell-Wagner expression.

3.3.2.6 Conductivity of material. The conductivity of ITO glass is larger than the suspension conductivity, but the conductivity of quartz glass is smaller than the suspension (Figure 3.40). The conductivity of a suspension of polyethylene particles (53-75 μm) in Mazola oil decreases with increasing the amount of Brij 30 (Figures 3.41-3.42). The

conductivity of a suspension of polyethylene particles in silicone oil increases with increasing the amount of Brij 30 (Figures 3.43-3.44).

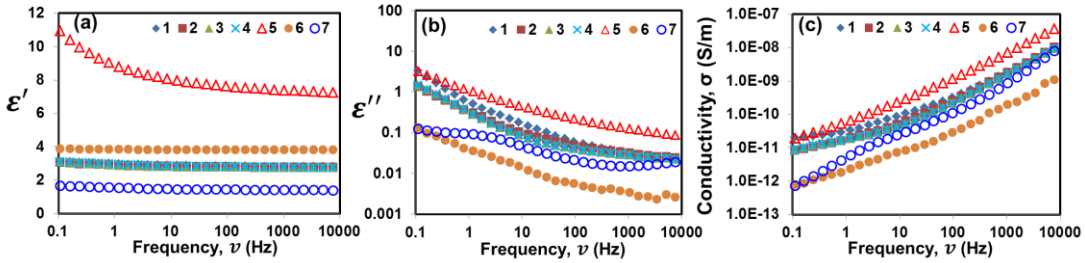

Figure 3.40 (a) The real part of permittivity; (b) the imaginary part of permittivity; (c) the conductivity: 1. Mazola Corn Oil; 2. 5 v/v% Polyethylene (53-75 μm); 3. 5 v/v% Polyalphaolefin (75-90 μm); 4. 5% Polyalphaolefin (4-5 μm); 5. ITO glass; 6. Quartz glass; 7. 3M Fluoropolymer.

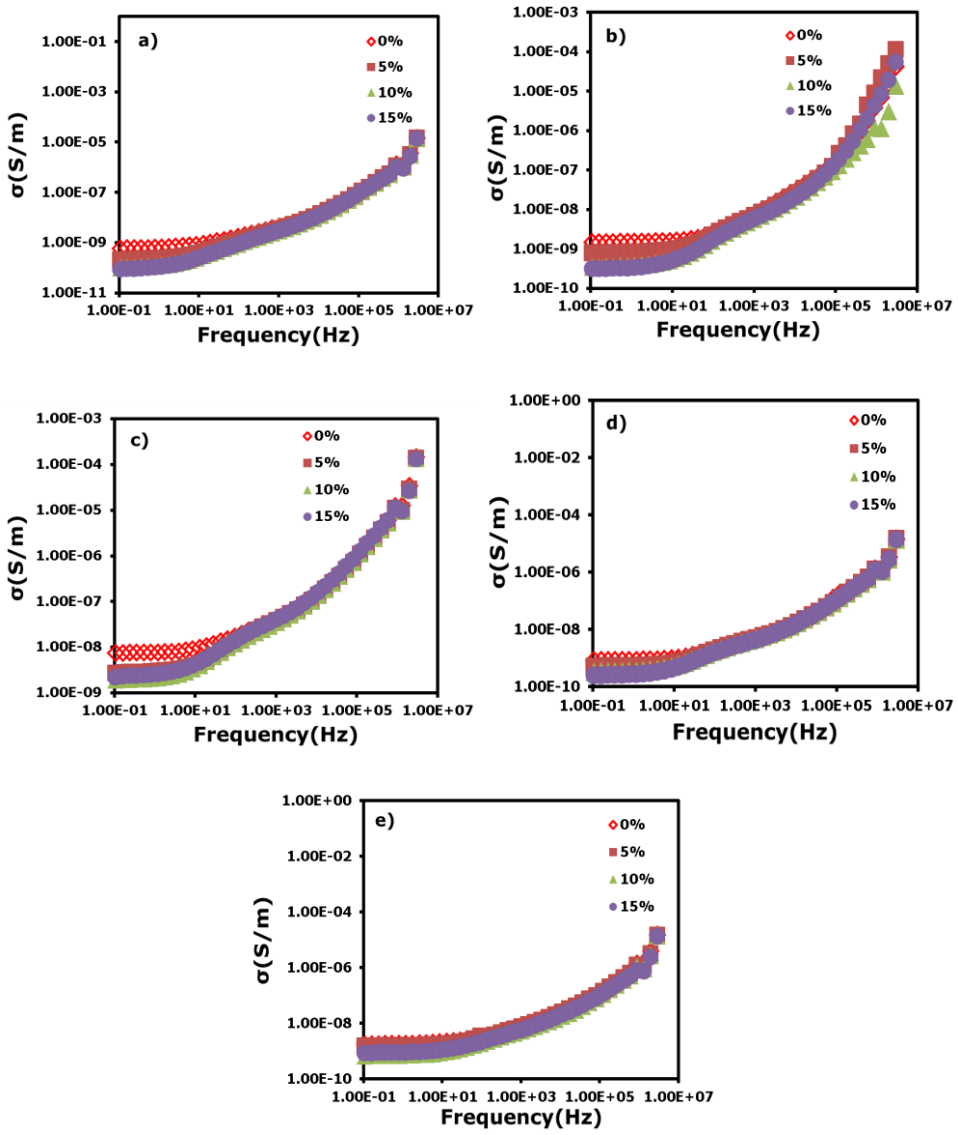

Figure 3.41 Conductivity of a suspension of polyethylene (53–75 μm) particles in Mazola oil with Brij 30: a) 0.5 v/v% Brij 30, b) 1 v/v% Brij 30, c) 1.5v/v% Brij 30, d) 2 v/v% Brij 30, e) 3 v/v% Brij 30.

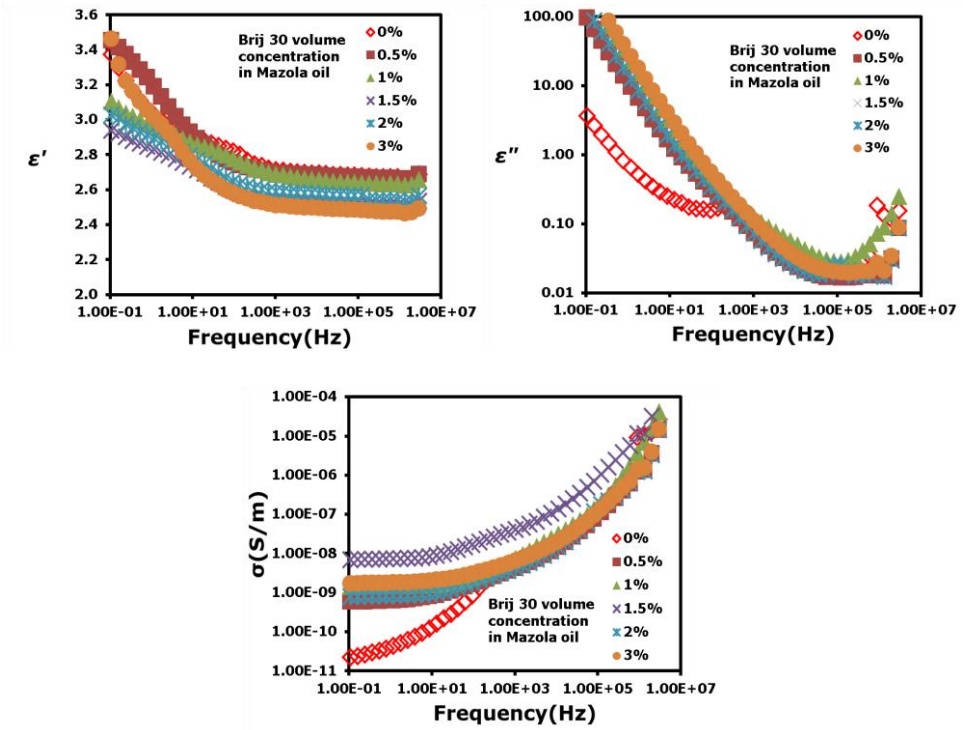

Figure 3.42 Conductivity of Mazola oil with added different volume concentration Brij 30

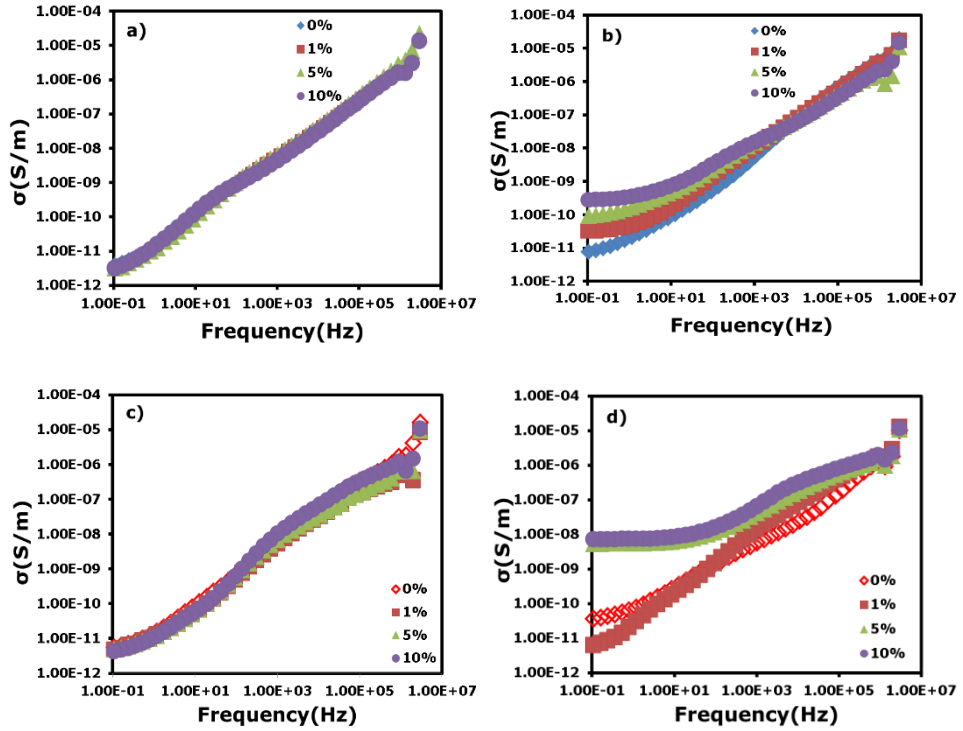

Figure 3.43 Conductivity of polyethylene (53–75 µm) in silicone oil with 1-3 v/v% Brij 30, a) 0 v/v% Brij 30, b) 1 v/v% Brij 30, c) 2 v/v% Brij 30, d) 3 v/v% Brij 30.

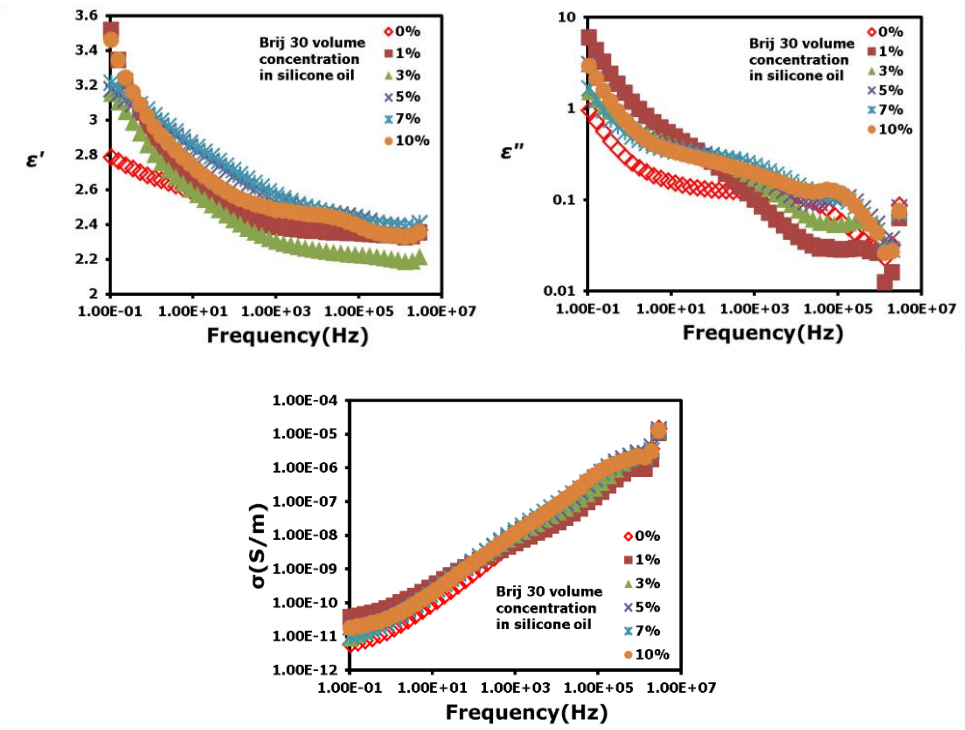

Figure 3.44 Conductivity of silicone oil with variable concentration c(v/v%) of Brij 30.

3.4 Methods of Data Processing

3.4.1 Image Processing

Images were processed using the open-source software ImageJ/Fiji (the public domain image-processing software developed at the National Institute of Health, USA). The number and the area of particles, chains/columns and voids were acquired using ImageJ/Fiji following procedures in Refs. [139, 140] and using our program developed in Matlab. Commands for the image quantification are described in the ImageJ/Fiji User Guide 1.46r revised edition (https://imagej.net/docs/guide/). Once a captured image is imported into ImageJ/Fiji, it is first calibrated to define the spatial scale in order to express results in calibrated units according to the posted scale bar at different magnifications by running the tool "Set Scale…". Then, the scanned color image is converted to an 8-bit

grayscale image by “Type” command. Next, the following set of preprocessing methods is applied to the grayscale image (Figure 3.45(a)). The “Noise” function removes pixel outliers with radius of two pixels and threshold 50; the “Smooth” function removes isolated pixels from edges and fills small holes, and the “Subtract Background” function uses a rolling bar with radius of 20 pixels to correct the uneven illuminated background and improve the image quality (Figure 3.45(b)). Our image processing procedures are mainly based on the segmentation of images by controlling all pixels intensity above a threshold to a foreground value and the remaining pixels to a background value that isolates objects by converting the corrected grayscale image (Figure 3.45(b)) into a binary image (Figure 3.45(c)) by running the “Threshold” function. The binary image displayed in Figure 3.45(c) shows a remarkable agreement between the raw and binary features that are visible in the image. The particles appear as black and the solvent appears as white. Finally, a size limitation (A) is applied to discriminate noise and out-of-focus objects from interested objects. To this end, areas smaller than the size of individual particles are ruled out by running the “Analyze Particle” function. The objects are counted, numbered and outlined (Figure 3.45(d)). The number of objects as a function of their size is used to compute the kinetics of the pattern formation.

Since the images are captured in a brightfield microscope leading to a slightly uneven illumination, a global thresholding method by running “Threshold…” command with “Default” method and a local thresholding method by running “Auto Local Threshold” function with “Bernsen” method in Fiji are both employed. The global thresholding uses a threshold to segment an image for all pixels. The local thresholding is used to examine the intensity values of the local neighborhood of each pixel and calculate a threshold h for each

pixel in the image to accommodate changing lighting conditions around this pixel. A typical outcome for images collected in our experiments is illustrated in Figure 3.46. It shows the area fraction of detected objects as a function of a contrast threshold that is defined as a difference between the maximum and minimum grey values. The global thresholding of the image yields the same area fractions within a certain range of a contrast threshold as the results computed from the local thresholding of this image. Therefore, the background illumination can be assumed approximately uniform over the image if the optic system is appropriately aligned. A global thresholding method is proper to binarize the image as the background noise reduced by the "Threshold" command.

The number density of objects detected strongly depends on the global contrast threshold. Once the background noise reduced, the contrast threshold parameter T is calibrated through analyzing the behavior of the number density of objects over a range of threshold parameters. A typical example of the calibration curve is shown in Figure 3.47 that displays a plateau of the number density of objects over a certain range of the threshold values. A rapid increase or a decrease of the number density appears only for the threshold values beyond this range, leading to an unreasonable number of the objects for very small and large threshold values. The critical value T is then determined for a contrast threshold parameter within the plateau region.

To quantify the morphology of a cellular pattern formed by a suspension of negatively polarized particles, the number of the particle-free domains of each size R_{fi} is measured and then the average size and the mean size are respectively calculated as $R_f = \frac{1}{N}\sum_i R_{fi}$ and$R_c = \sqrt{ab/\pi N}$, where N is the number of domains and ab is the image area (Figure 3.48). For a column-like pattern formed by a suspension of positively polarized

particles, the average diameter of an inscribed circle is used as a parameter to quantify the morphology of columns in the BIOP plugin of ImageJ/Fiji software (Figure 3.49). Figure 3.50 illustrates the typical workflow for processing suspension patterns with ImageJ/Fiji.

Nikon NIS-Elements Imaging Software, version 4.40, has several built-in methods for acquisition and stitching of large images. “Large image capture” in the acquisition function takes a specified number of images in the x and y directions around a center point and gives a stitched image (Figure 3.51). Also, the “scan large image with z direction” option allows one to define the top, bottom, left and right limits of an area of interest and will produce a single stitched 2D/3D image or save the images individually to be stitched later, including an option to set the percentage overlap between tiles needed for stitching.

The Nikon software was used to form large-scale 3D images of structures observed in our experiments. First, through a motorized focus control, the system creates stacks of 2D images at different locations in the plane parallel to the electrodes by scanning across the gap from the top to the bottom along the Z-axis and focusing at different heights. These images are then stitched together along and across the gap between the electrodes. The Z-series images can be displayed in various formats such as projections on the X-Z and Y-Z planes to form the cross-sectional slice views as well as in a rotatable 3D view (Figure 3.52). All the above described image processing functions are listed in the NIS-Elements AR User's Guide (Ver.4.50)

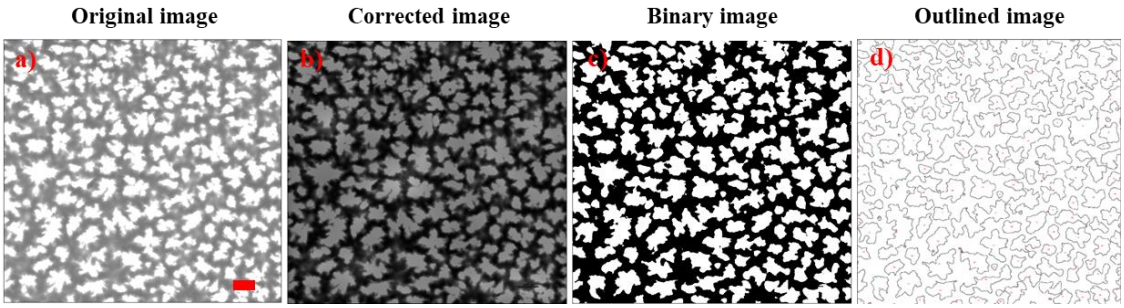

Figure 3.45 Comparison of the original, corrected, binary image and outlined images, scale bar is 1 mm. The cellular pattern includes a particle-free domain appearing in white and surrounded by a particle-rich wall in black.

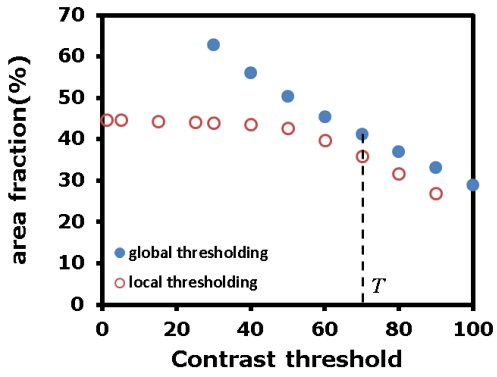

Figure 3.46 Plots of the area fraction of objects as a function of contrast threshold *T*. A contrast threshold is the subtraction value of a maximum threshold and a minimum threshold in the thresholding window. Full circles refer to the area fraction of objects obtained by the global thresholding methods; empty circles refer to the area fraction acquired by the local thresholding methods.

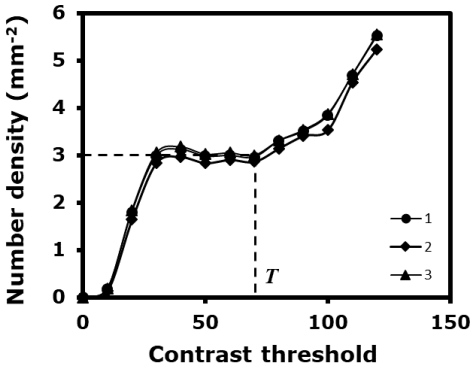

Figure 3.47 Number density of detected particle chains vs. contrast threshold *T*. Dashed horizontal and vertical lines show the value of parameter *T* chosen within the plateau. Data sets from three independent measurements are presented to verify the reproducibility of image processing, 3 v/v% suspension of poly-alpha-olefin particles in Mazola oil, gap size 1.5 mm.

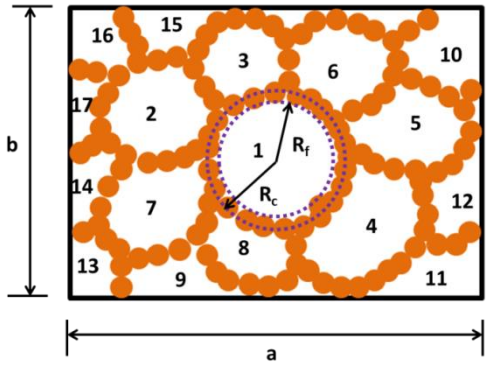

Figure 3.48 Characteristics of the particle-free domain in a cellular pattern formed by a suspension of negatively polarized particles.

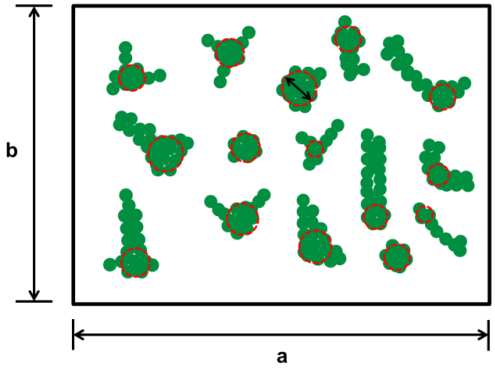

Figure 3.49 Characteristics of the columnar structure pattern formed by a suspension of positively polarized particles.

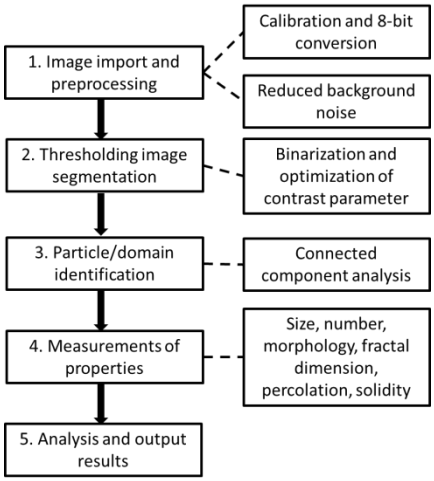

Figure 3.50 A typical workflow for the image-processing algorithm with ImageJ/Fiji.

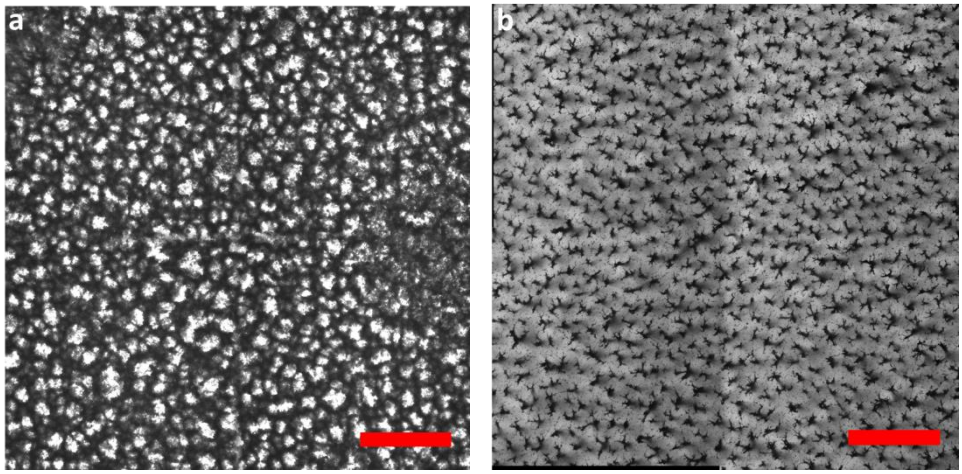

Figure 3.51 Images: (a) a cellular pattern formed in a suspension of negatively polarized polyalphaolefin (4-5 μm) particles in Mazola oil. Scale bar 5000 μm. (b) columns formed in a suspension of positively polarized polystyrene/polyaniline particles in silicone oil. Scale bar 1000 μm.

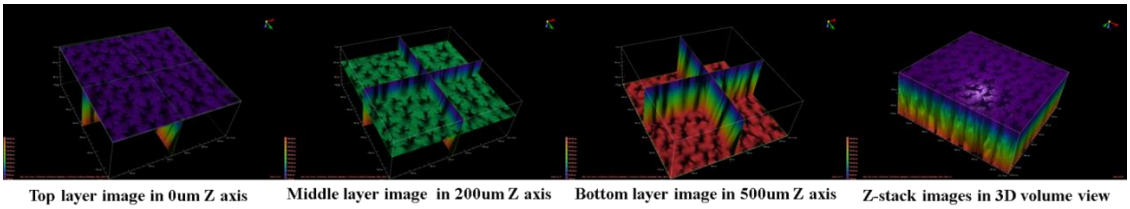

Figure 3.52 Z-stacks of 2D images and the constructed 3D image.

3.4.2 Statistical Method Analysis of Variance (ANOVA)

Analysis of Variance (ANOVA) in Microsoft Excel 2013 is used to analyze the influence of various experimental parameters on the pattern morphology. A null hypothesis proposes that a parameter varying in experiments has no statistically significant influence in a set of given observations. A test result calculated from the null hypothesis is considered statistically significant if it is deemed unlikely to have occurred by chance, as it is assuming by the null hypothesis. The rejection of the null hypothesis is justified if the probability (p-value) is less than a threshold (significance level) [119]. The null hypothesis is expressed as

$$H_0: \sum_{i=0}^{\alpha} \tau_i = 0 \tag{3.17}$$

$\tau =$ experimental factor, $\alpha =$ level of the factor, $\alpha = 0.05$ (for 95% confidence level).

Reject H_0 if: $F > F_\alpha$ or $p - value \ < \alpha$.

3.4.3 Percolation and Connectivity

The concept of percolation (connectivity) was used to quantify changes in the arrangement of particles on an image. A percolation theory was formulated in the 1950's as a mathematical theory to quantify the behavior of a network when nodes or links are added [120,121]. The percolation threshold is referred to a critical value of the occupancy probability of nodes or links that describes the appearance of long-range connectivity in a random system. Concepts of a percolation theory have been widely used in applications [122-126]. We used the SoilJ software as a plugin in ImageJ and Fiji/ImageJ II [127] as

well as ImageJ 1.x plugin BoneJ [128] to characterize the arrangement of particles and particle-free domains on an image. Specifically, we utilized the SoilJ options to flag pore clusters that are connected to one of several image sides, calculate the critical pore size that is the bottleneck in the connection from one image side to another and evaluate the connectivity of a pore network, such as the percolating porosity and the connection probability [129]. Examples of the usage of these options are presented in [131-132]. The sizes of individual particle-rich walls and islands and the particle-free domains on our images were measured using the Particle Analyzer option from the plugin BoneJ [128] to the software package ImageJ /FIJI [127]. Results of these measurements are expressed in terms of parameters F_p and F_L which respectively represent the fraction of connected particles and particle-free domains.

Images posted in Figure 3.53 illustrate the use of SoilJ/BoneJ plugins to quantify morphology of particle patterns formed in our experiments. Calculations of the particle connectivity in SoilJ/BoneJ are presented in Table 3.9.

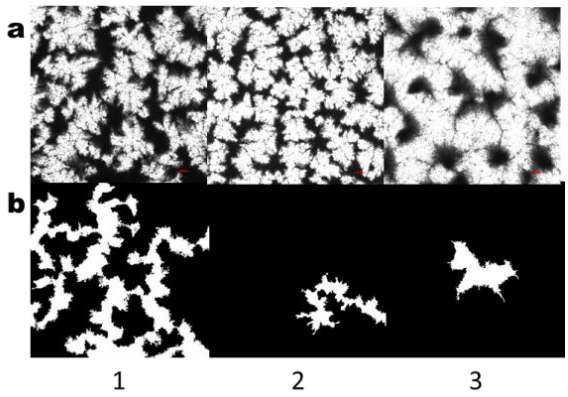

Figure 3.53 Image of the pattern structure of three typical examples on (a) a an original raw image and shown on a (b) processing image: 1, a percolating structure of the largest particle-rich wall; 2 and 3 are non-percolating structures of the largest particle-rich wall.

Table 3.9 Measurements of Connectivity of Cellular Pattern

ID	F_L(%)	F_P(%)
1	38.05 (percolation)	44.29
2	4.91 (non-percolation)	34.29
3	4.89 (non-percolation)	31.75

3.4.4 Solidity

Solidity, *S*, is the parameter to characterize the overall concavity of an object on an image. It is defined as the area of an object divided by the area of its convex hull, Equation (3.18). The convex hull is a convex polygon that contains all points of the object.

$$S = \frac{A}{A_C} = \frac{[Area]}{[Convex\ area]} \tag{3.18}$$

Figure 3.54 illustrates a difference between an object area, A (left) and the convex hull area, A_C (right). As the object area and the convex hull area approach each other, the value of *S* goes to one. The values of S for three images in Figure 3.55 computed by ImageJ are listed in Table 3.10. Figure 3.55 and data in Table 3.10 demonstrate that the value of S decreases, as the object shape becomes rougher changing from an ellipse to a 5-point star. The solidity value calculated from images in our experiments quantifies the extent of the isotropic growth of a particle cluster and a particle-free domain: large S for the isotropic growth and small S for the anisotropic growth.

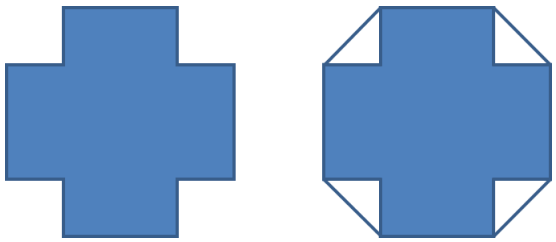

Figure 3.54 Area (left), A, and convex hull area (right), A_C, of an equivalent shape.

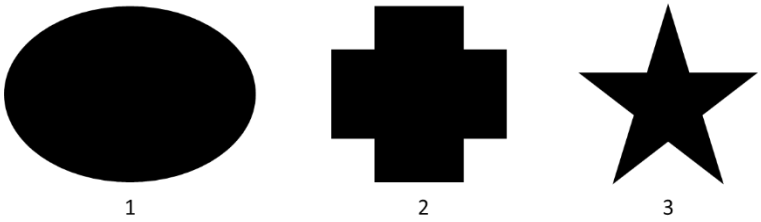

Figure 3.55 The values of solidity for objects 1-3 are listed in Table 3.10.

Table 3.10 Solidity of Objects in Figure 3.55.

ID	Shape Description	Solidity
1	Ellipse	1
2	Symmetric cross	0.87
3	5-point star	0.5

3.5 Results

3.5.1 Key Variables Affecting Formation of Cellular Pattern

Results of our preliminary experiments revealed that the combination of a strong AC electric field of a sufficiently high frequency and a weak DC field could cause a suspension of negatively polarized polyethylene and polyalphaolefin particles to form a cellular pattern of large particle-free domains surrounded by particle-rich walls. As an example, images in Figure 3.56 illustrate formation of a cellular pattern in 5 v/v% suspension of polyethylene particles in Mazola oil by applying AC field 1.5 kV/mm, 100 Hz and then adding DC field

0.03 kV/mm. The application of AC field for 5-6 min caused the particles to form chains and columns spanning the gap between electrodes. Once chains and columns formed, further exposure to the AC field did not change their uniform distribution in the plane parallel to the electrode, even over a period much longer than shown in Figure 3.56. Adding the DC field 30 min later initiated the growth of particle-free domains until a steady cellular pattern formed.

To explore the role of a DC field in formation of cellular patterns, experiments were carried out using one of the ITO glass electrodes partially covered with an insulating 3M fluoropolymer release liner and using quartz plates instead of ITO glass electrodes. The conductivity of a 3M fluoropolymer release liner and a quartz plate measured at 100 Hz are respectively $6.0 \times 10^{-11}(S/m)$ and $2.0 \times 10^{-11}(S/m)$ (see Sec 3.3.2.6). The conductivity of these materials is smaller than $1.0 \times 10^{-10}(S/m)$ at 100Hz of a 5v/v% polyalphaolefin (75-90 μm) suspension in Mazola oil used in these experiments. Images in Figure 3.57 show aggregation patterns formed by particles when the conducting surface of the bottom ITO glass electrode was partially covered with a 3M fluoropolymer release liner. While particles formed chains and columns all over the electrode gap, large particle-free domains appeared only in locations where the conducting surface was not coated. Experiments conducted on a suspension of 5v/v% polyethylene particles FR3 oil also demonstrate that large particle-free domains did not form in locations where the suspension was not in direct contact with a conducting layer on one of the electrodes. Moreover, the images presented in Figures 3.56-3.59 indicate that large particle-free domains appear regardless whether AC and DC fields are applied simultaneously or one after another.

Oil soluble dye SUDAN RED 7B (Sigma Aldrich, St Louis, MO) was used to visualize the flow of the solvent in the course of formation of a particle pattern. 20μL of the dye was mixed with 20mL of oil and about 100 μL of the dye was placed on the top of 5 v/v % suspension of polyethylene particles (53-75 μm) in Mazola oil before covering the sample cell. AC field 1.5kV/mm, 100 Hz was applied for 5 min and then DC field 0.03kV/mm was added for 10 min. Pattern formation was recorded with a digital camera Nikon DSLR 7200. Images presented in Figure 3.60 demonstrate that formation of large particle-free domains was not accompanied with the flow of the solvent.

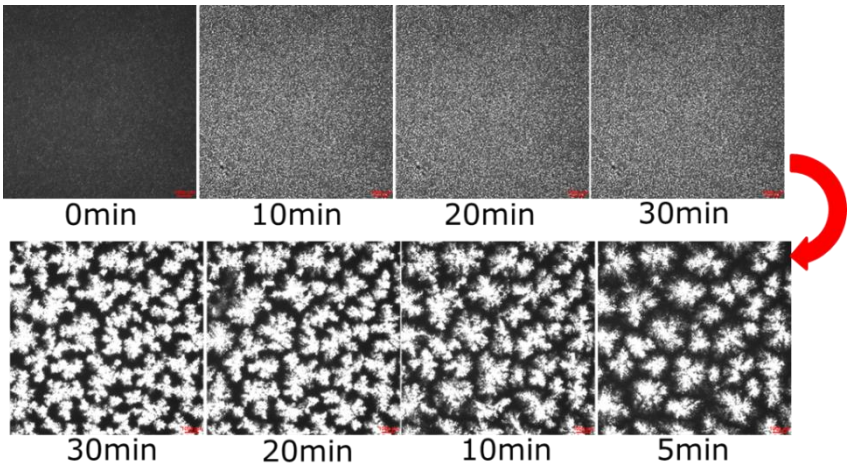

Figure 3.56 Patterns formed in a 5 v/v % suspension of polyethylene particles (53-75 μm) in Mazola oil; particles black, particle-free regions white; ITO conducting layers of both electrodes in direct contact with the suspension; top electrode energized, bottom grounded, interelectrode gap 2mm. Top: AC field 1.5kV/mm, 100 Hz applied. Bottom: DC field 0.03kV/mm added to the AC field.

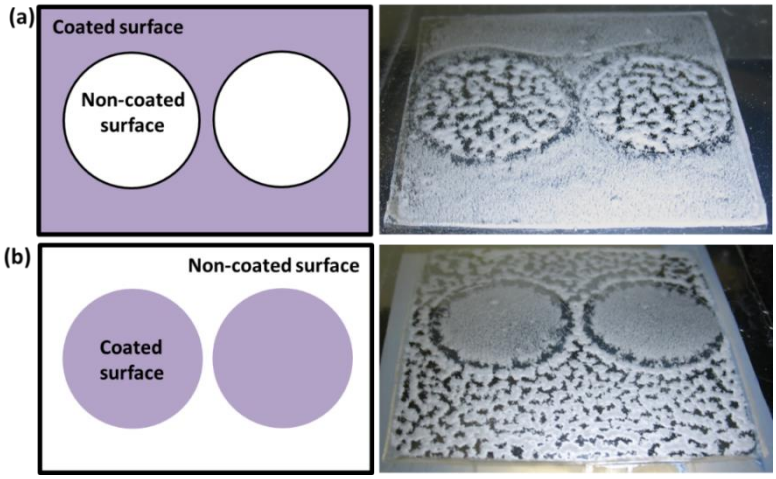

Figure 3.57 Patterns formed in 5 v/v % suspension of polyethylene particles (75-90 μm) in Mazola oil; particles white, particle-free regions black; top electrode energized, bottom grounded, interelectrode gap 2mm; AC field 1.5 kV/mm, 100 Hz and DC field 0.03 kV/mm applied simultaneously; ITO conducting layer of the bottom electrode coated with 3M insulating fluoropolymer (a) outside and (b) inside a circle.

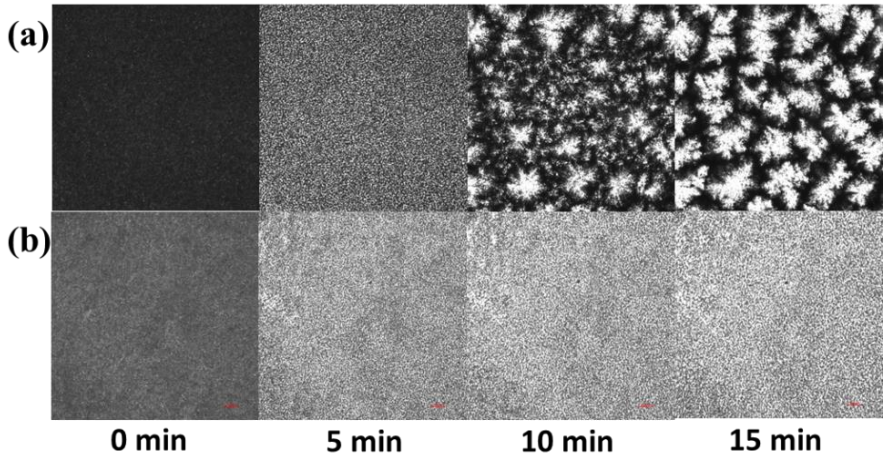

Figure 3.58 Patterns formed in 5 v/v % suspension of polyethylene particles (40-48 μm) in FR3 oil; particles black, particle-free regions white; top electrode energized, bottom grounded, interelectrode gap 2mm; AC field 1.5 kV/mm, 100 Hz applied for 5min and then DC field 0.03 kV/mm added. (a) ITO conducting layers of both electrodes in direct contact with the suspension; (b) ITO conducting layer of the bottom electrode coated with 3M insulating fluoropolymer release liner.

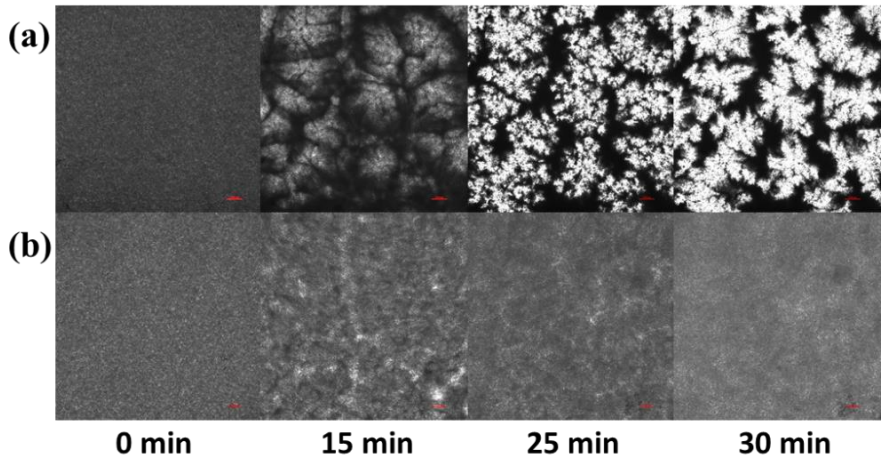

Figure 3.59 Patterns formed in 5 v/v % suspension of polyethylene particles (40-48 μm) in FR3 oil; particles black, particle-free regions white; top electrode energized, bottom grounded, interelectrode gap 2mm; DC field 0.03 V/μm applied for 15 min and then AC field 1.5 kV/mm, 100 Hz added. (a) ITO conducting layers of both electrodes in direct contact with the suspension; (b) ITO conducting layer of the bottom electrode coated with 3M insulating fluoropolymer release liner.

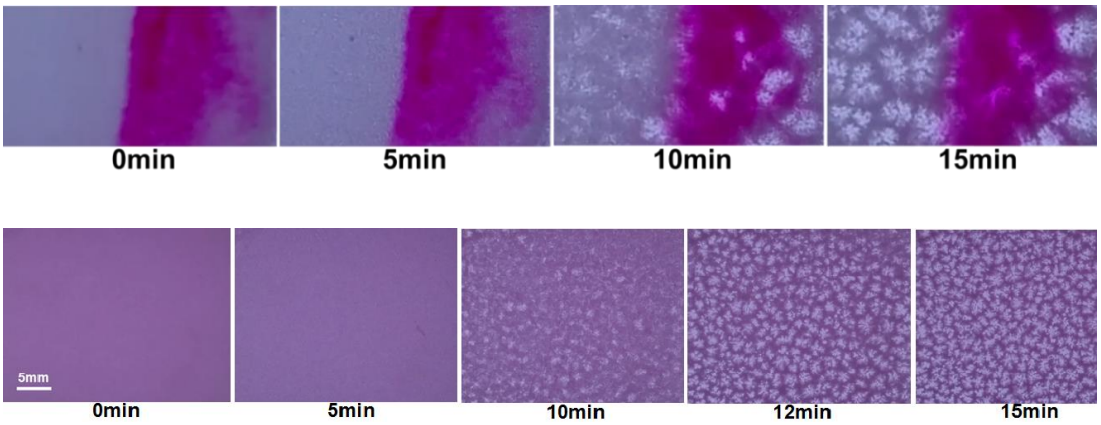

Figure 3.60 Pattern formation in 5 v/v % suspension of polyethylene particles (53-75 μm) in Mazola oil with added dye; particles black, particle-free regions white; top electrode energized, bottom grounded, interelectrode gap 2 mm; AC field 1.5 kV/mm, 100 Hz applied for 5 min and then DC field 0.03 kV/mm added for 10 min; images recorded at low (top) and high (bottom) magnification.

3.5.2 AC Field Strength and Frequency

To explore the effect of the AC field strength and frequency, experiments were carried out on 5 v/v% suspension of polyethylene particles (53-75 μm) in Mazola oil in a sample cell 1.5"×1.5" with the interelectrode gap 2 mm. The top electrode was energized and the bottom grounded. The DC field 0.03 kV/mm was applied together with the AC field. In most experiments, the ITO conducting layers of both electrodes were placed in direct contact with the suspension. A couple of experiments were conducted with the ITO conducting layers of the top or both electrodes directed outside from the sample cell.

Results of these experiments are summarized on the phase diagram presented in Figure 3.61. In region 1 of strong low frequency fields, $E_{AC} > 0.5 kV/mm$ and $< 1\ Hz$, some particles formed unstable islands and stripes arranged parallel to the electrodes. These islands, stripes and individual particle oscillated between the electrodes. In region 2 of strong high frequency fields, $E_{AC} > 1 kV/mm$ and $> 10\ Hz$, particles formed chains and columns spanning the interelectrode gap which then rearranged by forming large particle-free domains surrounded by particle-rich walls. In region 2 of low high frequency fields, $E_{AC} < 1 kV/mm$ and $\nu > 10\ Hz$, particles were driven by the DC field towards the top positive electrode and formed there large particle-free domains surrounded by particle-rich walls.

Taking data for the real part of permittivity ε' and conductivity σ of Mazola oil at 1 *Hz* and 10 *Hz* in Figure 3.40, we find that the frequency boundary between regions 1 and 2 is related to the charge relaxation time of Mazola oil $t_e = \varepsilon_0 \varepsilon'/\sigma$ as $\nu t_e \sim 1$. t_e provides a measure of how long it takes to neutralize an electric charge in the solvent by conduction

process. Accordingly, charge transport processes prevail in region 1 whereas polarization processes dominate in region 2.

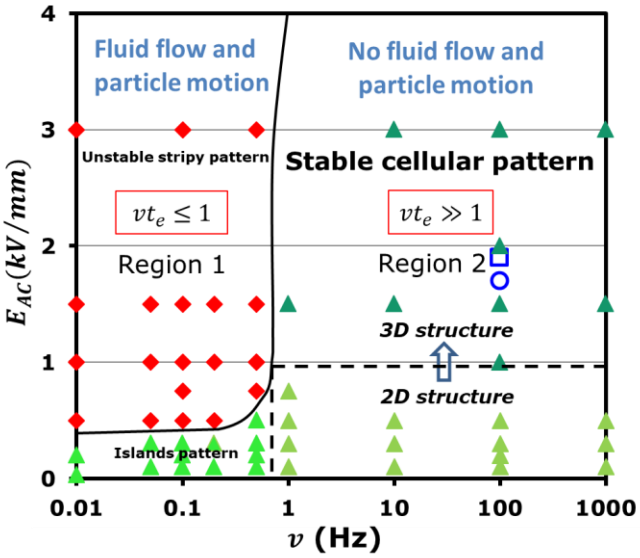

Figure 3.61 Phase diagram for pattern formation processes in 5 v/v% suspension of polyethylene particles (53-75 μm) in Mazola oil: Region 1, $vt_e < 1$, low frequency fields, particle form unstable islands in weak fields and stripes in strong fields. Region 2, $vt_e < 1$, high frequency fields, large particle-free regions surrounded by particle-rich walls mainly on the DC positive electrode in weak fields and across the interelectrode gap in strong fields. Filled symbols present data when ITO conducting layers of both electrodes in direct contact with suspension; open circle present data when ITO conducting layer of top electrode directed outside from the sample cell and open square when ITO conducting layers of both electrode directed outside from the sample cell.

3.5.3 High-Frequency AC Fields

To explore the effect of the AC field strength, experiments were carried out on 5 v/v% suspension of polyethylene particles (40-48μm) in FR3 oil in a sample cell 1.5"×1.5" with the interelectrode gap 0.5 mm for field strengths $E_{AC} = 0.03 - 3\text{kV/mm}$ at frequency 100Hz. The top electrode was energized and the bottom grounded. The DC field 0.03 kV/mm was added to the AC field after 5 min.

Plots and images presented in Figure 3.62 show the growth rate of the particle-free domains for different AC field strengths. As can be seen in Figure 3.62, cellular patterns

formed faster in low AC fields. Notice that cellular patterns in low AC fields were located close to the positive top electrode as the particle electrophoresis driven by the DC field dominated. For strong AC fields, chains and columns of particles formed cellular patterns across the entire interelectrode gap as the dipolar interaction between polarized particles prevailed. Plots and images presented in Figure 3.63 demonstrate the time variation of the area covered by particles in the plane parallel to the electrodes for strong AC fields. As the particles formed chains and columns following the application of an AC field, the area covered by them gradually reduced. The application of the DC field at 5 min later caused the chains and columns to widen. As they shrank while rearranging into a cellular pattern, the area covered by the particles gradually reduced to the same value as it was formed by the AC field. The images in Figure 3.63 (a) and the inset in Figure 3.63 (b) show that the size of particle-free domains increases with increasing the AC field strength.

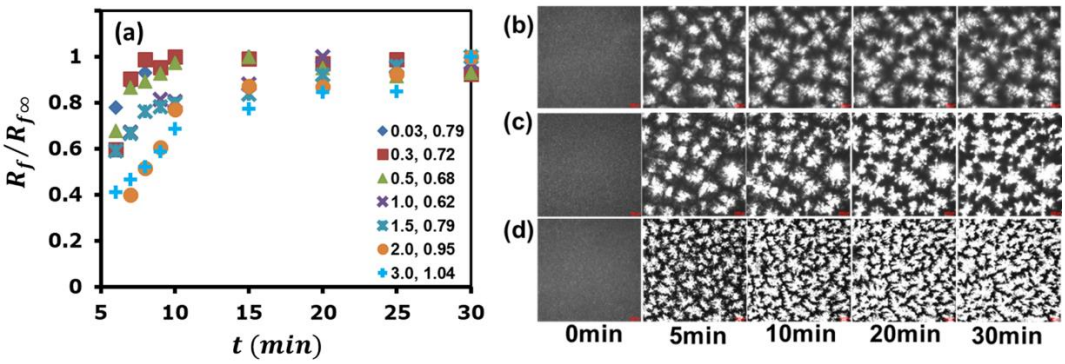

Figure 3.62 Pattern formation in 5 v/v % suspension of polyethylene particles (40-48μm) in FR3 oil; particles black, particle-free regions white; top electrode energized, bottom grounded, interelectrode gap 0.5 mm; AC field frequency 100 *Hz;* DC field 0.03 kV/mm added to AC field after 5 min: (a) $R_f/R_{f\infty}$ is the ratio of the average radius of particle-free domains the to the plateau value $R_{f\infty}$, listed are the AC field strength E_{AC} in kV/mm and plateau value $R_{f\infty}$ in mm; (b) $E_{AC} = 0.03kV/mm$, (c) $E_{AC} = 1.0kV/mm$, (d) $E_{AC} = 3.0kV/mm$.

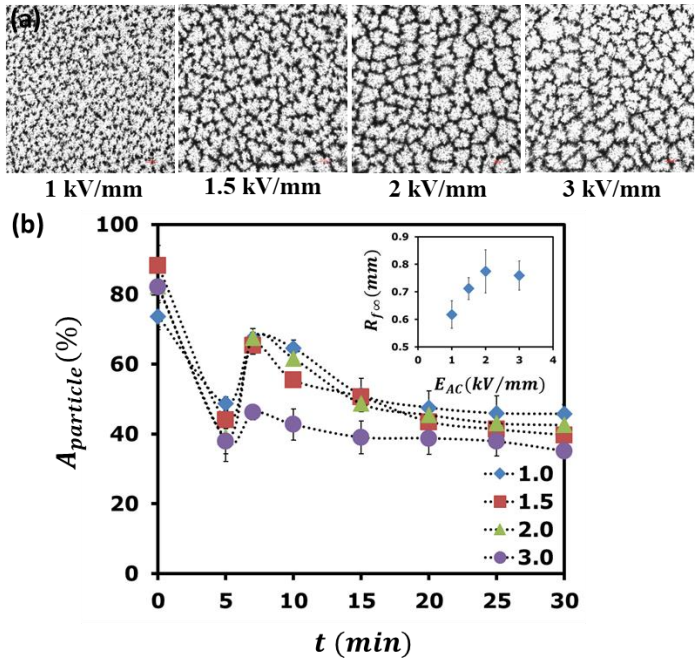

Figure 3.63 Pattern formation in 5 v/v % suspension of polyethylene particles (40-48μm) in FR3 oil; particles black, particle-free regions white; top electrode energized, bottom grounded, interelectrode gap 0.5 mm; AC field frequency 100 *Hz;* DC field 0.03 kV/mm added to the AC field after 5 min: (a) cellular patterns established for different strength E_{AC} of AC fields; (b) fraction of area occupied by particles over time for different AC field strength E_{AC} in kV/mm; inset shows the final size of particle-free domains $R_{f\infty}$ vs. E_{AC}.

3.5.4 DC Field Strength

Experiments were carried out on 5 v/v% suspension of polyethylene particles (53-75 μm) in Mazola oil and (40-48μm) in FR3 oil in a sample cell 1.5"×1.5" with the interelectrode gaps 0.5 mm and 2 mm. The top electrode was energized and the bottom grounded. An AC field of 0.3 kV/mm or 1.5 kV/mm at 100 Hz was applied and a DC field was added after 5 min.

For the AC field 1.5 kV/mm, 100 Hz, stable cellular patterns of particle-free domains formed in 5 v/v% suspension of polyethylene particles (53-75 μm) in Mazola oil at DC fields $0.02\ kV/mm < E_{DC} <$ 0.05kV/mm (Figure 3.64). The particle chains and

columns were arranged across the gap between the electrodes. Adding a DC field lower than 0.02 kV/mm to this AC field did not rearrange chains and columns formed across the interelectrode gap. When the DC field strength was raised to 0.1 kV/mm, an increase in the electrophoretic force exerted on particles generated oscillations of individual particles and particle clusters between the electrodes, rendering the circular-like pattern unstable (Figure 3.65). For the AC field 0.3 kV/mm, 100 Hz, the application of a DC field lower than 0.05 kV/mm drove particles towards the positive top electrode and formed there a stable cellular pattern of particle-free domains. However, in increase of the AC field strength to 1 kV/mm caused this cellular pattern to evolve and eventually span the interelectrode gap (Figure 3.65).

The application of the AC field 1.5 kV/mm, 100 Hz and the a DC field at $0.01\ kV/mm < E_{DC} < 0.05$kV to 5 v/v % suspension of polyethylene particles (40-48μm) in FR3 oil formed cellular patterns of particle chains and columns across the entire interelectrode gap. Plots and images presented in Figure 3.66 demonstrate the time variation of the area covered by particles in the plane parallel to the electrodes for different DC fields. When the particles formed chains and columns following the application of the AC field, the area covered by them gradually reduced. The application of the DC field at 5 min later caused the chains and columns to widen. As they shrank while rearranging into a cellular pattern, the area covered by the particles gradually reduced to the same value as it was formed by the AC field. The images in Figure 3.66 (a) and the inset in Figure 3.66 (b) show that the size of particle-free domains increases with increasing the DC field strength.

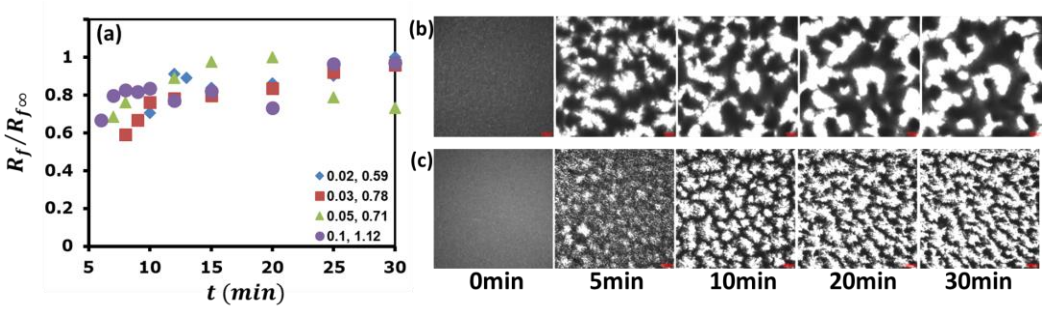

Figure 3.64 Pattern formation in 5 v/v % suspension of polyethylene particles (53-75 μm) in Mazola oil; particles black, particle-free regions white; top electrode energized, bottom grounded, interelectrode gap 2 mm; AC field 1.5 kV/mm,100 *Hz;* DC field added to AC field after 5 min: (a) $R_f/R_{f\infty}$ is the ratio of the average radius of particle-free domains the to the plateau value $R_{f\infty}$ at different DC field strengths E_{DC} in kV/mm; and plateau value $R_{f\infty}$ in mm; (b) $E_{DC} = 0.1kV/mm$, (c) $E_{DC} = 0.02kV/mm$

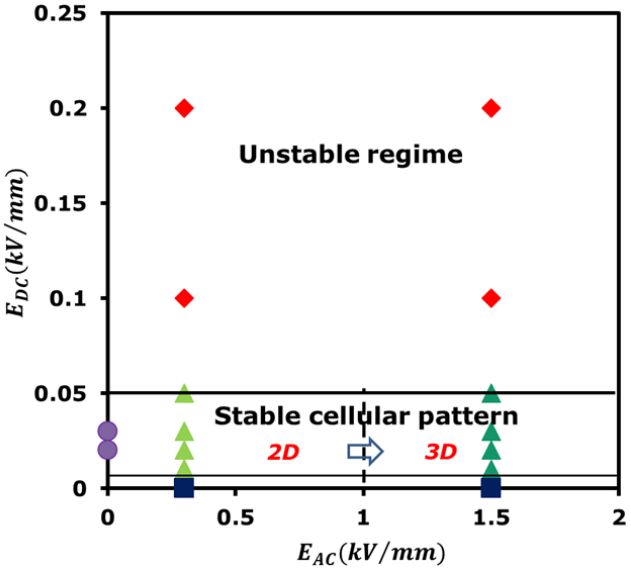

Figure 3.65 Stability of patterns formed in 5 v/v% suspension of polyethylene particles (53-75 μm) in Mazola oil; top electrode energized, bottom grounded, interelectrode gap 2 mm, frequency of AC fields 100 Hz, DC field added to the AC field after 5 min, filled circle present data when stripes pattern formed on electrodes after only DC field applied and filled square present data when chains/columns pattern formed in electrodes gap after only AC field applied..

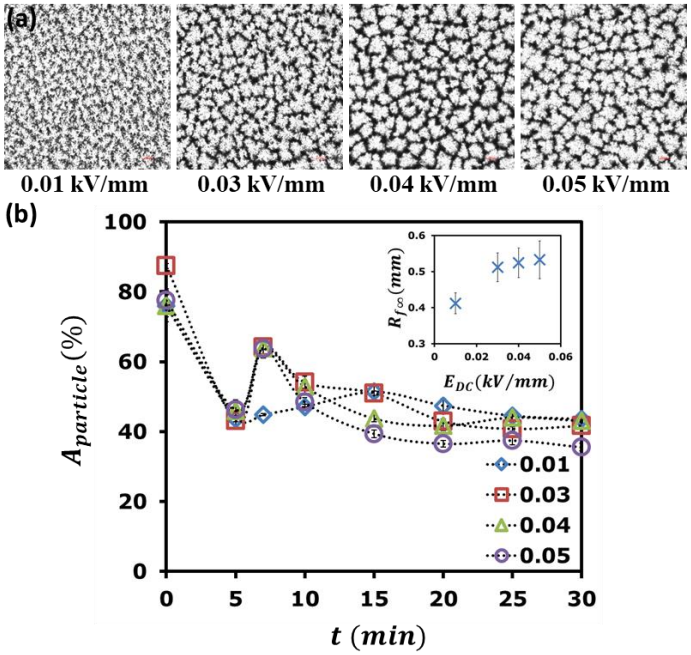

Figure 3.66 Pattern formation in 5 v/v % suspension of polyethylene particles (40-48μm) in FR3 oil; particles black, particle-free regions white; top electrode energized, bottom grounded, interelectrode gap 0.5 mm; AC field 1.5 kV/mm, 100 *Hz;* DC field added to the AC field after 5 min: (a) cellular patterns established for different strength of DC fields; (b) fraction of area occupied by particles over time for different DC field strength E_{DC} in kV/mm; inset shows the final size of particle-free domains $R_{f\infty}$ vs. E_{DC}

3.5.5 DC Field vs. Low Frequency AC Field

Two sets of tests were carried out on 5 v/v% suspension of polyethylene particles (53-75 μm) in Mazola oil and polyethylene particles (40-48μm) in FR3 oil in a sample cell 1.5"×1.5" with the interelectrode gap 2 mm. The top electrode was energized and the bottom grounded. The AC field of 1.5 kV/mm at 100 Hz was used in these experiments. In one set of these tests, a DC was added to the AC field after 5 min to form a cellular pattern of particle-free domains surrounded by particle-rich wall. In the other, a DC field switched over from $+0.03kV/mm$ to $-0.03kV/mm$ with the frequency 0.01Hz. Similar cellular patterns of chains and columns across the interelectrode gap were formed in both cases.

This outcome in Figure 3.67 demonstrates that the combination of a strong high-frequency field with a weak DC field or a low-frequency weak AC field can be used to form cellular patterns.

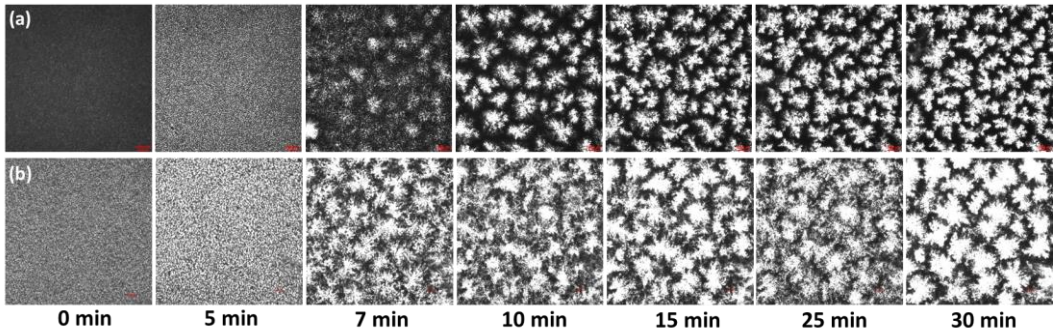

Figure 3.67 Pattern formation in 5 v/v % suspension of polyethylene particles; particles black, particle-free regions white; top electrode energized, bottom grounded, interelectrode gap 2 mm; AC field 1.5 kV/mm,100 *Hz;* (a) DC field 0.03 kV/mm added to AC field after 5 min; (b) a DC field switched over from $+0.03kV/mm$ to $-0.03kV/mm$ with the frequency 0.01Hz after 5 min.

3.5.6 Effect of AC Field Frequency

Experiments were carried out on 5 v/v% suspension of polyethylene particles (40-48µm) in FR3 oil in a sample cell 1.5"×1.5" with the interelectrode gap 0.5 mm. The top electrode was energized and the bottom grounded. AC field of different frequencies 0.1 kHz - 3.0 kHz and strength 1.5 kV/mm were used. A DC field of 0.03 kV/mm was added after 5 min.

For the AC field strength of 0.3 kV/mm with frequencies lower than 1 Hz, the application of a DC field drove particles towards the positive top electrode where they aggregated. However, these particle patterns were unstable due to the motion of particles and solvent. Increasing the AC field frequency to 10 Hz suppressed the motion of particles and solvent and stabilized the aggregation pattern formed by particles close to the top electrode.

Increasing the AC field strength to 1 kV/mm and the frequency to 100 Hz formed a stable cellular pattern of particle-free domains across the gap between electrodes. Plots and images presented in Figure 3.68 demonstrate the time variation of the area covered by particles in the plane parallel to the electrodes for different frequencies of the AC field 1.5 kV/mm. When the particles formed chains and columns following the application of the AC field, the area covered by them gradually reduced. The application of the DC field at 5 min later caused the chains and columns to widen. As they shrank while rearranging into a cellular pattern, the area covered by the particles gradually reduced to the same value as it was formed by the AC field. The images in Figure 3.68 (a) and the inset in Figure 3.68 (b) show that changing the field frequency above 100 Hz does not affect the size of particle-free domains. However, reducing the AC frequency to 1 Hz destroyed the particle chains and columns by generating intensive oscillations of particles and solvent.

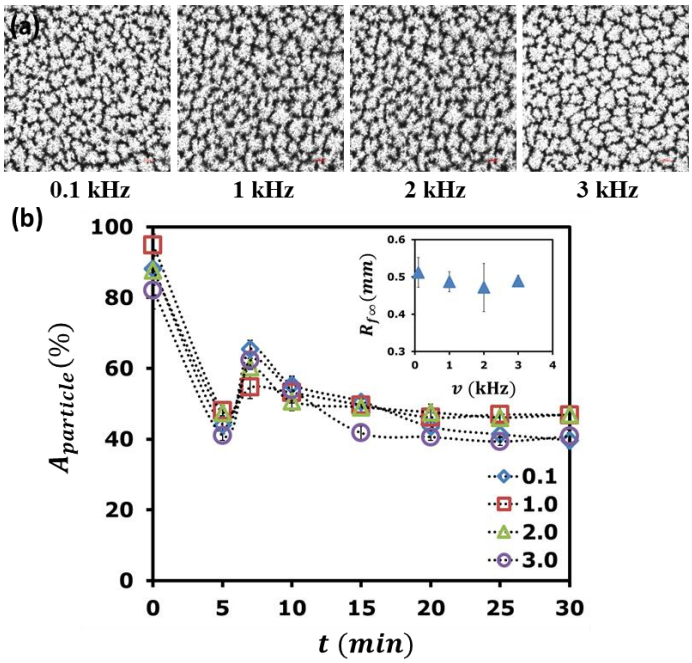

Figure 3.68 Pattern formation in 5 v/v % suspension of polyethylene particles (40-48μm) in FR3 oil; particles black, particle-free regions white; top electrode energized, bottom grounded, interelectrode gap 0.5 mm; AC field strength 1.5 kV/mm; DC field added to the AC field after 5 min: (a) cellular patterns established for different frequencies of AC fields; (b) fraction of area occupied by particles over time for different frequencies of AC fields v in kHz; inset shows the final size of particle-free domains $R_{f\infty}$ vs. AC field frequency v.

3.5.7 Repeatability of Cellular Patterns

Once a cellular pattern of particle-free domains surrounded by particle-rich walls is formed, it is possible to disperse the particles by applying a low-frequency AC field. The use of the combination of a strong high frequency AC electric field and a weak DC field allows one to form a cellular pattern again. We first consider the efficiency of stirring the suspension with a low frequency AC field and then explore whether there exist any correlations between cellular patterns built in succession.

3.5.7.1 Stirring suspension with low-frequency AC fields. Experiments were conducted on 5v/v% suspension of polyethylene particles (53-75μm) in Mazola oil in a sample cell

1.5"×1.5" with the interelectrode gap 2 mm. The top electrode was energized and the bottom grounded. The AC field 1.5 kV/mm, 100 Hz was applied for 5 minutes to form chains and columns across the interelectrode gap. The DC field 0.03 kV/mm was then added for 20 minutes to form a stable cellular pattern. The efficiency of low frequency AC fields to stir the suspension was then tested. Experiments demonstrated that the AC field 1.5 kV/mm, 0.5 Hz is capable to disperse particles (Figure 3.69(a)). Tests were then conducted to determine the strength of an AC field at 0.5 Hz sufficient to stir the suspension. The procedure to form a cellular pattern in these tests remained the same. Once a cellular pattern was formed, an AC field of a lower strength was applied for 5 min. Experiments showed that the AC field strength 0.75 kV/mm is sufficient for dispersing particles (Figure 3.69(b)).

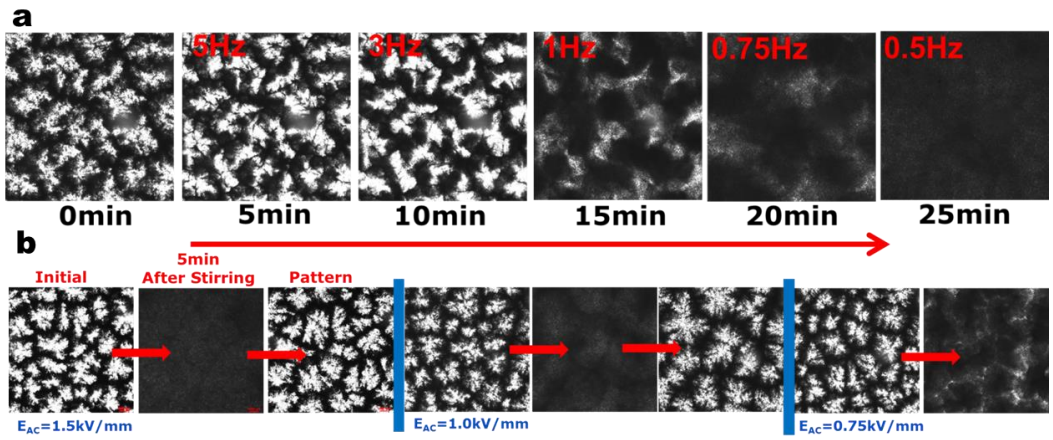

Figure 3.69 Patterns in 5v/v% suspension of polyethylene particles (53-75μm) in Mazola oil in a sample cell 1.5"×1.5" with the interelectrode gap 2.0 mm, top electrode energized, bottom grounded; particles black, particle-free regions white. Cellular patterns formed by applying AC field 1.5 kV/mm, 100 Hz for 5 min and then adding DC field 0.03 kV/mm for 20 min. a) AC field strength 1.5 kV/mm, stirring for 5 min at each frequency. (b) Stirring the AC field at 0.5 Hz for 5 min.

3.5.7.2 Effectiveness of stirring suspension with low frequency AC fields. Experiments were conducted on 5v/v% suspension of polyethylene particles (53-75μm) in Mazola oil

in a sample cell 1.5"×1.5" with the interelectrode gap 2 mm. We tested whether there exist any correlations between locations of particle-free domains in three cellular patterns (Figure 3.70) built in succession. The presence of correlations was analyzed by measuring the minimum separation distances between centers of particle-free domains in different cellular patterns. Results of these measurements were also compared with the data on the minimum separation distances between particle-free domains in cellular patterns formed in six different samples of this suspension. Cellular patterns in all these tests were formed by applying AC field 1.5 kV/mm, 100 Hz for 5 min and then adding DC field 0.03 kV/mm for 20 min. stirring with AC field 1.5 kV/mm, 0.5 Hz for 5 min was used to disperse particles in cellular patterns built in succession.

The histogram in Figure 3.71 shows that the normal distribution describes the minimum separation distances between centers of particle-free domains in three cellular patterns built in succession in the same suspension sample. The histogram in Figure 3.72 shows that the normal distribution also describes the minimum separation distances between centers of particle-free domains in cellular patterns formed in six different suspension samples.

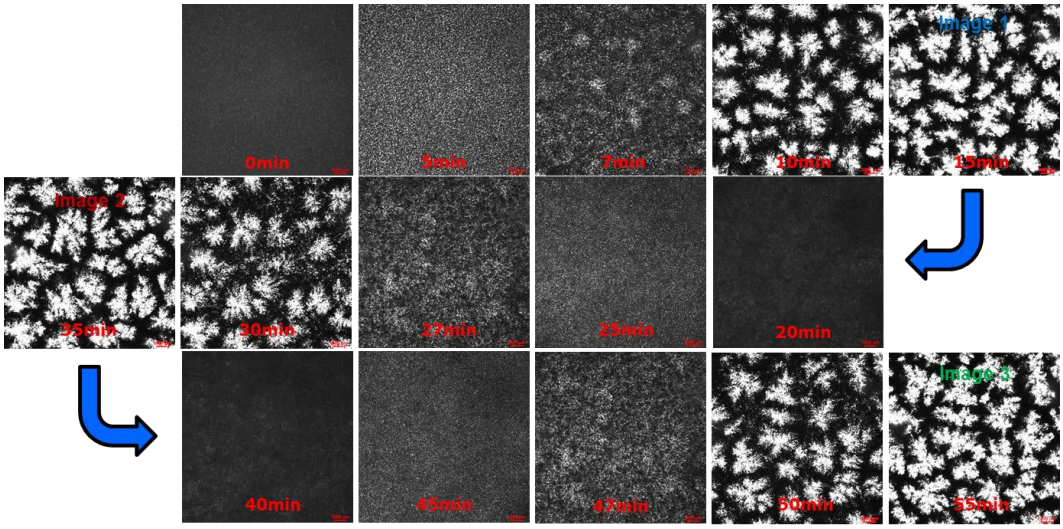

Figure 3.70 Patterns in 5v/v% suspension of polyethylene particles (53-75μm) in Mazola oil in a sample cell 1.5"×1.5" with the interelectrode gap 2.0 mm, top electrode energized, bottom grounded; particles black, particle-free regions white. Cellular patterns formed by applying AC field 1.5 kV/mm, 100 Hz for 5 min and then adding DC field 0.03 kV/mm for 20 min, stirring with AC field 1.5 kV/mm, 0.5 Hz for 5 min applied to disperse particles in three cellular patterns built in succession.

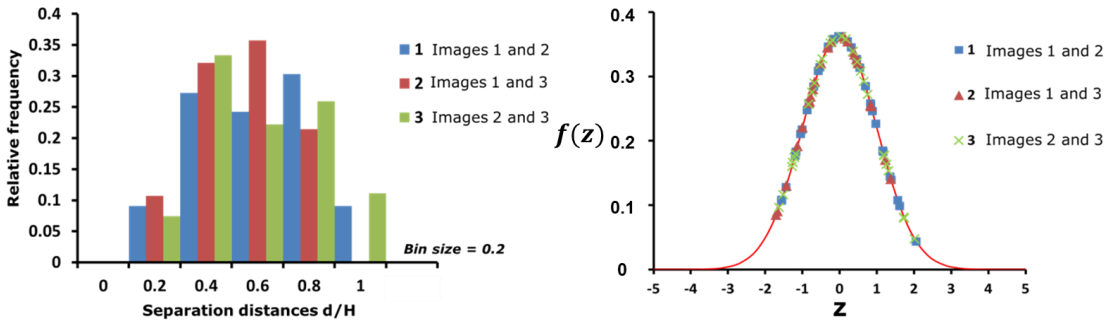

Figure 3.71 Left: histogram of minimum separation distances between centers of particle-free domains in three cellular patterns built in succession in the same sample of 5v/v% suspension of polyethylene particles (53-75μm) in Mazola oil; H=2.0 mm. Cellular patterns formed by applying AC field 1.5 kV/mm, 100 Hz for 5 min and then adding DC field 0.03 kV/mm for 20 min; AC field 1.5 kV/mm, 0.5 Hz for 5 min used for stirring. Right: transfer data into standard normal distribution with the corresponding curve in red, $f(z)$ refer to probability density function, and z refer to standardization of data.

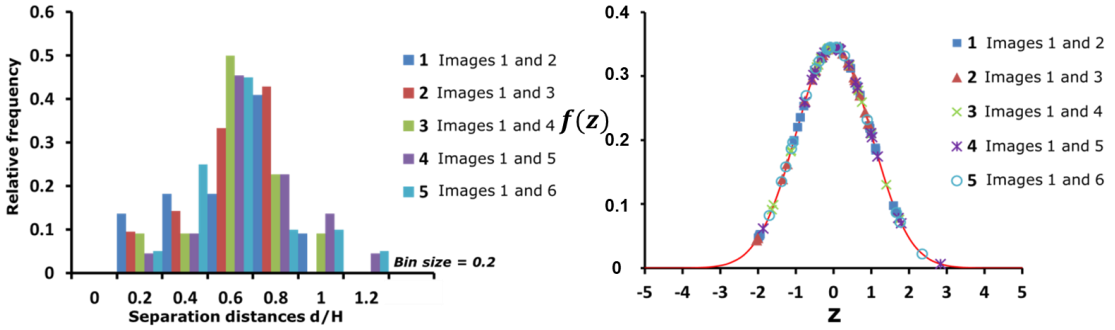

Figure 3.72 Left: histogram of minimum separation distances between centers of particle-free domains in cellular patterns formed in six different samples of 5v/v% suspension of polyethylene particles (53-75μm) in Mazola oil, H = 2 mm. Cellular patterns formed by applying AC field 1.5 kV/mm, 100 Hz for 5 min and then adding DC field 0.03 kV/mm for 20 min; Right: transfer data into standard normal distribution with the corresponding curve in red, $f(z)$ refer to probability density function, and z refer to standardization of data.

3.5.7.3 Manual mixing. Test was conducted on 5 v/v% suspension of polyethylene particles (53-75 μm) in Mazola oil in a sample cell 1.5"×1.5" with the interelectrode gap 2 mm. The top electrode was energized and the bottom grounded. The AC field 1.5 kV/mm, 100 Hz was applied for 5 minutes and the DC field 0.03 kV/mm was added for 20 minutes to form a stable cellular pattern. The electric field was then switched off, the top ITO glass electrode was removed and the suspense was vigorously stirred for about two minutes with a wooden coffee stirrer. After stirring, the sample cell was closed and the cellular pattern formed by using the same procedure.

The field was switched off and the cell was opened by removing the top ITO glass and stirred for about 2 minutes using a wooden coffee stirrer. After stirring, the cell was closed and structure formation experiments were repeated. The result showed that the cellular patterns formed before and after stirring have similar characteristics (Figure 3.73). Hence, mechanical and low frequency stirring in AC field are effective methods of initializing the suspension after structure formation.

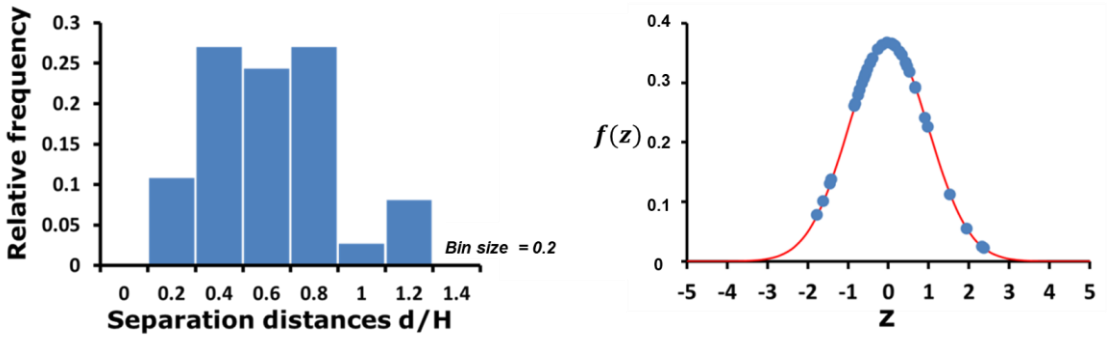

Figure 3.73 Left: histogram of minimum separation distances between centers of particle-free domains in two cellular patterns built in succession in the same sample of 5v/v% suspension of polyethylene particles (53-75μm) in Mazola oil, H=0.2 mm. Cellular patterns formed by applying AC field 1.5 kV/mm, 100 Hz for 5 min and then adding DC field 0.03 kV/mm for 20 min; stirring with a wooden coffee stirrer. Right: transfer data into standard normal distribution with the corresponding curve in red, $f(z)$ refer to probability density function, and z refer to standardization of data.

3.5.8 Comparison of Suspensions Forming Stable Pattern

Suspensions used in our experiments were prepared by dispersion of nearly neutrally buoyant polyalphaolefin and polyethylene particles in Mazola corn oil (Figure 3.74(a)), Cargill Envirotemp FR3 oil (Figure 3.74(b)) and Silicone oil with 1% Brij30 (Figure 3.74(b)) (Table 3.11). The application of a strong high-frequency filed AC field to suspensions of these particles in silicone oil without Brij30 did not form chains, most likely due to a very low electric conductivity.

When the particles formed chains and columns following the application of the AC field, the area covered by them gradually reduced. The application of the DC field at 5 min later caused the chains and columns to widen. As they shrank while rearranging into a cellular pattern, the area covered by the particles gradually reduced to the same value as it was formed by the AC field for 5 v/v% particle concentration. However, for 10 v/v% - 15 v/v% particle concentration, as particle chains and columns shrank while rearranging into

a cellular pattern, the area covered by the particles gradually reduced to the value much smaller that it was formed by the only AC field applied (Figure 3.74(d) and 3.74(e).

Table 3.11 Suspension Forming Stable Cellular Pattern

Particles	**Solvent**		
	Cargill Envirotemp FR3 oil	**Mazola corn oil**	**Silicone oil with 1% Brij30**
Polyalphaolefin (75-90μm and 4-5μm)	√	√	√
Polyethylene (40-48μm and 53-75μm)	√	√	√

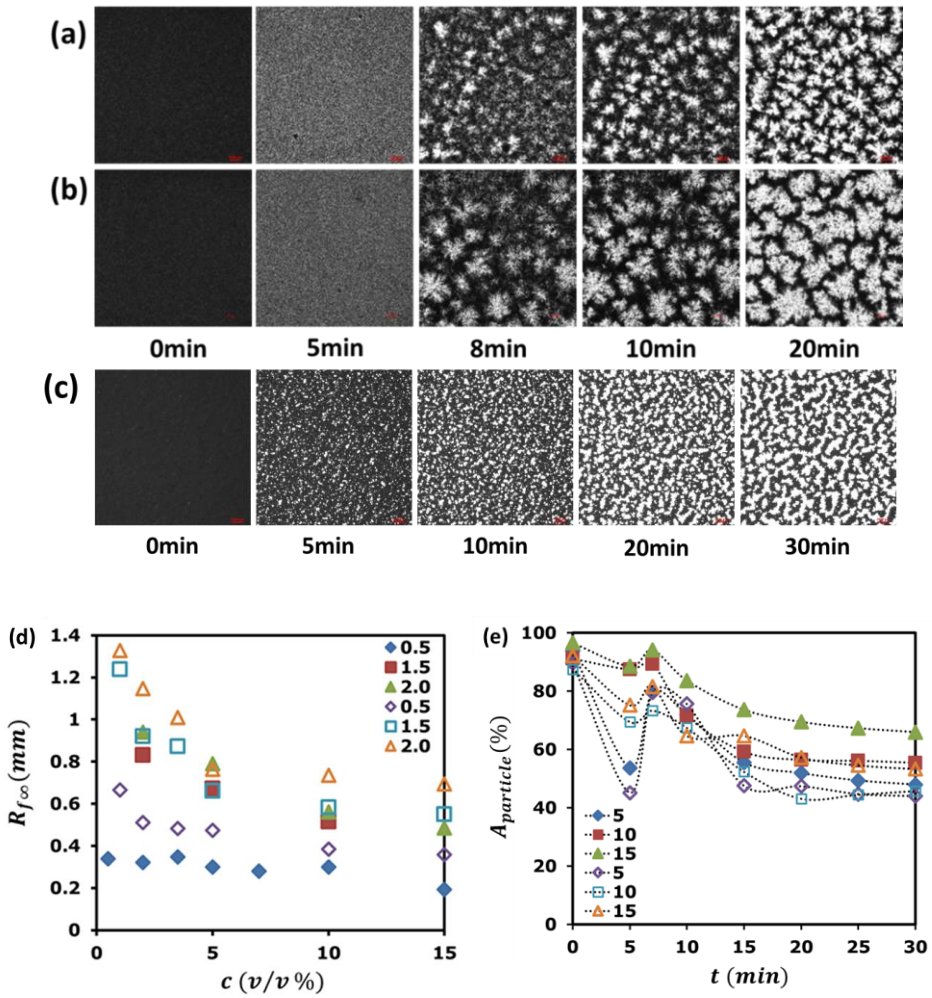

Figure 3.74 Patterns in 10v/v% suspension of polyethylene particles (53-75μm) in (a) Mazola oil, (b) FR3 oil and (c) Silicone oil with 1% Brij30 in a sample cell 1.5"×1.5" with the interelectrode gap 2 mm, top electrode energized, bottom grounded; particles black, particle-free regions white. Cellular patterns formed by applying AC field 1.5 kV/mm, 100 Hz for 5 min and then adding DC field 0.03 kV/mm (adding DC field 0.5kV/mm for suspension of Silicone oil with 1% Brij30). (d) Dependence of the final size of particle-free domains $R_{f\infty}$ formed in Mazola oil and FR3 oil suspensions on $0.5v/v\,\%$ - $15v/v\,\%$ particle concentration for different interelectrode gaps H in mm; (e) Fraction of area occupied by particles $A_{particle}(\%)$ over time for difference particle concentration $c(v/v\,\%)$ in Mazola oil and FR3 oil suspensions, interelectrode gap 1.5 mm. Filled symbol indicate suspension by Mazola oil and open symbol indicate suspension by FR3 oil. Scale bar 0.1mm.

3.5.9 Formation of Cellular Pattern Across Interelectrode Gap

The schematic diagram presented in Figure 3.75 summarizes our observations on three-step processes that cause the particles to form a cellular pattern following the application of a strong high frequency AC field and then a weak DC field. We will henceforth refer to this transformation as 3D->3D to differentiate it from the formation of a cellular pattern when a relatively weak DC field is firstly applied.

The first step of the 3D->3D transformation employs a strong high frequency AC field (Figure 3.75). It causes the particles to form chains and columns that are uniformly distributed in the plane parallel to the electrodes and evolve along the field direction to span the interelectrode gap. Accordingly, the area fraction covered by the particles in the plane parallel to the electrodes gradually decreases. Single chains prevail in dilute suspensions and multi-chain columns in concentrated suspensions. The second step is associated with the application of a weak DC field. It caused the chains and columns to partially break down and widen that rapidly increases the area fraction covered by the particles in the plane parallel to the electrodes. The third step is associated with the appearance of "repulsion centers," to be referred to as nuclei [113, 114], throughout the whole gap between electrodes. The particle chains and columns at these nucleation sites begin moving radially outward, without disintegrating, thereby creating particle-free domains spanning the gap between the electrodes. Accordingly, the area fraction covered by the particles in the plane parallel to the electrodes decreases, gradually approaching the value achieved by the application of the AC field for dilute suspensions and a lower value for concentrated suspensions.

Plots and images in Figure 3.76 show this 3D->3D transformation for 2 v/v% and 15 v/v% suspensions of polyethylene particles (40-48 μm) in Envirotemp FR3 oil following the application of AC field 1.5 kV/mm, 100 Hz and adding DC field 0.03 kV/mm 5 min later.

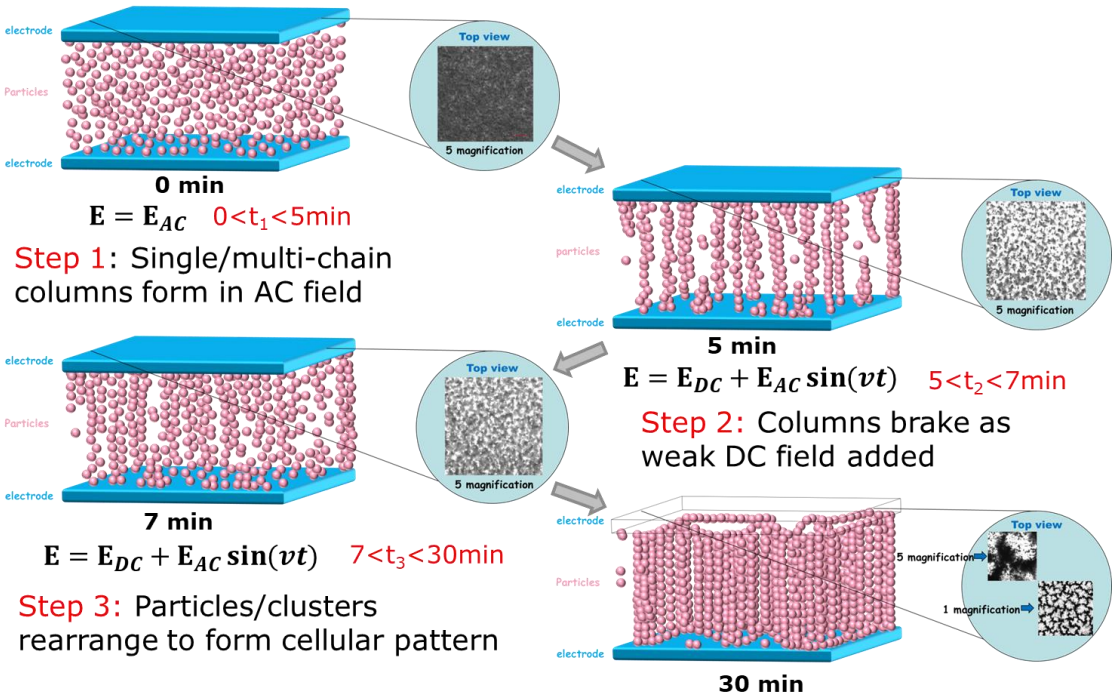

Figure 3.75 Schematics of 3D −> 3D transformation with typical durations of events to form cellular patterns in a suspension by applying a strong high frequency AC field and then a weak DC field.

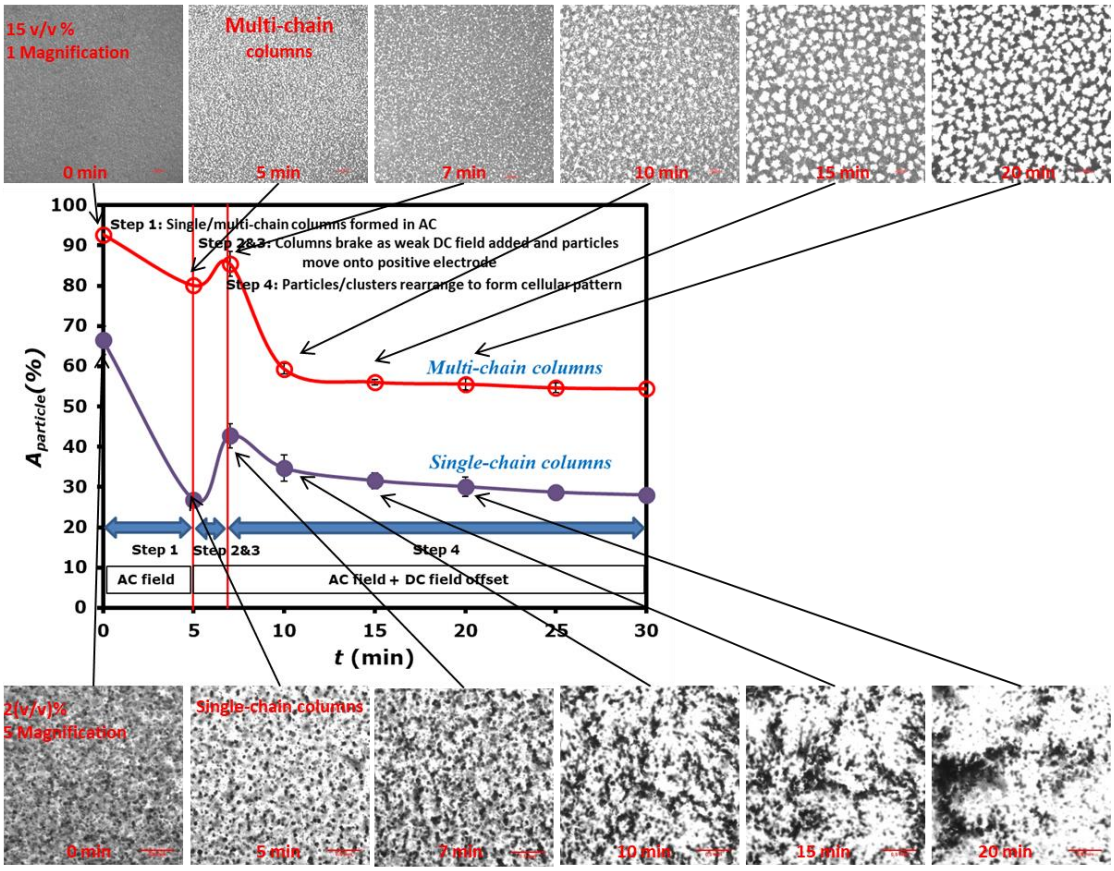

Figure 3.76 Three-step formation of cellular patterns in 2 v/v% and 15 v/v% suspensions of polyethylene particles (40-48 μm) in Envirotemp FR3 oil following the application of AC field 1.5 kV/mm, 100 Hz and adding DC field 0.03 kV/mm. A sample cell 1.5"×1.5" with the interelectrode gap 0.5 mm for 2 v/v% and 2 mm for 15 v/v%; top electrode energized, bottom grounded; particles black, particle-free regions white.

3.5.10 Three-step 3D -> 3D Formation of Cellular Patterns

3.5.10.1 Forming particle chains and columns in Step 1. ImageJ software was used to measure the radius of columns in images taken in the plane parallel to electrodes. Measurements of the ratio between the column size R_{agg} and the particle radius a, $n = R_{agg}/a$, formed by applying AC field 1.5 kV/mm, 100 Hz for 5 min (Step 1 end) to suspensions of polyalphaolefin ($2a \approx 5\ \mu m$) and polyethylene particles ($2a \approx 48\ \mu m$) in Envirotemp FR3 oil are presented in Figure 3.77. Columns defined as single-chain for $n < 1.4$ and multi-chain for $n > 1.4$. Data set presented in this figure show that increasing the

size of the interelectrode gap and the particle concentration facilitates formation of multi-particle columns.

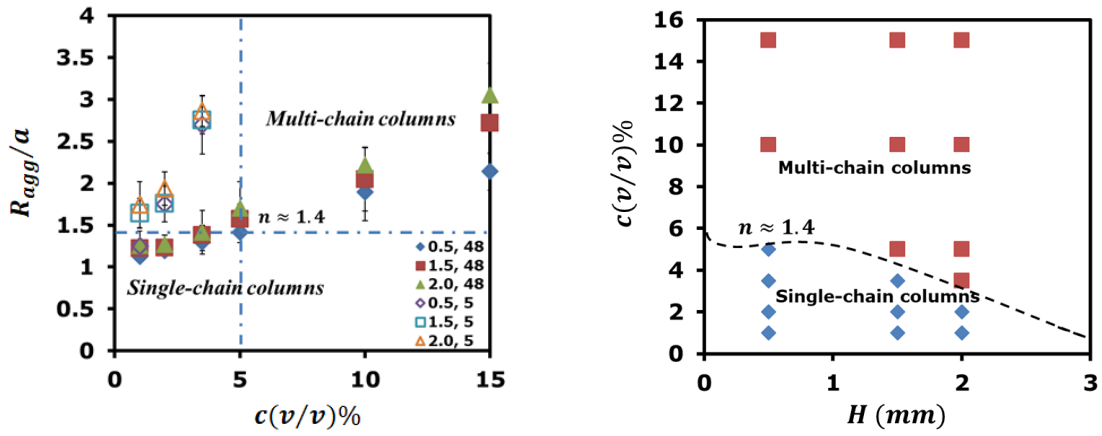

Figure 3.77 Left: Concentration $c(v/v)\%$ dependence of the ratio between the column size and the particle radius, $n = \mathrm{R_{agg}}/a$, for suspensions of polyalphaolefin ($2a \approx 5\ \mu m$) and polyethylene particles ($2a \approx 48\ \mu m$) in Envirotemp FR3 oil formed by applying AC field 1.5 kV/mm, 100 Hz for 5 min. Sample cell 1.5"×1.5", interelectrode gap *H* in mm listed; top electrode energized, bottom grounded. Images taken in the plane parallel to electrodes. Columns defined as single-chain for $n < 1.4$ and multi-chain for $n > 1.4$. Right: Map "particle concentration – interelectrode gap" for the appearance of single-chain and multi-chain columns.

3.5.10.2 Forming cellular pattern in Steps 2 and 3. ImageJ software was used to measure the area covered by particles in the plane parallel to the electrodes (Figure 3.76). Using the Analysis of Variance (ANOVA), we found that a difference between values of the area fraction covered by particles at the end of Steps 1 and 3 is statistically insignificant for suspensions of polyethylene particles (40-48 μm) in Envirotemp FR3 oil when the particle concentration is below 5 v/v%. This range of concentrations is associated with formation of single-particle columns (Figure 3.77). For the particle concentrations within 5-15 v/v% that is associated with formation of multi-chain columns (Figure 3.77), the value of the area fraction covered by particles at the end of Steps 3 is smaller than that at the end of

Step 1. That fact demonstrates that multi-chain columns shrink in the course of forming particle-free domains.

3.5.10.3 Morphology of Cellular Pattern. ImageJ software was used to find the mean radius of particle-free domains R_f and the thickness of a particle-rich wall between two nearest neighboring domains in experiments conducted on suspensions of polyalphaolefin (4-5μm) and polyethylene particles (40-48μm) in Envirotemp FR3 oil (Figure 3.78). Measurements presented in Figure 3.78(a) show that R_f increases with increasing the particle size and the gap size. Increasing the particle concentration up to 5 v/v% causes R_f to decrease. However, the effect of the particle concentration on R_f becomes insignificant beyond 5 v/v% where multi-particle columns prevail. The ratio between the radius of particle-free domains and the thickness of the particle-rich wall decreases with increasing the particle concentration (Figure 3.78(c)). It drops down to about 1.5 within the region where single-columns prevail. However, it is less pronounced within the region where multiple-columns prevail.

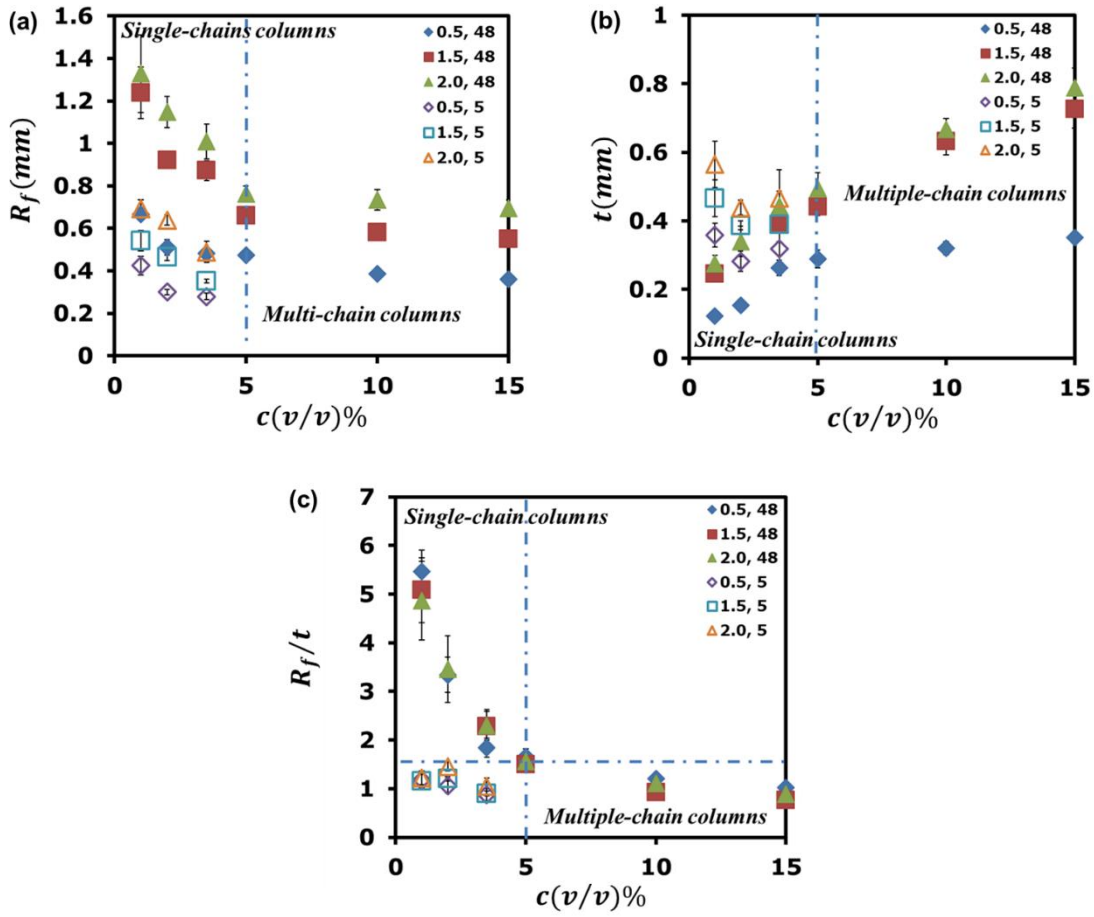

Figure 3.78 Cellular patterns formed in suspensions of polyalphaolefin ($2a \approx 5\ \mu m$) and polyethylene particles ($2a \approx 48\ \mu m$) in Envirotemp FR3 oil formed by applying AC field 1.5 kV/mm, 100 Hz for 5 min and then adding DC field 0.03 kV/mm for 30 min. Sample cell 1.5"×1.5", interelectrode gap H in mm listed; top electrode energized, bottom grounded. Images taken in the plane parallel to electrodes. (a) The mean radius of particle-free domains R_f in mm, (b) the thickness of particle-rich walls t in mm, (c) the ratio between the radius of particle-free domains and the thickness of the particle-rich wall R_f/t, as a function of particle volume concentration $c(v/v)\%$.

3.5.11. Radial and Orientation Distribution of Particle-free Domains

The 2D radial distribution function (or pair correlation function) $g(r)$ of particle-free domains in a cellular pattern describes how the number density of domains varies with distance r from a reference domain: $g(r) = \Delta N(r)/2\pi r \rho_{average} \Delta r$, where $\Delta N(r)$ is the number of centers of domains within a circular shell of radii r and $r + \Delta r$, $\rho_{average} =$

N/S_{area} is the average number of particle-free domains per unit area (Figure 3.79). ImageJ software was used to measure parameters needed for computing $g(r)$. Computations of $g(r)$ were conducted with homemade code by Matlab. The ratio between the shell width Δr used in these calculations and the average domain radius R_f was taken 0.25 for all experiments due to the low sensitivity of $g(r)$ to variations of $\Delta r/R_f$ from 0.2 to 0.33.

To explore the orientation distribution of particle-free domains in cellular pattern, the 2D six-fold bond-orientation order parameter was computed: $\varphi_6 =< exp(6i\theta) >$, where θ is the angle between a fixed axis and the line connecting the nearest neighboring particle-free domains. A schematic in Figure 3.80 illustrates the definition of the nearest neighbors to compute the orientation order parameter. Averaging is performed over all pairs of the nearest neighboring particles on the image. φ_6 is equal to one if centers of particle-free domains form a hexagonal grid and to zero if centers of particle-free domains are randomly arranged [134].

The radial distribution functions of particle-free domains in different cellular patterns formed in our experiments are shown in Figure 3.81. The position of the first peak (PFP) of $g(r)$ represents the ratio of the average separation distance between centers of neighboring particle-free domains and the average domain radius R_f. Oscillations of $g(r)$ around one indicate randomly uniform distribution of center position of particle-free domains that locations of enhanced and reduced probability of finding centers of two particle-free domains at a certain distance. The presented plots demonstrate that the ratio of the separation distance between centers of neighboring particle-free domains and the domain radius R_f (position of the first $g(r)$ peak, PFP) does not vary with increasing the interelectrode gap and increases with increasing the particle concentration. On the other

hand, the average domain radius R_f increases with increasing the interelectrode gap and decreases with increasing the particle concentration. These trends are more pronounced for dilute suspensions where single-chain columns prevail.

Figure 3.82 demonstrates plots of $g(r)$ computed for a cellular pattern formed in our experiments in 10 v/v% suspension of polyethylene particles (53-75μm) in Mazola oil by applying AC field 1.5 kV/mm, 100 Hz for 5 min and then adding DC field 0.03 kV/mm for 30 min. For comparison, $g(r)$ were also computed for cellular patterns formed in experiments by Kumar et al. [113] and Yethiraj et al [114]. As can be seen in Figure 3.82, the position of first peaks from radial distribution functions computed for cellular patterns observed in our experiments and experiments by Kumar et al. [113] and Yethiraj et al [114] are consistent. Figure 3.81 and 3.82 show that $\varphi_6 \sim 0.3 - 0.4$ for cellular patterns formed in our experiments as well as for experiments by Kumar et al. [113] and Yethiraj et al [114]. It indicates the presence of angular correlation among particle-free domains.

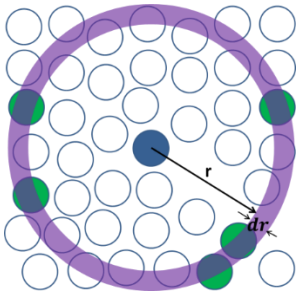

Figure 3.79 Calculation of radial distribution function g(r).

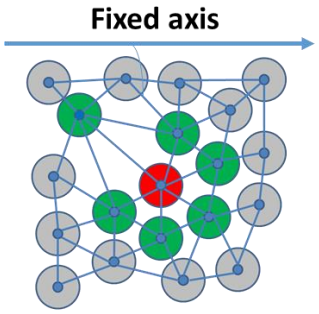

Figure 3.80 The Delaunay definition of nearest neighbors: the nearest neighbors of the red circle are highlighted in green to compute the six-fold bond-orientation order parameter φ_6
Source: [135].

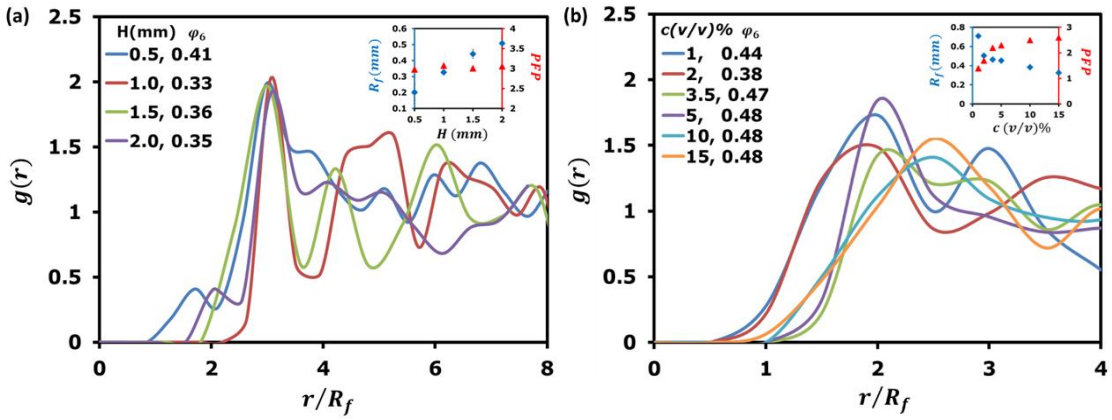

Figure 3.81 Basic characteristics of a cellular pattern. Radial distribution function *g(r)* and six-fold bond-orientation order parameter φ_6 of particle-free domains for the cellular patterns formed in (a) 15 v/v% suspensions of polyethylene particles (53-75μm) in Mazola oil for different interelectrode gaps *H*, mm; inset shows average domain radius R_f and the position of the first peak (*PFP*) vs. *H*; (b) suspensions with different volume concentrations *c(v/v)%*, interelectrode gap 0.5mm; inset shows R_f and the position of the first peak (*PFP*) vs. *c(v/v)%*. Sample cell 1.5"×1.5", top electrode energized, bottom grounded; AC field 1.5 kV/mm, 100 Hz applied for 5 min with then adding DC field 0.03 kV/mm for 30 min.

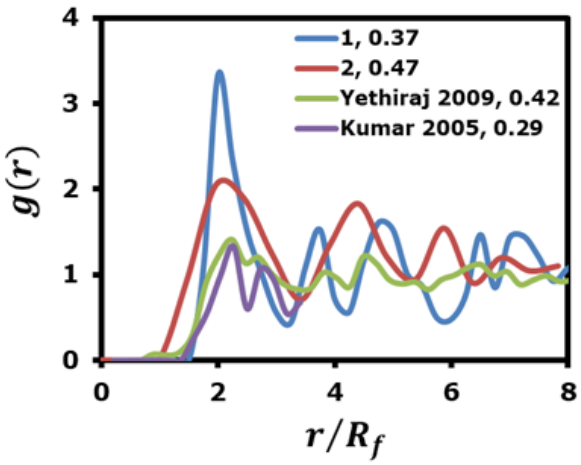

Figure 3.82 The radial distribution function *g(r)* of particle-free domains for the cellular pattern formed in 10v/v% suspension of polyethylene particles (53-75μm) in Mazola oil, sample cell 1.5"×1.5" with the interelectrode gap $H = 1mm$ and $H = 2mm$ listed, top electrode energized, bottom grounded; AC field 1.5 kV/mm, 100 Hz for 5 min with then adding DC field 0.03 kV/mm for 30 min. R_f is the average domain radius. In addition, the plotted are the radial distribution functions computed for cellular patterns formed in experiments by Kumar et al. ($c = 2\, v/v\%\,, H = 1.8mm$) [113] and Yethiraj et al. ($c = 0.6\, v/v\%\,, H = 0.1mm$) [114]. Six-fold bond-orientation order parameter φ_6 are also listed in figure.

3.5.12 Nucleation and Growth of Particle-Free Domain

Experiments were carried out on 5-15 v/v% suspensions of polyethylene (53-75μm) particles and 0.5 – 3.5 v/v% polyalphaolefin (75-90μm) particles in Mazola oil. The top electrode was always energized and the bottom was grounded. Three different arrangements of glass electrodes were tested: electrodes placed such that their conducting ITO layers were in direct contact with a suspension, only the top electrode had its conducting layer in direct contact with a suspension, conducting layers of both electrodes were not in direct contact with a suspension. Experiments were first conducted for the case when conducting layers of both electrodes were placed in direct contact with a suspension. When the top electrode or both electrodes were not in direct contact with the suspension, AC and DC voltages applied to the electrodes were computed to maintain the same field

strength as that in the case of both electrodes having conducting layers in direct contact with the suspension. Calculation of voltages was conducted using measurements of the complex permittivity of the suspension and electrodes.

High-magnification images in Figure 3.83(a) show the growth of a particle-free domain in 5% polyethylene particles (53-75 μm) in Mazola oil that was in direct contact with conducting layers of both electrodes. Low magnification of the objective was used when a strong high frequency AC field was applied to form chains and columns across the gap between electrodes. Once adding a weak DC field initiated the appearance of nuclei of particle-free domains, the objective was focused on a single nucleus and magnification was increased to record its growth. Plots presented in Figure 3.83(b) show that the arrangement of conducting layers of electrode does not influence the nucleus growth.

The growth rate of the average radius of particle-free domains initiated by applying a weak DC field is well approximated by the expression (3.19) (Figure 3.84 (a)):

$$R_f^2/R_{f\infty}^2 = 1 - \exp[-G^2(t-t_0)^2/R_{f\infty}^2] \text{ for } t > t_0 \qquad (3.19)$$

where t_0 is the incubation time that refers to the time when nuclei were first observed, G is its initial linear growth rate, and $R_{f\infty}$ is the plateau value of the domain radius. The growth rate was slowing down when neighboring particle-free domains approached each other (Figure 3.84 (a) and (b)). Data sets presented in Figure 3.84 (c) and (d) show that the values of the initial growth rate G are lying within the range $3 - 180\,\mu m/s$, increasing with raising the AC field strength and reducing the particle concentration. The incubation time was about $t_0 = (3 \pm 1)min$ for all experiments with conducting layers of both

electrodes placed in direct contact with a suspension and about $t_0 = (8 \pm 1)min$ when conducting layers of both electrodes were not in direct contact with a suspension.

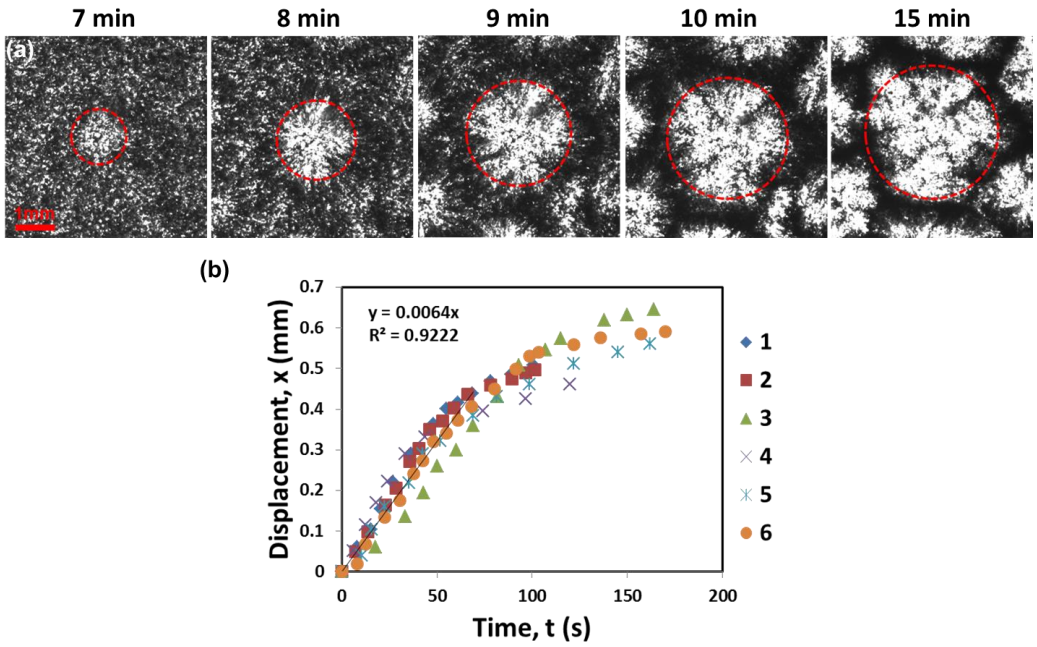

Figure 3.83 Growth of particle-free domains in 5 v/v% suspensions of polyethylene particles (53-75μm) in Mazola oil initiated by adding DC field 0.03 kV/mm after exposure to AC field, 100 Hz for 5 min, sample cell 1.5" x 1.5", interelectrode gap 2 mm: (a) conducting layers of both electrodes in direct contact with suspension, AC field 1.5 kV/mm, DC field 0.03 kV/mm; (b) two runs for every arrangement of conducting layers on electrodes: 1 and 2, both layers in direct contact with suspension, AC field 1.5 kV/mm, DC field 0.03 kV/mm; 3 and 4, layer of top electrode not in direct contact with suspension, AC field 1.88kV/mm, DC field 0.038 kV/mm; 5 and 6, layers of both electrodes not in direct contact with suspension, AC field 2.25 kV/mm, DC field 0.045 kV/mm. Initial slope computed using all data yields 6.5μm/s.

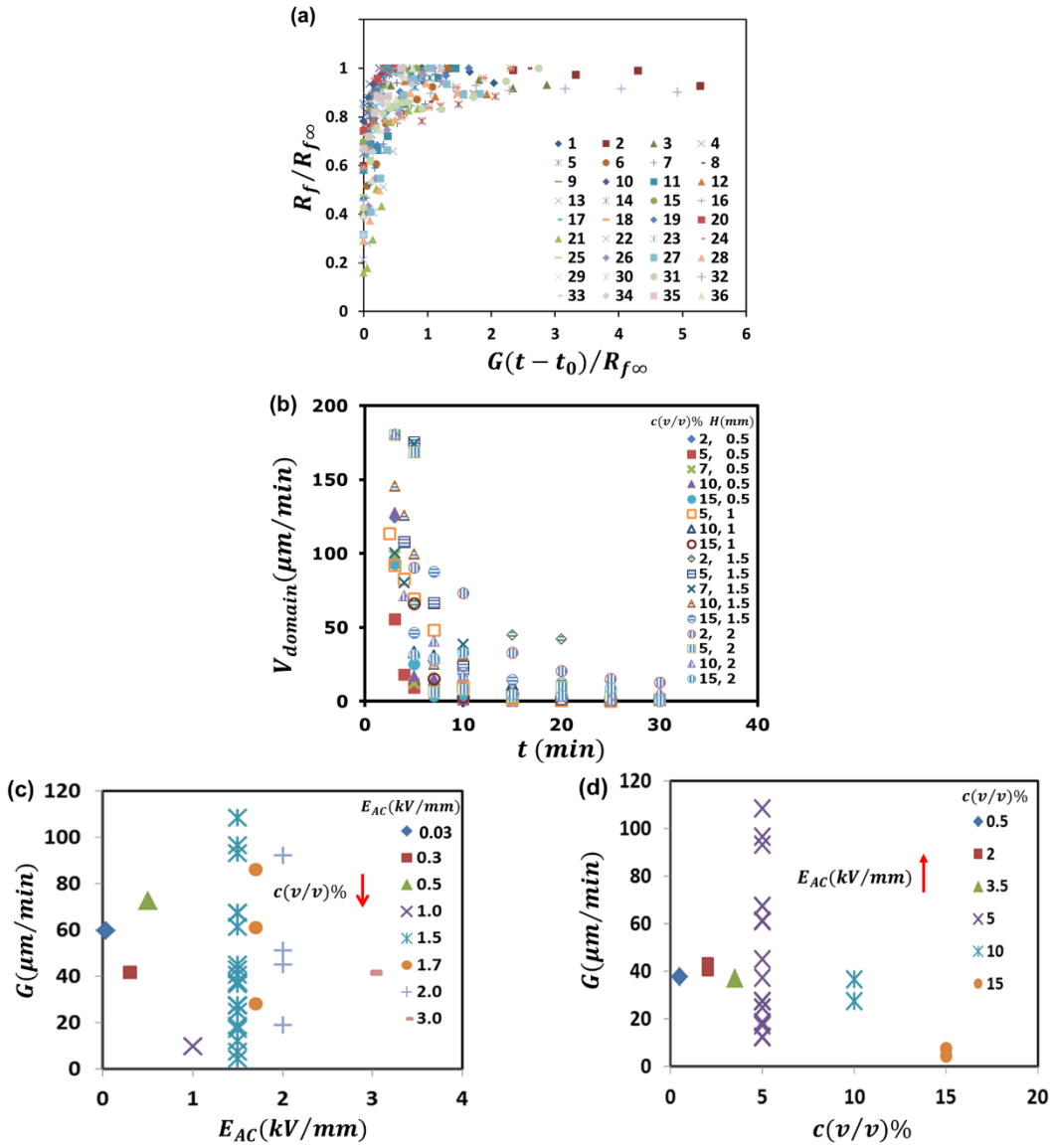

Figure 3.84 Growth of particle-free domains in 5-15 v/v% suspensions of polyethylene (53-75μm) particles and 0.5 – 3.5 v/v% polyalphaolefin (75-90μm) particles in Mazola oil initiated by adding DC field after exposure to AC field for 5 min, sample cell 1.5" x 1.5", conducting layers of both electrodes in direct contact with suspension: a) data on the domain growth for different particles, particle volume fractions, gap size, AC and DC fields listed in Table 3.12; b) velocity of the domain growth $V_{domain}(\mu m/min)$ in suspensions of polyethylene (53-75μm) particles for different particle concentration $c(v/v)\%$ and gap H,mm listed in figure by adding DC field 0.03 kV/mm after exposure to AC field 1.5 kV/mm, 100 Hz for 5 min. Data on initial growth rate $G(\mu m/min)$ for c) suspensions No. listed in Table 3.13 and d) suspensions No. in Table 3.14.

Table 3.12 Data on the Domain Growth for Figure 3.84(a)

Suspension No.	Particle	Particle size (um)	c(v/v)%	H (mm)	E_{AC} (kV/mm)	V (kHz)	E_{DC} (kV/mm)
1, 2, 3	Polyalphaolefin	75-90	0.5, 2, 3.5	2	1.5	0.1	0.03
4, 5, 6	Polyethylene	53-75	5, 10, 15	2	1.5	0.1	0.03
7, 8, 9, 10, 11, 12	Polyethylene	53-75	5	2	0.03, 0.3, 0.5, 1, 2, 3	0.1	0.03
13, 16	Polyethylene	53-75	5	2	1.5	0.1	0.02, 0.05
14, 15, 17	Polyethylene	53-75	5	2	1.5	0.001, 0.0001, 1	0.03
18, 19	Polyalphaolefin	75-90	0.5, 2	1.5	1.5	0.1	0.03
20 ,21, 22, 23,	Polyethylene	53-75	5, 7, 10, 15	1.5	1.5	0.1	0.03
24, 25	Polyethylene	53-75	2, 10	1	1.5	0.1	0.03
26, 27, 28	Polyalphaolefin	75-90	0.5, 2, 3.5	0.5	1.5	0.1	0.03
29, 30, 31, 32	Polyethylene	53-75	5, 7, 10, 15	0.5	1.5	0.1	0.03
33, 35	Polyalphaolefin	75-90	2	0.1, 0.2	1.5	0.1	0.03
34, 36	Polyethylene	53-75	10	0.1, 0.2	1.5	0.1	0.03

Table 3.13 Data on the Domain Growth for Figure 3.84(c)

E_{AC}(kV/mm)	Particle	Particle size(um)	c(v/v)%	H(mm)	v(kHz)	E_{DC}(kV/mm)
0.03	Polyethylene	53-75	5	2	0.1	0.03
0.3	Polyethylene	53-75	5	2	0.1	0.03
0.5	Polyethylene	53-75	5	2	0.1	0.03
1	Polyethylene	53-75	5	2	0.1	0.03
1.5	Polyalphaolefin	75-90	0.5, 2, 3.5	2	0.1	0.03
1.5	Polyethylene	53-75	5, 10, 15	2	0.1	0.03
1.5	Polyalphaolefin	75-90	0.5, 2	1.5	0.1	0.03
1.5	Polyethylene	53-75	5, 7, 10, 15	2	0.1	0.03
1.7	Polyethylene	53-75	5, 10, 15	2	0.1	0.03
2	Polyethylene	53-75	5, 7, 10, 15	2	0.1	0.03
3	Polyethylene	53-75	5	2	0.1	0.03

Table 3.14 Data on the Domain Growth for Figure 3.84(d)

c(v/v)%	Particle	Particle size(um)	H (mm)	E_{AC} (kV/mm)	v(kHz)	E_{DC} (kV/mm)
0.5	Polyalphaolefin	75-90	2	1.5	0.1	0.03
2	Polyalphaolefin	75-90	1.5,2	1.5	0.1	0.03
3.5	Polyalphaolefin	75-90	2	1.5	0.1	0.03
5	Polyethylene	53-75	2	0.03, 0.3, 0.5, 1, 1,5, 1.7 ,2,3	0.1	0.03
10	Polyethylene	53-78	2	1.5, 2	0.1	0.03
15	Polyethylene	53-75	2	1.5, 2	0.1	0.03

3.5.13 Formation of Cellular Pattern throughout the Interelectrode Gap

In previous sections, we showed that the combination of a strong high frequency AC electric field a relatively weak DC field caused a suspension of negatively polarized polyethylene and polyalphaolefin particles to form a cellular pattern of large particle-free domains across the interelectrode gap that were surrounded by particle-rich walls. Furthermore, this cellular pattern formed regardless whether a DC field was applied simultaneously with a strong AC field or later.

We now consider the formation of a cellular pattern when a weak DC field was applied first and a strong AC field was added later. Images in Figure 3.85 illustrate the formation of a cellular pattern in 5 v/v% suspension of polyethylene particles in Mazola oil by applying DC field 0.03 kV/mm and then adding AC field 1.5 kV/mm, 100 Hz. The application of the DC field for 30 min caused particles to move towards the top energized electrode to form multi-particle layers without bridging interelectrode gap. Nuclei of particle-free stripes and domains appeared there and grew slowly in the plane parallel to this electrode (Figure 3.85). A long exposure to the DC field caused the particles to form particle-free islands surrounded by particle-rich walls close to the top positive electrode (Figure 3.86). Once a strong AC field 1.5 kV/mm, 100 Hz was added, particle-rich walls began to grow eventually bridging the interelectrode gap. Images presented in Figure 3.87

and Figure 3.88 demonstrate this rapid transformation in 15 v/v% and 5 v/v% suspension of polyethylene particles in FR3 oil. The application of a strong high-frequency AC field did not destroy a set of particle-free islands formed close to the positive electrode. It just caused the particle-rich walls to grow away from the electrode and span the interelectrode gap. Images presented in Figures 3.85-3.88 indicate that raising the particle concentration in a suspension and reducing the size of interelectrode gap accelerate a 2D ->3D transformation but do not change substantially the morphology of a cellular pattern of particle-free domains across the gap between electrodes.

The schematic diagram presented in Figure 3.89 summarizes our observations on three-step processes that cause the particles to form a cellular pattern of particle-free domains across the interelectrode gap following the application of a weak DC field and then a strong high frequency AC field. We will henceforth refer to this transformation as 2D->3D to differentiate it from the formation of a cellular pattern when a strong high frequency AC field is firstly applied. The first step employs a weak DC field (Figure 3.89) to form multi-particle layers close to the positive electrode without bridging the interelectrode gap. The second step is associated with the particle rearrangement to form slowly growing particle-free stripes/domains close to the positive electrode, thereby reducing the area fraction covered by the particles in the plane parallel to the electrodes decreases. The third step is initiated by adding a strong high frequency AC that causes the particle-rich walls to shrink and grow away from the positive electrodes. Accordingly, the area fraction covered by the particles in the plane parallel to the electrodes continues to decrease. This process eventually forms a cellular pattern of particle-free domains spanning the gap between electrodes.

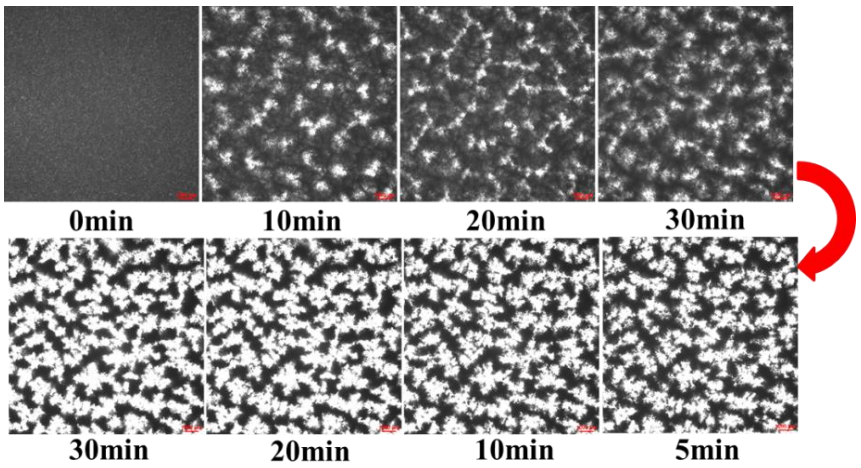

Figure 3.85 Patterns formed in a 5 v/v % suspension of polyethylene particles (53-75 μm) in Mazola oil; particles black, particle-free regions white; ITO conducting layers of both electrodes in direct contact with the suspension; top electrode energized, bottom grounded, interelectrode gap 2mm. Top: DC field 0.03kV/mm applied for 30min. Bottom: AC field 1.5kV/mm, 100 Hz added to the DC field. Scale bar 0.1mm.

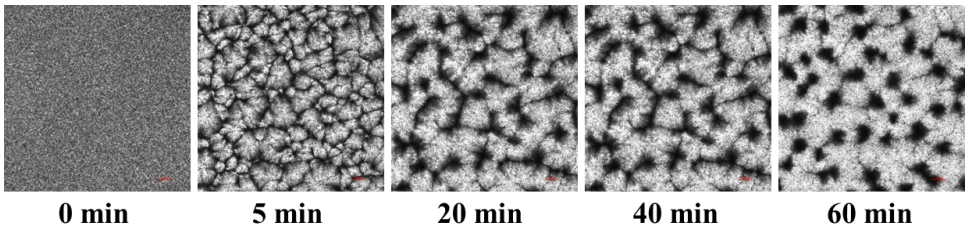

Figure 3.86 Patterns formed in a 2 v/v % suspension of polyethylene particles (40-48 μm) in FR3 oil; particles black, particle-free regions white; ITO conducting layers of both electrodes in direct contact with the suspension; top electrode energized, bottom grounded, interelectrode gap 1.5mm. DC field 0.03 kV/mm applied for 60mins. Scale bar 0.1mm.

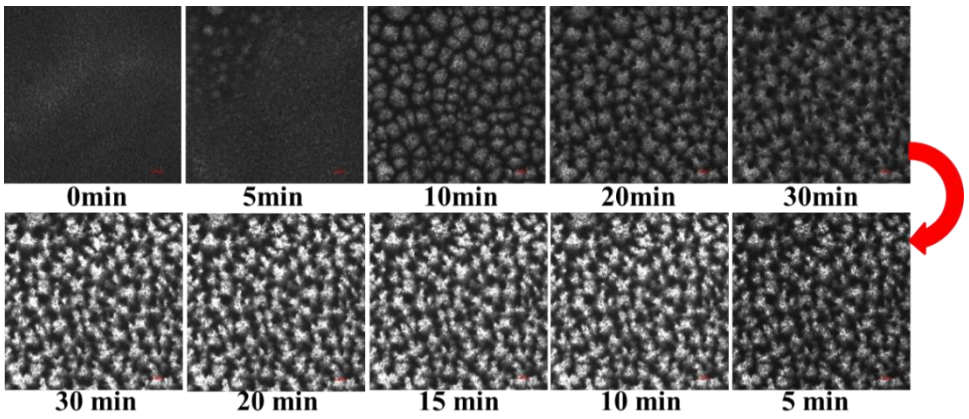

Figure 3.87 Patterns formed in a 15 v/v % suspension of polyethylene particles (40-48 μm) in FR3 oil; particles black, particle-free regions white; ITO conducting layers of both electrodes in direct contact with the suspension; top electrode energized, bottom grounded, interelectrode gap 0.5mm. Top: DC field 0.03kV/mm applied for 30min. Bottom: AC field 1.5kV/mm, 100 Hz added to the DC field. Scale bar 0.1mm.

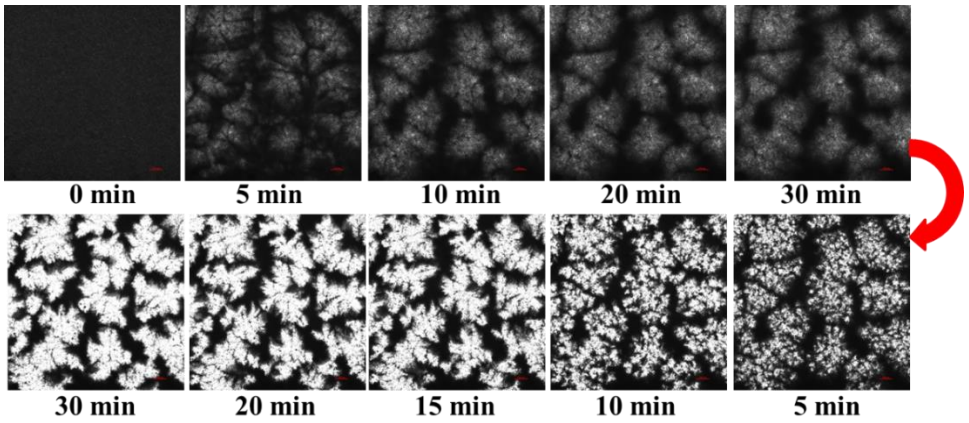

Figure 3.88 Patterns formed in a 5 v/v % suspension of polyethylene particles (40-48 μm) in FR3 oil; particles black, particle-free regions white; ITO conducting layers of both electrodes in direct contact with the suspension; top electrode energized, bottom grounded, interelectrode gap 2mm. Top: DC field 0.03kV/mm applied for 30min. Bottom: AC field 1.5kV/mm, 100 Hz added to the DC field. Scale bar 0.1mm.

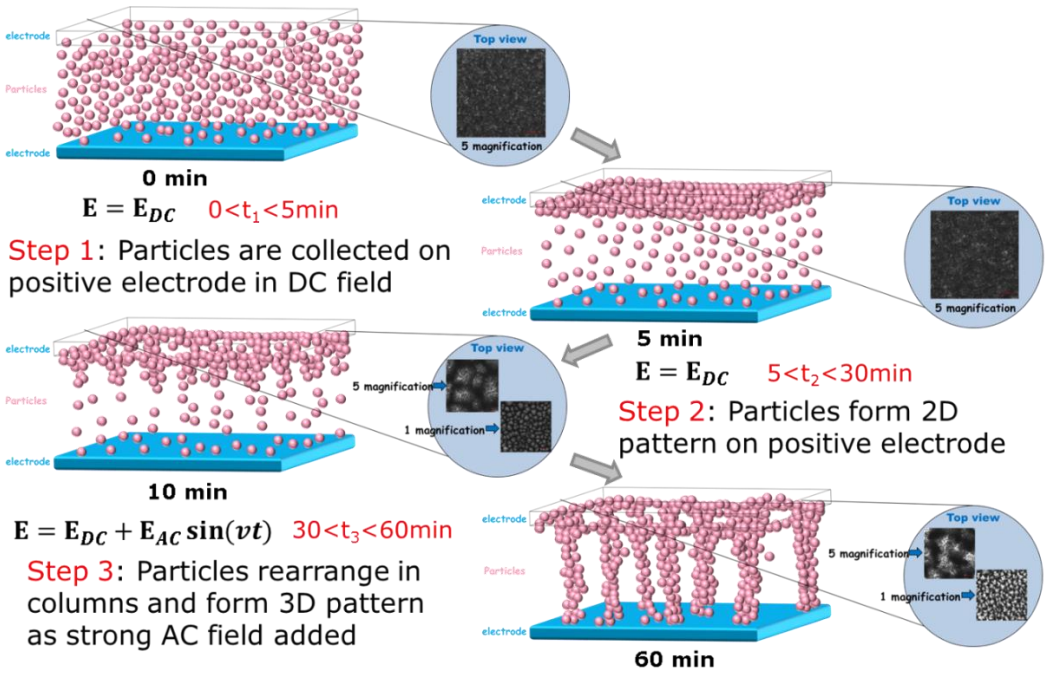

Figure 3.89 Schematics of 2D −> 3D transformation with typical durations of events to form a cellular pattern of particle-free domains across the interelectrode gap in a suspension by applying a weak DC field and then a strong high frequency field.

3.5.13.1 Percolation and connectivity. SoilJ software was used to calculate the number of percolating and non-percolating particle-rich wall/islands and the number of percolating and non-percolating particle-free domains on images acquired in the course of 2D ->3D transformation of a cellular pattern for different particle concentrations and interelectrode gaps. Figure 3.90 shows the number of percolating and non-percolating particle-rich wall/islands as a function of the area fraction covered by particles and the number of percolating and non-percolating particle-free domains as a function of the area fraction covered by solvent. The number of individual particle-rich wall/islands dramatically decreases with the increasing the area fraction of particles as small particle clusters merge into dominant clusters forming the percolating network. A box-and-whisker plot in Figure 3.91 shows the area fractions covered by particles and solvent within and out of the

percolating network between the top and bottom sides of the image. Figure 3.92 shows the area fraction of particle-rich walls and particle-free domains in the networks connecting the top and bottom sides of the image as a function of the area fraction covered by a) particles and b) solvent. The presented results indicate that the threshold to form the percolating network of particle-rich walls occurred when the area fraction covered by particles approaches 40%. Direct calculation of the threshold to form the percolating network of particle-free domains between the top and bottom sides of the image yields a consistent value of 60% for the area fraction covered by solvent.

Plots on Figure 3.93 show the area fraction covered by particles and solvent for 2D->3D transformation of cellular patterns formed in 2-15v/v% suspensions and different interelectrode gaps 0.5-2.0 mm. They demonstrate that increasing the particle concentration and the interelectrode gap facilitates from a set of individual particle-free domains surrounded by particle-rich walls to percolating networks of particle-free domains and particle-rich walls. Images of patterns in Figure 3.94 and 3.95 illustrate this trend to find a threshold of the transition from a set of individual particle-rich walls/islands to a percolating network of particle-rich walls as a function of the particle volume fraction and the size of the interelectrode gap.

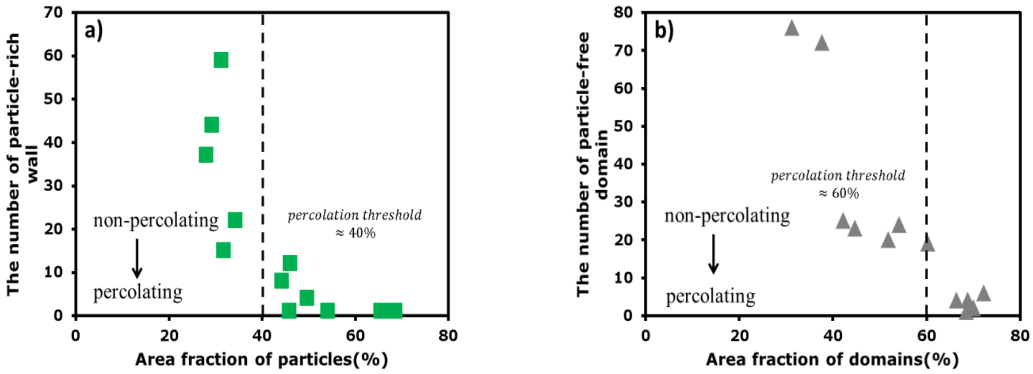

Figure 3.90 Morphology of cellular patterns. a) the number of particle-rich wall/islands as a function of the area fraction covered by particles; b) the number of particle-free domains as a function of the area fraction covered by solvent for 2D->3D transformation of the cellular pattern. Experiments conducted on suspensions of polyethylene particles (40-48µm) and (53-75µm) in Mazola oil and Cargill Envirotemp FR3 oil for different interelectrode gaps 0.5-2.0mm. DC field 0.03kV/mm applied in first 30 min and then the AC field 1.5 kV/mm, 100 Hz was added for 30min.

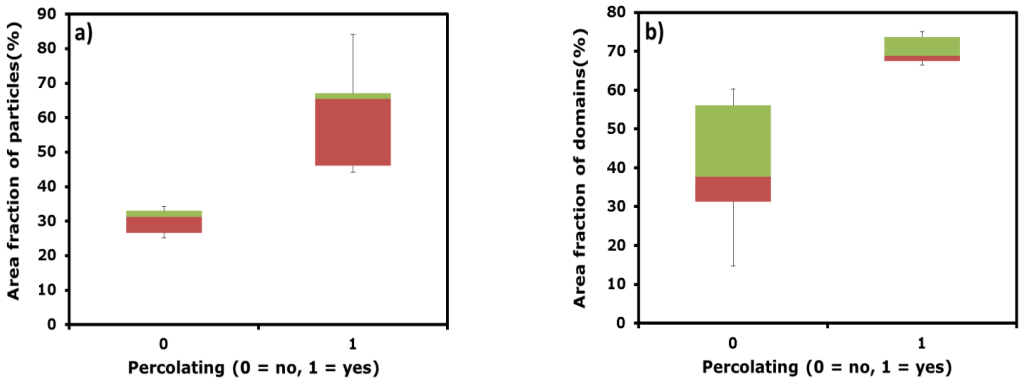

Figure 3.91 A box-and-whisker plot shows the area fraction of a) particles and b) solvent within and out of percolating network.

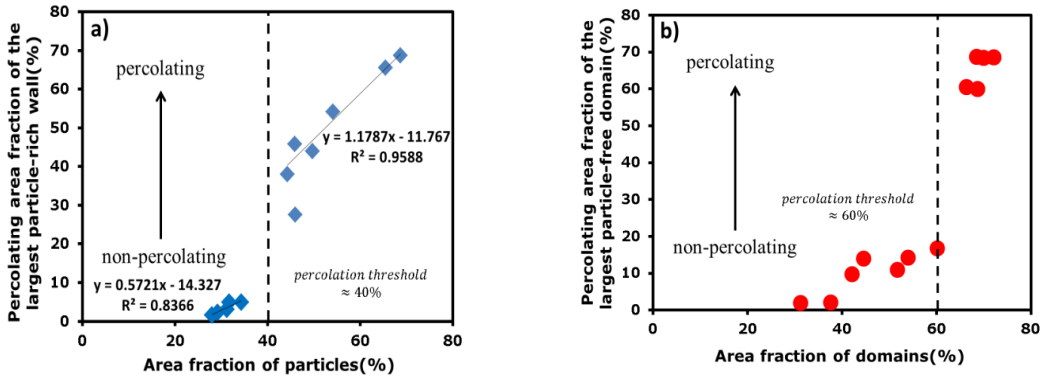

Figure 3.92 The fraction of particle-rich walls and particle-free domains in the networks connecting the top and bottom sides of the image as a function of the area fraction covered by a) particles and b) solvent.

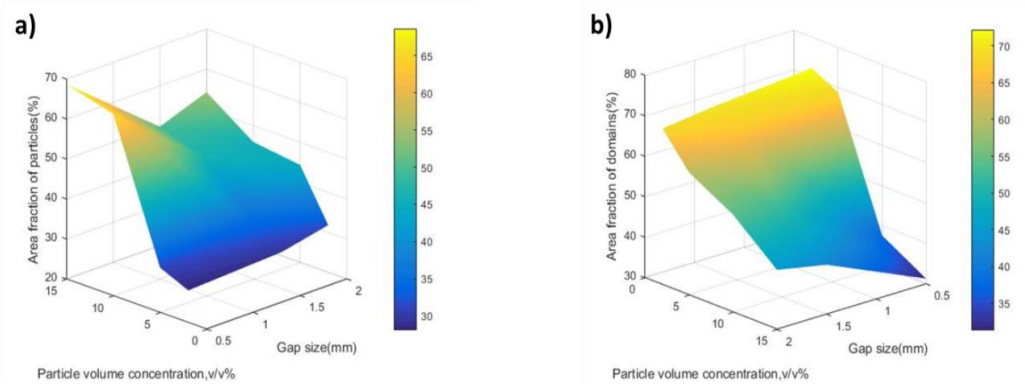

Figure 3.93 The area fraction covered by (a) particles and (b) solvent for 2D->3D transformation of cellular patterns in 2-15v/v% suspensions and different interelectrode gaps 0.5-2.0mm. (a) Colors represent the area fraction of particle-rich wall/island; a percolation threshold around 40% mm^2/mm^2 for the area fraction covered by particles. (b) Colors represent the area fraction of particle-free domains, a percolation threshold around 60% mm^2/mm^2 for the area fraction covered by solvent. AC field 1.5kV/mm, 100 Hz; DC field 0.03 kV/mm.

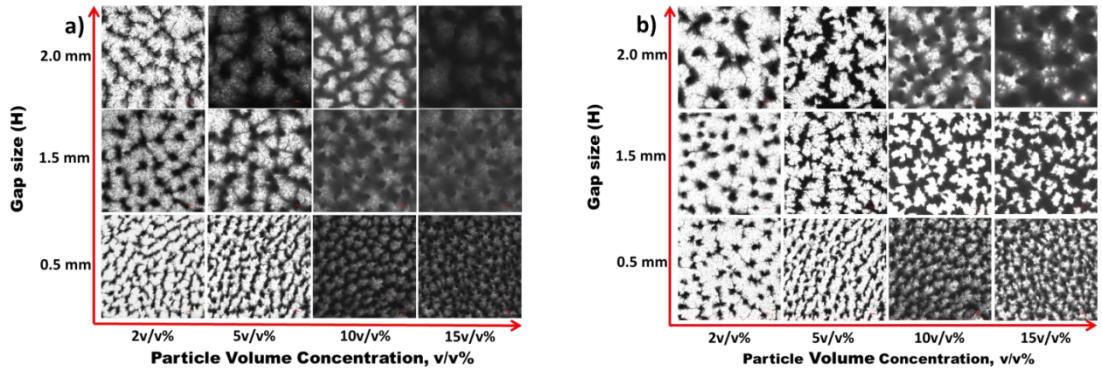

Figure 3.94 Images of cellular patterns formed in 2v/v%-15v/v% suspensions of polyethylene particles (40-48 μm) in FR3 oil in interelectrode gaps 0.5mm-2.0mm. (a) DC field 0.03 kV/mm applied for 30 min. (b) AC field 1.5 kV/mm, 100 Hz added for 30 min. Particle-rich wall/islands/clusters in black, particle-free domains in white.

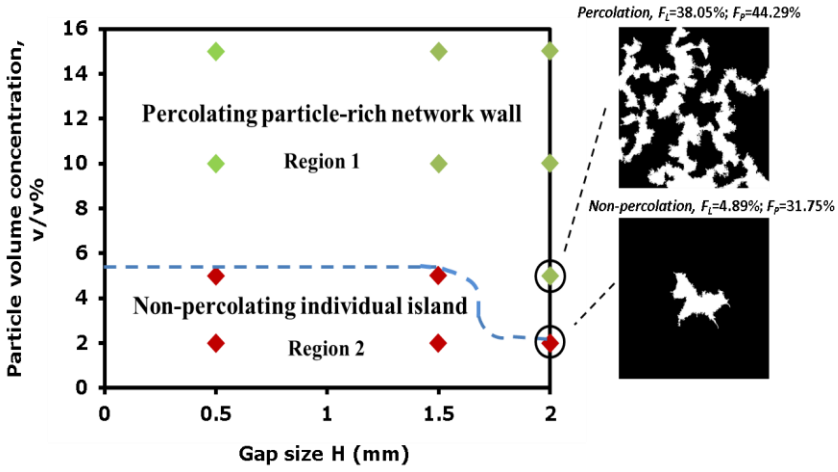

Figure 3.95 Threshold of a transition from a set of individual particle-rich walls/islands (red symbol) to a percolating network of particle-rich walls (green symbol) as a function of the particle volume fraction and the size of the interelectrode gap. White color in images show particle-rich regions in an image.

3.5.14 Comparison of 2D->3D and 3D->3D Transformations

We now compare in more detail the behavior of particles caused by applying three combinations of electric fields. 1) A weak DC field added to a strong high frequency AC field after 5 min; 2) A strong high frequency AC field added to a weak DC field after 30min;

3) Both strong high frequency AC and weak DC fields applied simultaneously. Cellular patterns formed by these combinations of electric fields in 5v/v% suspensions of polyethylene particles (40-48μm) in Envirotemp FR3 oil are shown in Figures 3.96 and Figure 3.97 for 0.5 mm and 2.0 mm gaps, respectively.

Once a weak DC electric field was applied, particles moved towards the positive electrode forming thick multi-layered aggregates/clusters situated on this electrode. Following the exposure to the DC field for about 30 min, nuclei of particle-free domains appeared in a region close to the electrode. The nuclei grew in the plane parallel to the electrode while the bulk of particles were slowly rearranging into a network of interconnected particle-rich walls. However, a few particles remained in the central part of these domains. Once a strong AC electric field added, particles situated inside domains moved away from the positive electrode and joined particle-rich walls growing towards the other electrode. This process ended up by forming a set of particle-free domains across the entire interelectrode gap.

In contrast, when the AC electric field was applied first, particles began to align rapidly along the field direction, rapidly forming chains and then columns spanning the interelectrode gap. These chains and columns remained uniformly distributed in the plane parallel to electrodes. When a weak DC field was added, the chains and columns partially broke down, widened and started moving towards the positive electrode, bringing one end to this electrode and disconnecting the other end from the negative electrode. Within next 20 min, these loose chains and columns began moving radially outward gradually rearranging into particle-rich walls and creating particle-free domains across the entire gap

between electrodes. The formation of a cellular pattern of particle-free domains ended up in about 30 min.

Comparison of 2D-> 3D and 3D->3D transformations indicates that nucleation of particle-free domains is triggered by repulsion of thick particle aggregates/clusters for the former and loose chains and columns formed across the interelectrode gap for the former. Both mechanisms operate when strong AC and weak DC fields are applied together. The critical feature in all three cases is the ability of fibrillose particle structures to slide in the plane parallel to the electrodes.

The mean radius of particle-free domains, the mean thickness of particle-rich walls and their ratio in the formed 3D structures as a function of the interelectrode gap size for the 5 v/v% suspension are presented in Figures 3.98 (a, b and c). Plots in Figures 3.99 (a, b) show the mean radius of particle-free domains and the ratio between the mean radius of particle-free domains and the mean thickness of particle-rich walls as a function of the particle volume fraction for three gap sizes. Both the average particle-free domain radius and the particle-rich thickness are found to increase with increasing the gap between electrodes and decrease with raising the particle concentration. Both are the largest when the DC field was applied first and both are the smallest when the AC field was applied first. However, their ratio is not affected by the sequence in which AC and DC fields were applied. It is solely determined by the gap size and the particle concentration, gradually decreasing to a plateau with increasing the gap size and the particle concentration. Changes in the average radius of particle-free domains and in the ratio between the particle-free domain radius and the particle-rich wall thickness are more pronounced for dilute suspensions where the formation of single-chain columns prevail.

Plots in Figure 3.100 show the solidity of particle-free domains as a function of the particle volume fraction for three gap sizes. The value of solidity quantifies the relative contribution of the isotropic and anisotropic factors to the growth of domains in the plane parallel to electrodes, decreasing with increasing the role of the anisotropic factor. As can be seen in this figure, the solidity is mainly affected by the sequence in which AC and DC fields were applied. A higher value of solidity is achieved when the AC field was applied first, whereas a lower value is achieved when the DC field was applied first. It is likely related to the fact that the lateral motion of long fibrillose particle structures formed across the gap by the AC field was more limited compared with short particle clusters formed close to the top electrode by the DC field.

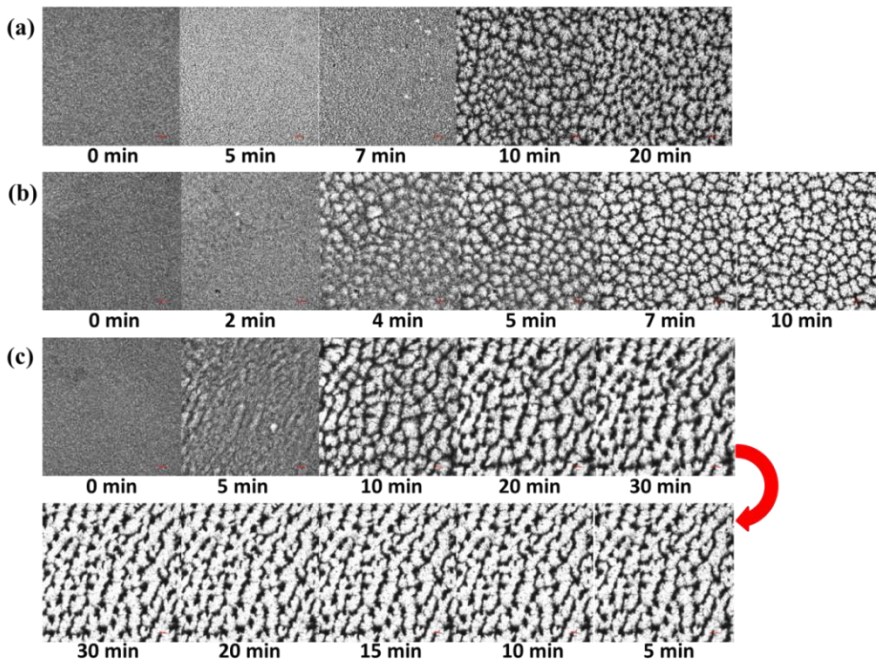

Figure 3.96 Comparison of pattern formation. Cellular patterns formed in 5v/v% suspensions of polyethylene particles (40-48μm) in Envirotemp FR3 oil by applying electric field by different combinations listed. (a) AC field 1.5 kV, 100 Hz applied first and DC field 0.03 kV/mm added after 5min; (b) AC field 1.5 kV, 100 Hz applied first and DC field 0.03 kV/mm applied simultaneously; (c) Top: DC field 0.03kV/mm applied for 30min; Bottom: AC field 1.5kV/mm, 100 Hz added to the DC field. Particles black, particle-free regions white; ITO conducting layers of both electrodes in direct contact with the suspension; top electrode energized, bottom grounded, interelectrode gap 0.5mm. Scale bar 0.1mm.

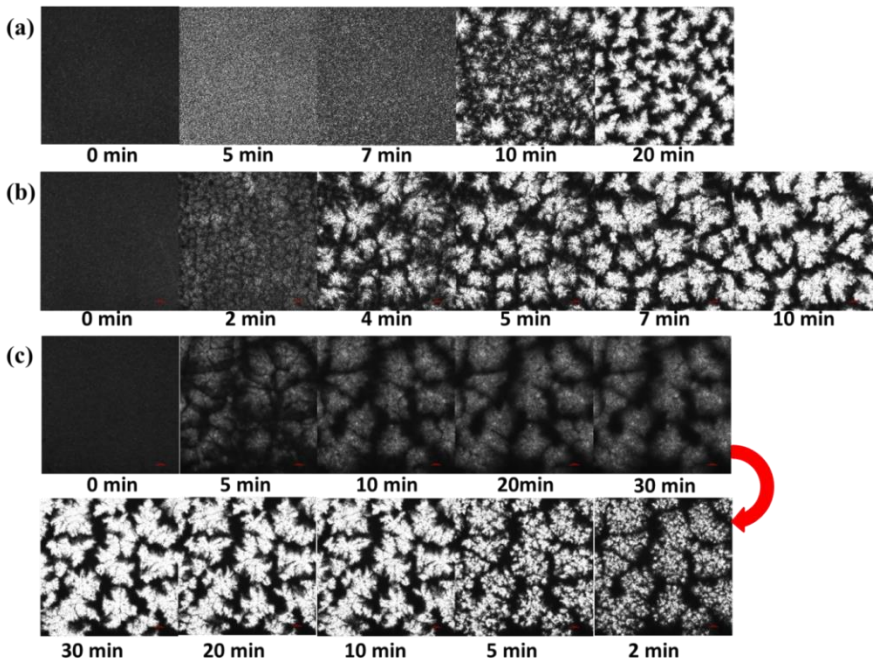

Figure 3.97 Comparison of pattern formation. Cellular patterns formed in 5v/v% suspensions of polyethylene particles (40-48μm) in Envirotemp FR3 oil by applying electric field by different combinations listed. (a) AC field AC field 1.5 kV, 100 Hz applied first and then DC field 0.03 kV/mm added after 5min; (b) AC field AC field 1.5 kV, 100 Hz and DC field 0.03 kV/mm applied simultaneously; (c) Top: DC field 0.03kV/mm applied for 30min; Bottom: AC field AC field 1.5 kV, 100 Hz added to the DC field. Particles black, particle-free regions white; ITO conducting layers of both electrodes in direct contact with the suspension; top electrode energized, bottom grounded, interelectrode gap 2.0mm. Scale bar 0.1mm.

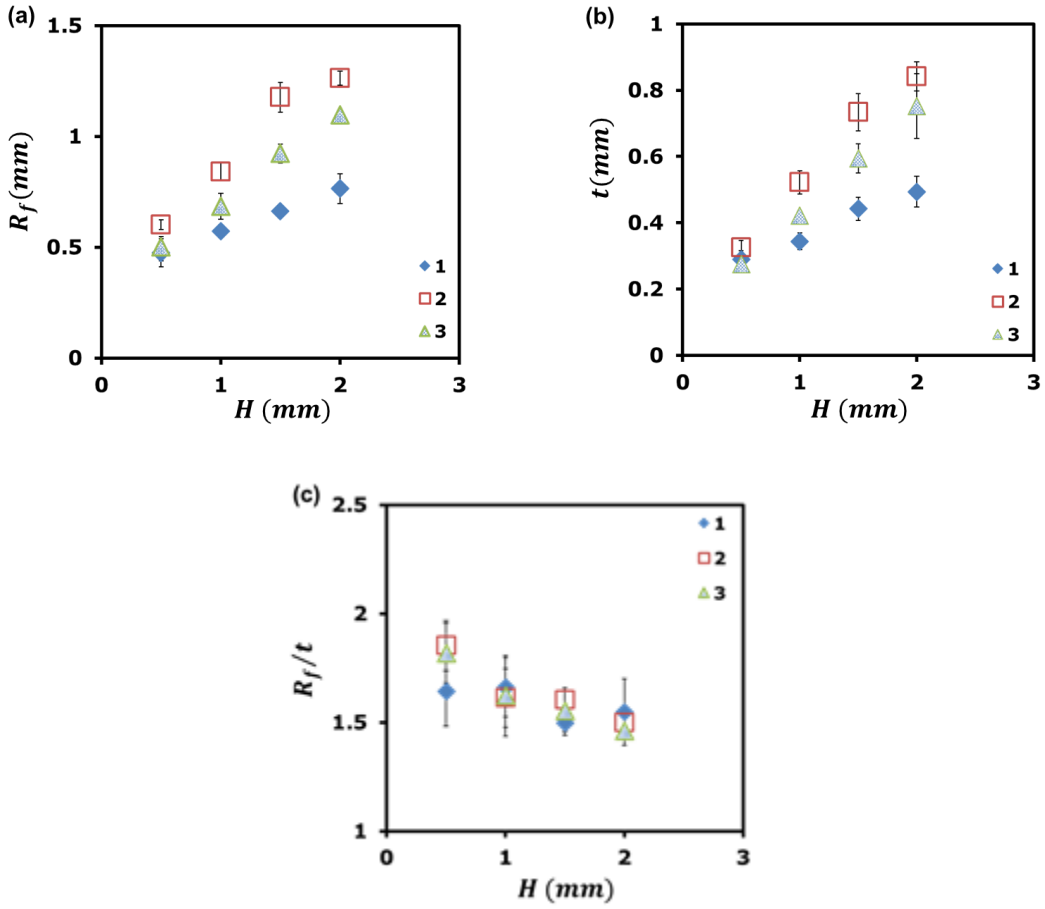

Figure 3.98 Characteristics of pattern. Cellular patterns formed in 5v/v% suspensions of polyethylene particles (40-48μm) in Envirotemp FR3 oil by applying electric field by different sequences listed. 1 (filled diamonds): AC field 1.5 kV, 100 Hz applied first and then DC field $E_{DC} = 0.03 kV/mm$ added after 5min; 2 (open squares): DC field $0.03\ kV/mm$ applied first and then AC field 1.5 kV, 100 Hz added after 30min; 3 (30% filled triangles): AC field $1.5\ kV, 100\ Hz$ and DC field $0.03\ kV/mm$ applied simultaneously. Sample cell 1.5"×1.5", top electrode energized, bottom grounded. Images taken in the plane parallel to electrodes. (a) The mean radius of particle-free domains R_f in mm, (b) the thickness of particle-rich walls t in mm, (c) the ratio between the radius of particle-free domains and the thickness of particle-rich walls R_f/t, as a function of interelectrode gap 0.5-2.0mm.

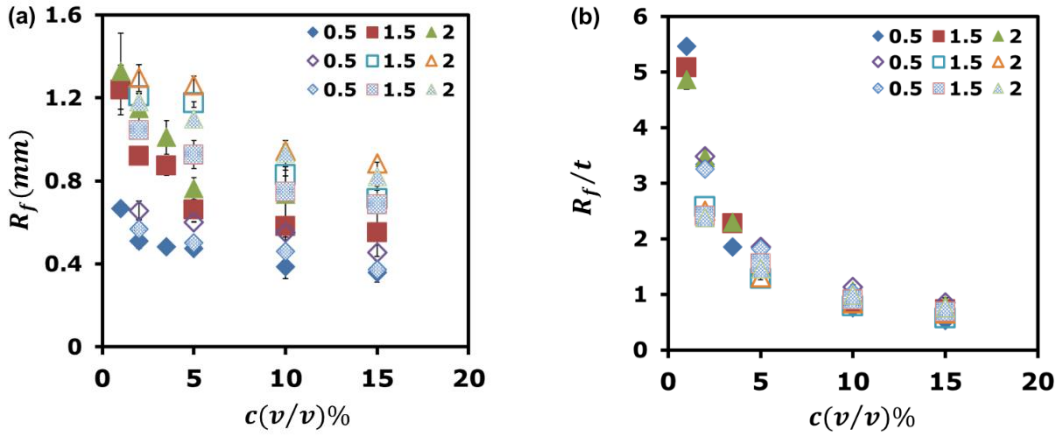

Figure 3.99 Characteristics of pattern. Cellular patterns formed in suspensions of polyethylene particles (40-48μm) in Envirotemp FR3 oil filled in interelectrode gap H in mm listed by applying electric field by different sequences listed. 1 (filled symbols): AC field 1.5 kV, 100 Hz applied first and then DC field 0.03 kV/mm added after 5min; 2 (open symbols): DC field 0.03 kV/mm applied first and then AC field 1.5 kV, 100 Hz added after 30min; 3 (30% filled symbols): AC field 1.5 kV, 100 Hz and DC field 0.03 kV/mm applied simultaneously. Sample cell 1.5"×1.5", top electrode energized, bottom grounded. Images taken in the plane parallel to electrodes. (a) The mean radius of particle-free domains R_f in mm, (b) the ratio between the radius of particle-free domains and the thickness of the particle-rich wall R_f/t, as a function of particle volume concentration $c(v/v)\%$ 1-15v/v%.

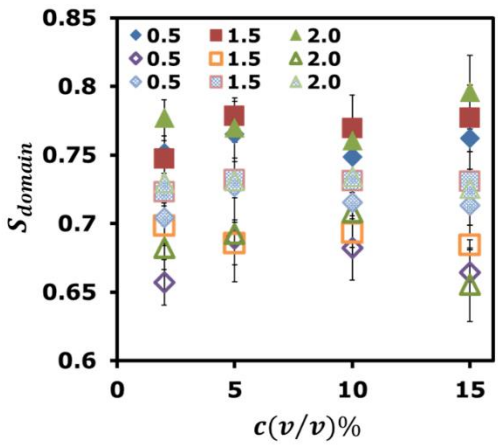

Figure 3.100 Comparison of solidity of particle-free domains. The mean solidity of particle-free domains S_{domain} computed as a function of particle volume concentration $c(v/v)\%$ 2-15v/v%. Cellular patterns formed in suspensions of polyethylene particles (40-48μm) in Envirotemp FR3 oil filled in interelectrode gap H in mm listed by applying electric field by different sequences. 1 (filled symbols): AC field 1.5 kV, 100 Hz applied first and then DC field 0.03 kV/mm added after 5min; 2 (open symbols): DC field 0.03 kV/mm applied first and then AC field 1.5 kV, 100 Hz added after 30min; 3 (30% filled symbols): AC field 1.5 kV, 100 Hz and DC field 0.03 kV/mm applied simultaneously. Sample cell 1.5"×1.5", top electrode energized, bottom grounded. Images taken in the plane parallel to electrodes.

3.5.15 Dilute Suspensions of Positively and Negatively Polarized Particles

A particle is referred to as polarized positively or negatively when the dipole moment induced by an applied electric field is respectively directed in the field direction or in the opposite direction. Suspensions of positively polarized particles were prepared by dispersing polystyrene/polyaniline core–shell spheres (PS/PANI) 1-2μm [138] in silicone oil (Millipore Sigma, St. Louis, MO) with density 0.96 g/cm^3 and viscosity 48.2 cP. The PS/PANI particles were provided by Dr. Hyoung Jin Choi, Professor of Polymer Science & Engineering at Inha University, Korea. Suspensions of negatively polarized particles were prepared by dispersing polyalphaolefin (PAO) particles S-391-N1, 4-5μm (Shamrock Technologies Inc., Newark, NJ) in Mazola corn oil (ACH Food Companies, Inc., Oakbrook Terrace, IL). For convenience, properties of these suspensions are summarized in Tables

3.15 and Table 3.16. As can be seen in these tables, both types of particles have density very close to that of a solvent and both carry a similar negative charge, but polarizability of a polystyrene/polyaniline particle is positive whereas polarizability of a polyalphaolefin particle is negative.

Following the application of a strong high-frequency AC field, particles in both suspensions aggregated head-to-tail to form chains and columns spanning the gap between the electrodes. As was demonstrated in previous sections on large negatively polarized polyethylene and polyalphaolefin particles, adding a weak DC field to the AC field caused the chain and columns in suspensions of these polyalphaolefin particles to rearrange and form a cellular pattern of particle-free domains surrounded by particle-rich walls. However, adding a weak DC field did not affect the arrangement of chains and columns formed by PS/PANI particles. In this section, we explore differences and similarities in the behavior of both suspensions in electric fields to analyze in more detail the effect of the sign of the particle polarizability.

Table 3.15 Properties of Suspensions

Particle	Particle Size (μm)	Density (g/cm^3)	Particle settling velocity (μm/s)	Δρ (g/cm3)	Solvent	Density (g/cm^3)	viscosity (cP)
Polyalphaolefin particle (PAO)	4-5	0.95±0.01	0.012±0.00094	0.068±0.0051	Mazola oil	0.92±0.02	59.8±0.4
Polystyrene/polyaniline core–shell spheres (PS/PANI)	1-2	1.05±0.03	0.002±0.00034	0.078±0.0068	Silicone oil	0.96±0.01	48.2±0.2

Table 3.16 Electrical Properties of Particles

Particle	$-\mu_p$(m^2/V.s) @ E<0.1kV/mm	STD	$-Q_p$(C)	STD	Re(β) @ 100Hz	Im(β) @ 100Hz
Polyalphaolefin particle (PAO)	1.10E-10	5.43E-11	3.10E-16	1.36E-16	-0.2	0.001
Polystyrene/polyaniline core–shell spheres (PS/PANI)	5.05E-10	7.77E-11	2.29E-16	3.43E-17	+0.7	0.24

3.5.15.1 Field-induced transitions. Images in Figure 3.101 illustrate patterns formed in a 0.5 v/v % suspension of polystyrene/polyaniline particles (1-2 μm) in silicone oil by applying AC field 1 kV/mm, 1 kHz and then adding DC field 0.03 V/μm. The application of the AC field for several seconds caused the particles to form chains and columns spanning the gap between electrodes. Adding the DC field however did not affect the arrangement of these chains and columns in the plane parallel to electrodes.

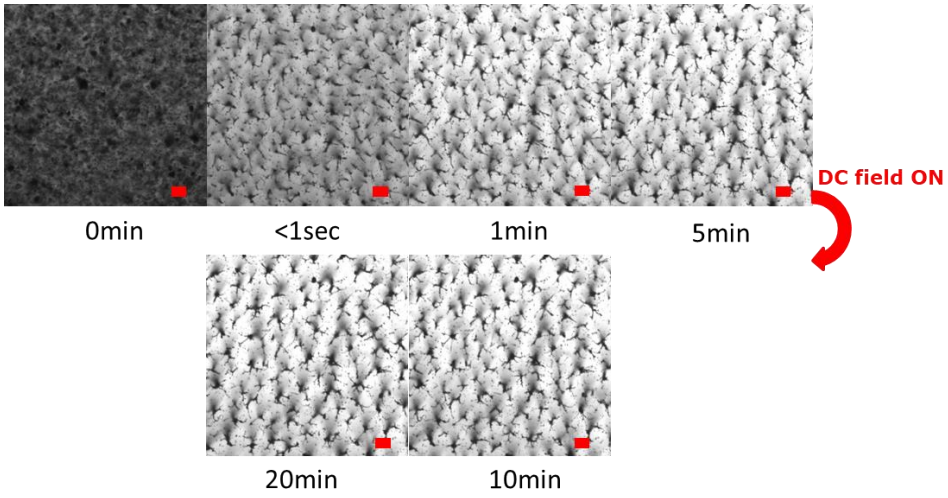

Figure 3.101 Patterns formed in a 0.5 v/v % suspension of polystyrene/polyaniline particles (1-2 μm) in silicone oil; particles black, particle-free regions white; sample cell 1.5"×1.5", conducting layers of both electrodes in direct contact with suspension; top electrode energized, bottom grounded, interelectrode gap 0.5mm. Top: AC field 1 kV/mm, 1 kHz applied. Bottom: DC field 0.03 kV/mm added to the AC field.

The schematic diagram presented in Figure 3.102(a) summarizes our observations on two-step processes of the arrangement of PS/PANI particles following the application of a strong high frequency AC field. In the first step, the particles rapidly form a network of interconnected chains and thin columns. Accordingly, the area fraction covered by the particles in the plane parallel to the electrodes dropped down in a few seconds. However different from polyalphaolefin particles, PS/PANI particles continued slowly rearranging

to form thicker columns that was associated with loosing connectivity between them (Figure 3.102(b)). Adding a weak DC field did not affect these fibrillose structures regardless that the conducting layer of the bottom electrode was partially coated with 3M insulating fluoropolymer liner. (Figure 3.102(c)). If the field frequency was not sufficiently high, the application of a strong AC field initiated an intensive circulating flow of a suspension so that particles formed chains and columns only once this flow ceased. The threshold for the field frequency to suppress the circulating flow increased with increasing the interelectrode gap. In particular, circulating flows did not appear in 1.5-mm gap for the AC field frequency above 1 kHz. While the field frequency influenced the dynamics of particle aggregation, it did not affect the final morphology of fibrillose structures formed in a suspension.

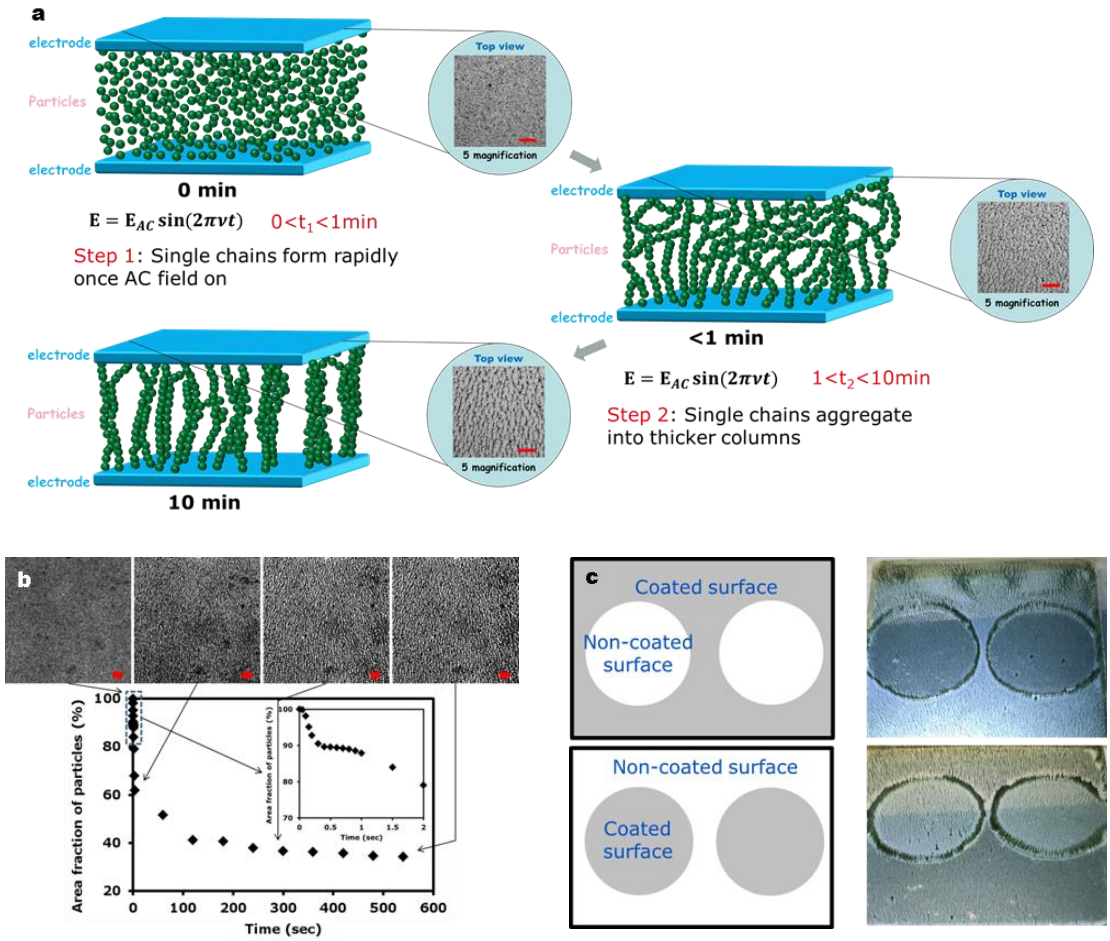

Figure 3.102 Aggregation of positively polarized PS/PANI (1-2 μm) particles suspended in silicone oil following the exposure to an electric field. (a) schematic diagram of two-step processes in strong high frequency AC fields; (b) images of patterns formed in 0.3 v/v % suspension (particles black) and time variation of the area fraction covered by particles in the plane parallel to electrodes, initial period shown in inset; sample cell 1.5" × 1.5",conducting layers of both electrodes in direct contact with suspension, top electrode energized, bottom grounded, interelectrode gap 1.5 mm, AC field 1 kV/mm, 1 kHz; (c) patterns (particles green) formed when conducting layer of bottom electrode was coated with 3M insulating fluoropolymer liner (thickness ~70μm) outside or inside a circle, circular sample cell of diameter 1" interelectrode gap 2 mm; AC field 1 kV/mm, 1 kHz; DC field 0.03 kV/mm added after 5 min.

For comparison, images in Figure 3.103 illustrate patterns that were formed in a dilute suspension of negatively polarized of polyalphaolefin (4-5 μm) in Mazola oil by applying AC fields of 1.5 kV/mm, 1 kHz and adding DC fields 0.03 kV/mm 30 min later. Following the application of the AC field, particles formed chains spanning the gap

between electrodes that gradually rearranged in the plane parallel to electrodes to form a cellular pattern of particle-free domains when the weak DC field was added to the AC field.

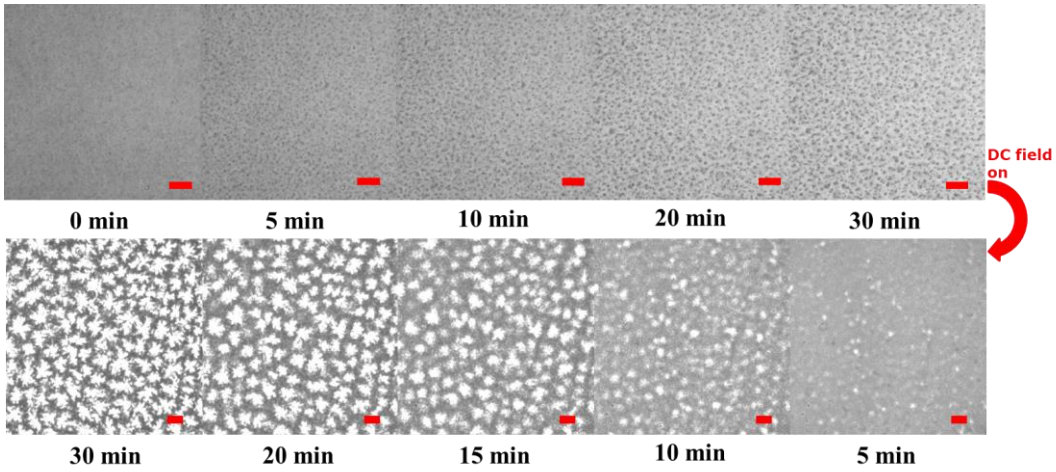

Figure 3.103 Patterns formed in 2 v/v % suspension of polyalphaolefin particles (4-5 μm) in Mazola oil; particles black, particle-free regions white; conducting layers of both electrodes in direct contact with the suspension; sample cell 1.5"×1.5", top electrode energized, bottom grounded, interelectrode gap 1.5 mm. Top: AC field 1.5 kV/mm, 1 kHz applied; scale bar 0.1 mm; Bottom: DC field 0.03 kV/mm added to the AC field; scale bar 1.0 mm.

The schematic diagram presented in Figure 3.104(a) summarizes our observations on three-step processes in 3D->3D transformation in suspensions of polyalphaolefin particles to form a cellular pattern following the application of a strong high frequency AC field and then a weak DC field. These processes appear to be very similar to processes observed in suspensions of large polyalphaolefin and polyethylene particles that were reported in previous sections. Step 1: Single- and multi-chain columns form in a strong high frequency AC field; Step 2: Columns break down and widen as a weak DC field is added; Step 3: Single- and multi-chain columns rearrange in the plane parallel to electrodes to form a cellular pattern of particle-free domains surrounded by particle-rich walls through the entire gap between electrodes.

Plots in Figure 3.104(b) show variation over time of the area fraction covered by particles in the plane parallel to electrodes. Application of a strong high frequency AC field caused the particles to form chains and columns that were evolving along the field direction to span the interelectrode gap. These fibrous particle structures were uniformly distributed in the plane parallel to the electrodes. Adding a weak DC field after 5 min caused them to partially break down and widen, thereby increasing the area fraction covered by the particles in the plane parallel to the electrodes for a period of about 5 min. The rearrangement of these fibrous particle structures to form a set of particle-free domains in the course of about 30 min was accompanied by their alignment and shrinking, gradually decreasing the area fraction covered by the particles in the plane parallel to the electrodes (Figure 3.104(b)). While particles formed chains and columns all over the electrode gap, particle-free domains appeared only in locations where the conducting layer on the bottom electrode was not coated with a 3M insulating fluoropolymer liner (Figure 3.104(c)). Images presented in Figure 3.105 demonstrate a similarity in the density and sizes of particle-free domains formed in circular and square sample cells with interelectrode gaps 1.5 mm and 2 mm, respectively. It indicates that formation of particle-free domains did not start at the outer sides of a sample cell but occurred through bulk nucleation inside the cell.

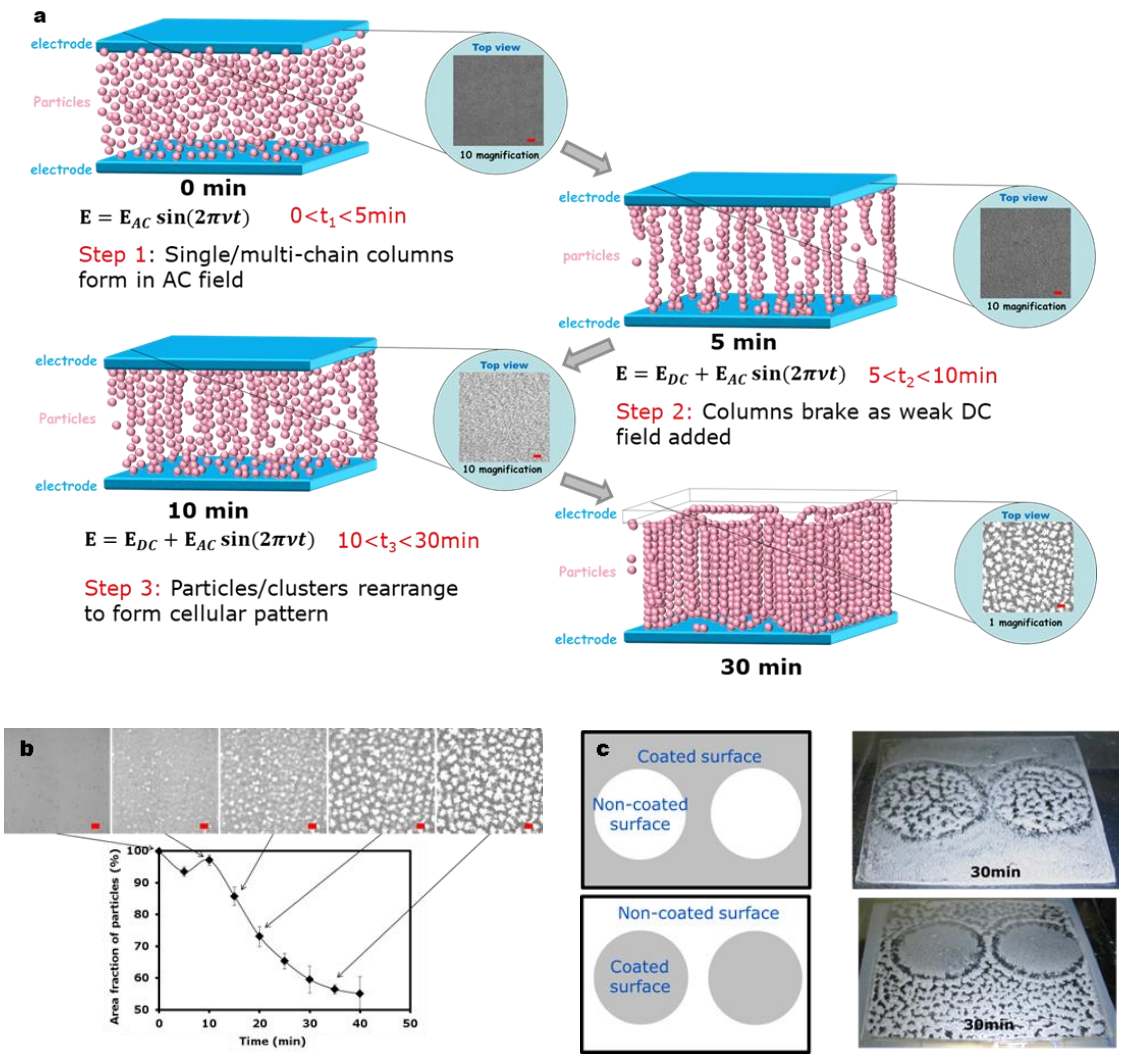

Figure 3.104 Aggregation of negatively polarized polyalphaolefin particles (4-5μm) in Mazola oil following the exposure to AC and DC electric fields. (a) schematic diagram of three-step processes in a strong high frequency AC field and a weak DC field; (b) images of patterns formed in 2 v/v % suspension (particles black) and time variation of the area fraction covered by particles in the plane parallel to electrodes, conducting layers of both electrodes in direct contact with suspension, circular sample cell of diameter 1", top electrode energized, bottom grounded, interelectrode gap 0.5 mm, AC field 1 kV/mm, 100 Hz; DC field 0.03 kV/mm added after 5 min; (c) particle-free domains (particles white) did not form in the region where conducting layer of bottom electrode was coated with 3M insulating fluoropolymer liner (thickness ~70μm), circular sample cell of diameter 1", interelectrode gap 2 mm; AC field 1 kV/mm, 100 Hz; DC field 0.03 kV/mm added after 5 min.

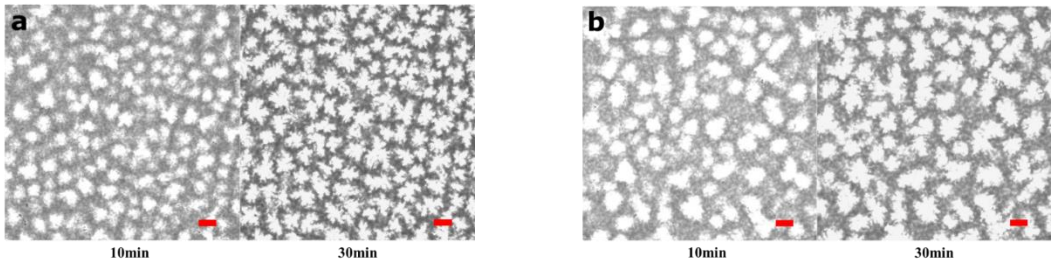

Figure 3.105 Cellular pattern of particle-free domains formed in 2 v/v% suspension of 4-5 μm polyalphaolefin particles (particles black and particle-free domains white), conducting layers of both electrodes in direct contact with suspension, top electrode energized, bottom grounded; AC field 1.5 kV/mm, 100 Hz; DC field 0.03 kV/mm added after 5 min. (a) circular sample cell of diameter 1", interelectrode gap 1.5 mm; (b) square sample cell 1.5"x1.5", interelectrode gap 2 mm. Scale bar 1 mm.

3.5.15.2 Key Variables Affecting Particle Aggregation

Positevly polarized particles. Diagrams presented in Figure 3.106 show the influence of the AC field strength and the sze of the interelectrode gap on the aggreaprocesses in 0.3 v/v% suspension of positively polarized polystyrene/polyaniline particles (~1 μm) in silicone oil. In region 1 of strong low frequency fields, $E_{AC} > 0.2 kV/mm$ and $\nu < 10\ Hz$, oscillations of particles from electrode to electrode initiate vigorous circulation flow in a sample cell that disperse particles clusters formed by an electric field (Figure 3.106(a)). The threshold for the field frequency to suppress the circulating flow increased with increasing the interelectrode gap (Figure 3.106(b)). In region 2 of strong high frequency fields, $E_{AC} > 0.5\ kV/mm$ and $\nu > 10\ Hz$, particles formed thick fibrous aggregates along the entire gap between electrodes. For weak high frequency AC fields, $E_{AC} < 0.5\ kV/mm$ and $\nu > 10\ Hz$, short thin fibrous aggregates formed by particles did not span the interelectrode gap. Therefore, most experiments were carried out by applying AC fields of about 1kV/mm, 1 kHz. Due to a relatively high conductivity of polystyrene/polyaniline

particles, application of higher strength AC fields for a long time lead to overheating of a suspension.

Taking measurements of the real part of permittivity ε' and conductivity σ of silicone oil at 1 *Hz* and 10 *Hz*, we find that the frequency boundary between regions 1 and 2 is related to the charge relaxation time of silicone oil $t_e = \varepsilon_0 \varepsilon' / \sigma$ as $\nu t_e \sim 1$. t_e provides a measure of how long it takes to neutralize an electric charge in the solvent by conduction process. Accordingly, charge transport processes prevail in region 1 whereas polarization processes dominate in region 2.

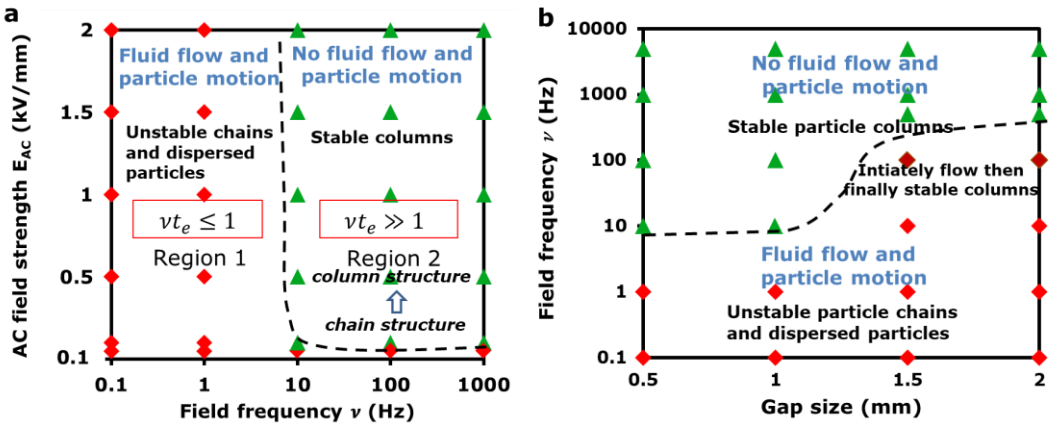

Figure 3.106 Phase diagram for aggregation processes in 0.3 v/v % suspension of positively polarized polystyrene/polyaniline particles (~1 μm) in silicone oil exposed to AC fields. (a) Region 1, $\nu t_e < 1$, low frequency fields, particles form unstable clusters; Region 2, $\nu t_e > 1$, high frequency fields, particles form unstable chains in low strength fields and multi-chain columns in high strength fields; circular sample cell of diameter 1", conducting layers of both electrodes in direct contact with suspension, top electrode energized, bottom grounded; interelectrode gap 1 mm. (b) The threshold for the field frequency to suppress the circulating flow increased with increasing the interelectrode gap size; circular cell of diameter 1", interelectrode gap 0.5mm; square sample 1.5"x1.5", interelectrode gaps 1.0mm, 1.5mm and 2.0mm; AC field 1.0kV/mm applied for 10 min.

Negatively polarized particles. Obseravtions of aggregation patterns formed by the application of a combination of AC and DC fields to suspensions of negatively polarized polyalphaolefin particles (4-5μm) in Mazola oil are summarized in Figure 3.107. They

appear to be very similar to observations of the effects of AC and DC fields on suspensions of large polyalphaolefin and polyethylene particles in Mazola oil that were reported in previous sections. In region 1 of low frequency AC fields of a moderate strength, $1kV/mm > E_{AC} > 0.5kV/mm$ and $\nu < 1Hz$, intensive oscillation of particles between electrodes formed stripy patterns of unstable particle clusters. Low frequency AC fields of a higher strength, $E_{AC} > 1kV/mm$ and $\nu < 1Hz$, generated an intensive circulation flow of a suspension preventing the formation of large particle clusters. Adding a DC field 0.03 kV/mm to a high frequency AC field with a strength within region 2 in Figure 3.107(a) formed stable cellular patterns of particle-free domains surrounded by particle-rich walls. These structures were situated close to the top positive electrode for low field AC field strengths and spanned the entire gap between electrodes for high AC field strengths (Figure 3.107(a)).

Adding a DC field lower than 0.02 kV/mm to a strong high frequency AC field did not cause the particle chains and columns to rearrange and form particle-free domains in the plane parallel to electrodes (Figure 3.107(b)). Stable cellular patterns of particle-free domains surrounded with particle-rich walls were formed for DC field strengths $0.02\,kV/mm < E_{DC} < 0.05kV/mm$. They were situated close to the top positive electrodes for low AC field strengths and spanned the entire gap between electrodes for high AC field strengths (Figure 3.107(b)). Increasing the DC field strength to 0.1kV/mm initiated a circulating flow that rendered particle structures unstable. Intensive circulating flow generated by adding a DC field with $E_{DC} > 0.1kV/mm$ broke down particle chains and columns formed by the application of a strong high frequency AC field (Figure 3.107(b)). Therefore, most experiments on suspension of negatively polarized PAO

spheres (4-5 μm) in Mazola corn oil were carried out by applying AC fields of about 1.5 kV/mm strength, 1kHz and the DC field 0.03kV/mm.

Taking measurements of the real part of permittivity ε' and conductivity σ of Mazola oil at 1 *Hz* and 10 *Hz*, we find that the frequency boundary between regions 1 and 2 is related to the charge relaxation time of silicone oil $t_e = \varepsilon_0 \varepsilon'/\sigma$ as $\nu t_e \sim 1$. t_e provides a measure of how long it takes to neutralize an electric charge in the solvent by conduction process. Accordingly, charge transport processes prevail in region 1 whereas polarization processes dominate in region 2.

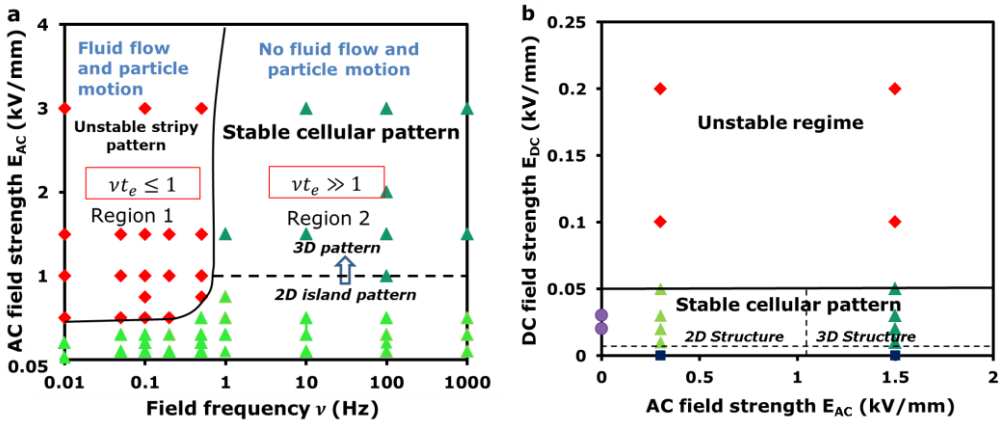

Figure 3.107 Phase diagram for aggregation processes in 2.0v/v% suspension of negatively polarized polyalphaolefin particles (4-5μm) in Mazola oil in AC and DC fields, square sample cell 1.5"x1.5", interelectrode gap 1.5 mm, conducting layers of both electrodes in direct contact with suspension, top electrode energized, bottom grounded. (a) AC field, DC field 0.03 kV/mm added after 5 min, Region 1, $\nu t_e < 1$, low frequency fields, unstable particle clusters formed. Region 2, $\nu t_e > 1$, formed stable particle-free islands on the top electrode in low AC fields and particle-free domains through the gap in strong AC fields; square sample cell 1.5"x1.5", interelectrode gap 1.5 mm. (b) AC field at 100 Hz applied, DC field added after 5 min; weak DC fields form stable particle-free islands on the top electrode in low AC fields and particle-free domains through the interelectrode gap in strong AC fields; unstable particle clusters form in strong DC fields.

3.5.15.3 Kinetics of Structure Formation in Electric Field

Positively polarized polystyrene/polyaniline particles in AC field. To analyze the kinetics of particle aggregation in an AC field, ImageJ software was used to measure time variation of the number of particle-rich columns $N(A)$ on an image whose area was greater than $A(mm^2)$. $N(A) = \int_A^\infty n(A)dA$, where $n(A)$ is the number density of columns with the area $A(mm^2)$. The image area covered by a single particle with a diameter of 1.2 μm is around 0.0000011 mm^2. Therefore $N(A)$ was measured by ImageJ for objects greater than the limiting area $A_{lim} = 0.000001$ mm^2. Time variations of $N(A)$ for $A > A_{lim}$ and for A greater than a set of selected values are respectively shown in Figure 3.108(a) and Figure 3.108(b) for a suspension with the particle concentration $c = 0.5$ v/v %. As can be seen in Figure 3.108(a) and Figure 3.108(b), $N(A)$ for a fixed value of A gradually converges to the steady state.

We were unable to describe variation of $N(A)$ over time with a single curve. It is likely because aggregation of polystyrene/polyaniline particles was associated with two processes. Following the application of an AC field, the particles rapidly formed interconnected fibrillose structures and then continued slowly rearranging to form thicker columns that was accompanied with loosing connectivity. We found that it was possible to approximate data on $N(A)$ at a certain time instant with the exponential fit $N_1(A) = N_0 \exp[-b(A/A^*)]$ for $A < A^*$ and the power-law fit $N_2(A) = N^*(A^*/A)^m$ for $A > A^*$, where A^* varies with time. The requirement for continuity of $N(A)$ and the number density $n(A)$ at $A = A^*$ yields $N_0 = N^*$ and $b = m$. To find parameters in these expressions, we took measurements of $N(A)$ at every time instant and fitted them with $N_1(A)$ for $A < A_k$ and with $N_2(A)$ for $> A_k$, where A_k is a discrete set of points for which ImageJ provided

data. A linear regression for $lnN(A)$ was used in both fittings. The value of A^* was evaluated by finding one or two neighboring points that minimized the squared correlation coefficients for these fittings. A homemade code for finding A^* was written in Matlab. We then computed coefficients N_0 and b.

Figure 3.108(c) shows that A^* decreases with time and approaches a constant value 0.00001 mm^2 at $t \approx 5$ min. Figure 3.108(d) and Figure 3.108(e) show that time variation of coefficients in fittings for three suspensions can be combined as $N_0 = a_0\, exp(pt)$ with $p(1/min) = 0.21 \pm 0.038$ and $ln(a_0) = 5.89 \pm 0.21$; ($b/A^*(1/m^2) = b_0(1/m^2)exp(qt)]$ with $q(1/min) = 0.56 \pm 0.049$ and $ln(b_0(1/m^2)) = 8.31 \pm 0.060$. Less than 10% difference between the computed value of N_0 and the value of N_0 directly given by ImageJ confirms the presented fittings.

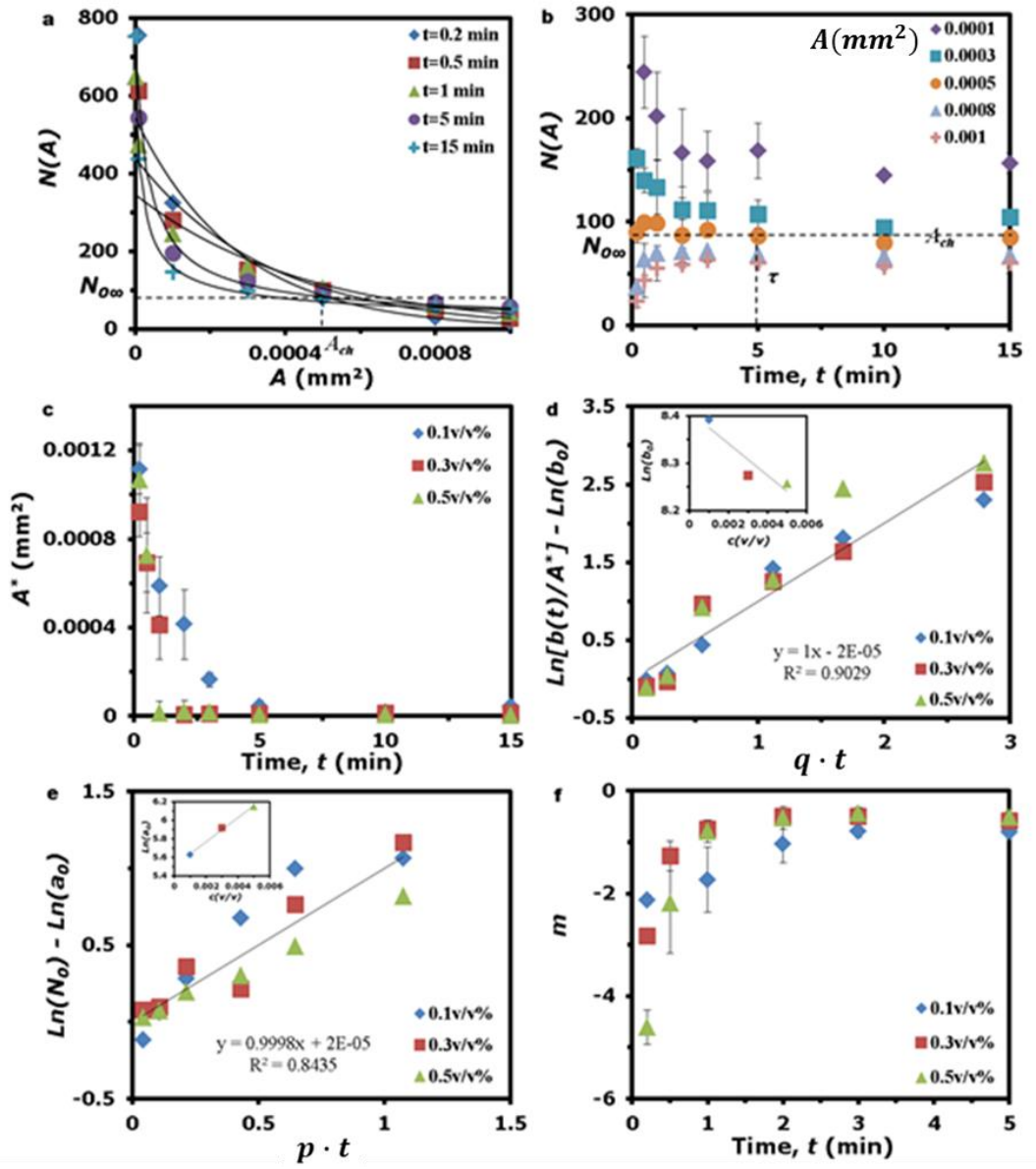

Figure 3.108 Number of particle-rich columns $N(A)$ on an image whose area is greater than $A(mm^2)$ measured with ImageJ at different times for suspensions of polystyrene/polyaniline particles (1-2 μm) in silicone oil. Particle concentrations $c =$ 0.1, 0.3, 0.5 v/v%; sample cell 1.5"×1.5", interelectrode gap 1.5 mm, top electrode energized, bottom grounded. AC field 1.0 kV/mm, 1 kHz. Three experiments conducted for every particle concentration. (a) Time variation of $N(A)$ for $A \geq A_{lim}$, $c =$ $0.5\ v/v\%$. (b) Time variation of $N(A)$ for A greater than a set of listed values, $c =$ $0.5\ v/v\%$. (d) b/A^* in units $1/m^2$.

Negatively polarized polyalphaolefin particles. A similar approach was used to analyze the aggregation kinetics of polyalphaolefin particle in an AC field and the growth of

particle-free domains when a DC field was added. The image area covered by a single particle with a diameter of 4-5 μm is around 0.0000012 mm^2. Therefore $N(A)$ for the particle aggregation in an AC field was measured by ImageJ for objects greater than the limiting area $A_{lim} = 0.000001$ mm^2.

Time variations of $N(A)$ for $A > A_{lim}$ and for A greater than a set of selected values are respectively shown in Figure 3.109(a) and Figure 3.109(b) for a suspension with the particle concentration $c = 3$ v/v %. As can be seen in Figure 3.109(a) and Figure 3.109(b), $N(A)$ for a fixed value of A gradually converges to the steady state. The exponential expression $N(A) = N_0 e^{-b(t)A}$ is able to fit measurements. Figure 3.109(c) and Figure 3.109(d) show that time variation of coefficients in this fitting for three suspensions can be combined as $N_0 = a_0\, exp(pt)$ with $p(1/min) = 0.043 \pm 0.021$ and $ln(a_0) = 5.76 \pm 0.052$; $b(1/m^2) = b_0(1/m^2)exp(qt)$ with $q(1/min) = 0.054 \pm 0.0045$ and $ln(b_0(1/m^2)) = 9.36 \pm 0.080$. Less than 10% difference between the computed value of N_0 and the value of N_0 directly given by ImageJ confirms the presented fittings.

To anlyze formation of particle-free domains caused by adding a DC field, ImageJ software was used to measure time variation of the number of particle-free domains $N(A)$ on an image of a cellular pattern whose area was greater than $A(mm^2)$; $A_{lim} = 0.001$ mm^2 was taken as the limiting area for domains. Time variations of the number of domains $N(A)$ for $A > A_{lim}$ and for A greater than a set of selected values are respectively shown in Figure 3.110(a) and Figure 3.110(b) for a suspension with the particle concentration $c = 3$ v/v %. As can be seen in Figure 3.109(b) and Figure 3.110(b), $N(A)$ for a fixed value of A gradually converges to the steady state. The exponential expression $N(A) = N_0 e^{-b(t)A}$ is able to fit measurements. Figure 3.110(c) and Figure 3.110(d) show that time

variation of coefficients in this fitting for three suspensions can be combined as $N_0 = a_0\, exp(pt)$ with $p(1/min) = -0.0349 \pm 0.0043$ and $ln(a_0) = 5.85 \pm 0.31$; $b(1/m^2) = b_0(1/m^2)exp(qt)$ with $q(1/min) = -0.1213 \pm 0.0054$ and $ln(b_0(1/m^2)) = 3.915 \pm 0.288$. Less than 10% difference between the computed value of N_0 and the value of N_0 directly given by ImageJ confirms the presented fittings.

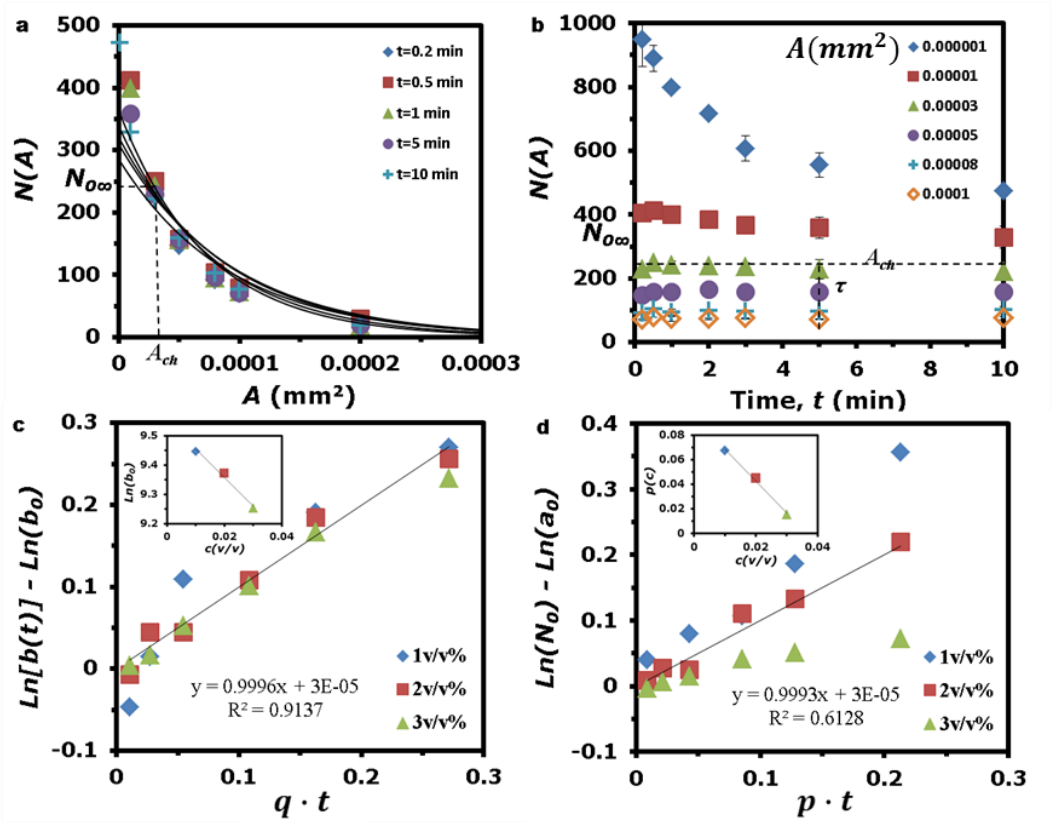

Figure 3.109 Number of particle-rich columns $N(A)$ on an image whose area is greater than $A(mm^2)$ measured with ImageJ at different times for suspensions of polyalphaolefin particles (4-5 μm) in Mazola oil. Particle concentrations c = 1, 2, 3 v/v%; sample cell 1.5"×1.5", interelectrode gap 1.5 mm, top electrode energized, bottom grounded. AC field 1.0 kV/mm, 1 kHz. Three experiments conducted for every particle concentration. (a) Time variation of $N(A)$ for $A \geq A_{lim}$, $c = 3\ v/v\%$. (b) Time variation of $N(A)$ for A greater than a set of listed values, $c = 3\ v/v\%$.

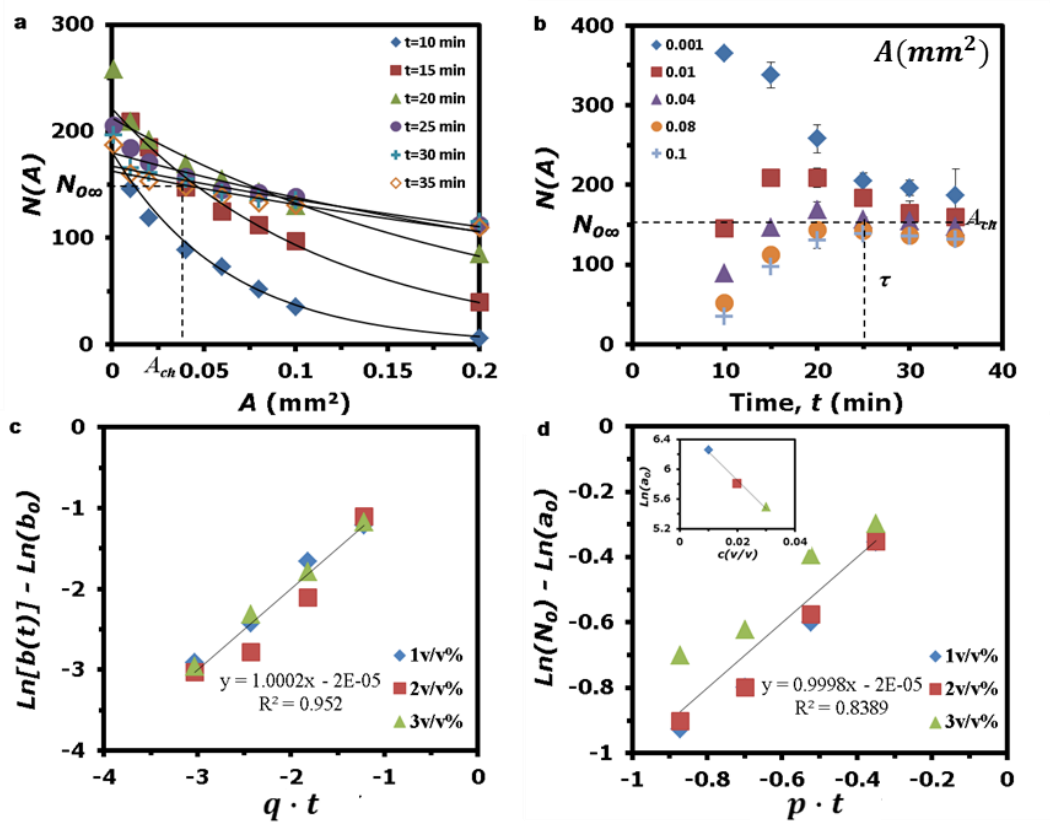

Figure 3.110 Number of particle-free domains $N(A)$ on an image of a cellular pattern whose area is greater than $A(mm^2)$ measured with ImageJ at different times for suspensions of polyalphaolefin particles (4-5 μm) in Mazola oil. Particle concentrations $c = 1,\ 2,\ 3$ v/v%; sample cell 1.5"×1.5", interelectrode gap 1.5 mm, top electrode energized, bottom grounded. DC field 0.03 kV/mm added to AC field 1.0 kV/mm, 1 kHz after 5 min. Three experiments conducted for every particle concentration. (a) Time variation of $N(A)$ for $A \geq A_{lim}$, $c = 3\ v/v\%$. (b) Time variation of $N(A)$ for A greater than a set of listed values, $c = 3\ v/v\%$.

3.6 Conclusion

Recent advances in the development and applications of microfluidic and nanofluidic devices have sparked intense interest in the motion, manipulation and assembly of particles by electrical fields due to low power consumption, no mechanical parts, electrical reversibility, fast response, and high performance. It has been known for centuries that the application of a strong AC or DC field to a suspension of polarized particles will cause the

particles to form head-to-tail chains in the field direction gradually coalescing into thick columns (often referred to as electrorheological effect). A new phenomenon in suspensions of polarized particles was discovered by Kumar, Khusid, Acrivos, Phys Rev Lett 95, 258301, 2005; Agarwal, Yethiraj, Phys Rev Lett 102, 198301, 2009. They found that under certain conditions chains formed by particles in an alternating current (AC) electric field rearrange in the plane perpendicular to the field direction into a cellular pattern of particle-free domains surrounded by particle-rich walls.

The main goal of our study was to find key variables affecting the formation of particle-free domains in suspensions of polarized particles subjected to external alternating (AC) and direct (DC) current fields. Experiments were carried out on a suspension sandwiched between parallel plate electrodes. Tested suspensions were prepared by dispersing polyethylene, polyalphaolefin and polystyrene/polyaniline core–shell (PS/PANI) particles in Mazola oil, Cargill Envirotemp FR3 oil, and silicone oil. To relate the suspension response to an applied electric field, the suspension complex permittivity, the particle sedimentation velocity, the electric charge carried by a particle, and the particle polarizability were measured. As expected, the application of a strong AC field caused particles in all tested suspensions to form head-to-tail chain structures along the field direction. However, rearrangement of these chains in the plane perpendicular to the field direction to form particle-free domains surrounded by particle-rich walls was achieved only in suspensions of negatively polarized particles. It is found that a combination of a strong high frequency AC field and a weak DC field, regardless whether AC and DC fields are applied simultaneously or one after another, is needed for this transition to occur. Presented findings provide detailed guidelines for the AC field strength and frequency, the DC field

strength, and the suspension properties required to suppress undesirable field effects and form a cellular structure of particle-free domains surrounded by particle-rich walls throughout the entire gap between electrodes. Our study demonstates that the coupling of AC and DC fields is a powerful technique for control, manipulation and assembly of polarized particle in various applications.

By accounting solely for dipole-dipole interaction between polarized particles exposed to an electric field, current theories for electric-field driven processes in polarized systems fail to describe the formation of a cellular pattern since they predict that the field effects should depend on the square of the particle polarizability and therefore be the same for negatively and positively polarized particles. Based on our observations, it is suggested that the formation of a cellular pattern by negatively polarized particles is driven by weak multi-particle repulsion. We hope that our findings may inspire further studies into the role of multi-particle interactions in polarized systems.

CHAPTER 4

CONCLUSION

There has been increasing interest in using external electric fields in miniaturized multiphase fluid systems for terrestrial and space applications due to low power consumption, no mechanical parts, electrical reversibility, and high performance. Presented findings show that the fast response and stable operation of single-bubble boiling over a broad range of temperatures pave the way for development of new devices to control heat transfer by forming surface domains with distinct thermal properties and wettability. The bubble lifetime can be adjusted by changing the water temperature. The ability of heating water on millimeter scales far above 100°C without an autoclave or a powerful laser provides a new approach for processing of biomaterials and chemical reactions. Our study demonstrates that the coupling of alternative (AC) and direct (DC) current fields is a powerful technique for control, manipulation and assembly of polarized particle in various applications. Results of our experiments provide detailed guidelines for the AC field strength and frequency, the DC field strength, and the suspension properties required to suppress undesirable field effects and form desired colloidal structures. We hope that our findings may inspire further development of electric-field based technologies for multiphase fluid systems.

REFERENCES

1. Di Macro, P., Grassi, W. Saturated pool boiling enhancement by means of an electric field, *Journal of Enhanced Heat Transfer*, 1, 99–114 (1993).

2. Di Macro, P., Grassi, W. Pool boiling in microgravity old and recent results, *Multiphase Science and Technology*, 19 (2), 141–165 (2007).

3. Winslow, W., Induced Fibration of Suspensions, *Journal of Applied Physics*, 20, 1137 (1949).

4. Kumar, A., Khusid, B., Qiu, Z.Y., Acrivos, A. New electric-field-driven mesoscale phase transitions in polarized suspensions, *Physical Review Letters*, 95, 258301 (2005).

5. Mudawar, I. Assessment of high-heat-flux thermal management schemes. *IEEE Transactions on Components, Packaging, and Manufacturing Technology*, 24, 122–141 (2001).

6. Zhang, H., Mudawar, I. & Hasan, M. Application of flow boiling for thermal management of electronics in microgravity and reduced-gravity space systems. *IEEE Transactions on Components, Packaging, and Manufacturing Technology*, 32, 466–477 (2009).

7. Dhir, V. K. Boiling heat transfer. *Annual Review of Fluid Mechanics*, 30, 365–401 (1998).

8. Workshop on Critical Issues in Microgravity Fluids, Transport, and Reaction Processes in Advanced Human Support Technology, Report No. NASA/TM-2004-212940 (NASA Glenn Research Center, 2004).

9. Recapturing a Future for Space Exploration: Life and Physical Sciences Research for a New Era (Washington, D.C: National Academies Press, 2011).

10. Pioro, I. L., Rohsenow, W., & Doerffer, S. S. Nucleate pool-boiling heat transfer. I: review of parametric effects of boiling surface. *International Journal of Heat and Mass Transfer*, 47, 5033-5044 (2004).

11. Pioro, I. L., Rohsenow, W., & Doerffer, S. S. Nucleate pool-boiling heat transfer. II: assessment of prediction methods. *International Journal of Heat and Mass Transfer*, 47, 5045-5057 (2004).

12. Straub, J. Boiling heat transfer and bubble dynamics in microgravity. *Advances in Heat Transfer*, 35, 57–172 (2001).

13. Kim, J., Benton, J. F., & Wisniewski, D. Pool boiling heat transfer on small heaters: effects of gravity and subcooling. *International Journal of Heat and Mass Transfer,* 45, 3921–3934 (2002).

14. Di Marco, P. Review of reduced gravity boiling heat transfer: European research. *International Journal of Microgravity Science and Application*, 20, 252-263 (2003).

15. Kim, J. Review of reduced gravity boiling heat transfer: US research. *International Journal of Microgravity Science and Application*, 20. 264–271 (2003).

16. Ohta, H. Review of reduced gravity boiling heat transfer: Japanese research, *International Journal of Microgravity Science and Application,* 20, 272-285 (2003).

17. Straub, J. & Zell, M. Transport-mechanisms in natural nucleate boiling in absence of external forces. *Heat Mass Trans*fer, 46, 1147–1157 (2010).

18. Raj, R., Kim, J. & McQuillen, J. Subcooled pool boiling in variable gravity environments. *The American Society of Mechanical Engineers (ASME) Journal of Heat Transfer*, 131, 091502-1-10 (2009).

19. Raj, R., Kim, J. & McQuillen, J. Gravity scaling parameter for pool boiling heat transfer. *The American Society of Mechanical Engineers (ASME) Journal of Heat Transfer,* 132, 091502-1-9 (2010)

20. Raj, R. & Kim, J. Heater size and gravity based pool boiling regime map: transition criteria between buoyancy and surface tension dominated boiling. *The American Society of Mechanical Engineers (ASME) Journal of Heat Transfer,* 132, 091503-1-10 (2010).

21. Raj, R., Kim, J. & McQuillen, J. On the scaling of pool boiling heat flux with gravity and heater size. *The American Society of Mechanical Engineers (ASME) Journal of Heat Transfer*, 134, 011502-1-13 (2012).

22. Di Marco, P. Influence of force fields and flow patterns on boiling heat transfer performance: a review. *The American Society of Mechanical Engineers (ASME) Journal of Heat Transfer,* 134, 030801-1-15 (2012).

23. Barrett, R.T. Fastener Design Manuel, NASA Reference Publication 1228 (Brook Park, Ohio: Lewis Research Center, 1990).

24. Green, D. W. & Perry, R. H. *Perry's Chemical Engineers' Handbook*, 8th Ed (New York City: McGrow Hill, 2007).

25. Lide, D. R. (ed). *CRC Handbook of Chemistry and Physics,* 84th Ed (Boca Raton, Florida: CRC Press, 2003).

26. Haynes, W. M. (ed). *CRC Handbook of Chemistry and Physics*, 95th Ed (Boca Raton, Florida: CRC Press, 2014).

27. Fuller, E.N., Schettler, P.D., Glddlngs, J.D. A new method for prediction coefficients of binary gas - phase diffusion, *Industrial & Engineering Chemistry Research*, 58, 19-27 (1966).

28. Welty, J.R., Rorrer, G.L. & Foster, D.G. *Fundamentals of Momentum, Heat, and Mass Transfer*, 6th Ed (Hoboken, New Jersey: Wiley, 2014).

29. Carslaw, H. S., & Jaeger, J. C., *Conduction of Heat in Solids*, 2nd Ed (Oxford, England: Oxford Univ. Press, 1959).

30. Di Marco, P. & Grassi, W. Effects of external electric field on pool boiling: Comparison of terrestrial and microgravity data in the ARIEL experiment. *Experimental Thermal and Fluid Science*, 35, 780–787 (2011).

31. Di Marco, P., Raj, R. & Kim, J. Boiling in variable gravity under the action of an electric field: results of parabolic flight experiments. *Journal of Physics: Conference Series*, 327, 012039-1-14 (2011).

32. Bari, S.D. & Robinson, A.J. Adiabatic bubble growth in uniform DC electric fields. *Experimental Thermal and Fluid Science*, 44, 114–123 (2013).

33. Di Marco, P., Kurimoto, R. Saccone, G., Hayashi, K. & Tomiyama, A. Bubble shape under the action of electric forces. *Experimental Thermal and Fluid Science*, 49, 160-168 (2013).

34. Saville, D. A. Electrohydrodynamics: The Taylor-Melcher leaky dielectric model. *Annual Review of Fluid Mechanics*, 29, 27-64 (1997).

35. Chu, I.-C., No, H.C. & Song, C.-H. Visualization of boiling structure and critical heat flux phenomenon for a narrow heating surface in a horizontal pool of saturated water. *International Journal of Heat and Mass Transfer*, 62, 142–152 (2013).

36. Chu, I.-C., No, H.C., Song, C.-H. & Euh, D.J. Observation of critical heat flux mechanism in horizontal pool boiling of saturated water. *Nuclear Engineering and Design*, 279, 189–199 (2014).

37. Kim, H., Park, Y. & Buongiorno, J. Measurement of wetted area fraction in subcooled pool boiling of water using infrared thermography. *Nuclear Engineering and Design*, 264, 103– 110 (2013).

38. Ahn, H. S. & Kim, M. K. Visualization study of critical heat flux mechanism on a small and horizontal copper heater. *International Journal of Multiphase Flow*, 41, 1–12 (2012).

39. Goel, P., Nayaka, A.K., Kulkarni, P. P. & Joshi, J. B. Experimental study on bubble departure characteristics in subcooled nucleate pool boiling. *International Journal of Multiphase Flow*, 89, 163–176 (2017).

40. Oka, T., Abe, Y., Mori, Y. H. & Nagashima, A. Pool boiling of n-pentane, CFC-113, and water under reduced gravity: parabolic flight experiments with a transparent heater. *ASME Journal of Heat Transfer*, 117(2), 408-417 (1995).

41. Qiu, D. M., Dhir, V. K., Chao, D., Hasan, M. M., Neumann, E., Yee, G. & Birchenough, A. Single-bubble dynamics during pool boiling under low gravity conditions. J. Thermophys. *Heat Transfer* 16, 336-345 (2002).

42. Bakhru, N. & Lienhard, J.H. Boiling from small cylinders, *International Journal of Heat and Mass Transfer*, 15, 2011-2025 (1972).

43. Inoue, T., Kawae, N. & Monde, M. Effect of subcooling on critical heat flux during pool boiling on a horizontal heated wire. *Heat and Mass Transfer*, 33, 481-488 (1998).

44. Wang, H., Peng, X.F., Wang, B.X. & Lee, D.J. Jet flow phenomena during nucleate boiling. *International Journal of Heat and Mass Transfer*, 45, 1359–1363 (2002).

45. Wang, H., Peng, X.F., Wang, B.X. & Lee, D.J. Bubble sweeping and jet flows during nucleate boiling of subcooled liquids. *International Journal of Heat and Mass Transfer*, 46, 863–869 (2003).

46. Wang, H., Peng, X.F., Lin, W.K., Pan, C. & Wang, B.X. Bubble-top jet flow on microwires. *International Journal of Heat and Mass Transfer*, 47, 2891–2900 (2004).

47. Wang, H., Peng, X.F., Christopher, D.M., Lin, W.K. & Pan, C. Investigation of bubble-top jet flow during subcooled boiling on wires. *International Journal of Heat and Fluid Flow*, 26, 485–494 (2005).

48. Zhou, L., Du, X., Yang, Y., Jiang, P. &Wang, B. Thermocapillary effect on bubble sweeping and circling during subcooled nucleate pool boiling of water over microwire. *International Journal of Heat and Mass Transfer*, 88, 276–283 (2015).

49. Lu, J.F., Peng, X.F. & Bourouga, B. Nucleate boiling modes of subcooled water on fine wires submerged in a pool. *Experimental Heat Transfer*, 19, 95–111 (2006).

50. Lu, J.F. & Peng, X.F. Bubble jet flow formation during boiling of subcooled water on fine wires. *International Journal of Heat and Mass Transfer*, 50, 3966–3976 (2007).

51. Fukada, Y., Haze, I. & Osakabe, M. The effect of fouling on nucleate pool boiling of small wires. *Heat Transfer - Asian Research Journal*, 33, 316-329 (2004).

52. Munro, T.R., Koeln, J.P., Fassmann, A.W., Barnett, R.J. & Ban, H. Phase change heat transfer and bubble behavior observed on twisted wire heater geometries in microgravity. *International Journal of Heat and Fluid Flow*, 47, 21–30 (2014).

53. Munro, T. R. & Ban, H. Flow and heat flux behavior of micro-bubble jet flows observed in thin, twisted-wire, subcooled boiling in microgravity. *Microgravity Science and Technology*, 27, 49–60 (2015).

54. Koeln, J.P., Boulware, J.C., Ban, H. & Dennison, J. Observations on braided thin wire nucleate boiling in microgravity. *International Journal of Heat and Fluid Flow*, 32, 973–981 (2011).

55. Shatto, D. P. & Peterson, G. P. Pool boiling critical heat flux in reduced gravity. *American Society of Mechanical Engineers (ASME) Journal of Heat Transfer*, 121, 865-873 (1999).

56. Lee, H. S. & Merte, H. Spherical vapor bubble growth in uniformly superheated liquids. *International Journal of Heat and Mass Transfer*, 39, 2427-2447 (1996).

57. Lee, H. S. & Merte, H. Hemispherical vapor bubble growth in microgravity: experiments and model. *International Journal of Heat and Mass Transfer*, 39, 2449-2461 (1996).

58. Robinson, A. J. & Judd, R. L. The dynamics of spherical bubble growth. *International Journal of Heat and Mass Transfer*, 47, 5101-5113 (2004).

59. Prosperetti, A. Vapor bubbles. *Annual Review of Fluid Mechanics*, 49, 221-248 (2017).

60. Arpaci, V. S. *Conduction Heat Transfer*, Ch 4 (Boston, Massachusetts: Addison-Wesley, 1966).

61. Petrovic, S., Robinson, T. & Judd, R. L. Marangoni heat transfer in subcooled nucleate pool boiling. *International Journal of Heat and Mass Transfer*, 47, 5115–5128 (2004).

62. Marek, R. & J. Straub, J. Analysis of the evaporation coefficient and the condensation coefficient of water. *International Journal of Heat and Mass Transfer*, 44, 39-53 (2001).

63. Warrier, G. R., Basu, N. & Dhir, V. K. Interfacial heat transfer during subcooled flow boiling. *International Journal of Heat and Mass Transfer*, 45, 3947–3959 (2002).

64. Bejan, A. *Convection Heat Transfer*, 4th Ed (Hoboken, New Jersey: John Wiley & Son, 2013).

65. Lewandowski, W.M., Kubski, P., Khubeiz, J.M., Bieszk, H., Wilczewski, T. & Szymanski, S. Theoretical and experimental study of natural convection heat transfer from isothermal hemisphere. *International Journal of Heat and Mass Transfer*, 40, 101-109 (1997).

66. Suzuki, K. Saitoh, H., Matsumoto, K. High heat flux cooling by microbubble emission boiling. *Annals of the New York Academy of Sciences*, 974, 364–377 (2002).

67. Wang, G. & Ping Cheng, P. Subcooled flow boiling and microbubble emission boiling phenomena in a partially heated microchannel. *International Journal of Heat and Mass Transfer*, 52, 79–91 (2009).

68. Ueno, I., Ando, J. Koiwa, Y., Saiki, T. Kaneko, T. Interfacial instability of a condensing vapor bubble in a subcooled liquid. *The European Physical Journal Special Topics*, 224, 415–424 (2015).

69. Gerlach, D., Biswas, G., Durst, F. & Kolobaric, V. Quasi-static bubble formation on submerged orifices. *International Journal of Heat and Mass Transfer*, 48, 425–438 (2005).

70. Lesage, F.J., Cotton, J.S. & Robinson, A.J. Analysis of quasi-static vapour bubble shape during growth and departure. *Physics of Fluids*, 25, 067103-1-21 (2013).

71. Lesage, F.J. & Marois, F. Experimental and numerical analysis of quasi-static bubble size and shape characteristics at detachment. *International Journal of Heat and Mass Transfer*, 64, 53–69 (2013).

72. Bari, S.D. & Robinson, A.J. Experimental study of gas injected bubble growth from submerged orifices. *Experimental Thermal and Fluid Science*, 44, 124–137 (2013).

73. Serway, R.A., Jewett, J.W. *Physics for Scientists and Engineers*, V. 2, 8th Ed. Boston, Massachusetts: Cengage Learning (2009).

74. Jones, T.B. *Electromechanics of Particles*, Cambridge, England: Cambridge University Press, (1995).

75. Russel, W.B., Saville, D.A., Schowalter, W.R. *Colloidal Dispersions*, Cambridge, England: Cambridge University Press (1989).

76. Dussaud, A., Khusid, B., Acrivos, A. Particle segregation in suspensions subject to high-gradient ac electric fields, *Journal of Applied Physics*, 88, 5463 (2001).

77. Qiu, Z., Markarian, N., Khusid, B., Acrivos, A. Positive dielectrophoresis and heterogeneous aggregation in high-gradient ac electric fields, *Journal of Applied Physics*, 82, 4839 (2002).

78. Yethiraj, A. Tunable colloids: control of colloidal phase transitions with tunable interactions, *Soft Matter*, 3, 1099–1115 (2007).

79. Gasser, U. Crystallization in three- and two-dimensional colloidal suspensions, *Journal of Physics: Condensed Matter*, 21, 203101 (2009).

80. Li, F., Josephson, D.P., Stein, A. Colloidal assembly: The road from particles to colloidal molecules and crystals, *Angewandte Chemie International Edition*, 50, 360-388 (2011).

81. Palberg, T. Crystallization kinetics of colloidal model suspensions: recent achievements and new perspectives (Topical Review), *Journal of Physics: Condensed Matter*, 26 33310-1-22 (2014).

82. Vogel, N., Retsch, M., Fustin, C.-A., del Campo, A., Jonas, U. Advances in colloidal assembly: The design of structure and hierarchy in two and three dimensions, *Chemical Reviews*, 115, 6265–6311 (2015).

83. Sanchez, C., Arribart, H., Guille, G.M.M. Biomimetism and bioinspiration as tools for the design of innovative materials and systems, *Nature Materials*, 4, 277−288 (2005).

84. Pethig, R. Dielectrophoresis: Status of the theory, technology, and applications (Review), *Biomicrofluidics* 4, 022811 (2010).

85. Sheng, P., Wen, W. Electrorheological fluids: mechanisms, dynamics, and microfluidics applications, *Annual Review of Fluid Mechanics*, 44, 143-174 (2012).

86. Liu, Y.D., Choi, H.J. Electrorheological fluids: smart soft matter and characteristic (review), *Soft Matter*, 8, 11961–11978 (2012).

87. Khusid, B., Acrivos, A. Effects of conductivity in electric-field-induced aggregation in electrorheological fluids, *Physical Review E*, 52(2), 1669-1693 (1995).

88. Khusid, B., Acrivos, A. Phase diagrams of electric-field-induced aggregation in conducting colloidal suspensions, *Physical Review E*, 60(3), 3015-3035 (1999).

89. Klass, D.L., Martinek, T.W. Electroviscous Fluids. I. Rheological Properties, *Journal of Applied Physics*, 38, 67 (1967).

90. Klass, D.L., Martinek, T.W. Electroviscous Fluids. II. Electrical Properties, *Journal of Applied Physic*, 38, 75 (1967).

91. Stangroom, J.E. Electrorheological fluids, *Physics in Technology*, 14, 290 (1983).

92. Bonnecaze, R. T., Brady, J. F. Yield stresses in electrorheological fluids, *Journal of Rheology*, 36(1), 73 (1992).

93. Felici, N.J., Foulc, J.N., Atten, P. A conduction model of electrorheological effects, *International Journal of Modern Physics B*, 8, 2731-2745 (1994).

94. Anderson, R.A. Electrostatic forces in an ideal spherical-particle electrorheological fluid, *Langmuir*, 10, 2917 (1994).

95. Otsubo, Y., Edamura, K. Electrorheology of dilute suspensions induced by hydrodynamic instability, *Journal of Non-Newtonian Fluid Mechanics*, 71, 183 (1997).

96. Ginder JM. Diffuse optical probes of particle motion and structure formation in an electrorheological fluid, *Physical Review E*, 47(5), 3418- 3429 (1993).

97. Halsey, T.C. Electrorheological Fluids, *Science*, 258, 761 (1992).

98. Martin, J.E., Odinek, J., Halsey, T.C. Evolution of structure in a quiescent electrorheological fluid, *Physical Review Letters*, 69, 1524-1527 (1992).

99. Martin, J.E., Odinek, J., Halsey, T.C., Kamien, R. Structure and dynamics of electrorheological fluids, *Physical Review*, 57(1), 756-774 (1998).

100. Tao, R., Sun, J.M. Three-dimensional structure of induced electrorheological solid, *Physical Review Letters* 67, 398-40 (1991).

101. Tao, R., Sun, J.M. Ground sate of electrorheological fluids from Monte Carlo simulation, *Physical Review A*, 44, 6181-6184 (1991).

102. Chen, T.J., Zitter, R.N., Tao R. Laser diffraction determination of the crystalline structure of an electrorheological fluid, *Physical Review Letters*, 68, 255-258, (1992).

103. Okubo, T., Ishiki, H. Kinetic analyses of colloidal crystallization in a sinusoidal electric field as studied by reflection spectroscopy, *Journal of Colloid and Interface Science*, 211, 151–159 (1999).

104. Dassanayake, U., Fraden, S., van Blaaderen, A. Structure of electrorheological fluids, *Journal of Chemical Physics*, 112, 3851-3858 (2000).

105. Hass, K.C. Computer simulations of nonequilibrium structure formation in electrorheological fluids, *Physical Review E*, 47, 3362-3372 (1993).

106. Gulley, G.L., Tao, R. Structures of an electrorheological fluid, *Physical Review E*, 56, 4328-4335, (1997).

107. Hynninen, A-P., Dijkstra, M. Phase diagram of dipolar hard and soft spheres: manipulation of colloidal crystal structures by an external field, *Physical Review Letters*, 94, 138303 (2005).

108. Tavares, J.M., Weis, J.J., Telo da Gama, M.M. Phase transition in two-dimensional dipolar fluids at low densities, *Physical Review E*, 73, 041507 (2006).

109. Richardi, J., Weis, J-J. Low density mesostructures of confined dipolar particles in an external field, *Journal of Chemical Physics*, 135, 124502 (2011).

110. Almudallal, A.M., Saika-Voivod, I. Simulation of a two-dimensional model for colloids in a uniaxial electric field, *Physical Review E*, 84, 011402 (2011).

111. Sherman, Z.M., Ghosh, D., Swan, J.W. Field-directed self-assembly of mutually polarizable nanoparticles, *Langmuir* 34, 7117−7134 (2018).

112. Markarian, N, Yeksel, M., Khusid, B., Kumar, A, Tin P. Effects of clinorotation and positive dielectrophoresis on suspensions of heavy particles, *Physics of Fluids*, 16, 1826-1829 (2004).

113. Kumar, A, Khusid, B, Qiu, Z.Y., Acrivos A. New electric-field-driven mesoscale phase transitions in polarized suspensions, *Physical Review Letters*, 95, 258301, (2005).

114. Agarwal, A.K., Yethiraj, A. Low-density ordered phase in brownian dipolar colloidal suspensions, *Physical Review Letters*, 102, 198301 (2009).

115. Flores, G.A., Liu, J, Mohebi, M., Jamasbi, N. Magnetic-field-induced nonequilibrium structures in a ferrofluid emulsion, *Physical Review E*, 59, 751- (1999).

116. Lide D.R. ed., *CRC Handbook of Chemistry and Physics*, Boca Raton, Florida: CRC Press (2005).

117. Lu, Z., Manias, E., Macdonald, D.D., Lanagan, M. Department dielectric relaxation in dimethyl sulfoxide/water mixtures studied by microwave dielectric relaxation spectroscopy, *Journal of Physical Chemistry A*, 113, 12207–12214 (2009).

118. Kumar, A., Qiu, Z., Acrivos, A., Khusid, B., Jacqmin, D. Combine negative dielectrophoresis and phase separation in nondilute suspensions subject to a high-gradient ac electric field, *Physical Review E*, 69, 021402 (2004).

119. Montgomery, D.C. *Design and Analysis of Experiments*, 8th Edition, Hoboken, NJ: John Wiley & Sons (2012).

120. Stauffer, D., Aharony, A. *Introduction to Percolation Theory* (2nd Edition). London: Taylor and Francis (1992).

121. Hunt, R.E., Ghanbarian, B. *Percolation Theory for Flow in Porous Media*, 3rd Edition. Heidelberg/Berlin Germany: Springer (2014).

122. Western, G. B., Grayson, R.B. Toward capturing hydrologically significant connectivity in spatial patterns. *Water Resources Research*, 37, 83 –97 (2001).

123. Schlüter, S., Vogel, H.-J. On the reconstruction of structural and functional properties in random heterogeneous media. *Advances in Water Resou*rces, 34, 314–325 (2011).

124. Renard, P., Allard, D. Connectivity metrics for subsurface flow and transport. *Advances in Water Resou*rces, 51, 168–196 (2013).

125. Nieber, J.L., Steenhuis, T.S., Walter, T., Bakker, M. Enhancement of seepage and lateral preferentialflow by biopores on hillslopes. *Biologia*, 61, S225 –S228 (2006).

126. Liu, J., Regenauer-Lieb, K. Application of percolation theory to microtomography of structured media: percolation threshold, critical exponents, and upscaling. *Physical Review E*, 83, 016106 (2011).

127. Schindelin, J., Arganda-Carreras, I., Frise, E., Kaynig, V., Longair, M., Pietzsch, T. Fiji: an open-source platform for biological-image analysis. *Nature Methods*, 9, 676–682 (2012).

128. Doube, M., Klosowski, M. M., Arganda-Carreras, I. F., Cordelieres, P., Dougherty, R. P., Jackson, J.S., BoneJ: free and extensible bone image analysis in ImageJ. *Bone* 47, 1076–1079 (2010).

129. Renard, P., Allard, D., Connectivity metrics for subsurface flow and transport. *Advances in Water Resou*rces, 51, 168–196 (2013).

130. Jarvis, N., Larsbo, M., Koestel, J., Connectivity and percolation of structural pore networks in a cultivated silt loam soil quantified by X-ray tomography, *Geoderma* 287, 71–79 (2017).

131. Koestel, J., SoilJ: An ImageJ plugin for the semiautomatic processing of three dimensional x-ray images of soils, *Vadose Zone Journal*, 03, 0062 (2017).

132. Schlüter, S., Sheppard, A., Brown, K., Wildenschild. D., Image processing of multiphase images obtained via X- ray microtomography: A review. *Water Resources Research*, 50, 3615–3639 (2014).

133. Hovadik, J. M., Larue, D. K. Static characterizations of reservoirs: Refining the concepts of connectivity and continuity, *Petroleum Geoscience*, 13(3), 195-211 (2007).

134. Watanabe, H., Non-equilibrium relaxation analysis on two-dimensional melting, *Progress in Theoretical Physics*, 178, 41 (2009).

135. Mickel W., Kapfer S.C., Schröder-Turk G.E., Mecke K., Shortcomings of the bond orientational order parameters for the analysis of disordered particulate matter, *Journal of Chemical Physics*,138, 044501 (2013).

136. Andrienko, Y. A., Brilliantov, N. V., Krapivsky, P. L. Pattern formation by growing droplets: The touch-and-stop model of growth, *Journal of Statistical Physics*, 75, 507-523. (1994).

137. Axilrod, B. M., Teller, E. Interaction of the van der Waals type between three atoms. *Journal of Chemical Physics*, 11, 299 (1943).

138. Liu, Y.D. Park, B.J. Kim, Y.H. Choi, H.J. Smart monodisperse polystyrene/polyaniline core–shell structured hybrid microspheres fabricated by a controlled releasing technique and their electro-responsive characteristics, *Journal of Materials Chemistry*, 21, 17396–17402 (2011)

139. J. Broeke, J. M. M. Perez, J. Pascau. *Image Processing with ImageJ*, 2rd edition, Birmingham, England: Packt Publishing (2015).

140. Vilanova, N., De Feijter, I., Voets, I.K. Synthesis and characterization of supramolecular colloids. *Journal of Visualized Experiments*. (110), e53934, doi:10.3791/53934 (2016).